AD-A193 525 WIND TUNNEL TESTS OF ELLIPTICAL MISSILE BODY CONFIGURATIONS AT MACH NUMBE..(U) AIR FORCE WRIGHT AERONAUTICAL LABS WRIGHT-PATTERSON AFB OH.. 1/2

UNCLASSIFIED D E SHEREDA ET AL. DEC 87 AFWAL-TR-87-3088 F/G 16/2.1 NL

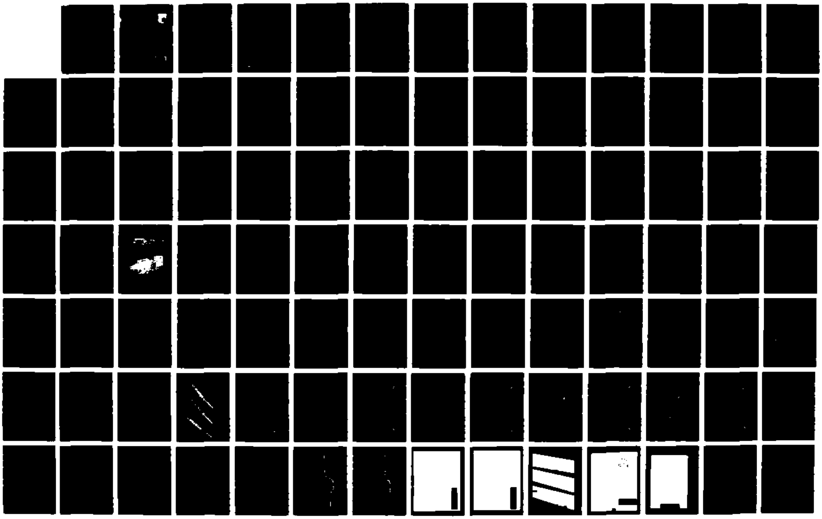

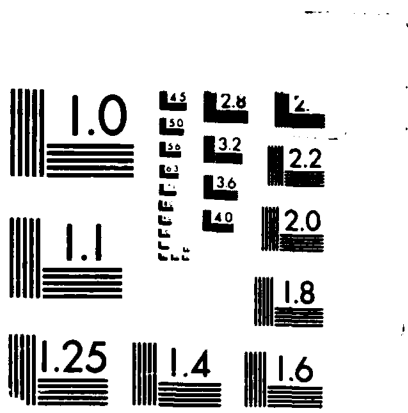

MICROCOPY RESOLUTION TEST CHART

IREAU STANDARDS 1963 A

AFWAL-TR-87-3088

WIND TUNNEL TESTS OF ELLIPTICAL MISSILE BODY CONFIGURATIONS AT MACH NUMBERS 0.4 TO 5.0

DONALD E. SHEREDA
Lt PAUL F. AMIDON
VALENTINE DAHLEM III
High Speed Aero Performance Branch
Aeromechanics Division

December 1987

FINAL REPORT FOR PERIOD FEBRUARY 1983 to JUNE 1986

APPROVED FOR PUBLIC RELEASE; DISTRIBUTION UNLIMITED

FLIGHT DYNAMICS LABORATORY
AIR FORCE WRIGHT AERONAUTICAL LABORATORIES
AIR FORCE SYSTEMS COMMAND
WRIGHT-PATTERSON AIR FORCE BASE OHIO 45433-6553

NOTICE

When Government drawings, specifications, or other data are used for any purpose other than in connection with a definitely Government-related procurement, the United States Government incurs no responsibility or any obligation whatsoever. The fact that the Government may have formulated or in any way supplied the said drawings, specifications, or other data, is not to be regarded by implication, or otherwise in any manner construed, as licensing the holder, or any other person or corporation; or as conveying any rights or permission to manufacture, use, or sell any patented invention that may in any way be related thereto.

This report has been reviewed by the Office of Public Affairs (ASD/PA) and is releasable to the National Technical Information Service (NTIS). At NTIS, it will be available to the general public, including foreign nations.

This technical report has been reviewed and is approved for publication.

Donald E. Shereda

DONALD E. SHEREDA
Project Engineer
High Speed Aero Performance Br.
Aeromechanics Division

Valentine Dahlem

VALENTINE DAHLEM, Chief
High Speed Aero Performance Branch
Aeromechanics Division

FOR THE COMMANDER

Alfred C. Draper

ALFRED C. DRAPER
Acting Chief, Aeromechanics Division
Flight Dynamics Laboratory

If your address has changed, if you wish to be removed from our mailing list, or if the addressee is no longer employed by your organization please notify AFWAL/FIMG, Wright-Patterson AFB, OH 45433-6553 to help us maintain a current mailing list.

Copies of this report should not be returned unless return is required by security considerations, contractual obligations, or notice on a specific document.

UNCLASSIFIED
SECURITY CLASSIFICATION OF THIS PAGE

REPORT DOCUMENTATION PAGE

Form Approved
OMB No. 0704-0188

1a. REPORT SECURITY CLASSIFICATION UNCLASSIFIED	1b. RESTRICTIVE MARKINGS
2a. SECURITY CLASSIFICATION AUTHORITY	3. DISTRIBUTION/AVAILABILITY OF REPORT Approved for Public Release Distribution Unlimited
2b. DECLASSIFICATION/DOWNGRADING SCHEDULE	
4. PERFORMING ORGANIZATION REPORT NUMBER(S) AFWAL-TR-87-3088	5. MONITORING ORGANIZATION REPORT NUMBER(S)
6a. NAME OF PERFORMING ORGANIZATION Aeromechanics Division Flight Dynamics Laboratory 6b. OFFICE SYMBOL *(If applicable)* AFWAL/FIMG	7a. NAME OF MONITORING ORGANIZATION
6c. ADDRESS *(City, State, and ZIP Code)* Wright-Patterson AFB, OH 45433-6553	7b. ADDRESS *(City, State, and ZIP Code)*
8a. NAME OF FUNDING/SPONSORING ORGANIZATION 8b. OFFICE SYMBOL *(If applicable)*	9. PROCUREMENT INSTRUMENT IDENTIFICATION NUMBER
8c. ADDRESS *(City, State, and ZIP Code)*	10. SOURCE OF FUNDING NUMBERS PROGRAM ELEMENT NO. 62201F PROJECT NO. 2404 TASK NO. 07 WORK UNIT ACCESSION NO. 75

11. TITLE *(Include Security Classification)*

Wind Tunnel Tests of Elliptical Missile Body Configurations at Mach Number 0.4 to 5.0.

12. PERSONAL AUTHOR(S)
Shereda, Donald E., Amidon, Lt Paul F., Dahlem, III, Valentine

13a. TYPE OF REPORT	13b. TIME COVERED	14. DATE OF REPORT *(Year, Month, Day)*	15. PAGE COUNT
Final	FROM Feb 83 TO Jun 86	December 1987	161

16. SUPPLEMENTARY NOTATION

17. COSATI CODES

FIELD	GROUP	SUB-GROUP
16	04	
01	01	

18. SUBJECT TERMS *(Continue on reverse if necessary and identify by block number)*

Missile Aerodynamics; Wind Tunnel Data; Elliptical Bodies.

19. ABSTRACT *(Continue on reverse if necessary and identify by block number)*

A large body of wind tunnel data was generated by tests of missile bodies of varying ellipticity ratios. The tests were conducted at subsonic through high supersonic speeds at angles of attack from -4 to 20 degrees. Measurements of both surface pressure and total forces and moments were made at a variety of Mach numbers and Reynolds number combinations. This data was supplemented with flow visualization data such as vapor screens, oil flows and shadowgraphs at selected supersonic Mach numbers. The missile bodies were power-law bodies with an exponent of 0.5 and ellipticity ratios of 2.0, 2.5, and 3.0 to 1. Comparisons of selected data with various prediction codes (Supersonic/Hypersonic Arbitrary Body Program, NSWC Euler Code, Missile Datcom, and FLO-57 Euler Code) were made. The test data provided insight into the effects of several variables and will provide a good data base for correlations with numerical techniques.

20. DISTRIBUTION/AVAILABILITY OF ABSTRACT ☒ UNCLASSIFIED/UNLIMITED ☐ SAME AS RPT. ☐ DTIC USERS	21. ABSTRACT SECURITY CLASSIFICATION UNCLASSIFIED
22a. NAME OF RESPONSIBLE INDIVIDUAL Donald E. Shereda	22b. TELEPHONE *(Include Area Code)* 513-255-5464 22c. OFFICE SYMBOL AFWAL/FIMG

DD Form 1473, JUN 86 *Previous editions are obsolete.*

SECURITY CLASSIFICATION OF THIS PAGE
UNCLASSIFIED

FOREWORD

This technical report summarizes research performed in-house at the High Speed Aero Performance Branch, Aeomechanics Division, Flight Dynamics Laboratory, Air Force Wright Aeronautical Laboratories, Wright-Patterson Air Force Base, Ohio. The work was performed under Project 2404, "Aeromechanics," Task 240407, "Aeroperformance and Aeroheating Technology," Work Units 24040754, "Aerodynamic Flow Field Approximations," and 24040775, "Lifting Entry Configurations." The study period was February 1983 to June 1986.

The experimental program described in this report produced a very large amount of data. The results are summarized here, but in many cases the results of a particular test condition are omitted. Data lists are available to qualified research engineers upon request from the High Speed Aero Performance Branch.

TABLE OF CONTENTS

TABLE OF CONTENTS (Continued)

LIST OF ILLUSTRATIONS

LIST OF ILLUSTRATIONS

LIST OF ILLUSTRATIONS

LIST OF TABLES

SECTION 1.0

INTRODUCTION

The prediction of the aerodynamic characteristics of the latest missile configurations being studied has involved elliptical cross-section missile bodies. Past efforts in this area have shown deficiencies in predicting the aerodynamic characteristics of these type of configurations. The first task of an AFWAL/FIMG contracted effort entitled, "Aerodynamic Analysis for Missiles" was the evaluation of 10 aerodynamic prediction methods for four classes of missile configurations. The lifting missile class consisted of elliptical body configurations with wings and tails. The limited comparisons made of the Supersonic-Hypersonic Arbitrary Body Program (S/HABP) with the elliptical bodies for Mach numbers from 2.0 to 4.0 showed poor results, particularly at the lower Mach numbers.

An in-house work element was then initiated to more completely determine which methods or combination of methods available in the S/HABP code could give acceptable results for this type of missile body. Test data for several missile bodies ranging from circular to a 3-to-1 ellipticity ratio for Mach numbers 1.5 to 4.63 were compared with the results from the S/HABP code using a variety of pressure methods. The results of the effort showed that no typical application of any of the pressure methods in S/HABP would provide good results across the Mach number range and that parametric wind tunnel data, particularly pressure data, would be required to determine the cause of the mismatch of theory versus test.

To provide these data, a series of wind tunnel tests were conducted in the AEDC VKF Tunnel A facility on basic elliptical missile bodies. Three elliptical body models with ellipticity ratios of 3.0:1, 2.5:1, and 2.0:1 were built and tested at Mach numbers from 1.5 to 5.0. Both force and moment and pressure data were obtained as well as flow visualization data such as vapor screens, oil flow, and shadowgraphs.

To complete the test data base, the three elliptical body models were tested in the Aerodynamic Wind Tunnel (4T) of the Propulsion Wind Tunnel Facility at Mach numbers from 0.4 to 1.3. Both force and moment and pressure data were obtained. In addition to model surface pressures, data were also obtained on two static pressure pipes mounted near the tunnel top and bottom walls for one of the configurations at Mach numbers up to 1.05. The pipe pressure data were used to determine if there were any significant wall interference effects on the model surface pressure distribution.

This report summarizes the results presented previously in five AFWAL Technical Memorandums (References 1 through 5). The information in the sections on apparatus and test description has been extracted from the AEDC test reports (References 6 and 7).

SECTION 2.0

APPARATUS

2.0 Test Facilities

AEDC VKF Tunnel A (Figure 1) is a continuous, closed-circuit, variable density wind tunnel with an automatically driven flexible-plate-type nozzle and a 40- by 40-inch test section. The tunnel can be operated at Mach numbers from 1.5 to 5.5 at maximum stagnation pressure from 29 to 195 psia, respectively, and stagnation temperatures up to 750°R at Mach number 5.5. Minimum operating pressures range from about one-tenth to one-twentieth of the maximum at each Mach number. The tunnel is equipped with a model injection system which allows removal of the model from the test section while the tunnel remains in operation. A description of the tunnel and airflow calibration information may be found in Reference 8.

The AEDC Aerodynamic Wind Tunnel (4T) is a closed-loop continuous flow, variable-density tunnel in which the Mach number can be varied from 0.1 to 1.3 and can be set at discrete Mach numbers of 1.6 and 2.0 by placing nozzle inserts over the permanent sonic nozzle. At all Mach numbers, the stagnation pressure can be varied from 300 to 3,400 psfa. The test section is 4-feet square and 12.5 feet long with perforated, variable porosity (0.5- to 10-percent open) walls. It is completely enclosed in a plenum chamber from which air can be evacuated, allowing part of the tunnel airflow to be removed through the perforated walls of the test section. The model support system consists of a sector and sting attachment which has a pitch angle capability of -8 to 27 degrees with respect to the tunnel centerline and a roll capability of ±180 degrees about the sting centerline. A more complete description of the tunnel may be found in Reference 8.

2.2 Test Articles

The test articles were elliptic missile body configurations with ellipticity ratios of 2.0, 2.5, and 3.0 to 1.0. The three models were designed and fabricated from aluminum at AEDC, based upon criteria provided by

AFWAL/FIMG. The models were power-law bodies with an exponent of 0.5 and had the same longitudinal distribution of cross-sectional area. These models were based on one of a series of related bodies with cross-sectional ellipticity tested by NASA at Langley Research Center (Reference 9). The semimajor and semiminor axis ordinates were derived from the following equations:

For horizontal projection (semimajor axis)

$$a = \frac{a_{max}}{LM^{0.5}} \cdot X^{0.5}$$

and for vertical projection (semiminor axis)

$$b = \frac{b_{max}}{LM^{0.5}} \cdot x^{0.5}$$

Details of the models are given in Figure 2. Model configuration designation is presented in Table 1 and a listing of the configurations tested is given in Table 2.

For the pressure phase, each model was instrumented with 191, 0.045 inch diameter surface pressure orifices and one base pressure orifice. The location and designation of the pressure orifices are presented in Figure 3a and were identical for all three models. Table 3 provides nominal axial locations from the nosetip and nominal radial locations from the top ray (positive clockwise looking upstream) of the pressure orifices. Base pressure was measured with an orifice located halfway between the sting and model outer surface as shown in Figure 3c. For the transonic pressure test, static pressure pipes were mounted on the centerline of the top and bottom walls. Details of the pressure pipes are shown in Figure 4. Each pipe had 30 pressure orifices on each of the model and wall sides of the pipes. A more detailed discussion is given in Reference 5. Two thermocouples were attached to the inner wall of each model and the general location is given in Table 3.

For the Tunnel A force phase, the pressure tubes were cut, sealed and secured as required to prevent interference on the balance measurements. Base pressure was measured with a fast-response pressure transducer module located in a sting component approximately 18 inches downstream of the model base. An 8-degree prebend installation arrangement was used to provide the angle-of-attack range from -4 to 20 degrees. One set of sting components was used for the pressure and oil-flow phases and a different, but similar set of components was used for the force and vapor-screen phases. Sketches of the installation arrangements for both Tunnel A and 4T are shown in Figure 5.

2.3 Test Instrumentation

During the pressure phases of testing, model surface and base pressures were measured with Pressure Systems Incorporated electronically-scanned pressure modules referenced to a near vacuum. Six Model ESP-32 modules were used for the VKF supersonic testing; four 2.5-psid range and two 5-psid range. Each ESP-32 module has 32 pressure ports with a silicon pressure transducer for each port that can be digitally addressed and calibrated on-line. The relatively small size of each pressure module (1.0 X 2.0 X 2.5 inch) permitted on-board mounting, which resulted in a significant reduction in pressure stabilization time and a significant increase in the data acquisition rate. Nine Model ESP-48 modules, each with a 15-psid range, were used in the 4T transonic testing; five 48-port modules located in the model and two 48-port and two 16-port modules located outside the test section and connected to the static pressure pipes. Model wall temperatures were measured with two Chromel-Alumel thermocouples attached to the inner wall of the model.

During the Tunnel A force phase, model base pressures were measured with a miniature pressure transducer module manufactured by the Scanivalve Corporation. The module contains eight fast-response pressure transducers with a range of 1 psid referenced to a near vacuum. The transducers are diffused silicon-diaphragm-type strain gage sensors fabricated by Druck Incorporated. The small size of the pressure module (0.5 X 1.2 X 1.3 inch) permitted mounting in a sting component downstream of the model base.

In Tunnel A model shadowgraph or schlieren photographs were obtained with a double-pass optical flow-visualization system with a 35-in-diameter field of view. Vapor-screen photographs were obtained with two Hasselbald 70-mm still cameras mounted on the operating side of the test section and a D.B. Milliken-55, 16-mm movie camera at 12 frames per second mounted on the non-operating side of the test section. Model flow field illumination was provided with a 15-mw helium-neon continuous wave laser with the output beam expanded in one direction with a 8-mm cylindrical lens. The cylindrical lens was rotated so that the light plane was perpendicular to the model centerline for each model angle of attack.

Oil-flow photographs were obtained with three Varitron 70-mm still cameras mounted on the operating side of the test section to facilitate simultaneous photo acquisition along the full length of the model. An automatic camera control system was used to provide automatic shutter sequencing at 4-second intervals. For the second phase of oil flow testing, Hasselbald 70-mm still cameras were used to photograph the models in the access tank.

SECTION 3.0

TEST DESCRIPTION

3.1 Test Conditions

A complete listing of test conditions, configurations, and run numbers is presented in Table 2.

3.2 Test Procedures

3.2.1 General

In the VKF wind tunnels, (A, B, C), the model is mounted on a sting support mechanism in an installation tank directly underneath the tunnel test section. The tank is separated from the tunnel by a pair of fairing doors and a safety door. When closed, the fairing doors, except for a slot for the pitch sector, cover the opening to the tank and the safety door seals the tunnel from the tank area. After the model is prepared for a data run, the personnel access door to the installation tank is closed, the tank is vented to the tunnel flow, the safety and fairing doors are opened, the model is injected into the airstream, and the fairing doors are closed. After the data are obtained, the model is retracted into the tank and the sequence is reversed with the tank being vented to atmosphere to allow access to the model in preparation for the next run. The sequence is repeated for each configuration change.

The tunnel 4T test section (4 feet square by 12 feet long) is accessed through a removable side wall. Model changes require shutting down the tunnel and opening the side wall. For this reason, model changes are done after all of the required Mach numbers are completed. For each Mach number the tunnel conditions are held constant while varying model attitude. The data are recorded at selected angles using the pitch/roll-pause technique. This sequence is repeated for each configuration.

3.2.2 Data Acquisition and Reduction

3.2.2.1 Tunnel A

Model attitude positioning and data recording were accomplished with the point-pause and sweep modes of operation, using the Model Attitude Control System (MACS). Model pitch and roll requirements were entered into the controlling computer prior to the test. Model positioning and data recording operations were performed automatically during the test by selecting the list of desired model attitudes and initiating the system.

Point-pause force data were obtained for finite values of ALPHA and BETA with a delay before each point to allow the base pressure to stabilize. Each data point for this mode of operation is the result of a Kaiser-Bessel digital filter utilizing 16 samples over a time span of 0.33 seconds.

The continuous sweep force data were obtained for a fixed value of PHI with a sweep (ALPHA) rate of 0.5 deg/sec. A data sample was recorded every 0.0208 seconds and a Kaiser-Bessel digital filter was applied to every 16 samples to produce a sample data point every 0.01 degrees in pitch. The data were then interpolated to obtain the data at the requested model attitudes. The data mode for each force run is identified in the Test Run Summary (Table 2).

Model shadowgraph or schlieren photographs were obtained on selected configurations at selected model attitudes and test conditions during the pressure phase and on all configurations at all test conditions and selected model attitudes during the force phase.

The force and moment measurements were reduced to coefficient form using the digitally filtered data points and correcting for first and second order balance interaction effects. Vehicle coefficients were also corrected for model tare weight and balance-sting deflections. Model attitude and tunnel stilling chamber pressure were also calculated from digitally filtered values.

Vehicle aerodynamic force and moment coefficients are presented in the body- and stability-axis systems. Pitching and yawing moment coefficients are referenced to a point on the model centerline 24.0 inches from the nose. The stability-axis system coefficients (CLS and CDS) were calculated using the forebody axial force coefficient (CA). Model diameter and base area were used as the reference length and area for the aerodynamic coefficients. Model reference dimensions are given in the Nomenclature.

3.2.2.2 PWT 4T

All steady-state measurements were sequentially recorded by the facility on-line computer system and reduced to the desired final form. The data were then tabulated in the Tunnel 4T control room, recorded on magnetic tape, and transmitted to the AEDC central computer file. The data stored in the central computer file were generally available for plotting and analysis on the PWT Interactive Graphics System within 30 seconds after data acquisition. The immediate availability of the tabulated data permitted continual on-line monitoring of the test results.

Surface and base pressure data were normalized by the free stream static pressure and the surface and pipe pressure data were reduced to pressure coefficient form. Selected surface pressure data were also presented graphically by constructing three-dimensional color contour plots over the model shape.

The model force and moment data were reduced to coefficient form in the body- and stability-axes systems. The model reference area is given in the Nomenclature and the reference lengths are given in Table 1. The moment reference point is shown in Figure 2. The stability-axis system coefficients (CLS and CDS) were calculated using the forebody axial force coefficient (CA) and the normal force coefficient (CN). The base pressure and its area (given in Nomenclature) were used to calculate the base axial force.

3.3 Uncertainty of Measurements

3.3.1 VKF

In general, instrumentation calibration and data uncertainty estimates were made using methods recognized by the National Bureau of Standards (NBS) presented in Reference 10. Measurement uncertainty is a combination of bias and precision errors defined as:

$$U = \pm(B + t_{95}\, S)$$

where B is the bias limit, S is the sample standard deviation, and t_{95} is the 95th percentile point for the two tailed student's "t" distribution (95 percent confidence interval), which for sample sizes greater than 30 is taken equal to 2.

With the exception of the force and moment balance, data uncertainties are determined from in-place calibrations through the data recording system and data reduction program. Static load hangings on the balance simulate the range of loads and center-of-pressure locations anticipated during the test, and measurement errors are based on differences between applied loads and corresponding values calculated from the balance equations used in the data reduction. Load hangings to verify the balance calibration are made in place on the assembled model.

Propagation of the bias and precision errors of measured data through the calculated data were made in accordance with Reference 10. Uncertainties for the calculated data are calculated for the largest measured value at the primary test condition on each parameter at each Mach number.

3.3.2 4T

The aircraft angles-of-attack and sideslip were corrected for sting deflections caused by aerodynamic loads. The flow angularity (AFA) in the tunnel pitch plane was determined by testing the aircraft model upright and inverted and the flow angularity corrections were then applied to the data. Corrections for the components of model weight, normally termed static tares, were also accounted for before the measured loads were reduced to coefficient form.

Uncertainties (combinations of system and random errors) of the basic tunnel parameters, shown in Figure 6, were estimated from repeat calibrations of the instrumentation and from the repeatability and uniformity of the test section flow during tunnel calibration. Uncertainties in the instrumentation systems were estimated from repeat calibration of the systems against secondary standards whose uncertainties are traceable to the National Bureau of Standards calibration equipment. The tunnel parameter and instrument uncertainties, for a 95-percent confidence level, were combined using the Taylor series method of error propagation described in Reference 10 to determine the uncertainties of the parameters in Table 4.

SECTION 4.0

METHODOLOGY DESCRIPTION

4.0 Supersonic/Hypersonic Arbitrary Body Program (S/HABP)

This digital computer program was written by the Douglas Aircraft Company and is documented in AFFDL-TR-73-159 (Reference 11). The program is a combination of techniques and capabilities necessary in performing a complete aerodynamic analysis of supersonic and hypersonic shapes. The program was originally designed primarily for computing the aerodynamic characteristics of high-speed arbitrary reentry vehicles. Because the program will provide aerodynamic coefficients for any complex arbitrary shape at any angle of attack for Mach numbers equal to one or greater, the code is finding renewed interest. Many of the new state-of-the-art missile designs are now non-circular/non-conventional shaped configurations operating at higher angles of attack and supersonic Mach numbers.

The program calculates the inviscid aerodynamic coefficients by using simple pressure coefficient methods, such as Newtonian Impact, on the external geometry of a configuration which is described to the program as panels of flat quadrilateral elements as shown in Figure 7a. The majority of the pressure methods are simply a function of the local angle of attack or slope of the element and the freestream Mach number. The viscous or skin friction effects are computed on a simplified flat plate geometry, Figure 7b, using methods such as Reference Temperature. The program has 15 different compression (impact angle greater than 0) and 9 expansion (impact angle less than 0) methods for computing inviscid pressure coefficients plus 9 choices of combinations of skin friction methods. The individual forces and moments of each element are summed up by the program to give component, such as wing, or tail, aerodynamic characteristics. These results may in turn be summed up to give parametric buildup or complete configuration aerodynamic characteristics.

4.2 Pressure Integration

An integration of the pressure measurements over the surface of the model was performed to determine the inviscid aerodynamic forces and moments. The integrated forces and moments can be used to compare directly with the inviscid theoretical calculations and by subtracting them from the test total force and moment results provide the increments due to viscous effects. The instrumented stations did not extend forward of station 3.2 so a theoretical value of the nose aerodynamics was generated using Tangent Cone and Prandtl-Meyer methods. The nose analysis used the S/HABP code with the methods described above. Between station 3.2 and 36.0 the pressure data was integrated using a scheme which used the pressures around each cross section to determine a value at each station, then the integration proceeded from the first station to the base to produce a value of the surface integral (Reference 12).

The pressure at each tap has a component in each of the three cartesian directions. The component is determined from the direction cosines of the surface at the tap location. The direction cosines were calculated from the model geometry. The direction cosines are the coefficients of the unit vector normal to the surface. The unit normal vector was determined by the vector product of two orthogonal vectors defined by the surface geometry functions.

The maximum span at any station is defined as:

$$a = \frac{a_{max}}{6} (x)^{1/2}$$

and the maximum height at any station is:

$$b = \frac{b_{max}}{6} (x)^{1/2}$$

The cross section at any station is an ellipse, with a and b the semimajor and semiminor dimension. The remainder of the dimensions and angles may now be determined. Referring to Figure 7c, the direction cosines of the surface at a point P are evaluated as follows, using the values of a and b from the relations shown above and a specified value of the meridian angle U.

$$y = ((a^2 * b^2)/(b^2 + a^2 \tan^2 U))^{1/2}$$

$$z = y * \tan U$$

$$W = \text{atan}\ ((b^2/z) * (y/a^2))$$

$$V = \text{atan}\ (0.5 * (y^2 + z^2)^{1/2}/x)$$

the two orthogonal vectors are therefore

$$\vec{A} = A_1\vec{i} = A_2\vec{j} + A_3\vec{k}$$

$$\vec{B} = B_1\vec{i} + B_2\vec{j} + B_3\vec{k}$$

$$A_1 = 0$$

$$A_2 = \cos W$$

$$A_3 = -\sin W$$

$$B_1 = \cos V$$

$$B_2 = \sin V * \cos\ (90-U)$$

$$B_3 = \sin V * \sin\ (90-U)$$

The unit normal at the surface is written as

$$\vec{C} = C_1\vec{i} + C_2\vec{j} + C_3\vec{k}$$

and the direction cosines are

$$C_1 = B_2 * A_3 - B_3 * A_2$$

$$C_2 = B_3 * A_1 - B_1 * A_3$$

$$C_3 = B_1 * A_2 - B_2 * A_1$$

The force and moment coefficients may be determined by integrating the pressure coefficients over the surface. The formulation for the longitudinal coefficients is:

$$C_A = 1/A_R \int\int C_p * C_1 \, ds \, dh$$

$$C_N = 1/A_R \int\int C_p * C_3 \, ds \, dh$$

$$C_m = 1/(A_R * 1_R)\int\int ((Cp*C_1*z)-(Cp * C_3 * x)) \, ds \, dh$$

The computerized integration routine used the trapezoidal rule, first around the cross section on the distance s, then down the body along the length h.

Approximations were used for s and h. The chord length between pressure taps was computed as the arc length. They were summed at each station from the top center to the bottom center. The distance h was computed as the slant height of a right conic solid, with $s(x_1)$ and $s(x_2)$ being the periphery of the ends of the solid.

$$h_{1-2} = ((x_2 - x_1)^2 + (s(x_2)/2\pi - s(x_1)/2\pi)^2$$

4.3 NSWC Euler Code

In addition to comparing pressure, force, and moment predictions determined with the Supersonic/Hypersonic Arbitrary Body Program to the experimental data, we made similar comparisons with predictions from a numerical computation technique. Only inviscid computer codes were considered since, at the time, it seemed unwarranted for the conditions of interest (i.e., Mach number; Reynolds number; and body configuration) to introduce the additional complications of a viscous method such as, for example, a Parabolized Navier Stokes Code for what would be small effects.

Experience had been gained on one particular inviscid code during previous in-house studies. This code, herein called the NSWC code, is a forward marching solution to the steady, inviscid, supersonic flow equations. It was originally written at the Naval Surface Weapons Center (hence, the NSWC identification) and which they called the D3CSS computer code (References 13 and 14).

We need an initial flow field data plane where the flow field is everywhere supersonic in order to run the NSWC code for a body in supersonic flow. For the original use, this was supplied through three pre-programs called BNT, DDD, and BETA which, essentially, provided a blunt body solution for a spherical nose at angle-of-attack (Reference 15). The complete package of codes was run successfully for data comparison with experimental biconic data and the results reported by Scaggs (Reference 16). Use of the blunt body pre-programs placed a lower limit on free stream Mach number of about 4 and, since the Mach number range of the data on the elliptical power law bodies was between 1.76 and 5.03 an alternative solution was needed.

The code chosen to provide the starting solution was the CM3DT computer program, written by Science Applications International Corporation (SAIC) for the Ballistic Missile Office (BMO) (Reference 17). The code is a time-dependent, steady-state solution for supersonic/hypersonic flow over nosetips of arbitrary shape and yields the asymptotic limit of the unsteady flow problem. The NSWC code was modified to accept input from the CM3DT code by SAIC as part of an earlier contract effort (Reference 18).

For all cases produced for this report, a perfect gas condition was used and calculations were stopped at an angle of attack of 10 degrees since the NSWC code, like other supersonic inviscid codes, fails if either the axial velocity component becomes subsonic or if axial flow separation occurs. This seemed to be at just above 10-degrees angle of attack, especially for the higher ellipticity body, since the 12-degree angle-of-attack case always failed. Finally, although the bodies of interest were symmetrical ellipses in cross section, this particular option did not exist in the code. Therefore, the bi-ellipse option was used with the $\phi = 0°$ and 180° values of y the same at each X location. Ten planes of body geometry were required to properly describe the nose shape up to an axial location 1 inch from the nosetip.

4.4 FL057 Euler Code

FL057 is a finite volume Euler method which was modified to permit arbitrary geometries through the use of multiple grid blocks. The volume or cells are defined by eight neighboring grid points. Conservation of mass, momentum, and energy are satisfied in an integral form on each volume by a pseudo-time-stepping four-stage Runge-Kutta scheme. Flow variables are assumed to be located at cell centers, permitting centered differences to be used to provide second-order-accurate spatial derivatives. Artificial dissipation is added to suppress the odd-even point decoupling that is typical of center-differenced Euler methods and also to reduce non-physical pressure oscillation around shocks and stagnation points. The dissipative terms are calculated by blending fourth and second differences and are scaled by second derivatives of pressure. To increase convergence rates, both enthalpy damping and implicit residual smoothing is used. Surface boundary condition is normal-flow imposed using only the cell adjacent to the surface. Far field boundary conditions are of a nonreflecting type (Reference 19). The FL057 is a time-dependent solution that allows solutions to be obtained at subsonic as well as supersonic speeds.

We did not attempt to generate the missile grid to align the 3-D grid with the bow shock shape since the grid was used for a range of Mach numbers and angles of attack. The bow shock is dependent on the configuration angle of attack and freestream Mach number. Shock smearing will occur when the bow shock is unaligned with the grid, introducing an unknown amount of error into the solution. At the nose of the configuration the shock would approximate the shape of the blunt nose and therefore align with the grid at moderate supersonic Mach numbers (Reference 20).

4.5 Missile Datcom

Missile Datcom provides an aerodynamic design tool with the predictive accuracy suitable for preliminary design, yet has the utility to be extended by rapid substitution of methods to fit specific applications. The code uses a component build-up approach to calculate the static stability and control characteristics of missiles with both unconventional fin arrangements and arbitrary cross sections. The primary advantage of component build-up methods over panel methods is speed of operation.

SECTION 5.0

TEST RESULTS

5.1 VKF Tunnel A

5.1.1 Force and Moment Testing

The effect of ellipticity ratio on the basic aerodynamic characteristics is shown in Figures 8 and 9 for the elliptical bodies at Mach 2.0 and 5.0. The trends in the normal force and pitching moment coefficients are consistent. Increasing the ellipticity of the body increases the normal force coefficient, lift-to-drag ratio and the pitching moment coefficient. At angles of attack less than 5 degrees the axial force coefficient increases with increasing ellipticity ratio. Interestingly, at higher angles of attack, the 2.5:1 body shows a higher axial force coefficient than either the 2.0:1 or the 3.0:1. In fact, in most cases, the 3.0:1 ratio body axial force coefficient approaches the value of the 2.0:1 body at higher angles of attack.

Figures 10 and 11 show the effects of Mach number on the 3.0:1 body at a length Reynolds number of two million per foot. For clarity, five Mach numbers are plotted in each set of figures; Mach 2.0, 2.5, 3.0, 4.0, and 5.0 in one set and Mach 1.76, 2.0, 2.5, 3.0, and 3.5 in the other. The plots show that the normal force and pitching moment coefficients decrease with increasing Mach number. At small angles of attack (less than 6 degrees) axial force coefficient decreases for increasing Mach number. The axial force coefficient increases, however, for increasing Mach number at higher angles of attack. This corresponds to a decrease in lift-to-drag ratio. This trend reversal occurs at higher angles of attack for the 2.0:1 and 2.5:1 bodies, and is attributed to the formation of large leeside vortices.

The effects of Reynolds number are shown in Figures 12 and 13. As expected, this range of change in Reynolds number had virtually no effect on either normal force or pitching moment coefficients at either Mach 2.0 or 5.0. The effects of Reynolds number on axial force coefficient varied with Mach number. At Mach 2.0 (Figure 12), the axial force at zero angle of attack was only slightly higher at the lower Reynolds number, but the difference increases with increasing angle of attack. This is surprising since the only difference in axial force should be due to skin friction which should be relatively constant. At Mach 5.0 (Figure 13), axial force coefficient decreases as expected for increasing Reynolds number at low angles of attack. Above 10-degrees angle of attack, axial force coefficient for the 3.0:1 body is essentially independent of Reynolds number.

5.1.2 Pressure Results

During the theoretical/experimental comparison effort, plots were made of pressure ratio vs x-station for the top and bottom centerlines at zero angles of attack for all the test Mach numbers. These plots showed some unexpected trends in the pressure data. At zero angle of attack, one would expect symmetrical pressure distribution for the top and bottom centerlines. The data, however, showed jumps in the pressure coefficient midway down the body on both the top and bottom (Figure 14). Consultation with the test engineers at AEDC confirmed suspicions that the fluctuations were tunnel induced, and could be expected for any pressure test at very low angles of attack. Further investigation showed that the variations in small values of pressure have a negligible effect when measuring and integrating pressures at larger angles of attack.

Figure 15 shows representative plots of pressure coefficient versus body radial angle for all 11 x-stations. Data shown is for 3.0:1 body at 12-degrees angle of attack at Mach 2.0 and 5.0.

5.1.3 Flow Visualization

5.1.3.1 Vapor Screens

Results of the vapor screen test are shown in Figure 16 for the 3:1 ellipticity model at Mach 3 and 16-degrees angle of attack. Both upstream and downstream views are included. Figure 17 includes upstream views for 12- and 20-degrees angle of attack as well (Reference 6). These composite photos show the location and growth of the shocks and leeside vortices. The darker areas in the photographs indicate less water vapor than the lighter regions. Several explanations for this phenomenon have been proposed. One explanation is that the high rotational velocities of the vortex ejects the water droplets. Another is that the water vapor does not penetrate through the shear layer into the boundary layer, which feeds the vortex. Another possibility is that the water undergoes a phase change and vaporizes due to the temperature increase produced by the shock (Reference 21). A good description of the basic techniques used for vapor screen testing is contained in Reference 22.

For the large angles of attack shown in the figures, the shocks are clearly visible with the leeside vortices. Secondary vortices are also visible, especially in the upstream views. They are located just inboard of the leading edge, under the sheet feeding the primary vortex.

5.1.3.2 Shadowgraph/Schlieren

Samples of the shadowgraph and schlieren data are shown in Figures 18 and 19. Both are for the 3:1 ellipticity model at 12-degrees angle of attack. The shadowgraph data is Mach 3.0 and the schlieren photo is for a Mach 2.5 run. Figure 20 shows the comparisons of the experimentally obtained shock shape with the NSWC Euler code. The code predicts the compression shock very well; on the expansion side, however, the code underpredicts the shock angle especially at higher angles of attack.

5.1.3.3 Oil Flows

Samples of the oil flow photographs are shown in Figure 21 for the 3:1 configuration at Mach 3.0 and 12-degrees angle of attack. Figure 22 shows the primary and secondary separation angles, measured graphically from the photographs. The primary separation angle is defined as the line of separation just past the leading edge as the flow moves from the windward to the leeside of the body. The secondary separation angle is the separation line further inboard on the leeside where the flow reattaches.

Figure 22 shows that for all angles of attack, the primary separation point gets closer to the leading edge as the flow moves down the body. In general, the radial separation angle increases with increasing angle of attack. The trends are reversed for secondary separation angles. The angle gradually decreases as the flow moves down the model, and separation angle decreases for increasing angle of attack. The data drops sharply in the nose region, probably due to the initial formation of the vortices. The complex flow in the nose region is evident in the oil flow photographs.

5.2 PWT 4T

5.2.1 Force and Moment Test

The effects of ellipticity ratio on the longitudinal aerodynamic characteristics are shown in Figures 23 through 25 for Mach numbers 0.4, 0.8, and 1.3.

The trends in the test data are consistent for varying ellipticity ratio and Mach number. Increasing the ellipticity of the body increases normal force coefficient, lift-to-drag, and the pitching moment coefficient. The axial force coefficient generally increases slightly with increasing ellipticity ratio, the exception being at higher angles of attack and at the lowest Mach numbers, where it shows either a very small decrease or no change at all. The lateral directional derivatives are also consistent for changing ellipticity ratio (Figure 26). The rolling moment derivative becomes increasingly negative with increasing ellipticity ratio and the yawing moment derivative becomes less negative at all Mach numbers. The side force coefficient is more positive with increasing ellipticity ratio at all angles of attack for Mach 0.4 and 0.55. This trend is reversed above 10-degrees angle of attack at the higher Mach numbers, where the side force coefficient decreases with increasing ellipticity ratio.

5.2.2 Pressure Test

The transonic tunnel force and moment data showed dramatic changes in side force and yawing moment with varying angle of attack below Mach 0.6

and 4-degrees yaw angle. The side force coefficient goes from -0.02 to +0.06 between 8- and 14-degrees angle of attack, while the yawing moment coefficient changes slope and even goes positive for the 3.0:1 model (Figure 26). Analysis of the pressure coefficient data showed large changes in pressure distribution with changing angle of attack, particularly in the negative pressure coefficients about the leading edge. To illustrate this, Figure 27 shows a polar plot of Cp versus body radial angle for the 3.0:1 body at 6- and 12-degrees angle of attack and Mach 0.4 at the 16-inch x-station. The plot shows that at 6 degrees the negative pressure coefficients balance out and a negative side force results from the unbalanced positive pressure coefficients on the bottom surface. At 12 degrees the positive pressure coefficients are slightly unbalanced, but the negative Cp on the one side is much higher than the other, resulting in a positive side force. These same types of changes caused by the vortices on the upper surface result in a change in the lengthwise pressure distribution which affects the yawing moment as well.

SECTION 6.0

DATA/PREDICTION COMPARISONS

6.0 Force and Moment Comparisons

6.1.1 Supersonic/Hypersonic Arbitrary Body Program (S/HABP)

Some typical elliptical body S/HABP theoretical results compared with the test data are shown in Figures 28 and 29, (3.0:1 body at Mach numbers 2.0 and 5.0). These theoretical results use the S/HABP Tangent Cone pressure method for compression surfaces and Van Dyke Unified method for expansion. Turbulent skin friction was selected for the viscous computations. At lower Mach numbers the only coefficient predicted with reasonable accuracy is lift-to-drag ratio. The overprediction of both normal force and axial force compensated each other to give a reasonable value for L/D. Above Mach 3.0 the agreement between normal force, pitching moment, and L/D was fairly good. Axial force coefficient was still slightly overpredicted, however.

6.1.2 Transonic Force and Moment Data

Typical Missile Datcom theoretical results compared with the static longitudinal force and moment test data are shown in Figures 30 through 32 for the 3.0:1 ellipticity ratio configuration at Mach numbers 0.4, 0.8, and 1.3. These theoretical results used the second-order shock-expansion method for axisymmetric bodies at supersonic speeds and turbulent skin friction at all Mach numbers. The Missile Datcom did a good job of predicting normal force coefficient below 10-degrees angle of attack, where C_N is fairly linear. At higher angles of attack, it underpredicted the values. At subsonic Mach numbers the predicted pitching moment coefficient is about twice the test data value at corresponding values of normal force coefficient. At Mach 1.3 the predicted pitching moment values agree very well with test data even to the highest angles of attack. Because the base axial force coefficient is such a large portion of the body total axial force coefficient, both of these coefficients have been plotted and compared with predicted values. The predicted axial force coefficients due to the base pressure are low at all three Mach numbers, particularly at Mach 1.3. The total axial force coefficient is fairly well predicted at Mach 0.4, but is low at Mach 0.8 and very low at Mach 1.3 where it drops off drastically with increasing angle of attack. The lift-to-drag ratio predictions are not too bad at Mach numbers of 0.4 and 0.8, but are high at Mach 1.3.

Comparisons of the Missile Datcom with the lateral directional coefficients for the 3.0:1 ellipticity ratio configurations at Mach numbers 0.4, 0.8, and 1.3 are shown in Figures 33-35. The present version of Missile Datcom gave no values for rolling moment coefficient. The side force coefficient was predicted very well at low angles of attack for all three Mach numbers. The yawing moment was predicted as being more negative in value than the test data at Mach 0.4 and 0.8 and slightly less negative at Mach 1.3. The test data shows a reversal in sign for the side force coefficient near 8 degrees angle of attack, going from negative values of - 0.01 to positive values as high as 0.06.

6.1.3 FL057 Euler Code

Figure 36a presents a comparison between measured and predicted values of normal force and pitching moment coefficient versus angle of attack for the 2.5:1 configuration at Mach 0.55. Below 6-degrees angle of attack FL057 does an excellent job of predicting C_N and C_M. Above 6-degrees, where the data is no longer linear, the code underpredicts the test data. The differences between test and prediction in both plots is evidence that the influence of vortices is not present in the Euler results.

Figure 36b shows comparisons for the same configuration at Mach 2.0. The predicted and test values are in excellent agreement below 6-degrees angle of attack. Above 6-degrees, the slopes are the same but are shifted by approximately 0.5-degrees angle of attack. One possible explanation for this is the smearing of the bow shock and grid (Reference 20). The C_N versus C_m curve throws excellent agreement throughout the angle-of-attack range.

6.2 Integrated Pressures

Figures 37 and 38 show the comparison of the integrated pressure forces and moments with the force and moment test data. Also plotted are the theoretical results from the NSWC Euler code. The agreement between the integrated normal force and pitching moment coefficients and the force and moment test data was excellent. The forces and moments on the nose to the X = 3.2 station were calculated with the S/HABP code using the Tangent Cone/Prandtl-Meyer methods, and were then added to the test pressure forces and moments. The excellent agreement indicates that the theoretical methods used for the nose section are quite good. The increment in the axial force coefficient between the integrated pressure data and the force test data is due to the viscous forces; i.e., the skin friction. The plots show almost a constant increment in axial force coefficient due to skin friction until about 10-degrees angle of attack where the increment starts to increase. The increase in the axial force coefficient increment is very large at the highest angles of attack for the lower Mach numbers. As an example, the increment of axial force coefficient goes from about 0.05 at 8-degrees angle of attack to 0.11 at 20-degrees angle of attack for the 3-to-1 ellipticity ratio configuration at Mach 2.0. Figure 39 shows the axial force coefficient increment for the 3.0:1 ellipticity ratio configuration for Mach numbers 2.0, 3.0, 4.0, and 5.0. Also shown on the figures are the skin friction predictions from the S/HABP code. The S/HABP skin friction methods calculate about the right value for the skin friction increment at low angles of attack, but the increment is essentially constant with increasing angle of attack. At the highest angles of attack for all three configurations the predicted axial force coefficients due to skin friction were less than half what the test data indicated.

6.3 Cp versus Body Radial Angle

6.3.1 Supersonic/Hypersonic Arbitrary Body Program (S/HABP)

Typical S/HABP theoretical pressure results compared with test data at x-stations of 3.2, 16.0, and 35.2 inches are shown in Figures 40 and 41 at Mach 2.0 and 5.0 for the 3:1 body. The S/HABP theoretical results shown are for the Tangent Cone method for compression surfaces and Van Dyke Unified method for expansion.

The plots show that the bottom surface pressures are generally predicted very well by the Tangent Cone method until the leading edge of the body is approached; there the test pressure coefficients drop off and become negative around 10 degrees before the leading edge at $\emptyset$ = 90 degrees. The S/HABP code calculates positive local deflection angles for all points on the lower surface of the body up to and including the leading edge when the body is at positive angle of attack (Figure 42). None of the compression methods in the S/HABP code which are functions of local deflection angle and Mach number will give negative pressure coefficients for positive deflection angles. The plots show that the test pressure coefficients at angle of attack have fairly high negative values on the top in the vicinity of the leading edge which are more negative than predicted. The predicted values further up on the top reach the maximum negative values of the test and remain constant across the rest of the upper surface to the center of the body, while the test data becomes much less negative, even slightly positive in some cases, on the leeside away from the leading edge.

The large negative pressure coefficients about the leading edges of the elliptical bodies strongly influences their aerodynamic characteristics. The importance of the leading edge pressures is directly related to the amount of surface area over which they act. The ratio of wetted area (A_W) to total band area (A_T) for a 0.2-inch-length band of body about X = 16 inches is plotted versus the body angle in Figure 43 for the 2-to-1 and 3-to-1 ellipticity ratio bodies. The plot shows that for a 10-degree increment in body angle the amount of wetted area near the leading is proportionally larger so that the large negative pressures near the leading edge (ϕ = 80 to 100 degrees) are acting over a very large surface area.

6.3.2 NSWC Euler Code

Comparisons of the pressure coefficients predicted by the NSWC Euler code for x-stations of 3.2, 16.0, and 35.2 are also shown in Figures 40 and 41 for which the program provided values. The plots show that the NSWC program does a very good job of predicting the pressure coefficients about the body. The program predicts both the negative pressure coefficients on the compression side just before the leading edge and the drop off in negative pressure coefficients on the leeside away from the leading edge wall. The good agreement with test data indicates the potential for these types of codes in predicting elliptical body aerodynamics. Techniques for extending their range of applicability and methods for calculating viscous forces for inclusion with the invicid results should be investigated further.

6.3.3 FL057 Euler Code

Figure 44 shows comparisons of pressure coefficient versus span for three x stations; 3.2, 16.0, and 35.2. Data shown are for the 2.5:1 model at Mach 2.0 and 12-degrees angle of attack. At the x=3.2 station the shapes of the curves are the same but the FL057 prediction is shifted in the negative Cp direction. At the x=16.0 station, the code still predicts an attached flow condition, while the flow visualization test data shows the formation of vortices on the upper surface. This effect is also present at the x=35.2 station. The shift in Cp may be due to a smeared bow shock, which creates angularity in the flow and results in an apparent angle-of-attack change (Reference 20).

6.4 Cp versus Local Deflection Angle

Since the prediction methods in the S/HABP code are functions of the freestream Mach number and the local deflection angle, a set of charts was prepared to show the relation between the measured pressure coefficient and the calculated local deflection angle. The charts show the extent of correlation with local deflection angle and reveal the difficulty of devising a new pressure function which would predict the aerodynamics more accurately.

The pressure coefficients are shown with the local deflection angle in Figures 45 and 46. Each graph shows all the measured values on the model at a single angle of attack. Representative data was selected at angles-of-attack increments of approximately 4 degrees. The data symbol indicates the general region of the pressure tap as being on the top, the leading edge, or the bottom of the model. Tangent Cone theory is also marked on the graphs. The highest values of the pressure coefficient, which occur on the bottom center, are very near the theory. At locations other than the bottom center the pressure coefficient is less than theory. For these tests, the Tangent Cone theory represents an upper bound.

The effect of Mach number is most evident at negative surface deflection angles. The measurements on the top of the model indicate a flow field which is influenced by parameters other than the local angle. The range of pressures on the top indicate the effects of boundary layer separations and the development of vortices in the flow field. At Mach 2.0 the pressures are very sensitive to boundary layer separation. The pressure coefficients have values from $Cp = 0$ to a lower bound near $Cp = -1/M^2$. The lower bound is based on past work using base pressure measurements from wind tunnel and flight tests which has shown that the maximum attainable suction pressure is about 7-tenths vacuum. The equation for pressure coefficient as pressure goes to zero is $-2/\alpha M^2$ which, for $\alpha = 1.4$, when multiplied by 0.7 equals $-1/M^2$.

The correlation with local deflection angle also shows that the leading edge pressures are much lower than Tangent Cone theory would predict. The difference is larger at low Mach numbers, but still significant at Mach 5.

SECTION 7.0

RESULTS AND CONCLUSIONS

An extensive data base for elliptical cross section bodies has been generated for use in missile design activities as well as establishing a benchmark for the evaluation of aerodynamic performance prediction programs. The comprehensive combination of force, pressure and flow visualization data will allow identification of the source of deficiencies in current analysis techniques and indicate improvements to be made. This data base has been documented in a series of in-house Technical Memorandums.

During this study a number of different types of analysis codes have been used to generate theoretical results for data/theory comparisons. Both of the Euler codes used in this study, FL057 and NSWC, did a very good job of predicting the pressure distribution, normal force and pitching moment at angles of attack of 6 degrees or less. Since the Euler codes are inviscid the axial forces predicted do not include the viscous effects and the correct prediction of the axial force coefficient requires that the viscous effects be accounted for. The large differences between the integrated test pressure axial force coefficients and total force axial force coefficients show the importance of the viscous forces, particularly at higher angles of attack. Analysis methods for predicting viscous effects other than just simple strip theory skin friction calculations, as in S/HABP, will be required. Evaluations of the importance of the effects of flow field vortices, boundary layer separation, and boundary layer transition should be done. Computational Fluid Dynamics (CFD) codes such as a Parabolized Navier-Stokes code need to be evaluated for this class of configuration.

SECTION 8.0

REFERENCES

1. Amidon, P. F., Shereda, D. E., "Static Force Test of Three Elliptical Missile Body Configurations at Mach Numbers 1.5 to 5.0," AFWAL-TM-84-199-FIMG, June 1984.

2. Amidon, P. F., Brown-Edwards, E., Dahlem, V., Shereda, D. E., "Pressure Test of Three Elliptical Missile Body Configurations at Mach Numbers 1.5 to 5.0," AFWAL-TM-84-236-FIMG, December 1984.

3. Shereda, D. E., "Static Force Test of Three Elliptical Missile Body Configurations at Mach Numbers 0.4 to 1.3," AFWAL-TM-85-255-FIMG, September 1985.

4. Amidon, P. F., Dahlem, V., "Flow Visualization Test of Three Elliptical Missile Body Configurations at Mach Numbers 1.5 to 5.0," AFWAL-TM-86-188-FIMG, May 1986.

5. Shereda, D. E., "Pressure Test of Three Elliptical Missile Body Configurations at Mach Numbers 0.4 to 1.3," AFWAL-TM-86-208-FIMG, June 1986.

6. Sellers, M. E., Siler, L. G., "Pressure and Static Force Test of Three Elliptic Missile Body Configurations at Mach Numbers 1.5 to 5.0," AEDC-TSR-84-V44, November 1983.

7. Sellers, Marvin E., "Static Stability Test of Three Elliptic Missile Body Configurations," AEDC-TSR-85-P8, May 1985.

8. Test Facilities Handbook (Twelfth Edition), Arnold Engineering Development Center, March 1984.

9. Fournier, R. H., Spencer Jr., B., and Corlett, W. A., "Supersonic Aerodynamic Characteristics of a Series of Related Bodies with Cross-Sectional Ellipticity," NASA TN-D-3539, August 1966.

10. Abernethy, R. B., and Thompson, J. W., et al, "Handbook Uncertainty in Gas Turbine Measurements," AEDC-TR-73-5, February 1973.

11. Gentry, A. E., Smith, D. N., and Oliver, W. R., "The Mark IV Supersonic-Hypersonic Arbitrary Body Program - Volume I, II, III," AFFDL-TR-73-159, November 1973.

12. Dahlem, V., "A Digital Computation Method for Determining the Hypersonic Aerodynamic Characteristics of Arbitrary Bodies," ASRMDF-TM-62-61, September 1962.

13. Solomon, J. M., Ciment, M., Ferguson, R. E., Bell, J. B., Wardlaw, A. B., "A Program for Computing Steady Inviscid Three Dimensional Supersonic Flow on Re-Entry Vehicles, Volume I - Analysis," NSWC-WOL-TR-77-28, February 1977.

14. Solomon, J. M., et al, "A Program for Computing Steady Inviscid Three Dimensional Supersonic Flow on Re-Entry Vehicles, Volume II - Users Manual," NSWC/WOL-TR-77-82, May 1977.

15. Solomon, J. M., Ciment, M., et al, "Users Manual for the BNT-DDD-BETA Package," NSWC/WOL, February 1976.

16. Scaggs, N. E., "Pressure Distributions on Biconic Geometries at Mach 14," AFWAL-TM-84-207-FIMG, July 1984.

17. Hall, D. W., Dougherty, C. M., "Performance Technology Program (PTP-SII). Volume III, Inviscid Aerodynamic Predictions for Ballistic Re-Entry Vehicles with Ablated Nosetips," Appendix - Users Manual, BMO-TR (to be published), September 1979.

18. Hall, D. W., Dougherty, C. M., "Coupling of the CM3DT Inviscid Nosetip Flow Field Code to the NSWC Inviscid Afterbody Code - Final Report," SAI-067-81R-018, November 1980.

19. Jameson, A., and Baker, T. J., "Multigrid Solution of the Euler Equations for Aircraft Configurations," AIAA-84-0093.

20. Sirbaugh, J. R., "Euler Analysis of an Elliptic Missile Body," AIAA-86-2079-CP, August 1986.

21. Miller, D. S., Wood, R. M., "Leeside Flow Over Delta Wings at Supersonic Speeds," NASA TP 2430, June 1985.

22. Jones, J. H., and O'Hare, J. E., "Flow Visualization Photographs of a Yawed Tangent Ogive Cylinder at Mach Number 2," AEDC-TR-73-45, AFATL-TR-73-39, March 1973.

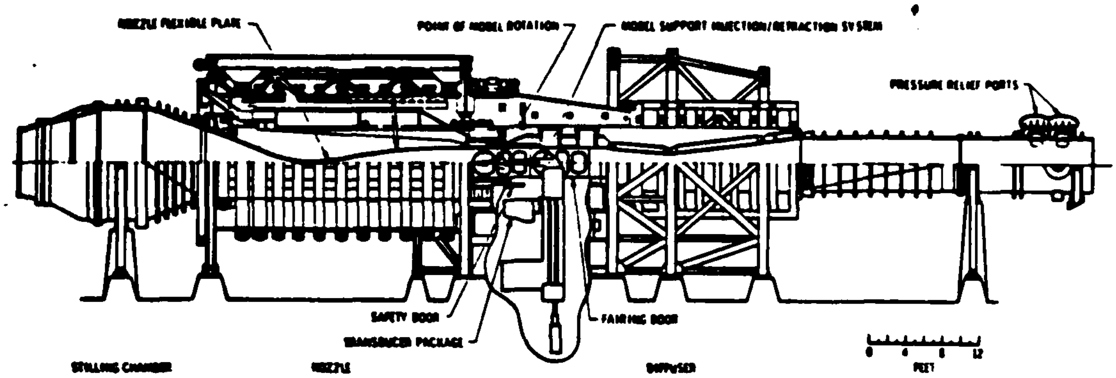

a. Tunnel assembly

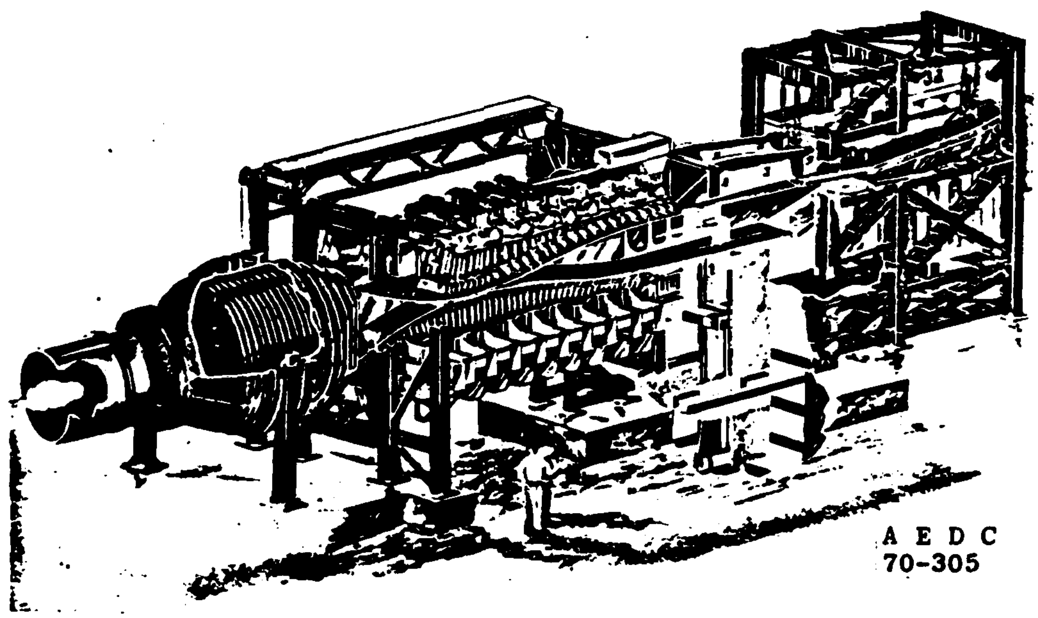

b. Tunnel test section

Figure 1. Tunnel A

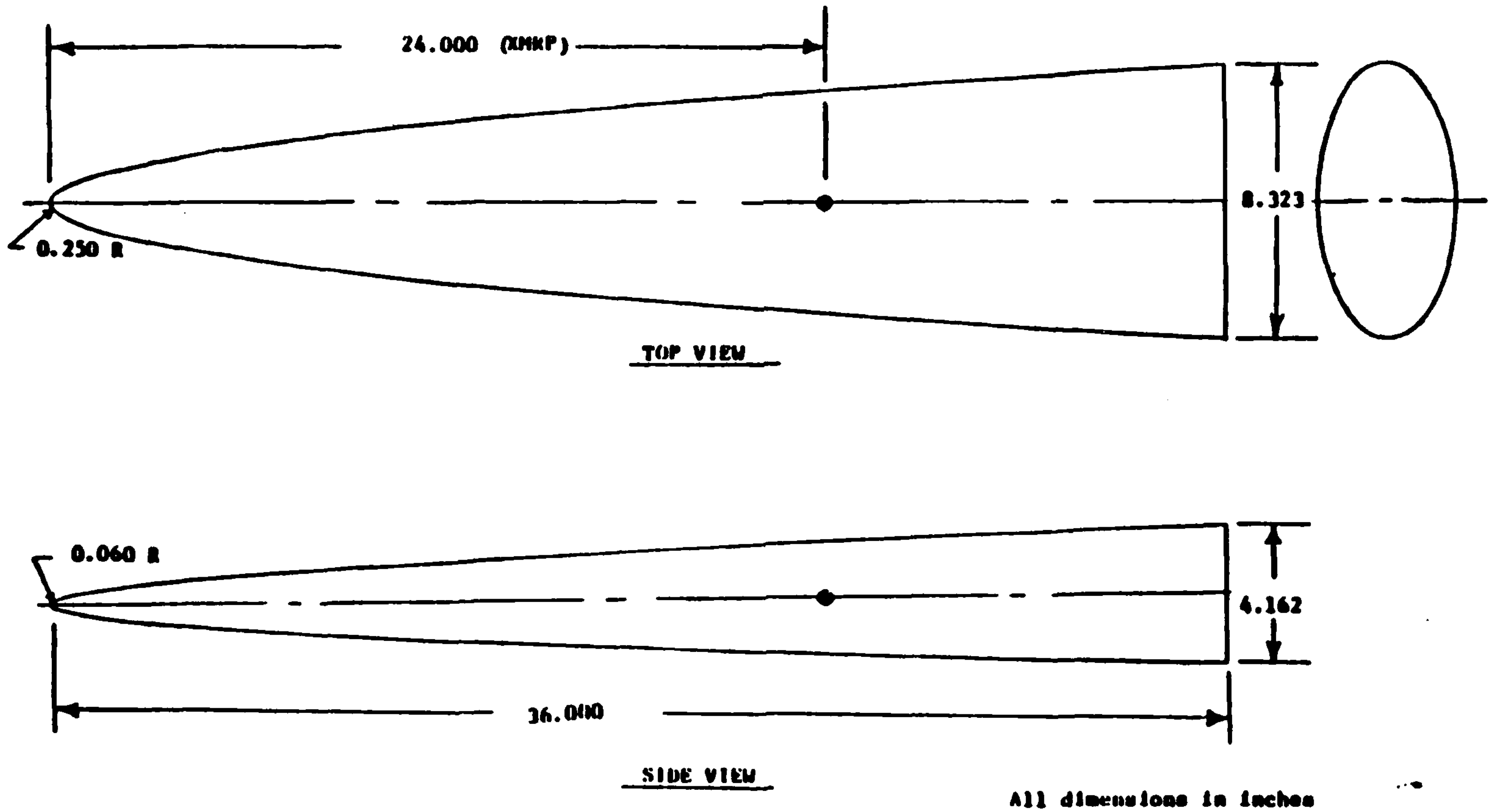

a. B20 Configuration

Figure 2. Model Details

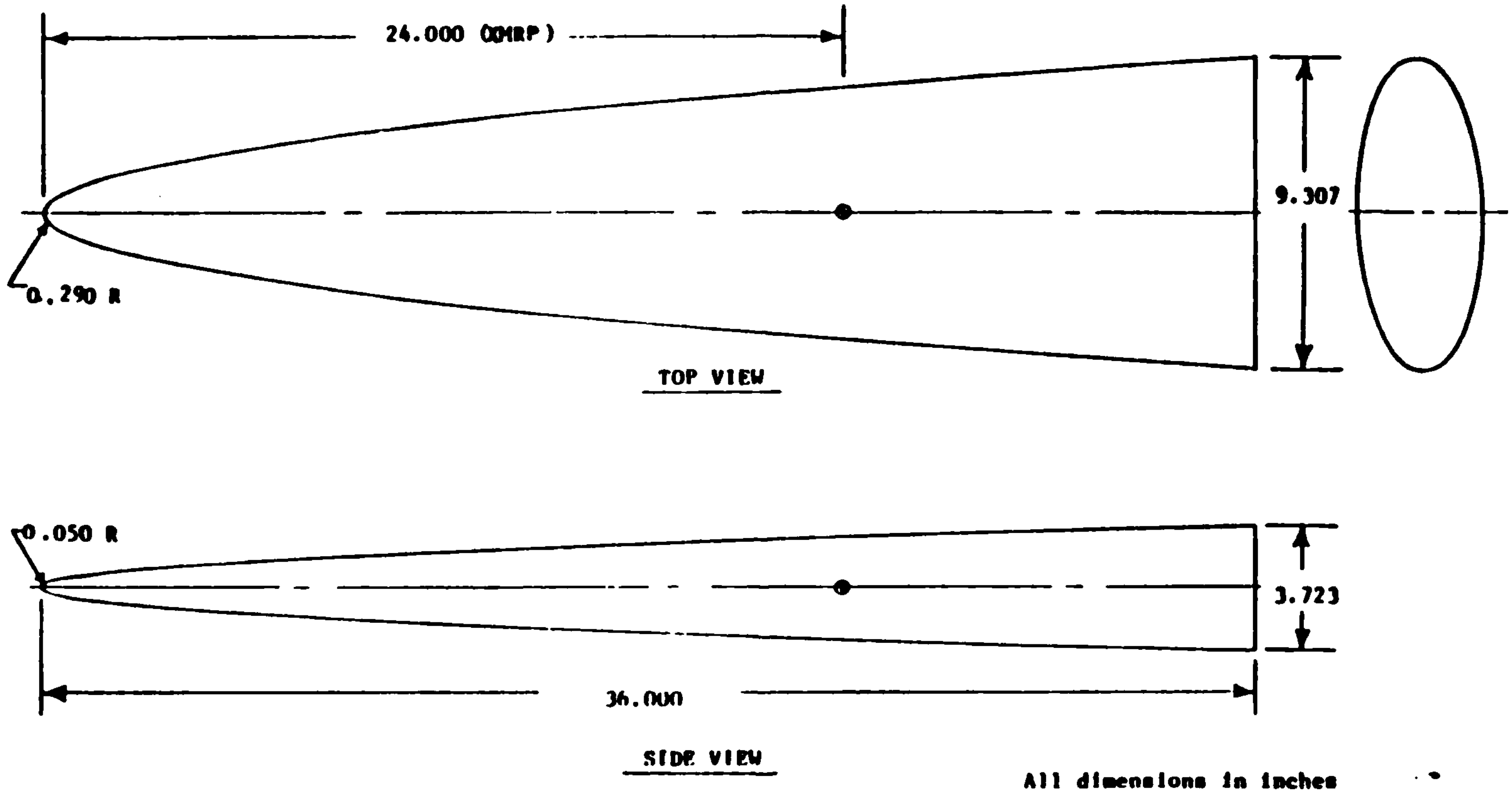

b. B25 Configuration

Figure 2. Model Details (Continued)

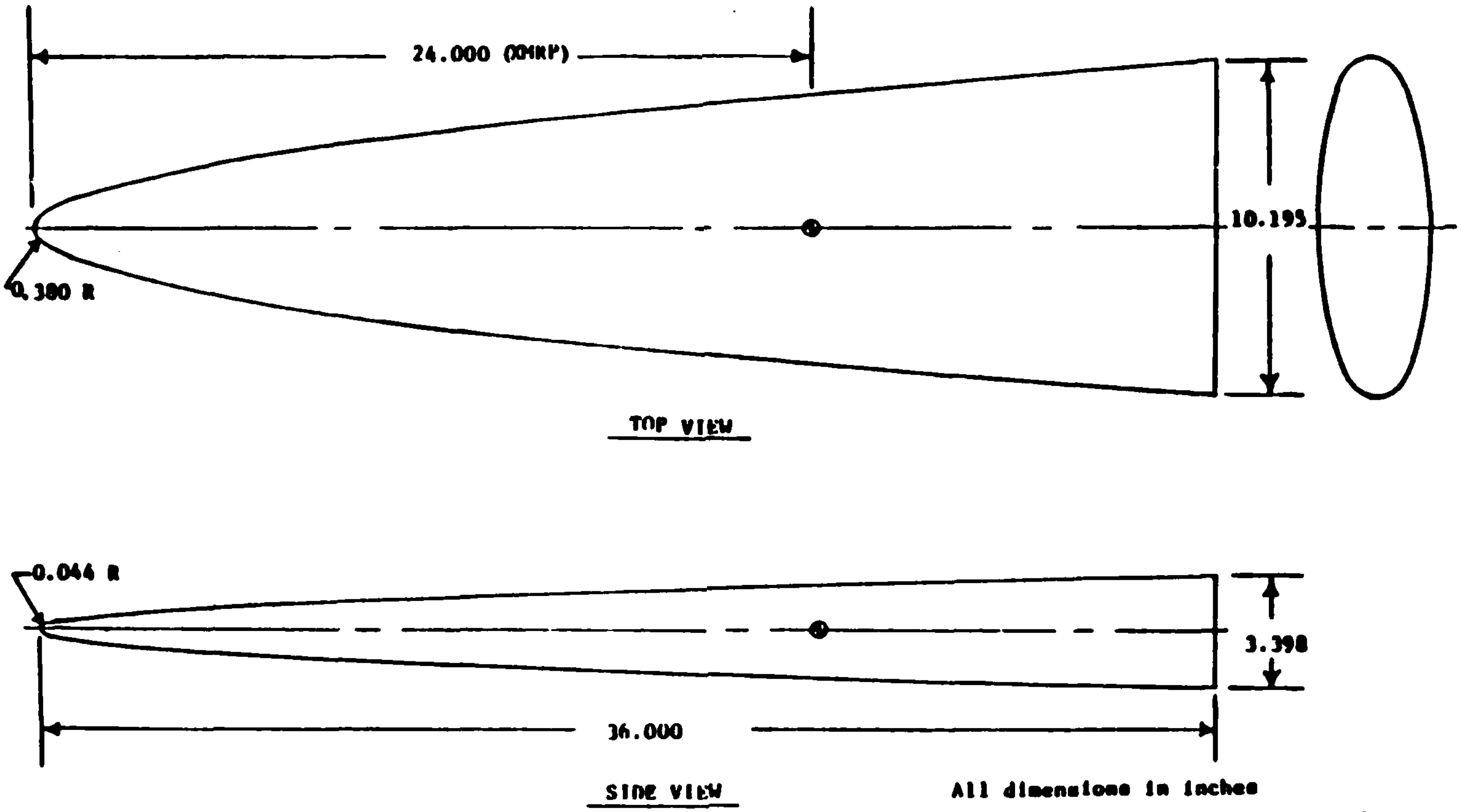

c. B30 Configuration

Figure 2. Model Details (Concluded)

TABLE 1. Model Configuration Designation

CONFIGURATION	DESCRIPTION
B20	2.0:1 ELLIPTICAL BODY, a_{max} = 4.162 in. b_{max} = 2.081 in. L = 8.324 in.
B25	2.5:1 ELLIPTICAL BODY, a_{max} = 4.654 in. b_{max} = 1.862 in. L = 9.308 in.
B30	3.0:1 ELLIPTICAL BODY, a_{max} = 5.098 in. b_{max} = 1.699 in. L = 10.196 in.

TABLE 2. TEST RUN SUMMARY

VKF Tunnel A Run Log

Force and Moment Test

CODE	M	ALPHA	RE x10^{-6}	PITCH RUN AT CONSTANT BETA		
				0	2	4
20	1.76	A3	2.0	37		
	2.00	A1	2.0	33		
		A2			34	35
		A1	1.0	36		
	2.50	A1	2.0	31		
		A2				32
	3.01	A1	2.0	27		
		A2			28	29
		A1	1.0	26		
		A1	3.0	30		
	3.51	A1	2.0	72		
		A2				73
	4.02	A1	2.0	38		
		A2			39	40
	4.51	A1	2.0	51		
		A2				52
	5.03	A1	2.0	53		
		A2			54	55
	5.04	A1	3.0	56		
		A1	4.0	57		
25	1.76	A3	2.0	14		
	2.00	A1	2.0	16		
		A2			17	18
		A1	1.0	15		
	2.50	A1	2.0	19		
		A2				20
	3.01	A1	2.0	22		
		A2			23	24
		A1	1.0	25		
		A1	3.0	21		
	3.51	A1	2.0	70		
		A2				71
	4.02	A1	2.0	41		
		A2			42	43
	4.51	A1	2.0	49		
		A2				50
	5.03	A1	2.0	60		
		A2			61	62
	5.04	A1	3.0	59		
		A1	4.0	58		
30	1.76	A3	2.0	13		
	2.00	A1	2.0	9		
		A2			10	11
		A1	1.0	12		
	2.50	A1	2.0	7		
		A2				8
	3.01	A1	2.0	3		
		A2			4	5
		A1	1.0	6		
		A1	3.0	1*		
				2		

TABLE 2. TEST RUN SUMMARY (Continued)

VKF Tunnel A Run Log

Force and Moment Test

CODE	M	ALPHA	RE $x10^{-6}$	PITCH RUN AT CONSTANT BETA		
				0	2	4
30	3.51	A1	2.0	68		
		A2				69
	4.02	A1	2.0	44		
		A2			45	46
	4.51	A1	2.0	47		
		A2				48
	5.03	A1	2.0	63		
		A2			64	65
	5.04	A1	3.0	66		
		A1	4.0	67		

NOTES:

1. Runs for BETA = 0 were run in continuous sweep mode, except as noted, and for BETA = 2 and 4 were run in point-pause mode.
2. * indicates point-pause mode.
3. ALPHA schedule: A1 = -4,-3.5,-3,-2.5,-2,-1.5,-1,-0.5,0,0.5,1,1.5,2,2.5, 3,3.5,4,5,6,7,8,9,10,11,12,13,14,15,16,17,18,19,20
   A2 = -4,-2,-1,0,1,2,4,6,8,10,12,16,20
   A3 = -2,-1.5.-1,-0.5,0,0.5,1,1.5,2,2.5,3,3.5,4,5,6,7,8, 9,10,11,12,13,14,15,16,17,18,19

TABLE 2. TEST RUN SUMMARY (Continued)

VKF Tunnel A Run Log

Shadowgraph/Schlieren Flowfield Photographic Log

FDL Elliptic Bodies Test

CODE	RUN	M	RE/FT x10^6	ROLL NO.	ALPHA						P.S.
30	2	3.01	3.0	496	-0.18	4.32	8.66	13.01	17.53	21.88	1-6
	3		2.0		-0.23	4.19	8.39	12.61	16.95	21.15	
	6		1.0		-0.20	4.08	8.17	12.26	16.46	20.54	
	7	2.50	2.0	505	-0.21	4.23	8.50	12.80	17.21	21.47	
	12	2.00	1.0	496	-0.22	4.12	8.26	12.44	16.76	20.91	
	13	1.76	2.0	465	-0.13	4.28	8.60	13.01	17.61		1-5
25	14	1.76	2.0		-0.14	4.22	8.48	12.81	17.34		1-5
	15	2.00	1.0		-0.18	4.10	8.20	12.35	16.62	20.74	1-6
	16		2.0		-0.23	4.20	8.47	12.79	17.28	21.61	
	19	2.50	2.0		-0.20	4.18	8.42	12.68	17.07	21.31	
	21	3.01	3.0	718	-0.25	4.26	8.55	12.87	17.34	21.64	
	22		2.0		-0.24	4.15	8.34	12.52	16.86	21.02	
	25		1.0		-0.24	4.05	8.13	12.20	16.41	20.46	
20	26	3.01	1.0		-0.22	4.05	8.11	12.18	16.36	20.40	
	27		2.0		-0.21	4.10	8.25	12.40	16.69	20.81	
	30		3.0		-0.19	4.19	8.42	12.66	17.06	21.29	
	31	2.50	2.0	455	-0.23	4.16	8.34	12.53	16.88	21.07	
	36	2.00	1.0	718	-0.19	4.07	8.16	12.25	16.50	20.60	
	37	1.76	2.0		-0.13	4.17	8.38	12.62	17.09		1-5
	38	4.02	2.0		-0.27	4.04	8.13	12.21	16.44	20.52	1-6
25	41	4.02	2.0		-0.18	4.09	8.19	12.31	16.55	20.65	
30	44	4.02	2.0		-0.19	4.11	8.22	12.35	16.62	20.73	
	47	4.51	2.0		-0.18	4.08	8.18	12.28	16.52	20.61	
25	49	4.51	2.0		-0.18	4.07	8.15	12.23	16.45	20.53	
20	51	4.51	2.0		-0.19	4.06	8.14	12.20	16.41	20.45	
	53	5.03	2.0		-0.18	4.03	8.09	12.16	16.34	20.38	
	56	5.04	3.0		-0.16	4.07	8.17	12.27	16.51	20.61	
	57		4.0		-0.18	4.12	8.25	12.41	16.71	20.86	
25	59	5.04	3.0		-0.17	4.10	8.22	12.35	16.64	20.76	
	60	5.03	2.0		8.15	16.40	20.47				1-4
30	63	5.03	2.0		-0.18	4.07	8.15	12.24	16.47	20.54	1-6
	66	5.04	3.0		-0.16	4.12	8.25	12.39	16.68	20.83	
	67		4.0		-0.14	4.19	8.39	12.58	16.95	21.17	
	68	3.51	2.0		-0.23	4.14	8.33	12.51	16.85	21.02	
25	70	3.51	2.0		-0.21	4.13	8.27	12.43	16.74	20.88	
20	72	3.51	2.0		-0.20	4.09	8.22	12.35	16.62	20.74	

NOTES: 1. RUN No. and Photo Sequence No. (P.S.) are first and second number, respectively, on photographs.

TABLE 2. TEST RUN SUMMARY (Continued)

VKF Tunnel A Pressure Test

CODE	M	RE $x10^{-6}$	BETA	ALPHA -4	-2	-1	0	1	2	4	6	8	10	12	14	16	18	20
20	1.51	2.0	0		704	705	706	707	708	709	710	711	712	713	714	715	716	
	1.76		0		691	692	693	694	695	696	697	698	699	700	701	702	703	
	2.00	2.0	0	608	609	610	611	612	613	614	615	616	617	618	619	620	621	622
			2	623	624	625	626	627	628	629	630	631	632	633		634		635
			4	636	637	638	639	640	641	642	643	644	645	646		647		648
			-2	649	650	651	652	653	654	655	656	657	658	659		660		661
			-4	662	663	664	665	666	667	668	669	670	671	672		673		674
		1.0	0	675	676	677	678	679	680	681	682	683	684	685	686	687	689	690
	2.50	2.0	0	567	568	569	570	571	572	573	574	575	576	577	578	579	580	581
			4	582	583	584	585	586	587	588	589	590	591	592		593		594
			-4	595	596	597	598	599	600	601	602	603	604	605		606		607
	3.01	3.0	0	469	470	471	472	473	474	475	476	477	478	479	480	481	482	483
		2.0	0	484	485	486	487	488	489	490	491	492	493	494	495	496	497	498
			2	499	500	501	502	503	504	505	506	507	508	509		510		511
			4	513	514	515	516	517	518	519	520	521	522	523		524		525
			-2	526	527	528	529	530	531	532	533	534	535	536		537		538
			-4	539	540	541	542	543	544	545	546	547	548	549		550		551
		1.0	0	552	553	554	555	556	557	558	559	560	561	562	563	564	565	566
	3.51	2.0	0	717	718	719	720	721	722	723	725	726	727	728	729	730	731	732
			4	733	734	735	736	737	738	739	740	741	742	743		744		745
			-4	746	747	748	749	750	752	753	754	755	756	757		758		759
	4.02	2.0	0	760	761	762	763	764	765	766	767	768	769	770	771	772	773	774
			2	775	776	777	778	779	780	781	782	783	784	785		786		787
			4	788	789	790	791	792	793	794	795	796	797	798		799		800
			-2	801	802	803	804	805	806	807	808	809	810	811		812		813
			-4	814	815	816	817	818	819	820	821	822	823	824		825		826
	4.51	2.0	0	827	828	829	830	831	832	833	834	835	836	837	838	839	840	841
			4	842	843	844	845	846	847	848	849	850	851	852		853		854
			-4	855	856	857	858	859	860	861	862	863	864	865		866		867

TABLE 2. TEST RUN SUMMARY (Continued)

VKF Tunnel A Pressure Test

CODE	M	RE x10^{-6}	BETA	ALPHA -4	-2	-1	0	1	2	4	6	8	10	12	14	16	18	20
20	5.04	4.0	0	868	869	870	871	872	873	874	875	876	877	878	879	880	881	882
		3.0	0	883	884	885	886	887	888	889	890	891	892	893	894	895	896	897
	5.03	2.0	0	898	899	900	901	902	903	904	905	906	907	908	909	910	911	912*
			2	913	914	915	916	917	918	919	920	921	922	923		924		925
			4	926	927	928	929	930	931	932	933	934	935	936		937		938
			-2	939	940	941	942	943	944	945	946	947	948	949		950		951
			-4	952	953	954	955	956	957	958	959	960	961	962		963		964
25	1.51	2.0	0		1198	1199	1200	1202	1203	1204	1205	1206	1207	1208	1209	1210	1211	
	1.76	2.0	0		1185	1186	1187	1188	1189	1190	1191	1192	1193	1194	1195	1196	1197	
	2.00	2.0	0	1103	1104	1105	1106	1107	1108	1109	1110	1111	1112	1113	1114	1115	1116	1117*
			2	1118	1119	1120	1121	1122	1123	1124	1125	1126	1127	1128		1129		1130
			4	1131	1132	1133	1134	1135	1136	1137	1138	1139	1140	1141		1142		1143
			-2	1144	1145	1146	1147	1148	1149	1150	1151	1152	1153	1154		1155		1156
			-4	1157	1158	1159	1160	1161	1162	1163	1164	1165	1166	1167		1168		1169
		1.0	0	1170	1171	1172	1173	1174	1175	1176	1177	1178	1179	1180	1181	1182	1183	1184
	2.50	2.0	0	1062	1063	1064	1065	1066	1067	1068	1069	1070	1071	1072	1073	1074	1075	1076*
			4	1077	1078	1079	1080	1081	1082	1083	1084	1085	1086	1087		1088		1089
			-4	1090	1091	1092	1093	1094	1095	1096	1097	1098	1099	1100		1101		1102
	3.01	3.0	0	965	966	967	968	969	970	971	972	973	974	975	976	977	978	979
		2.0	0	980	981	982	983	984	985	986	987	988	989	990	991	992	993	994*
			2	995	996	997	998	999	1000	1001	1002	1003	1004	1005		1006		1007
			4	1008	1009	1010	1011	1012	1013	1014	1015	1016	1017	1018		1019		1020
			-2	1021	1022	1023	1024	1025	1026	1027	1028	1029	1030	1031		1032		1033
			-4	1034	1035	1036	1037	1038	1039	1040	1041	1042	1043	1044		1045		1046
		1.0	0	1047	1048	1049	1050	1051	1052	1053	1054	1055	1056	1057	1058	1059	1060	1061
	3.51	2.0	0	1212	1213	1214	1215	1216	1217	1218	1219	1220	1221	1222	1223	1224	1225	1226
			4	1227	1228	1229	1230	1231	1232	1233	1234	1235	1236	1237		1238		1239
			-4	1240	1241	1242	1243	1244	1245	1246	1247	1248	1249	1250		1251		1252
	4.02	2.0	0	1253	1254	1255	1256	1257	1258	1259	1260	1261	1262	1263	1264	1265	1266	1267*
			2	1268	1269	1270	1271	1272	1273	1274	1275	1276	1277	1278		1279		1280
			4	1281	1282	1283	1284	1285	1286	1287	1288	1289	1290	1291		1292		1293
			-2	1294	1295	1296	1297	1298	1299	1300	1301	1302	1303	1304		1305		1306
			-4	1307	1308	1309	1310	1311	1312	1313	1314	1315	1316	1317		1318		1319

TABLE 2. TEST RUN SUMMARY (Continued)

VKF Tunnel A Pressure Test

CODE	M	RE x10^{-6}	BETA	ALPHA														
				-4	-2	-1	0	1	2	4	6	8	10	12	14	16	18	20
25	4.51	2.0	0	1320	1321	1322	1323	1324	1325	1326	1327	1328	1329	1330*	1331	1332	1333	1334*
			4	1335	1336	1337	1338	1339	1340	1341	1342	1343	1344	1345		1346		1347
			-4	1348	1349	1350	1351	1352	1353	1354	1355	1356	1357	1358		1359		1360
	5.03	2.0	0	1361	1362	1363	1364	1365	1366	1367	1368	1369	1370	1371*	1372	1373	1374	1375*
			2	1376	1377	1378	1379	1380	1381	1382	1383	1384	1385	1386		1387		1388
			4	1389	1390	1391	1392	1393	1394	1395	1396	1397	1398	1399		1400		1401
			-2	1402	1403	1404	1405	1406	1407	1408	1409	1410	1411	1412		1413		1414
			-4	1415	1416	1417	1418	1419	1420	1421	1422	1423	1424	1425		1426		1427
	5.04	3.0	0	1428	1429	1430	1431	1432	1433	1434	1435	1436	1437	1438	1439	1440	1441	1442
		4.0	0	1443	1444	1445	1446	1447	1448	1449	1450	1451	1452	1453	1454	1455	1456	1457
30	2.00	2.0	0	140	141	142	143	144	145	146	147	148*	149	150*	151	152*	153	154*
			2	155	156	157	158	159	160	161	162	163	164	165		166		167
			4	168	169	170	171	172	173	174	175	176	177	178		179		180
			-2	181	182	183	184	185	186	187	188	189	190	191		192		193
			-4	194	195	196	197	198	199	200	201	202	203	204		205		206
		1.0	0	207	208	209	210	211	212	213	214	215	216	217	218	219	220	221
	2.50	2.0	0	99	100	101	102	103	104	105	106	107	108	109*	110	111	112	113*
			4	114	115	116	117	118	119	120	121	122	123	124		125		126
			-4	127	128	129	130	131	132	133	134	135	136	137		138		139
	3.01	3.0	0				1											
			0	2	3	4	5	6	7	8	9	10	11	12	13	14	15	16
		2.0	0	17	18	19	20	21	22	23	24	25*	26	27*	28	29*	30	31*
			2	32	33	34	35	36	37	38	39	40	41	42		43		44
			4	45	46	47	48	49	50	51	52	53	54	55		56		57
			-2	58	59	60	61	62	63	64	65	66	67	68		69		70
			-4	71	72	73	74	75	76	77	78	79	80	81		82		83
		1.0	0	84	85	86	87	88	89	90	91	92	93	94	95	96	97	98
	3.51	2.0	0	428	429	430	431	432	433	434	435	436	437	438*	439	440	441	442*
			4	443	444	445	446	447	448	449	450	451	452	453		454		455
			-4	456	457	458	459	460	461	462	463	464	465	466		467		468

TABLE 2. TEST RUN SUMMARY (Continued)

VKF Tunnel A Pressure Test

CODE	M	RE $x10^{-6}$	BETA	ALPHA														
				-4	-2	-1	0	1	2	4	6	8	10	12	14	16	18	20
30	4.02	2.0	0	360	361	362	363	364	365	366	367	368	369	370*	371	372	373	374*
			2	375	376	377	378	379	380	381	382	383	384	385		386		387
			4	388	389	390	391	392	393	394	395	396	397	398		399		400
			-2	401	402	403	404	405	406	407	408	409	410	411		412		413
			-4	415	416	417	418	419	420	421	422	423	424	425		426		427
	4.51	2.0	0	319	320	321	322	323	324	325	326	327	328	329*	330	331	332	333*
			4	334	335	336	337	338	339	340	341	342	343	344		345		346
			-4	347	348	349	350	351	352	353	354	355	356	357		358		359
	5.04	4.0	0	222	223	224	225	226	227	228	229	230	231	232	233	234	235	236
		3.0	0	237	238	239	240	241	242	243	244	245	246	247	248	249	250	251
	5.03	2.0	0	252	253	254	255	256	257	258	259	260	261	262*	263	264	265	266*
			2	267	268	269	270	271	272	273	274	275	276	277		278		279
			4	280	281	282	283	284	285	286	287	288	289	290		291		292
			-2	293	294	295	296	297	298	299	300	301	302	303		304		305
			-4	306	307	308	309	310	311	312	313	314	315	316		317		318

NOTES:

1. Runs 414, 512, 688, 724, 751, and 1201 do not exist.
2. Reflected model nose shock impinged on model for Runs 709-716, 1198, 1204-1211.

* Color graphics output

TABLE 2. TEST RUN SUMMARY (Continued)

VKF Tunnel A - Run log

Vapor-Screen Test

CODE	M	ALPHA	PHI	X: 9.6	X: 16.0	X: 22.4	X: 28.8	X: 35.2
20	2.00	8	0	51	52	53	54	55*
		12		56	57	58	59	60
		16		61	62	63	64	65*
		20		66	67	68	69	70
25		8		31	32	33	34	35*
		12		36	37	38	39	40
		16		41	42	43	44	45*
		20		46	47	48	49	50
30		0		1	2	3	4	5
		4		6	7	8	9	10
		8		11	12	13	14	15*
		12		16	17	18	19	20
		16		21	22	23	24	25*
		20		26	27	28	29	30
20	3.01	8		76	77	78	79	80*
		12		71	72	73	74	75*
		16		81	82	83	84	85*
		20		86	87	88	89	90
25		8		91	[illegible]	93	94	95*
		12		96	97	98	99	100
		16		101	102	103	104	105*
		20		106	107	108	109	110
30		8		111	112	113	114	115*
		12		116	117	118	119	120
		16		121	122	123	124	125*
		20		126	127	128	129	130
		16	-45	131	132	133	134	135

Note:

1. * indicates movies also obtained at this angle of attack. The model was driven continuously through the plane of light at the specified angle of attack.

TABLE 2. TEST RUN SUMMARY (Continued)

VKF Tunnel A - Run log

Phase 1 Oil-Flow Test

CODE	M	ALPHA	PHI	RUN NO.	OIL VISCOSITY, CS TOP	OIL VISCOSITY, CS BOTTOM	APPLICATION METHOD
20	2.00	8	0	18	Medium	Heavy	SPOT
		12		19			
		16		20		↓	
		20		21		100	
25		8		22		Heavy	
		12		23			
		16		24		↓	
		20		25		100	
30		8		26		Heavy	
		12		27			
		16		28		↓	
		20		29		100	
20	3.01	8		14		Heavy	
		12		15			
		16		16		↓	
		20		17		100	
25		8		10		Heavy	
		12		11			
		16		12		↓	
		20		13	↓	100	↓
30		0		1	10	10	DAUB
		4		2	Medium	Heavy	
		8		3	Medium	Heavy	↓
		8		4	Heavy	100	
		8		5	Heavy	Heavy	SPOT
		12		6	Heavy		
		16		7	Medium		
		20		8	Medium	↓	
		16	-45	9	Heavy	-	↓

Note:

1. Medium oil was 80% 10 cs and 20% 100 cs oil and heavy oil was 50% 10 cs and 50% 100 cs oil.

TABLE 2. TEST RUN SUMMARY (Continued)

VKF Tunnel A - Run log

Phase 2 Oil Flow Test

RUN	MACH NO.	MODEL	ALPHA deg	OIL VISCOSITY TOP/BOTTOM
1	3.0	B30	10	Light/Medium
2			10	Heavy/Heavy
3			8	
4			6	
5			12	
6			14	
7			4	
8		B25	14	
9			12	
10			10	
11			8	
12			6	
13		B20	14	
14			12	
15			10	
16			8	
17			6	
18	2.0	B20	14	
19			12	
20			10	
21			8	
22			6	
23		B30	14	
24			12	

Note:

1. Light oil was 80% 10 Centi Stokes (CS) and 20% 100CS
   Medium oil was 50% 10CS and 50% 100CS
   Heavy oil was 100% 1000CS

TABLE 2. TEST RUN SUMMARY (Continued)

PWT 4T Force and Moment Test Run Log

Test Run Number Summary

CONFIG	ALPHA	BETA	M							
			0.4	0.55	0.8	0.95	1.05	1.1	1.2	1.3
B20	A1	0	47 72	50	54	57	60	63	66	70
		4	48	51	55	58	61	64	67	71
B25	A1	0	82	84	86	88	90	92	94	96
		4	83	85	87	89	91	93	95	97
B30	A1	0	106	108	111	113	115	118	120	122 123
		4	107	109	112	114	116	119	121	124

Notes: ALPHA Schedule: A1= -4,-3,-2,-1,0,1,2,3,4,6,8,10,12,16,20 deg

TABLE 2. TEST RUN SUMMARY (Continued)

PWT 4T Pressure Test Run Log

CONFIG	M	BETA	ALPHA														
			-4	-3	-2	-1	0	1	2	3	4	6	8	10	12	16	20
B20	1.2	-4	1096	1097	1098	1099	1100	1101	1102	1103	1104	1105	1106	1107	1108	1109	1110
		0	1112	1113	1114	1115	1116	1117	1118	1119	1120	1121	1122	1123	1124	1125	1126
		4	1128	1129	1130	1131	1132	1133	1134	1135	1136	1137	1138	1139	1140	1141	1142
	1.3	-4	1144	1145	1146	1147	1148	1149	1150	1151	1152	1153	1154	1155	1156	1157	1158
		0	1160	1161	1162	1163	1164	1165	1166	1167	1168	1169	1170	1171	1172	1173	1174
		-4	1176	1177	1178	1179	1180	1181	1182	1183	1184	1185	1186	1187	1188	1189	1190
B25	0.4	-4*	556	557	558	559	560	561	562	563	564	565	566	567	568	569	570
		0*	572	573	574	575	576	577	578	579	580	581	582	583	584	585	586
		4*	588	589	590	591	592	593	594	595	596	597	598	599	600	601	602
	0.55	-4*	349	350	351	352	353	354	355	356	357	358	359	360	361	362	363
		0*	365	366	367	368	369	370	371	372	373	374	375	376	377	378	379
		4*	381	382	383	384	385	386	387	388	389	390	391	392	393	394	395
	0.8	-4*	398	399	400	401	402	403	404	405	406	407	408	409	410	411	412
		0*	415	416	417	418	419	420	421	422	423	424	425	426	427	428	429
		4*	431	432	433	434	435	436	437	438	439	440	441	442	443	444	445
	0.95	-4*	447	448	449	450	451	452	453	454	455	456	457	458	459	460	461
		0*	463	464	465	466	467	468	469	470	471	472	473	474	475	476	477
		4*	479	480	481	482	483	484	485	486	487	488	489	490	491	492	493

TABLE 2. TEST RUN SUMMARY (Concluded)

PWT 4T Pressure Test Run Log

CONFIG	M	BETA	ALPHA														
			-4	-3	-2	-1	0	1	2	3	4	6	8	10	12	16	20
B30	0.4	-4	1634	1635	1636	1637	1638	1639	1640	1641	1642	1643	1644	1645	1646	1647	1648
		0	1650	1651	1652	1653	1654	1655	1656	1657	1658	1659	1660	1661	1662	1663	1664
		4	1666	1667	1668	1669	1670	1671	1672	1673	1674	1675	1676	1677	1678	1679	1680
	0.55	-4	1586	1587	1588	1589	1590	1591	1592	1593	1594	1595	1596	1597	1598	1599	1600
		0	1602	1603	1604	1605	1606	1607	1608	1609	1610	1611	1612	1613	1614	1615	1616
		4	1618	1619	1620	1621	1622	1623	1624	1625	1626	1627	1628	1629	1630	1631	1632
	0.8	-4	1300	1301	1302	1303	1304	1305	1306	1307	1308	1309	1310	1311	1312	1313	1314
		0	1317	1318	1319	1320	1321	1322	1323	1324	1325	1326	1327	1328	1329	1330	1331
		4	1333	1334	1335	1336	1337	1338	1339	1340	1341	1342	1343	1344	1345	1346	1347
	0.95	-4	1349	1350	1351	1352	1353	1354	1355	1356	1357	1358	1359	1360	1361	1362	1363
		0	1365	1366	1367	1368	1369	1370	1371	1372	1373	1374	1375	1376	1377	1378	1379
		4	1381	1382	1383	1384	1385	1386	1387	1388	1389	1390	1391	1392	1393	1394	1395
	1.05	-4	1397	1398	1399	1400	1401	1402	1403	1404	1405	1406	1407	1408	1409	1410	
		0	1413	1414	1415	1416	1417	1418	1419	1420	1421	1422	1423	1424	1425	1426	1427
		4	1429	1430	1431	1432	1433	1434	1435	1436	1437	1438	1439	1440	1441	1442	
	1.1	-4	1445	1446	1447	1448	1449	1450	1451	1452	1453	1454	1455	1456	1457	1458	
		0	1460	1461	1462	1463	1464	1465	1466	1467	1468	1469	1470	1471	1472	1473	
		4	1476	1477	1478	1479	1480	1481	1482	1483	1484	1485	1486	1487	1488	1489	

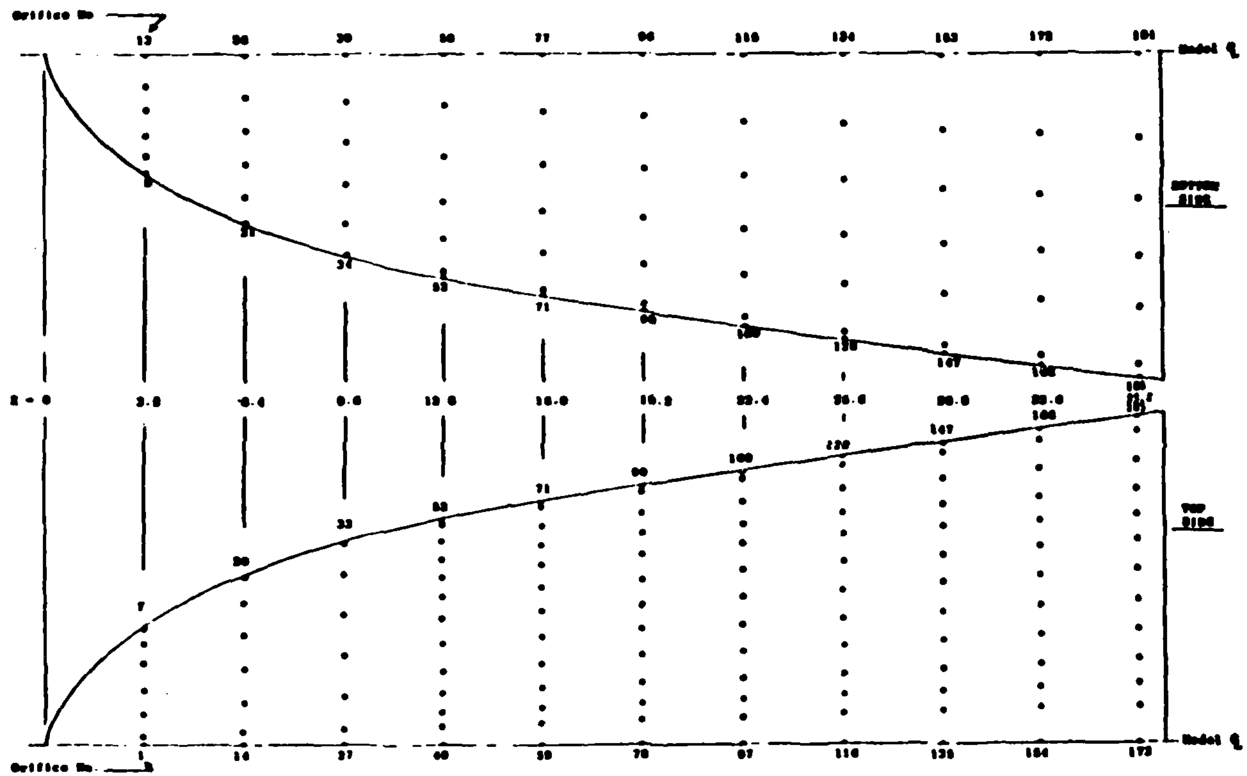

a. Axial Location

Figure 3. Pressure Orifice Locations

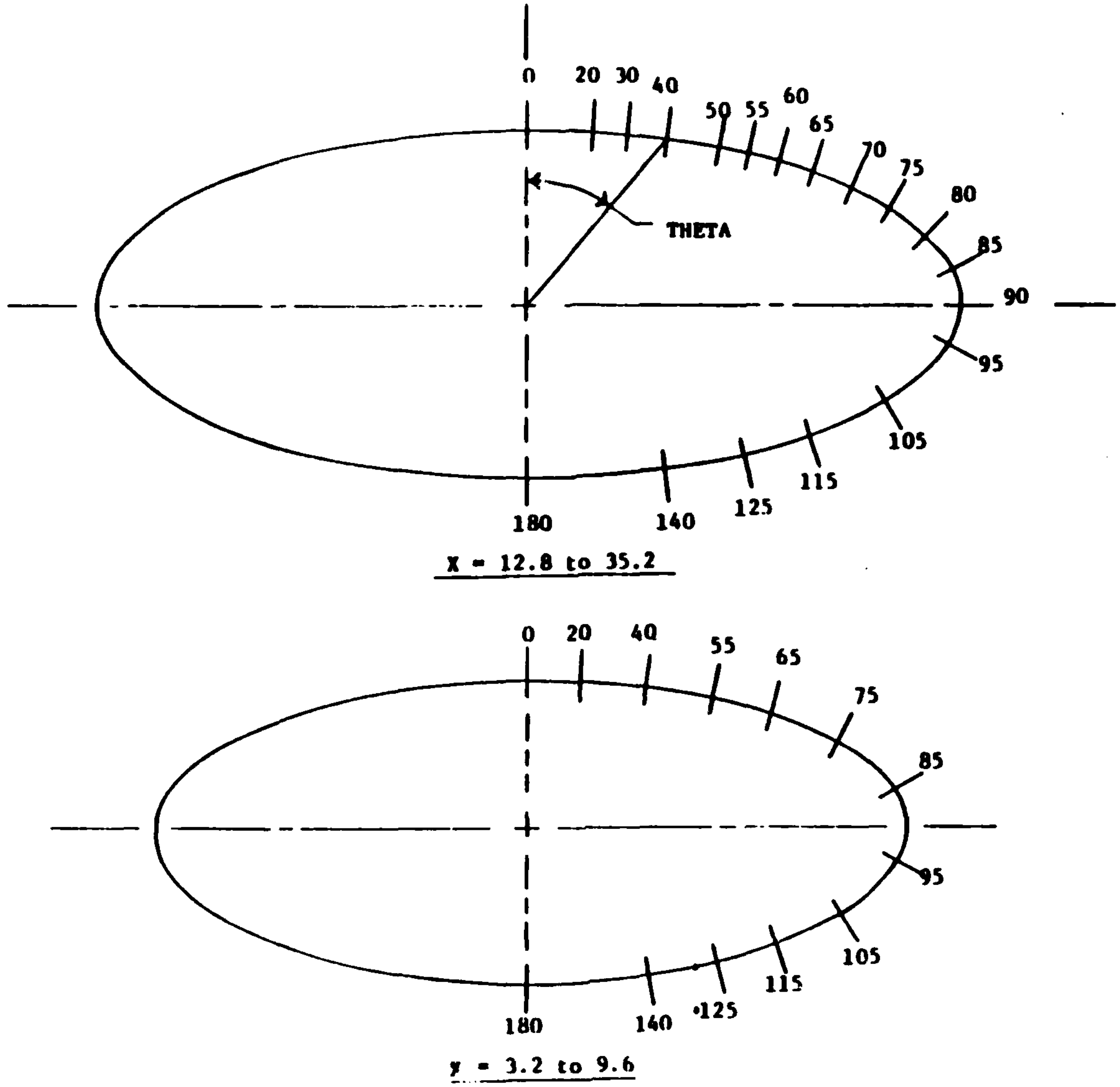

b. Radial Location

Figure 3. Pressure Orifice Locations (Continued)

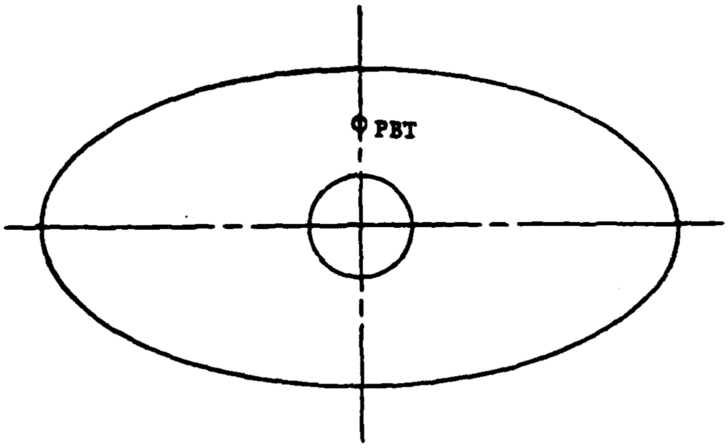

Pressure Phase

Looking Upstream (PHI = 0)

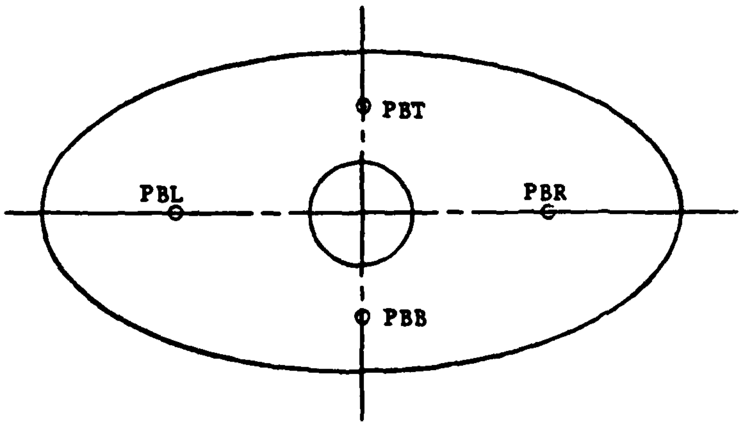

Force Phase

c. Base Pressure Orifice Location

Figure 3. Pressure Orifice Locations (Concluded)

Table 3. Pressure Orifice Location and Designation

THETA \ X	3.2	6.4	9.6	12.8	16.0	19.2	22.4	25.6	28.8	32.0	35.2
0	1	14	27	40	59	78	97	116	135	154	173
20	2	15	28	41	60	79	98	117	136	155	174
30				42	61	80	99	118	137	156	175
40	3	16	29	43	62	81	100	119	138	157	176
50				44	63	82	101	120	139	158	177
55	4	17	30	45	64	83	102	121	140	159	178
60				46	65	84	103	122	141	160	179
65	5	18	31	47	66	85	104	123	142	161	180
70				48	67	86	105	124	143	162	181
75	6	19	32	49	68	87	106	125	144	163	182
80				50	69	88	107	126	145	164	183
85	7	20	33	51	70	89	108	127	146	165	184
90				52	71	90	109	128	147	166	185
95	8	21	34	53	72	91	110	129	148	167	186
105	9	22	35	54	73	92	111	130	149	168	187
115	10	23	36	55	74	93	112	131	150	169	188
125	11	24	37	56	75	94	113	132	151	170	189
140	12	25	38	57	76	95	114	133	152	171	190
180	13	26	39	58	77	96	115	134	153	172	191

NOTE: Thermocouples located at approximately X = 22.4 and THETA = 0 and 180.

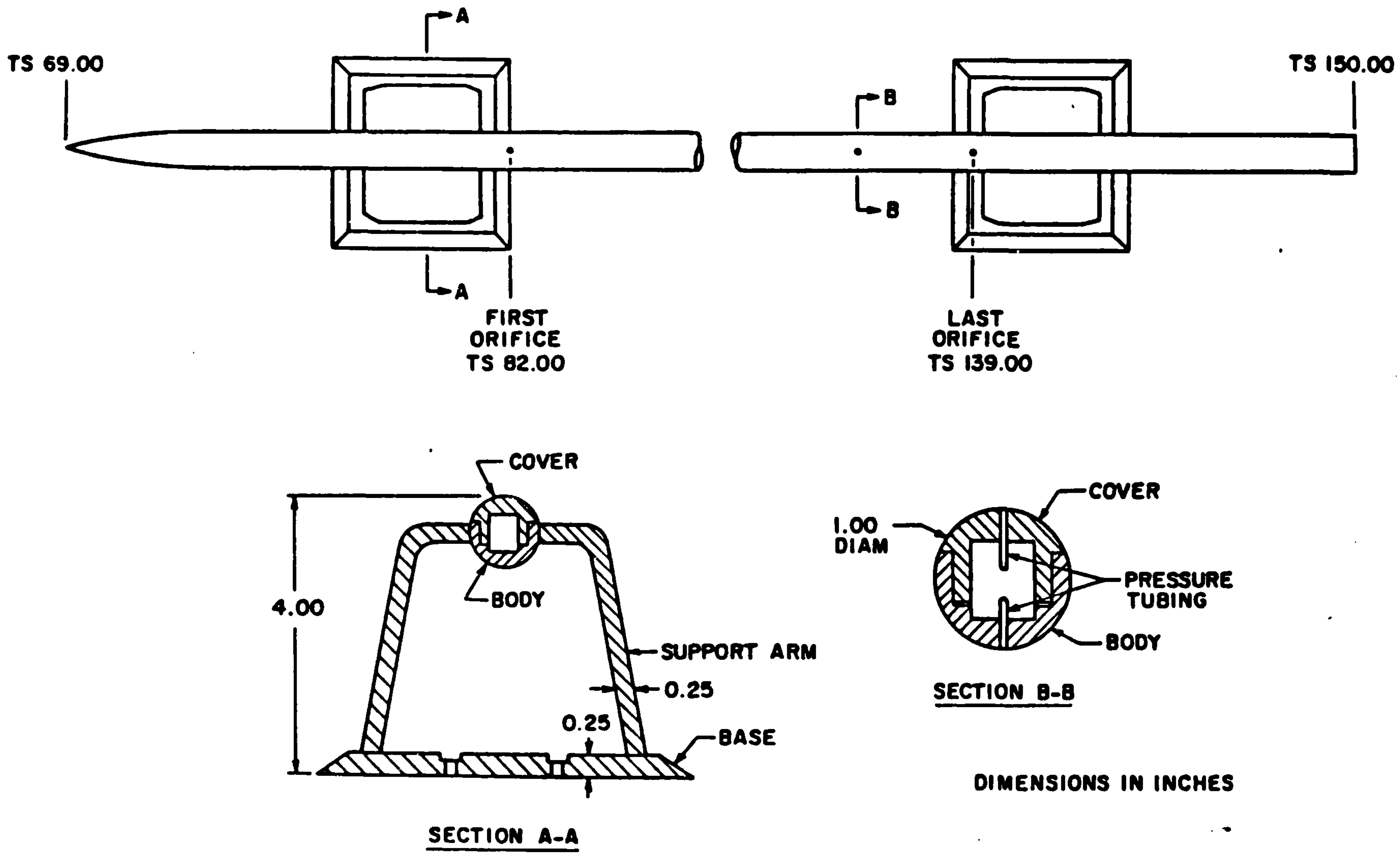

a. Details

Figure 4. Static Pressure Pipe

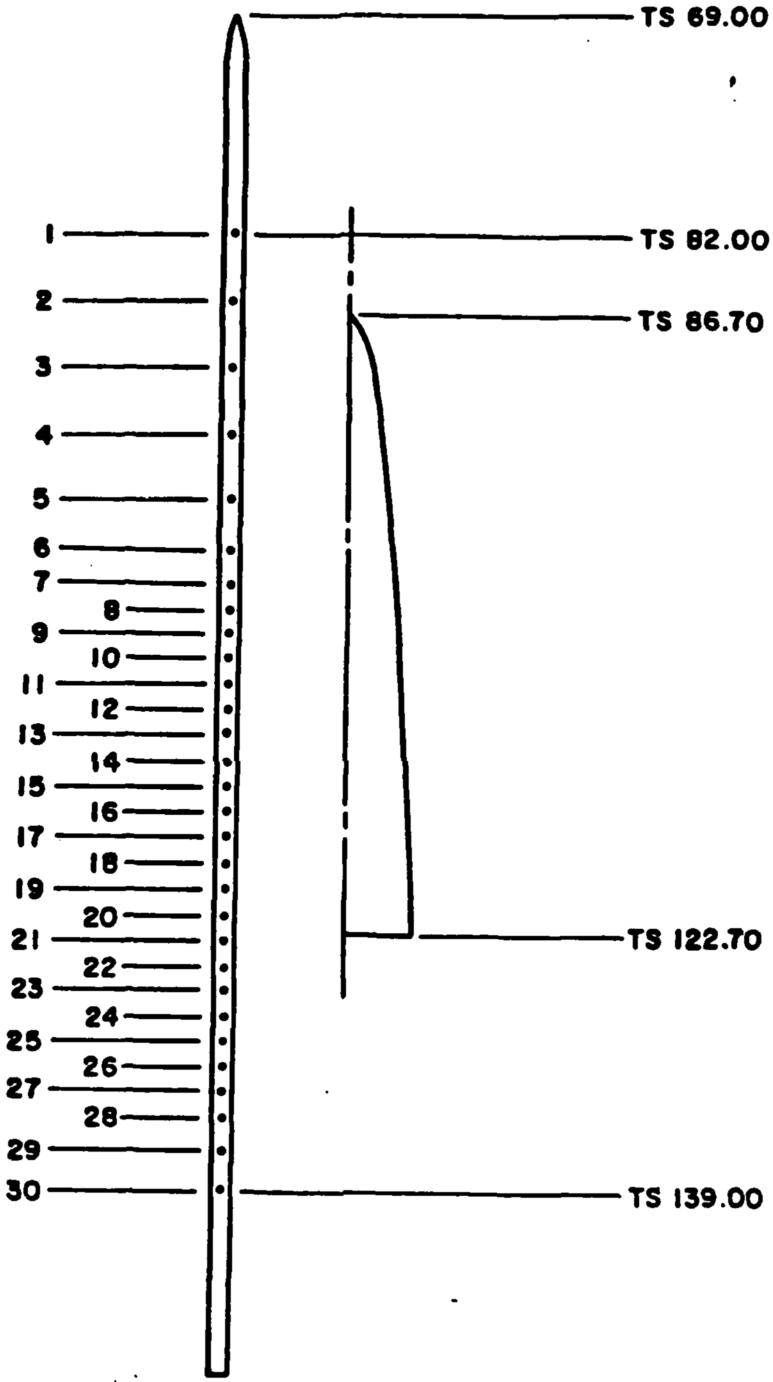

b. Relationship of Model to Wall Pipe

Figure 4. Static Pressure Pipe (Concluded)

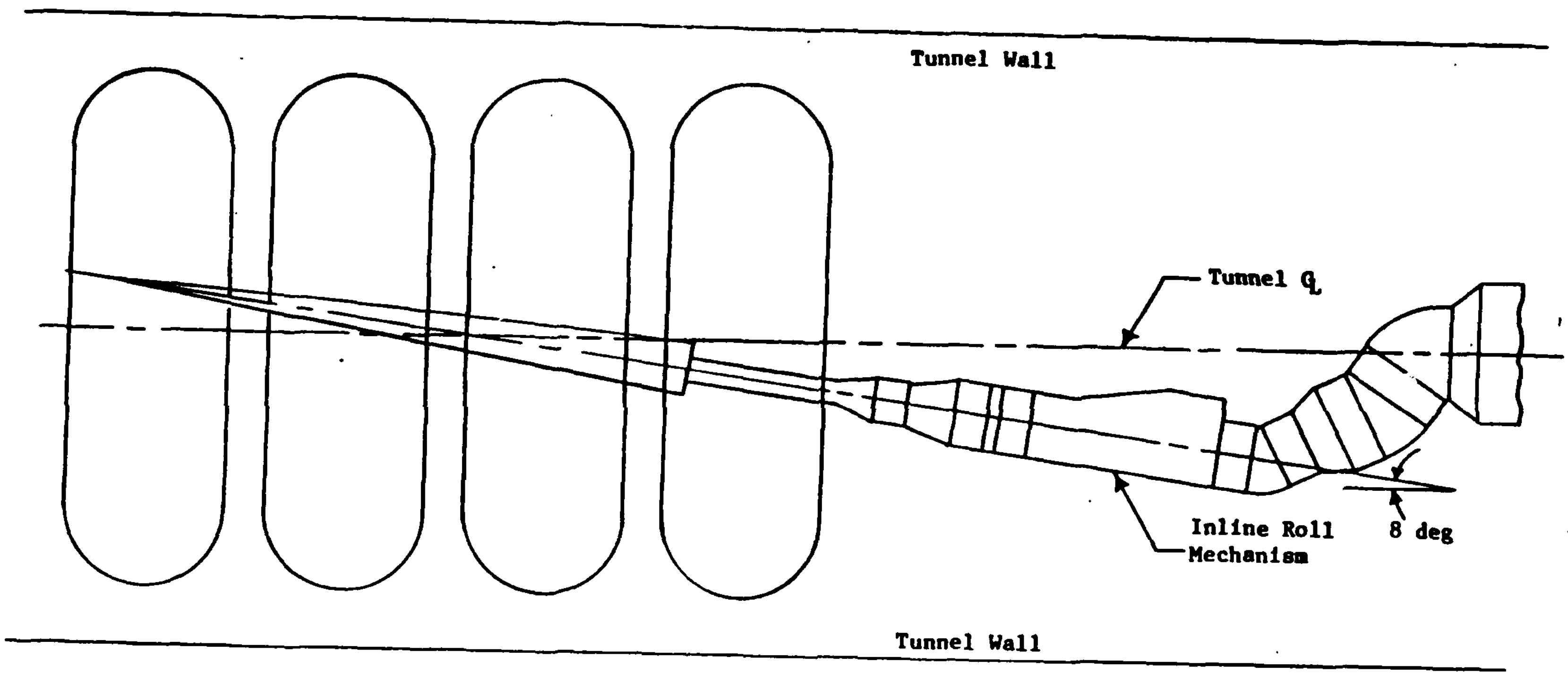

a. Tunnel A

Figure 5. Tunnel Model Installation

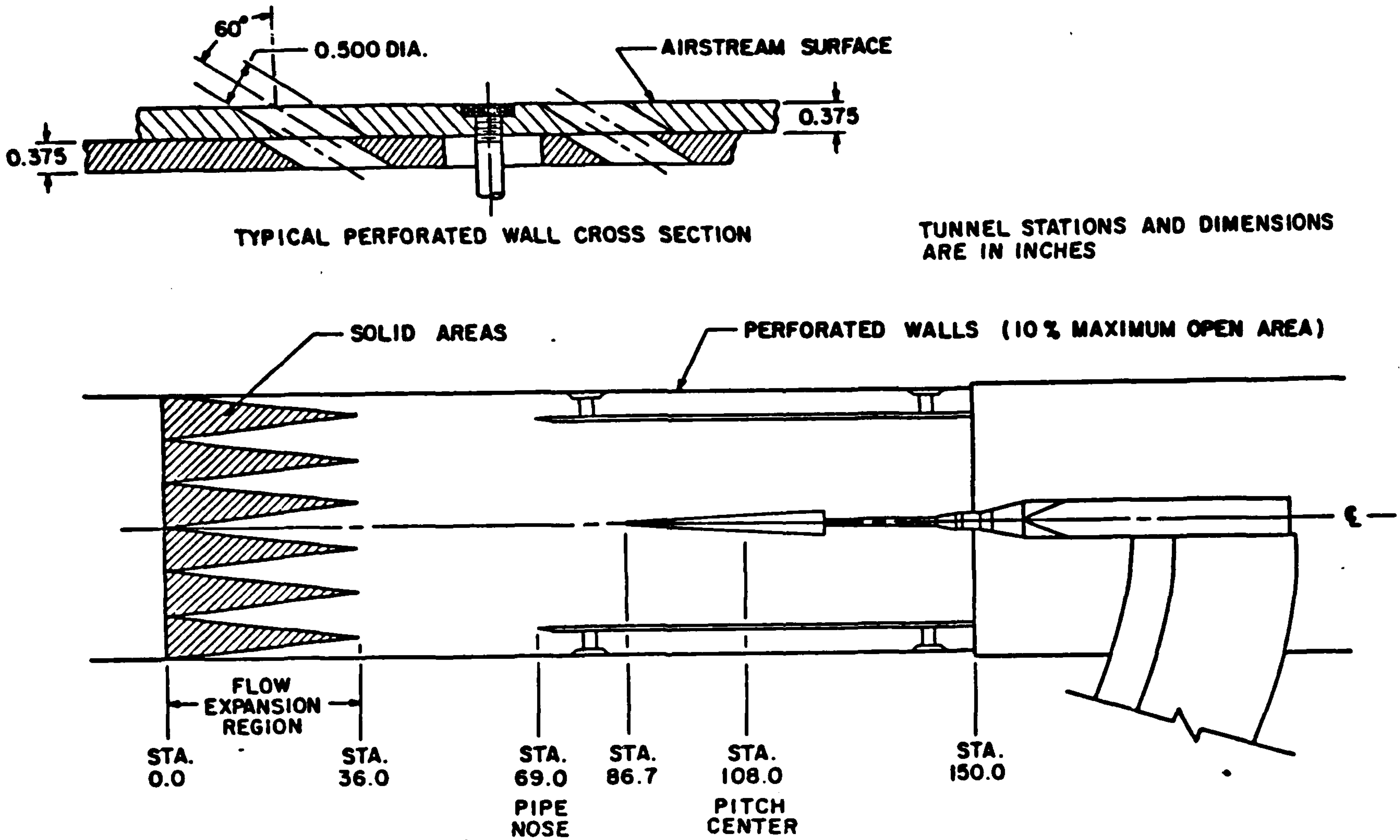

b. Tunnel 4T

Figure 5. Tunnel Model Installation (Concluded)

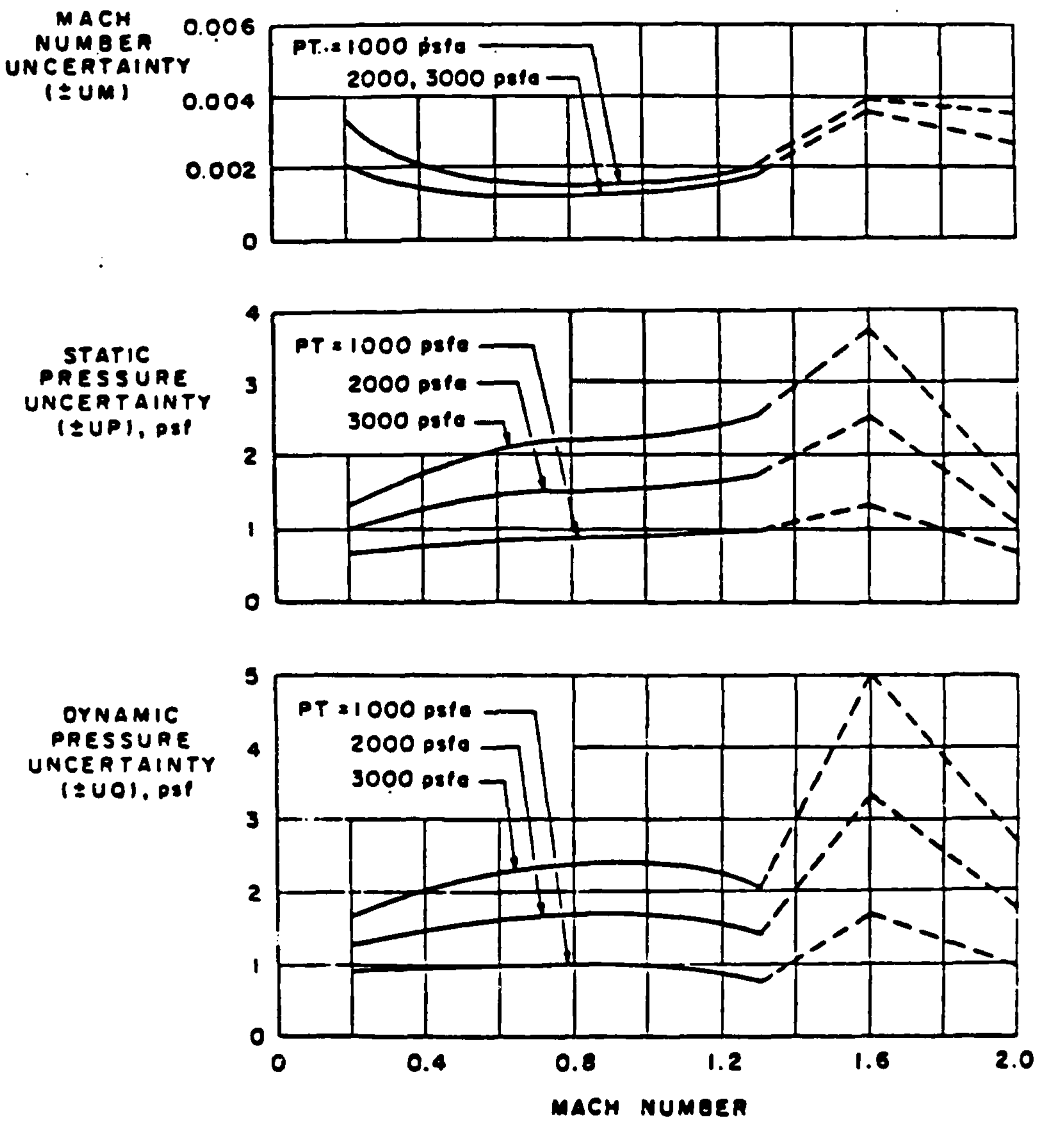

Figure 6. Estimated Uncertainties in 4T Tunnel Parameters

Table 4. Estimated Uncertainties

a. CONFIG B20

PARAMETER	M							
	0.4	0.55	0.8	0.95	1.05	1.1	1.2	1.3
CN	0.070	0.060	0.038	0.034	0.032	0.031	0.030	0.029
CLM	0.029	0.025	0.015	0.014	0.013	0.013	0.012	0.012
CY	0.039	0.034	0.022	0.020	0.019	0.019	0.018	0.017
CLN	0.032	0.028	0.018	0.016	0.015	0.015	0.014	0.014
CLL	0.020	0.017	0.011	0.0099	0.0096	0.0093	0.0089	0.0086
CAT	0.014	0.012	0.0076	0.0068	0.0065	0.0063	0.0060	0.0059
CA	0.016	0.014	0.0086	0.0076	0.0073	0.0070	0.0067	0.0066
CAB	0.0088	0.0080	0.0041	0.0035	0.0032	0.0032	0.0030	0.0030

b. CONFIG B25

PARAMETER	M							
	0.4	0.55	0.8	0.95	1.05	1.1	1.2	1.3
CN	0.073	0.063	0.039	0.035	0.033	0.032	0.030	0.029
CLM	0.028	0.023	0.015	0.013	0.012	0.012	0.011	0.011
CY	0.039	0.034	0.022	0.020	0.019	0.018	0.018	0.017
CLN	0.032	0.028	0.018	0.016	0.015	0.015	0.014	0.014
CLL	0.020	0.017	0.011	0.0099	0.0096	0.0093	0.0088	0.0086
CAT	0.014	0.012	0.0076	0.0068	0.0065	0.0063	0.0060	0.0059
CA	0.016	0.014	0.0086	0.0076	0.0073	0.0070	0.0067	0.0066
CAB	0.0088	0.0080	0.0041	0.0035	0.0032	0.0032	0.0030	0.0030

Table 4. Concluded

c. CONFIG B30

PARAMETER	M							
	0.4	0.55	0.8	0.95	1.05	1.1	1.2	1.3
CN	0.077	0.065	0.041	0.036	0.034	0.033	0.031	0.030
CLM	0.027	0.023	0.014	0.012	0.012	0.011	0.011	0.010
CY	0.039	0.034	0.022	0.020	0.019	0.018	0.018	0.017
CLN	0.032	0.028	0.018	0.016	0.015	0.015	0.014	0.014
CLL	0.020	0.017	0.011	0.0099	0.0096	0.0093	0.0088	0.0086
CAT	0.014	0.012	0.0076	0.0068	0.0065	0.0063	0.0060	0.0059
CA	0.016	0.014	0.0086	0.0076	0.0073	0.0070	0.0067	0.0066
CAB	0.0088	0.0080	0.0041	0.0035	0.0032	0.0032	0.0030	0.0030

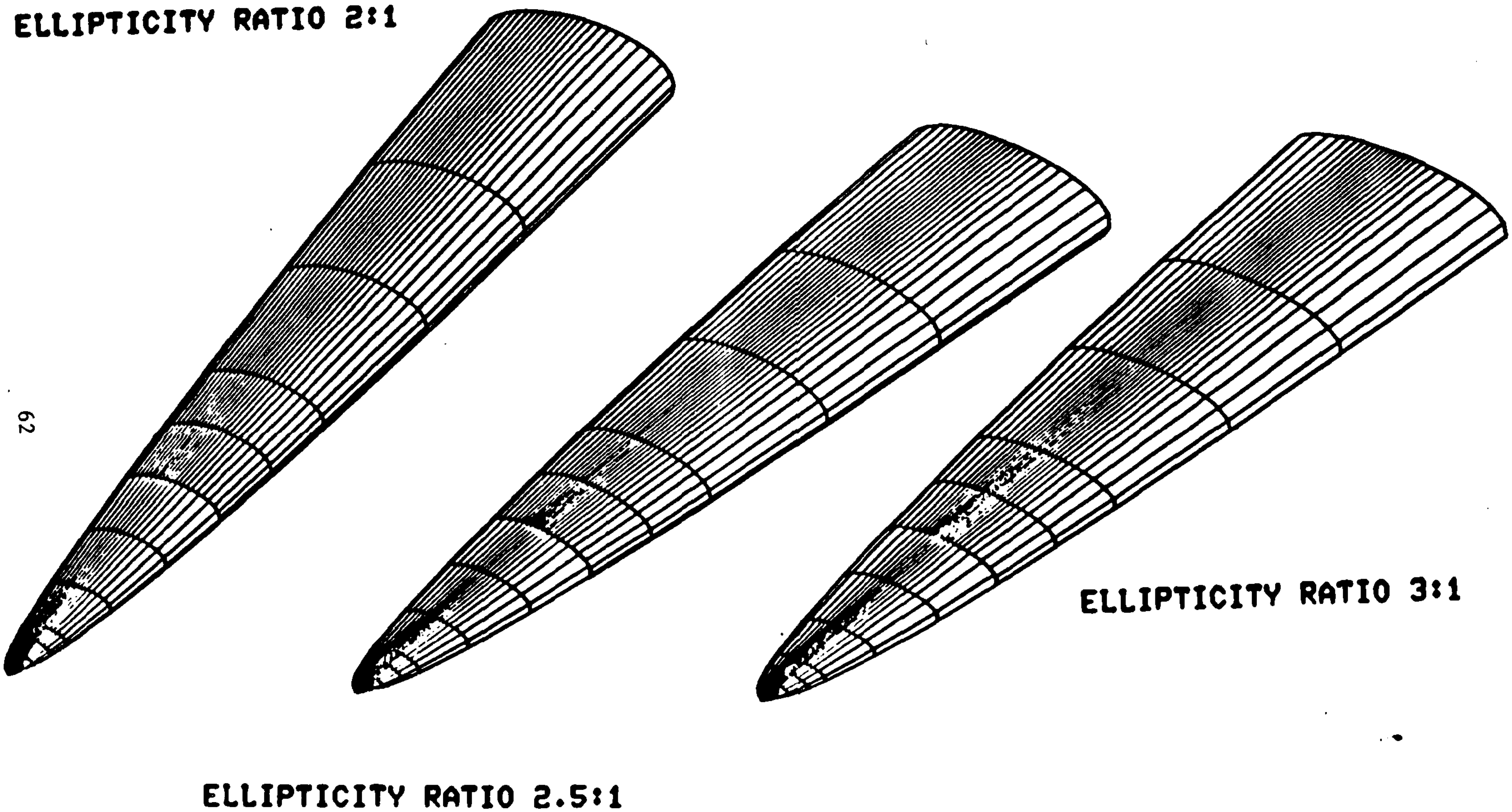

a. Inviscid Geometry

Figure 7. S/HABP Geometry

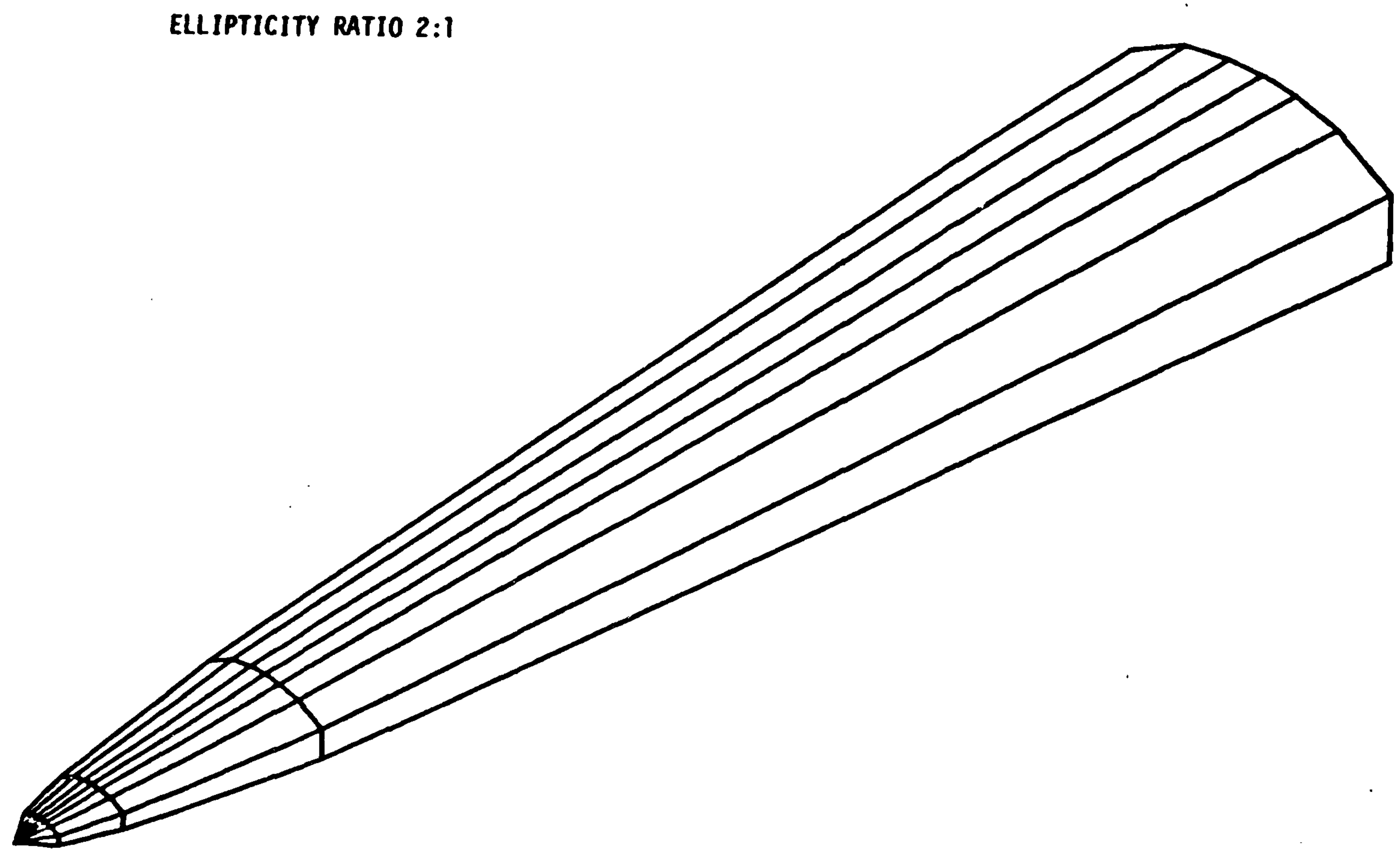

b. Skin Friction Geometry

Figure 7. S/HABP Geometry (Continued)

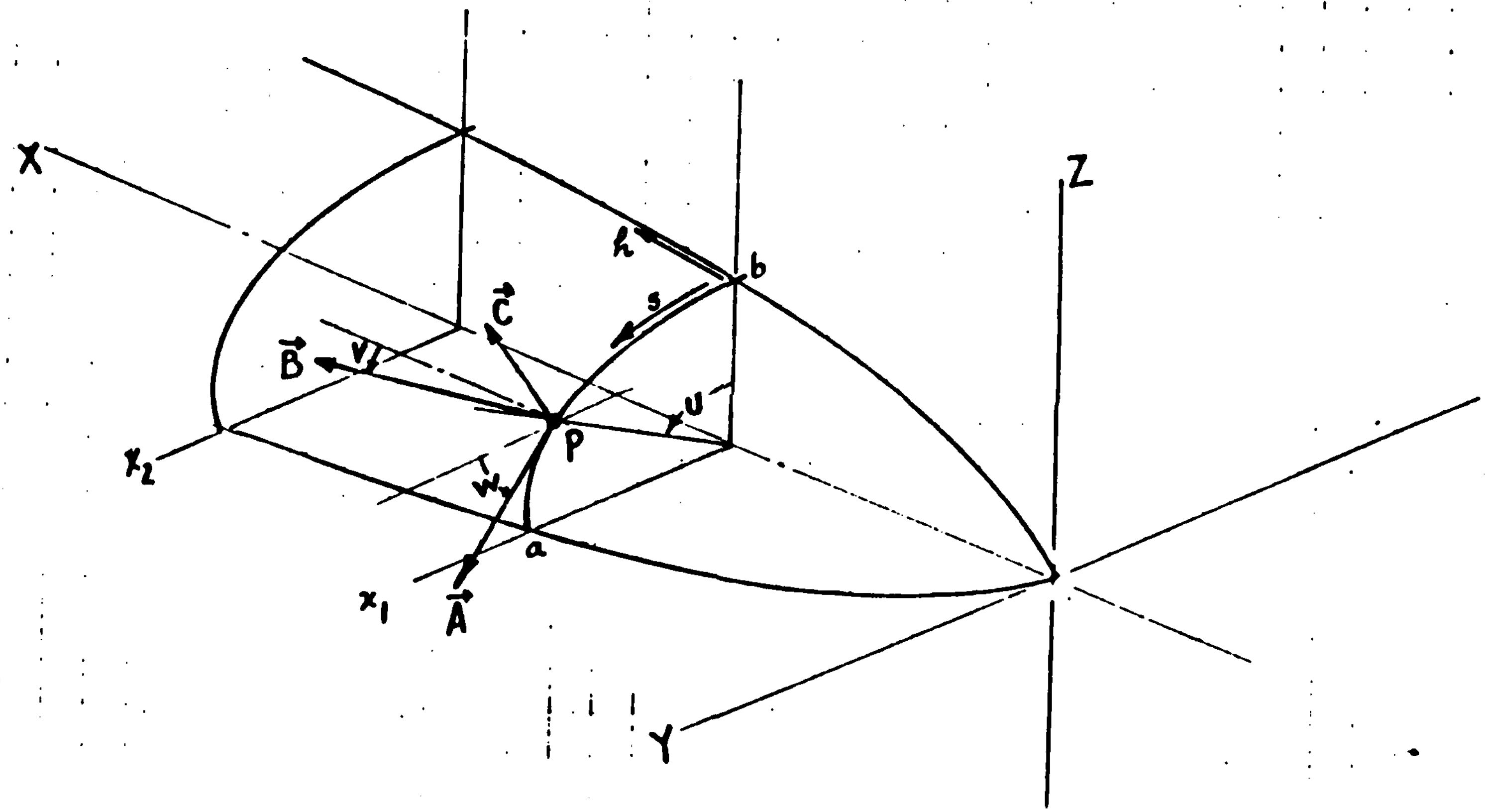

c. Pressure Integration Direction Cosines

Figure 7. S/HABP Geometry (Concluded)

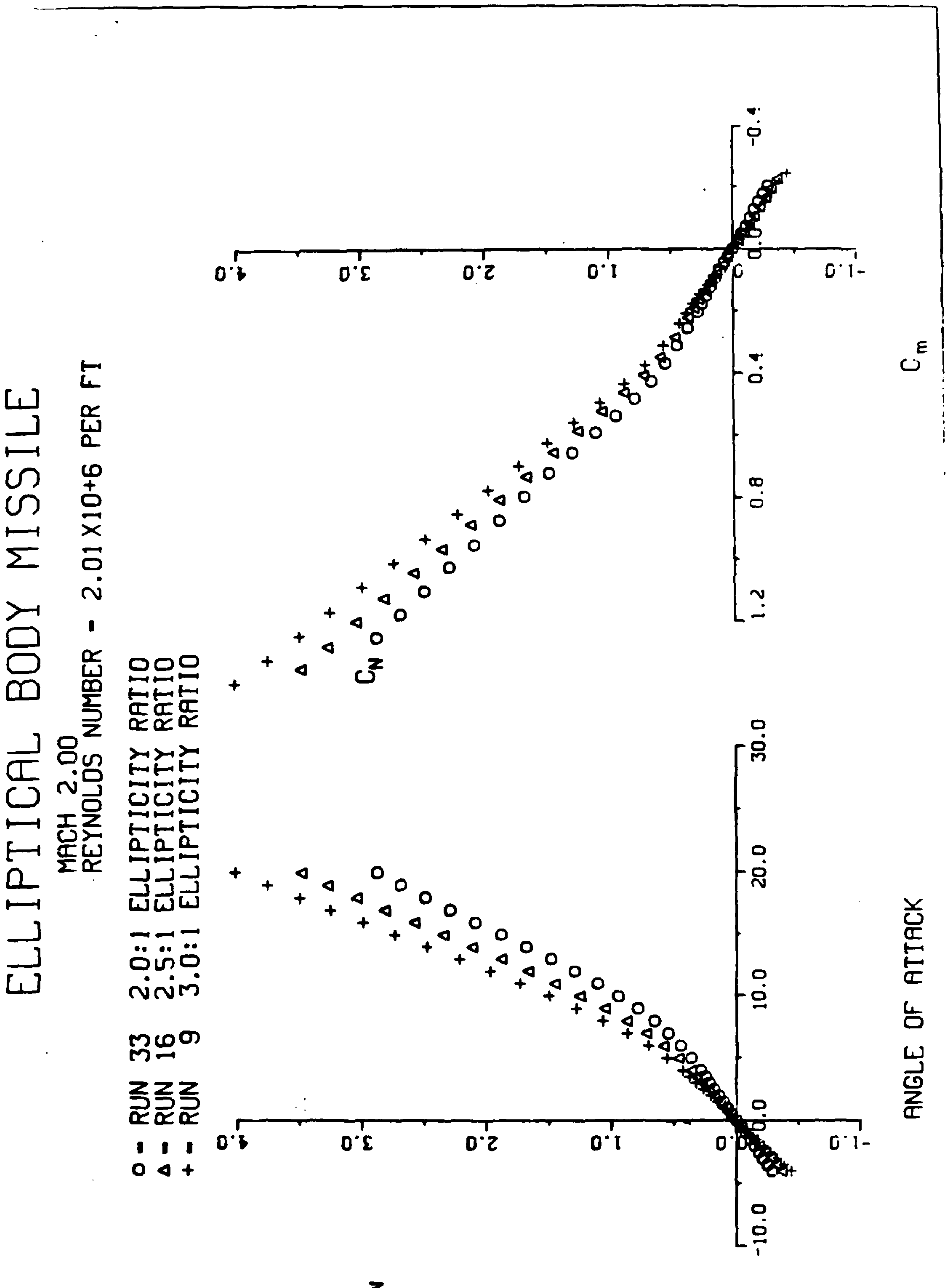

Figure 8. Ellipticity Ratio Effects, M = 2.0

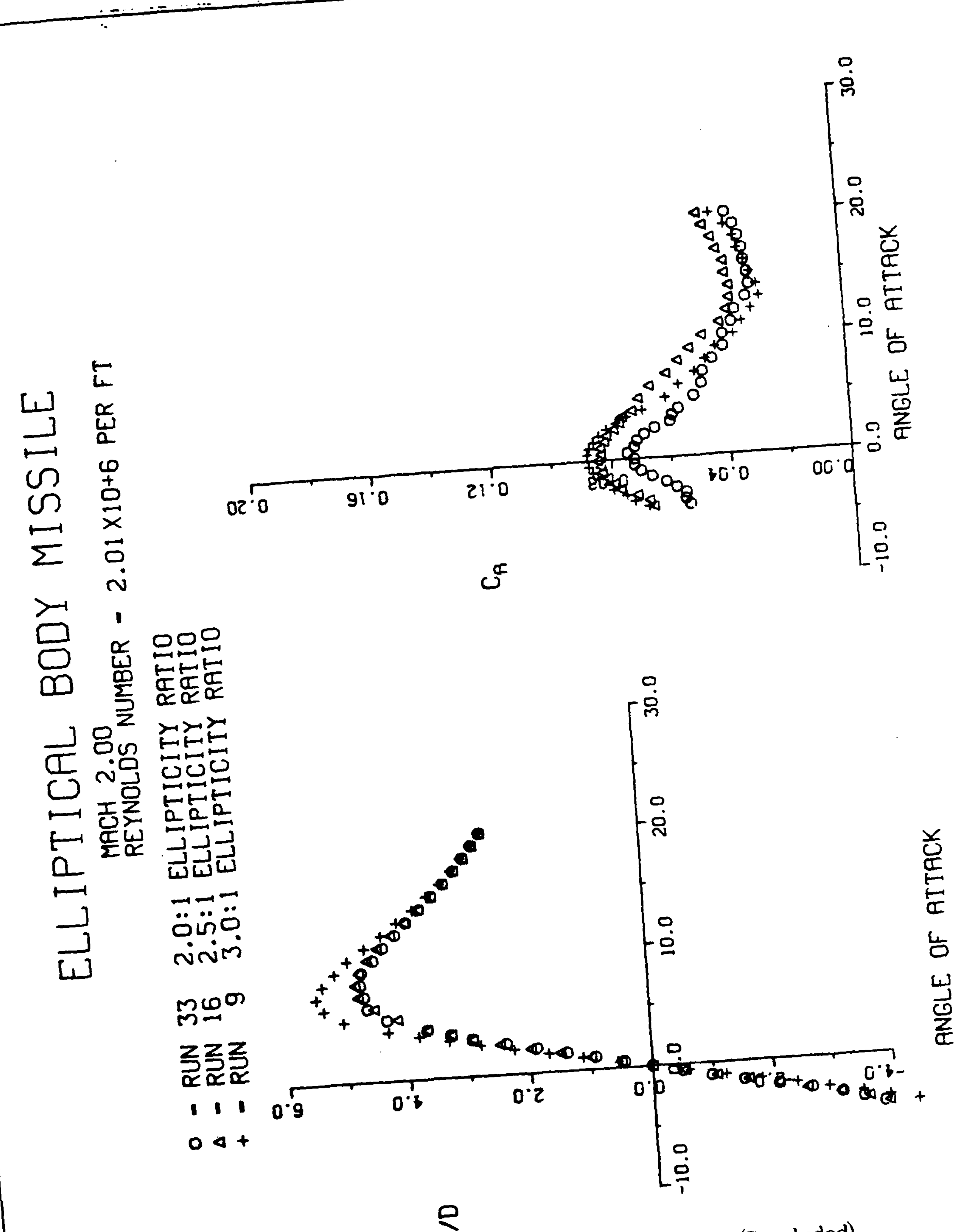

Figure 8. Ellipticity Ratio Effects, M = 2.0 (Concluded)

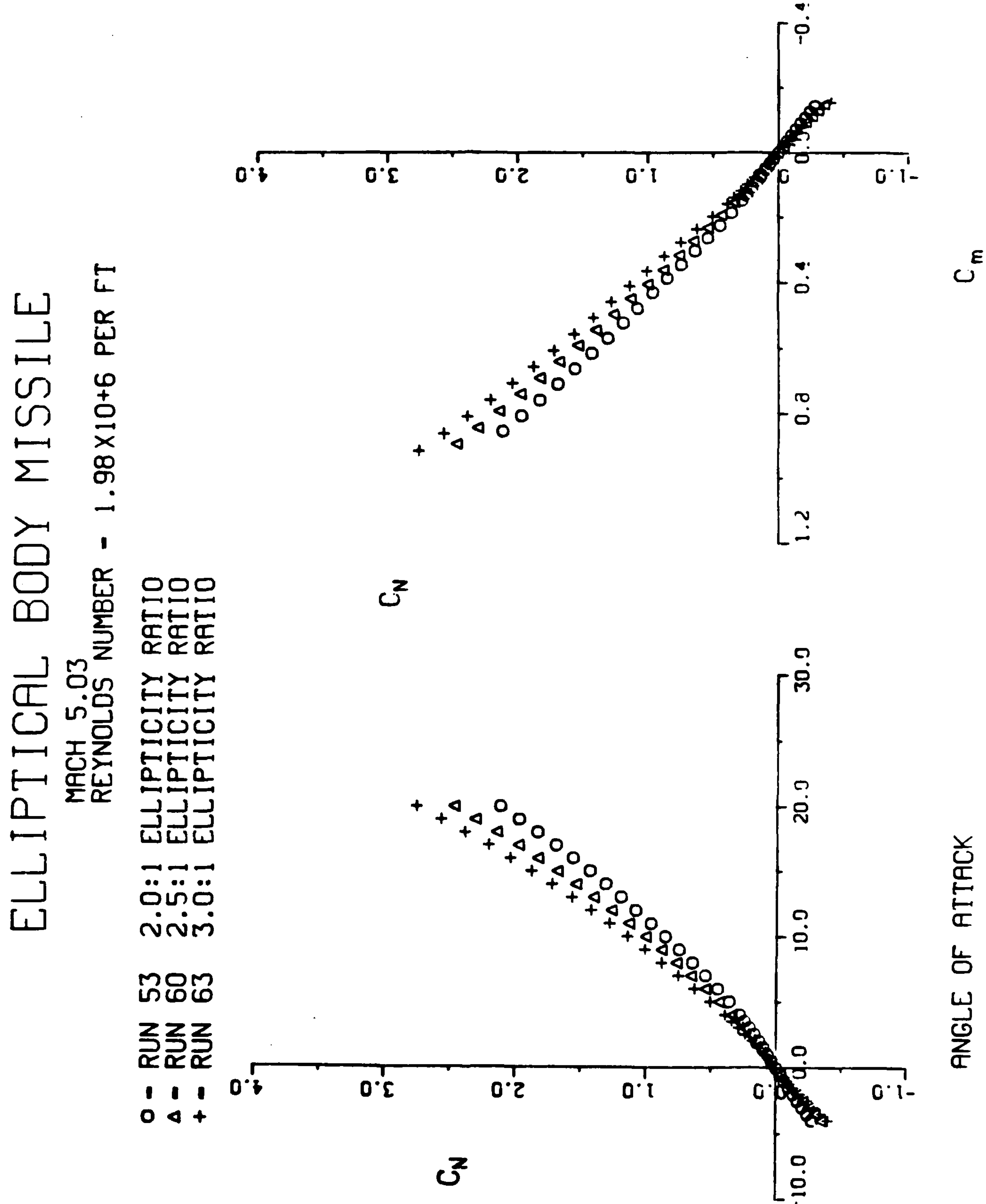

Figure 9. Ellipticity Ratio Effects, M = 5.0

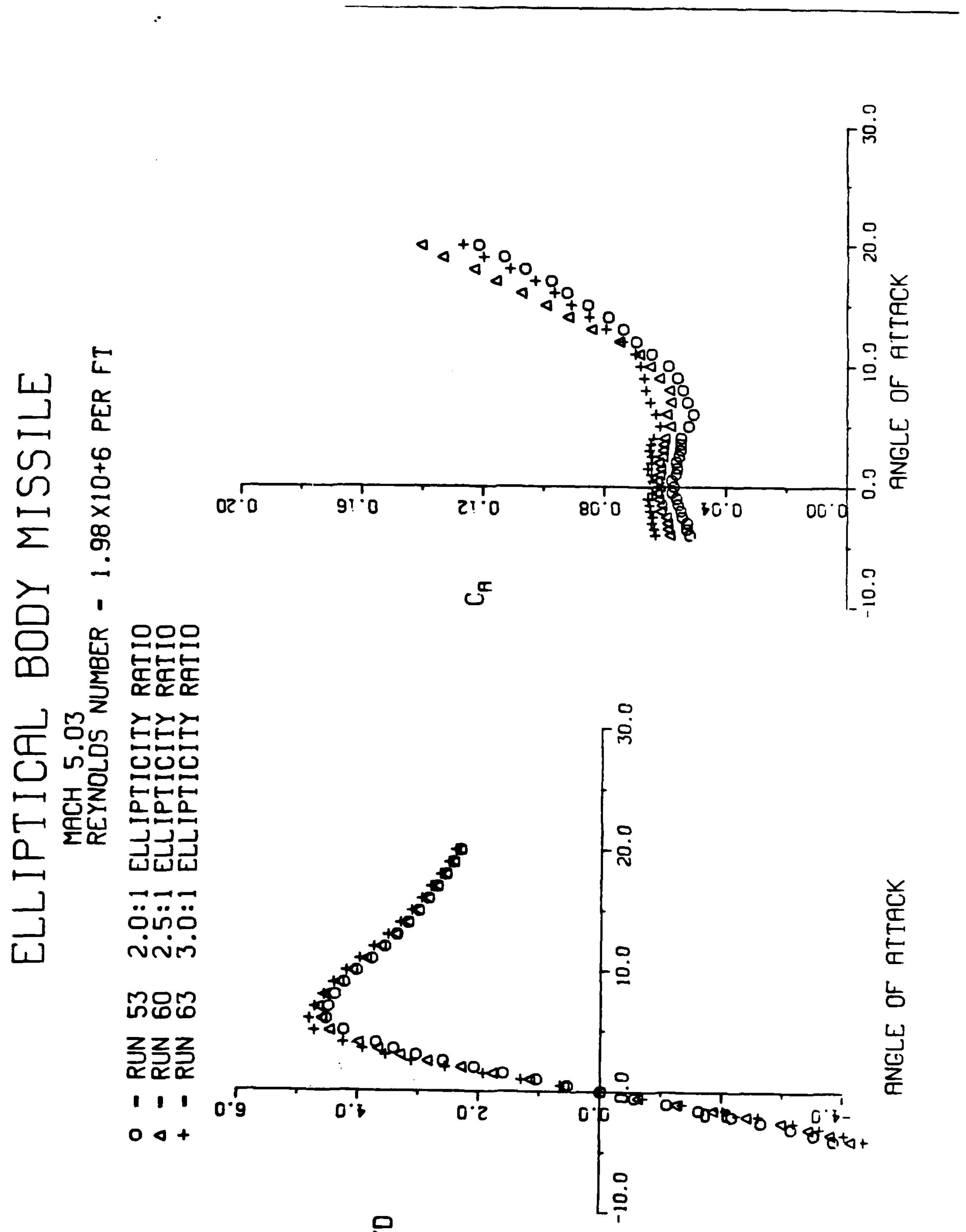

Figure 9. Ellipticity Ratio Effects, M = 5.0 (Concluded)

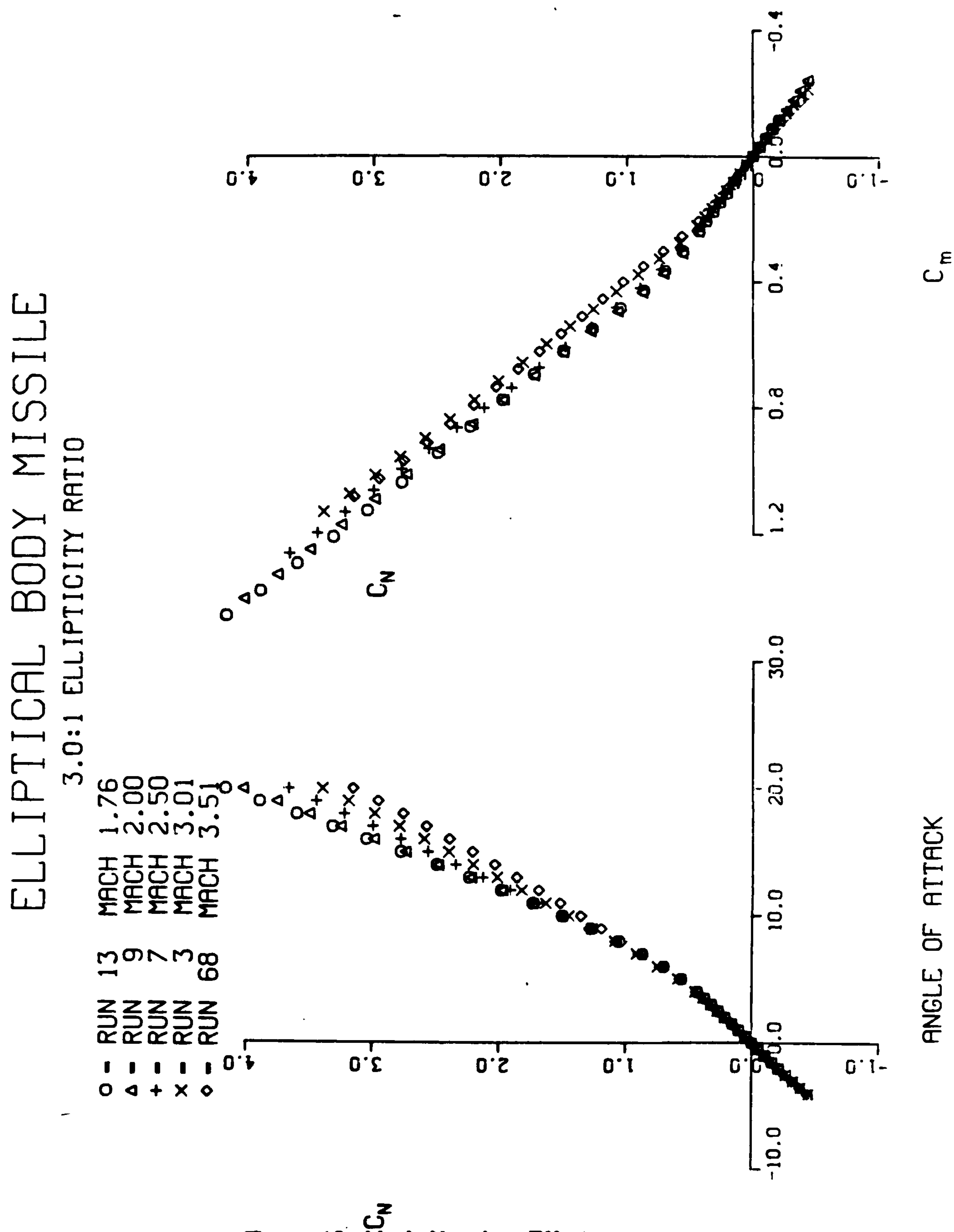

Figure 10. Mach Number Effects

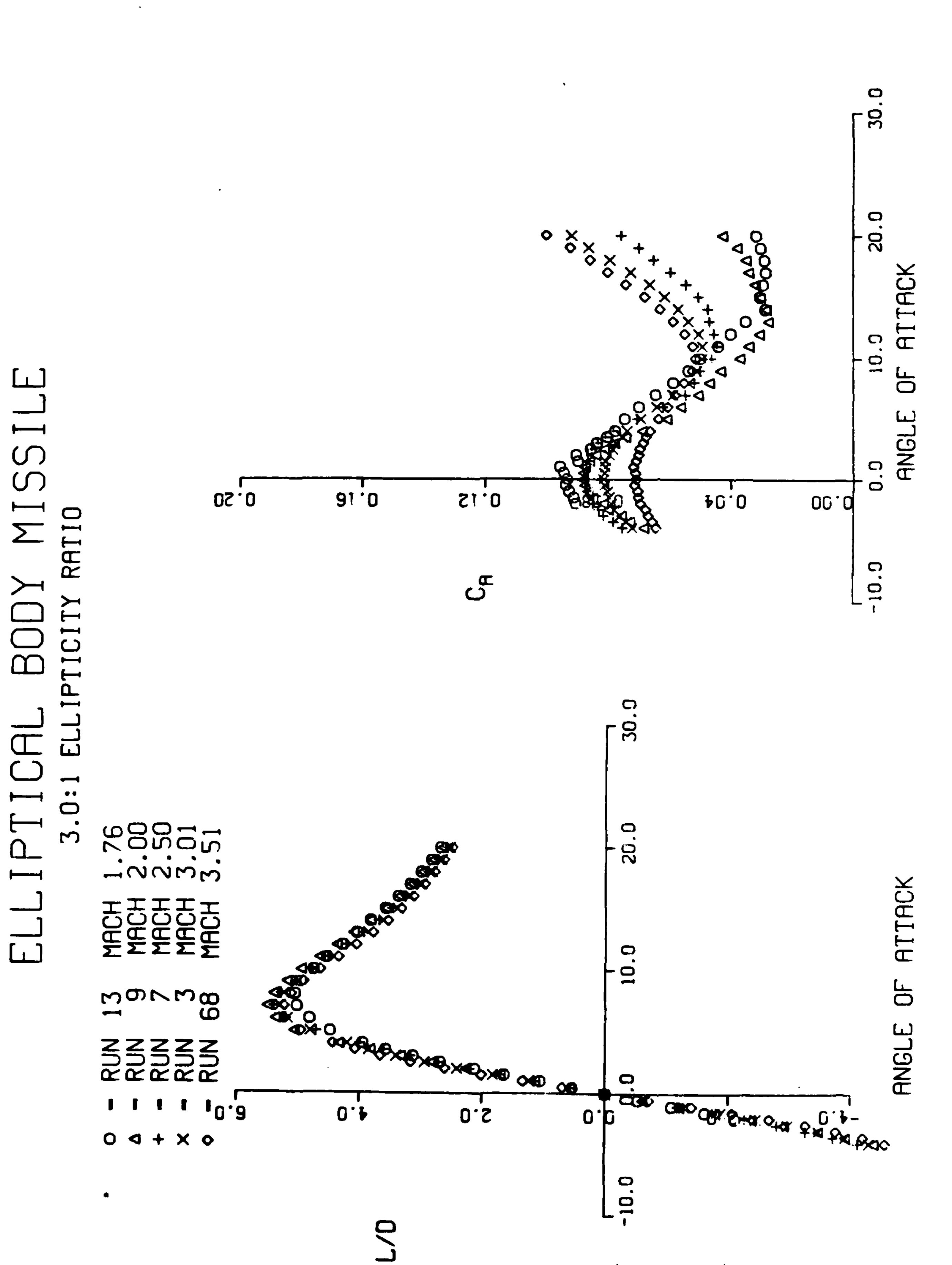

Figure 10. Mach Number Effects (Concluded)

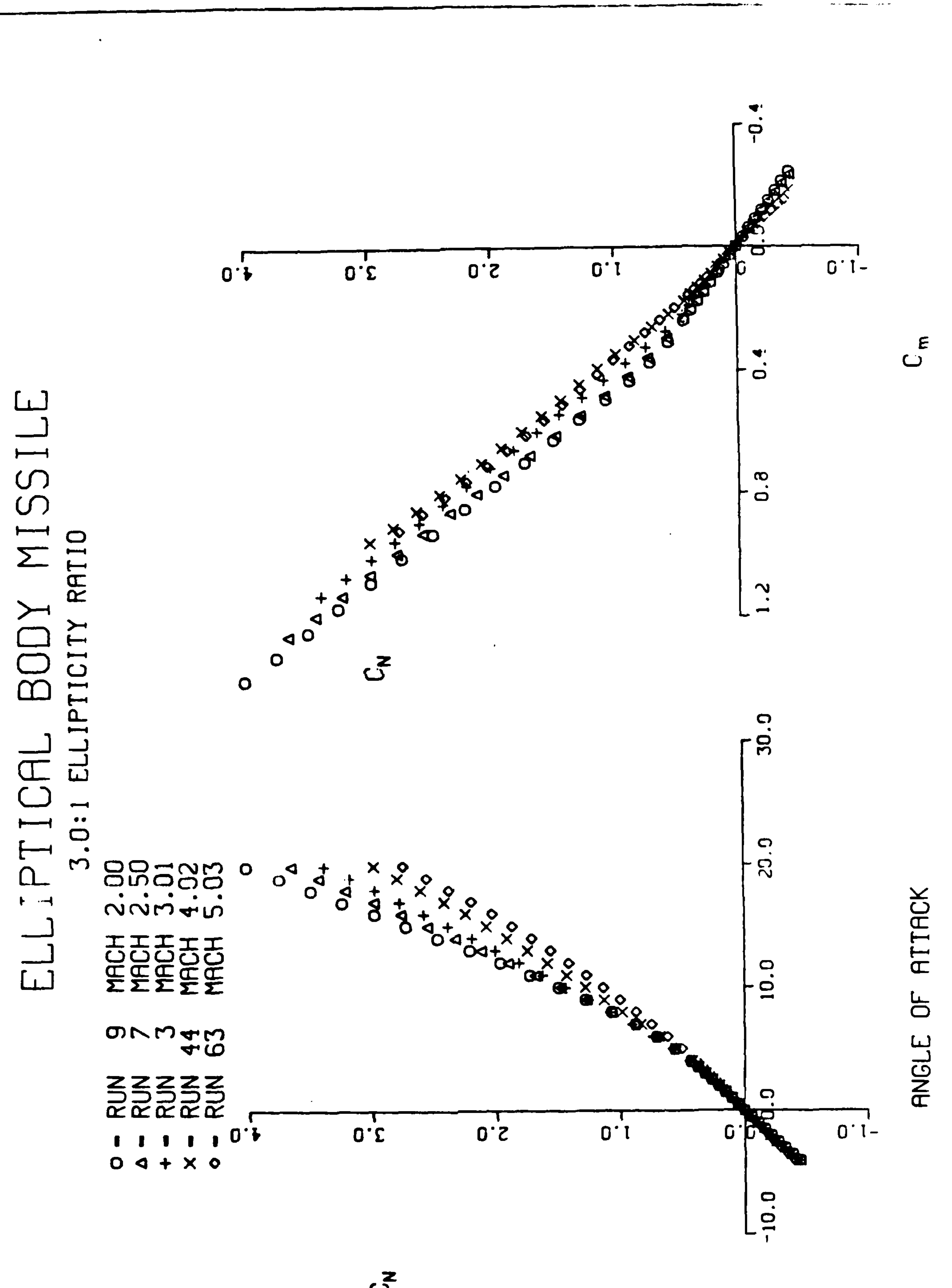

Figure 11. Mach Number Effects

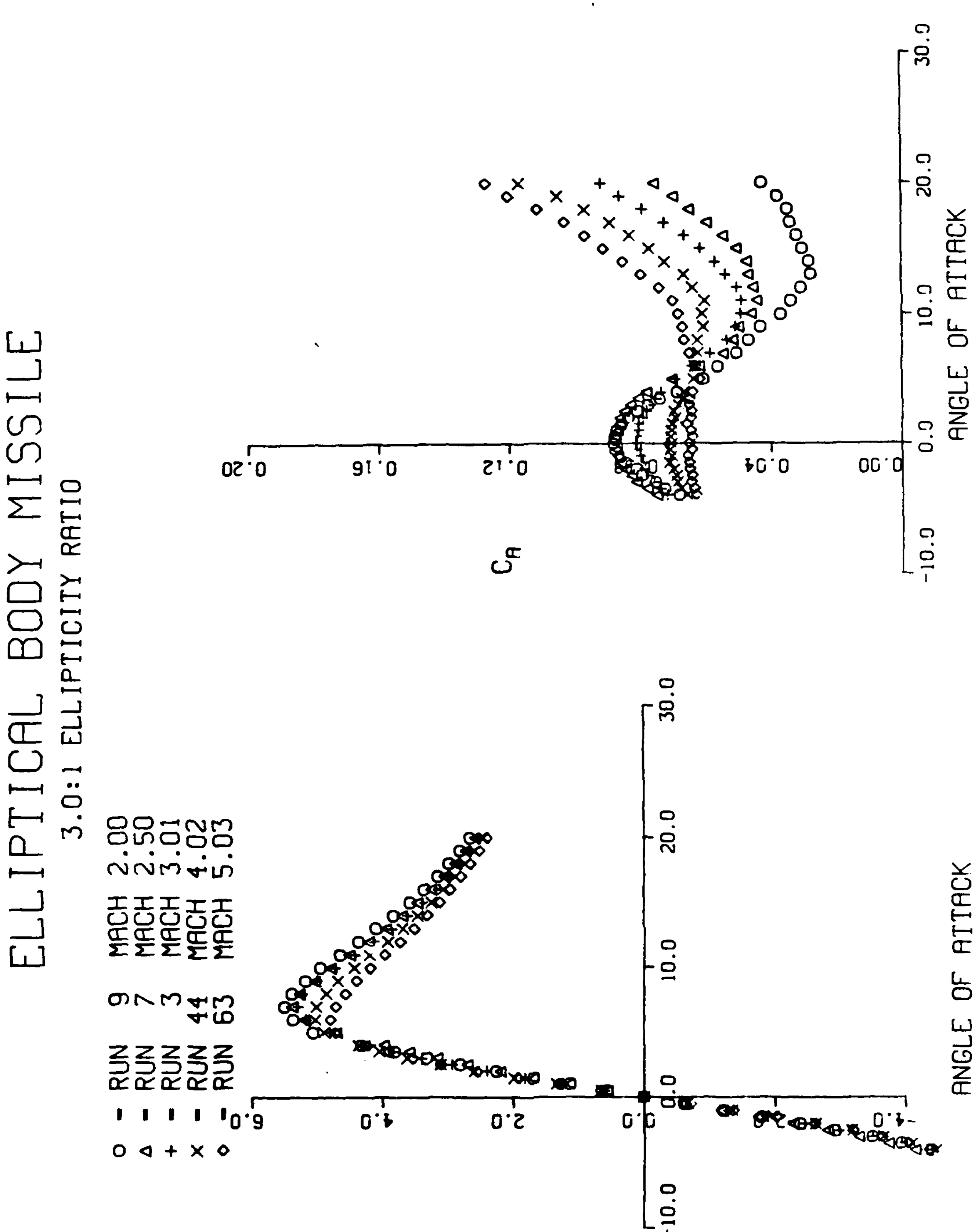

Figure 11. Mach Number Effects (Concluded)

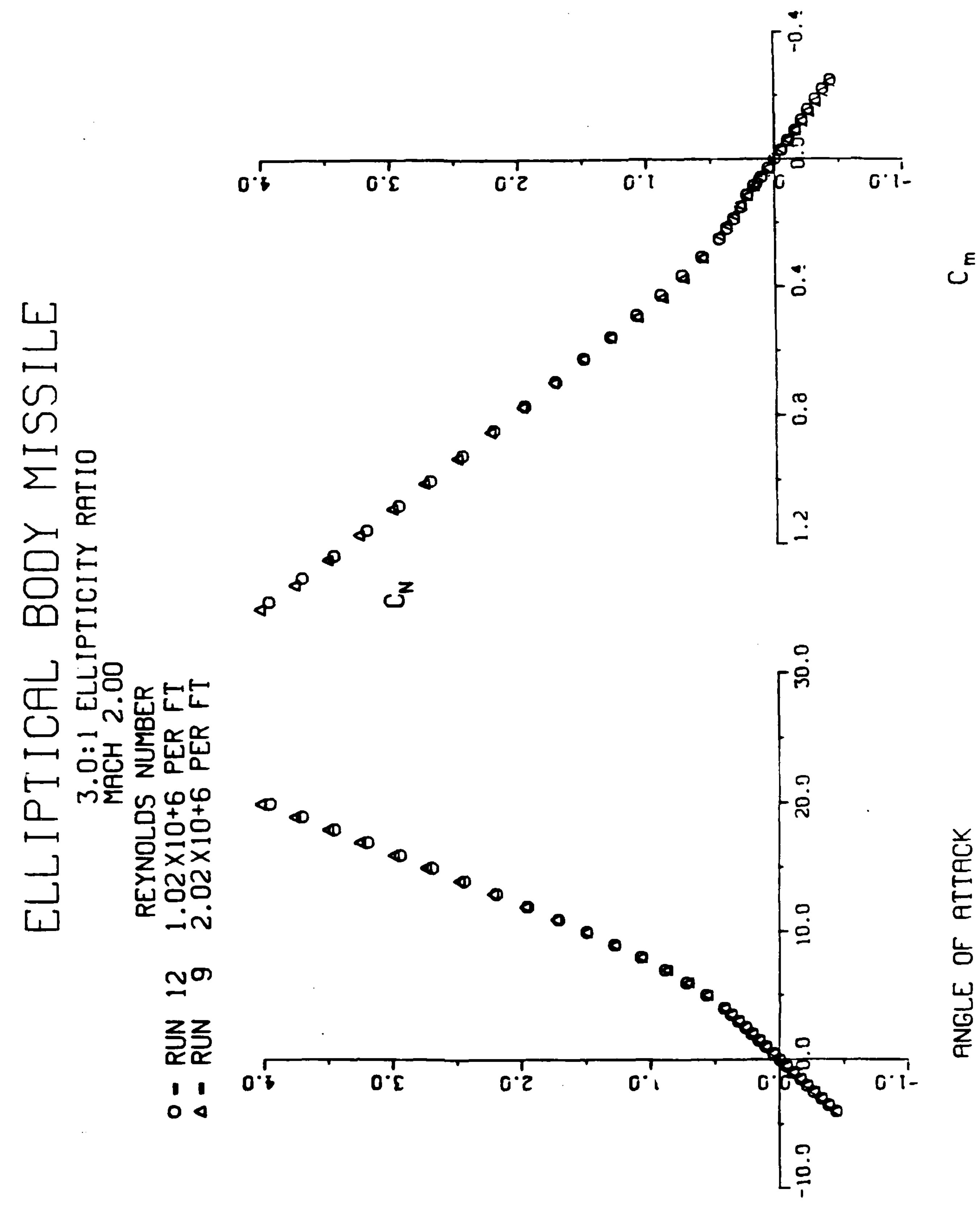

Figure 12. Reynolds Number Effects, M = 2.0

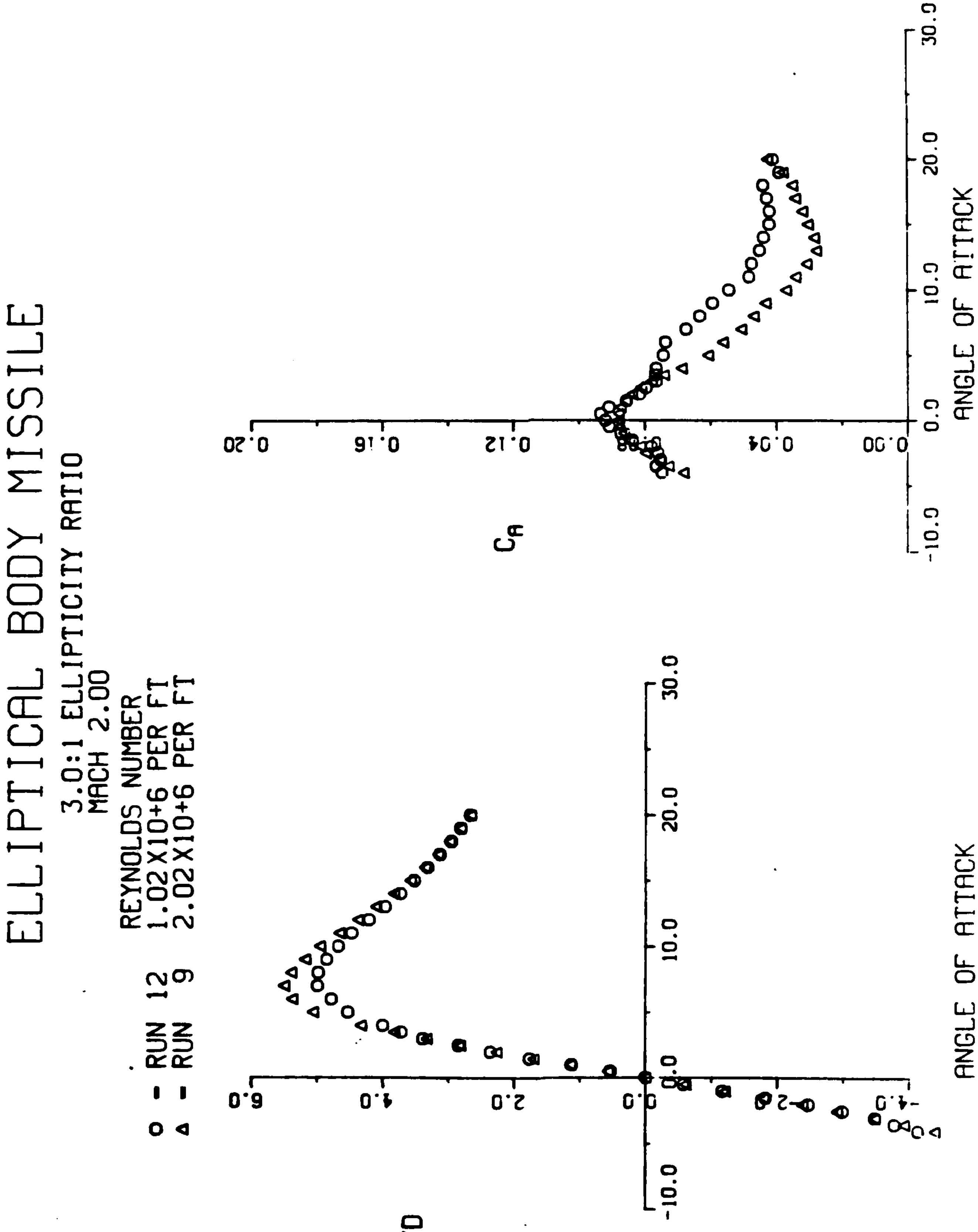

Figure 12. Reynolds Number Effects, M = 2.0 (Concluded)

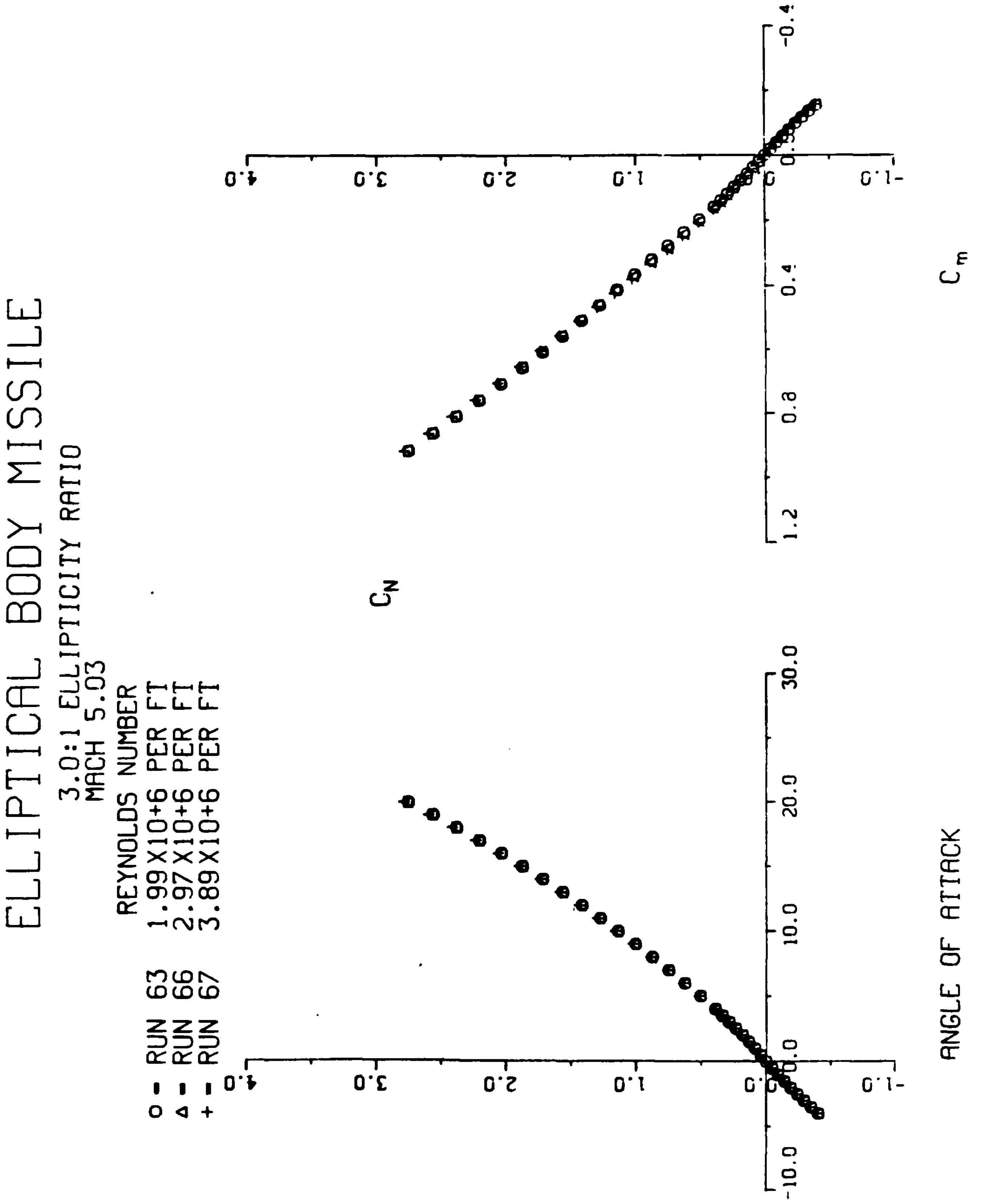

Figure 13. Reynolds Number Effects, M = 5.0

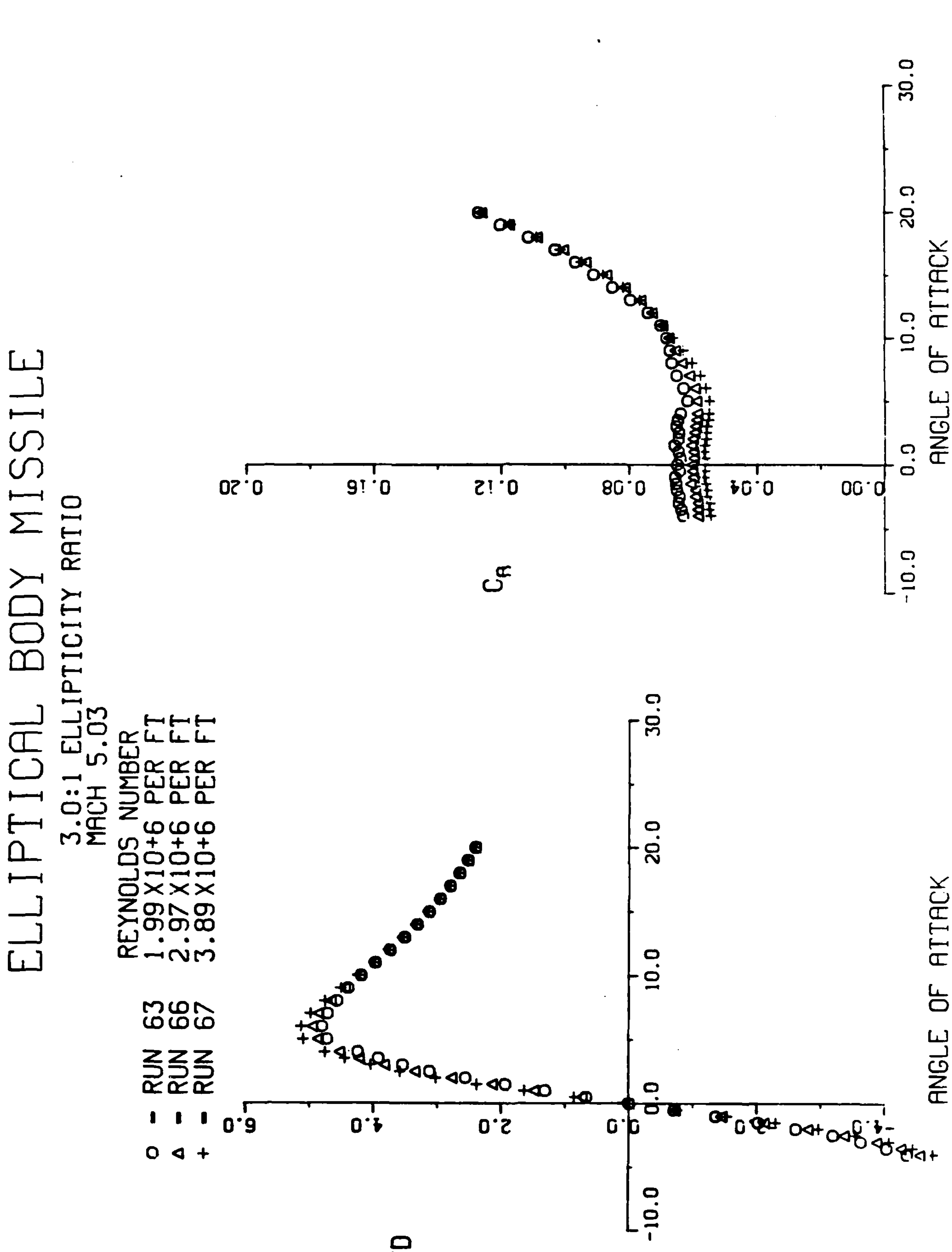

Figure 13. Reynolds Number Effects, M = 5.0 (Concluded)

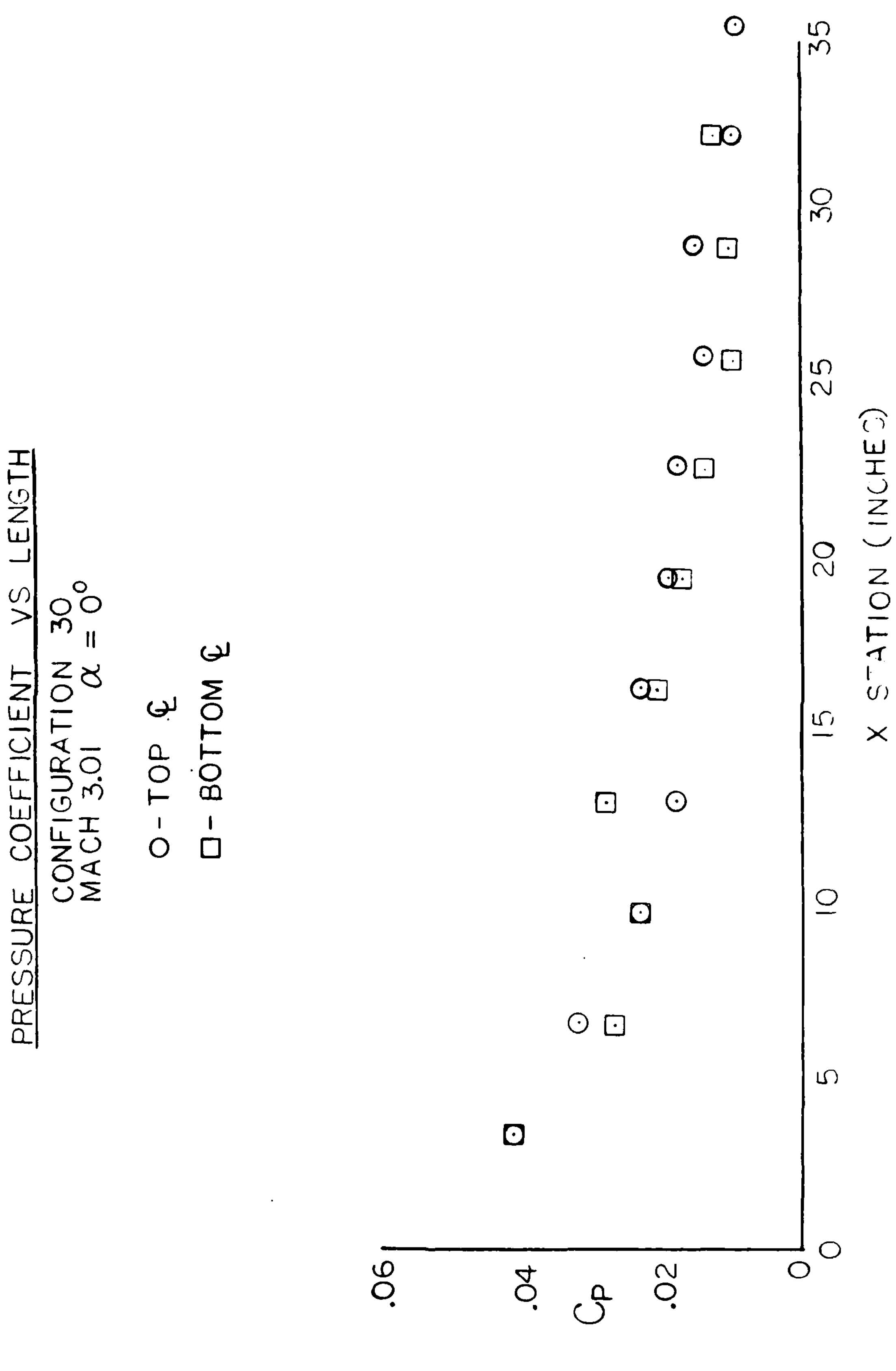

Figure 14. C_P vs. Length

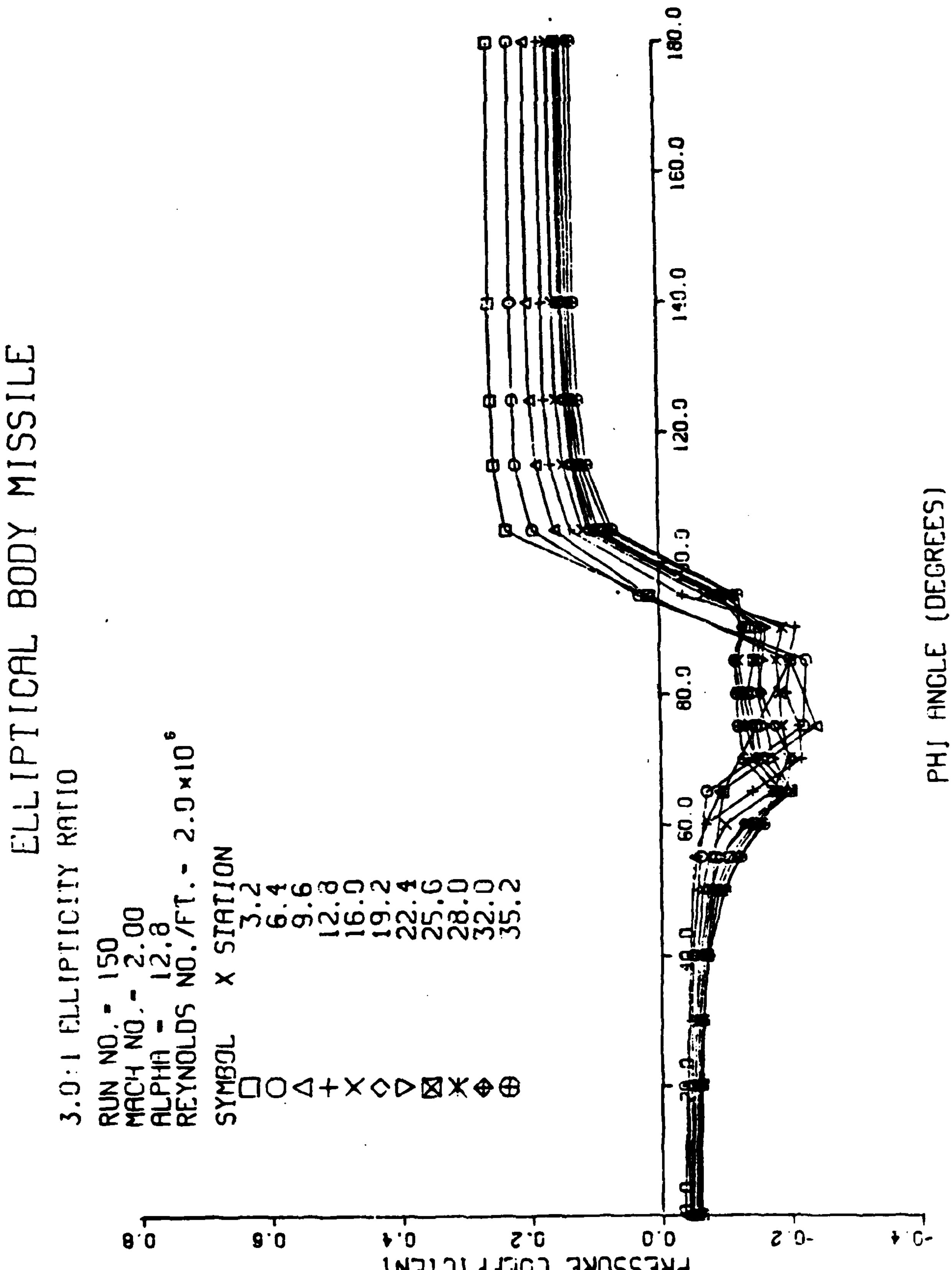

a. Mach 2.0

Figure 15. Pressure Coefficient About Body

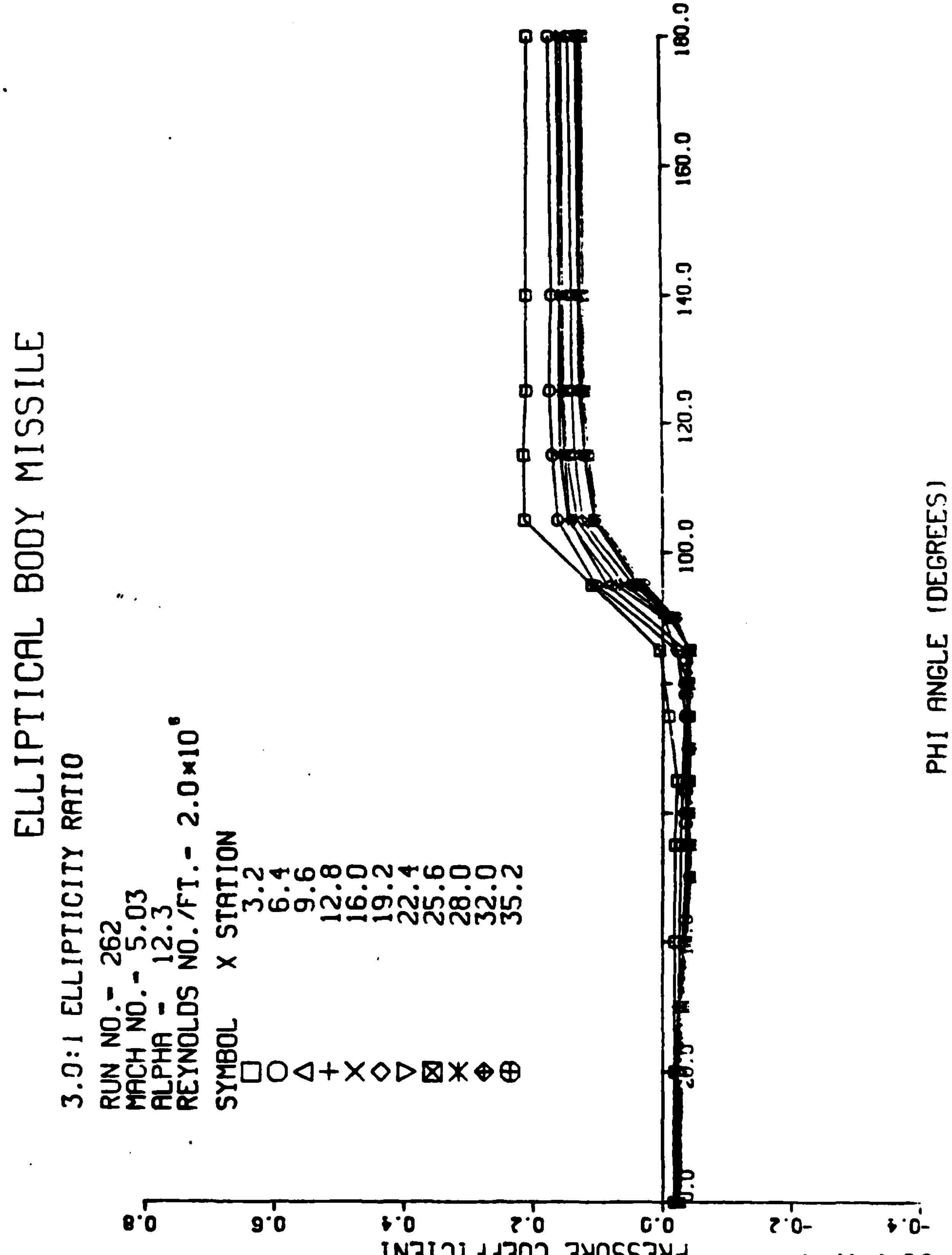

b. Mach 5.0

Figure 15. Pressure Coefficient About Body (Concluded)

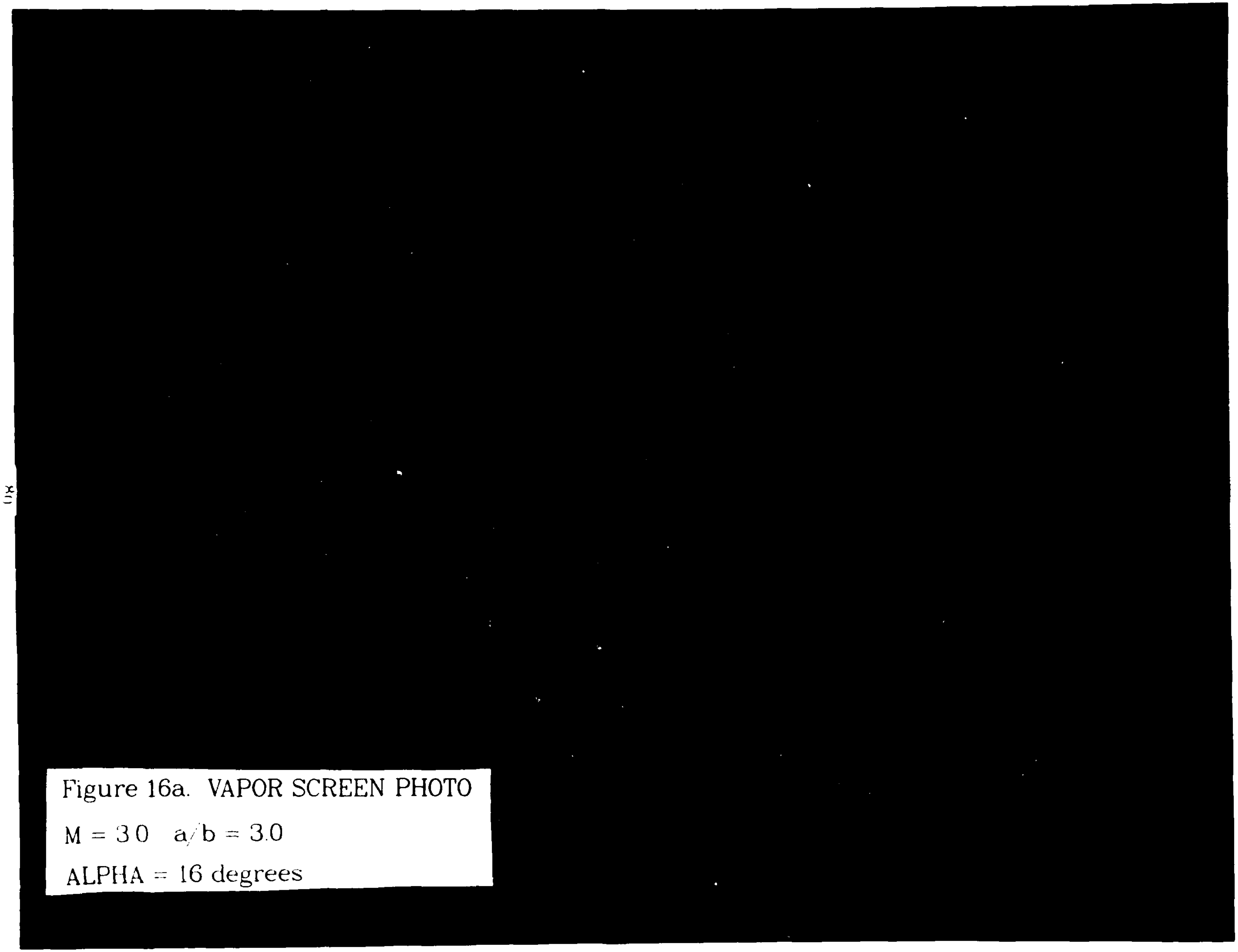

Figure 16a. VAPOR SCREEN PHOTO

M = 3.0   a/b = 3.0

ALPHA = 16 degrees

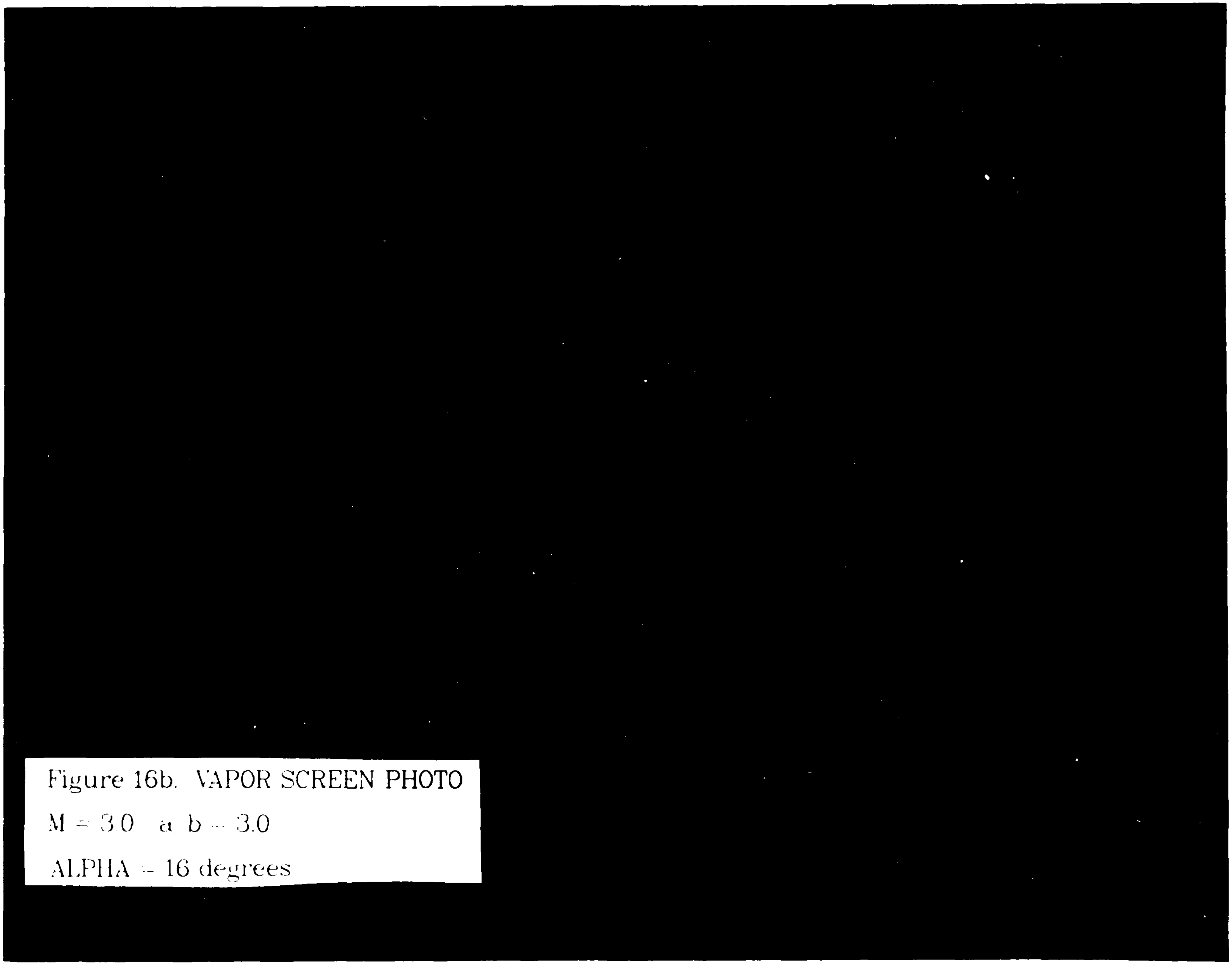

Figure 16b. VAPOR SCREEN PHOTO

M = 3.0 a/b = 3.0

ALPHA = 16 degrees

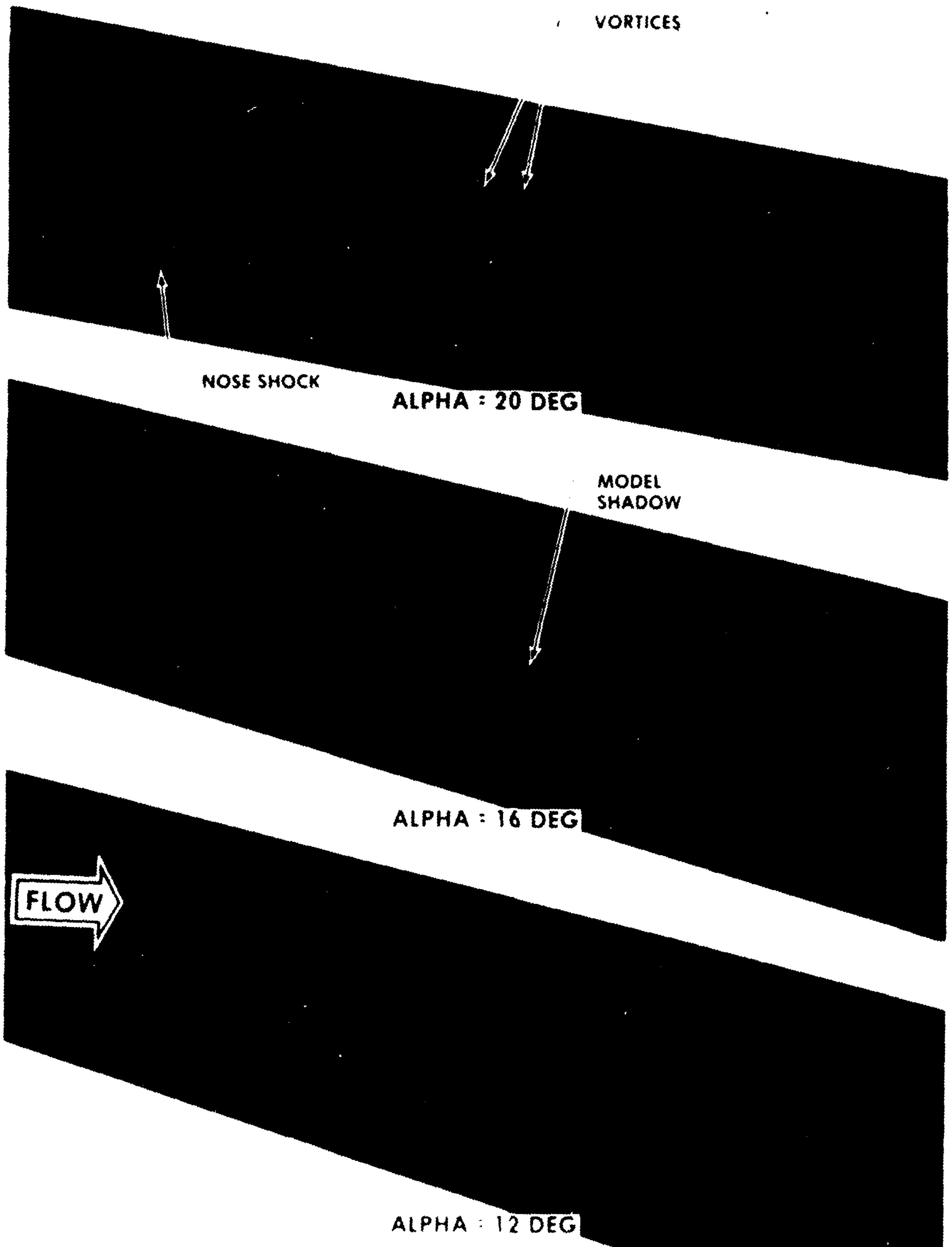

Figure 17. VAPOR SCREEN PHOTOGRAPH COMPOSITES
FDL ELLIPTIC BODY CONFIG B30
TUNNEL A MACH NO. 3 SEPT 1983

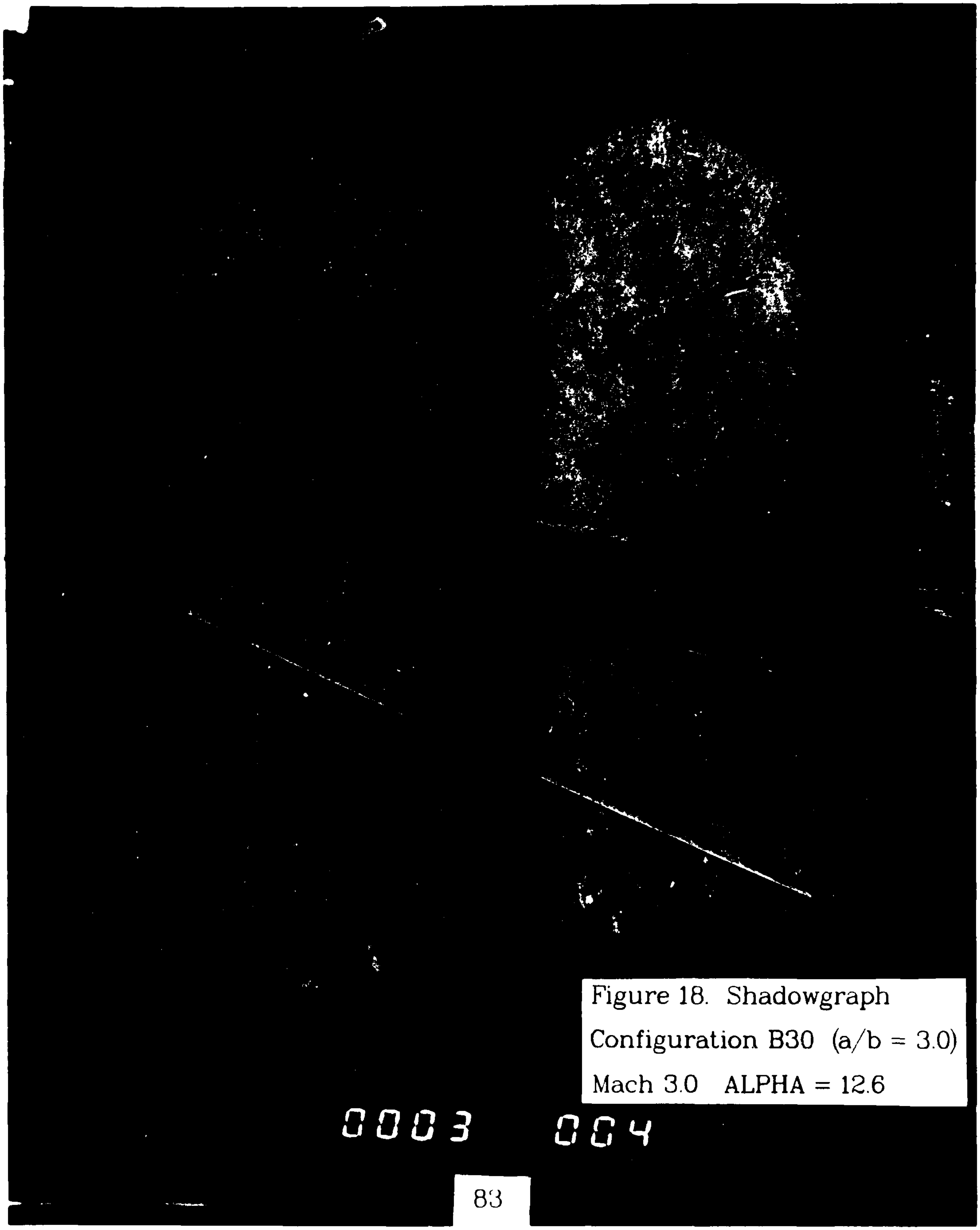

Figure 18. Shadowgraph
Configuration B30 (a/b = 3.0)
Mach 3.0 ALPHA = 12.6

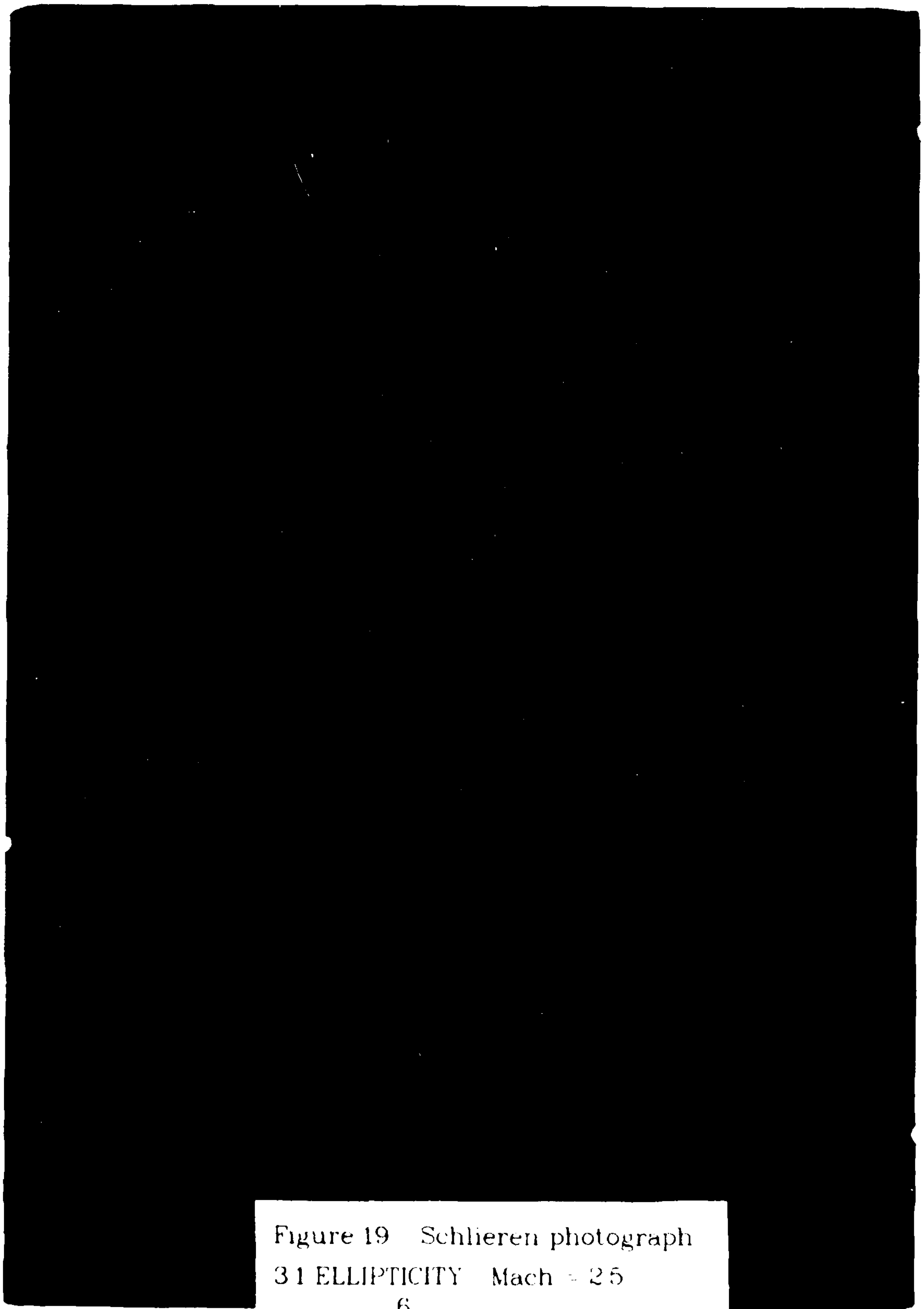

Figure 19 Schlieren photograph
3:1 ELLIPTICITY Mach = 2.5
Re = 2×10^6/ft α = 12.8

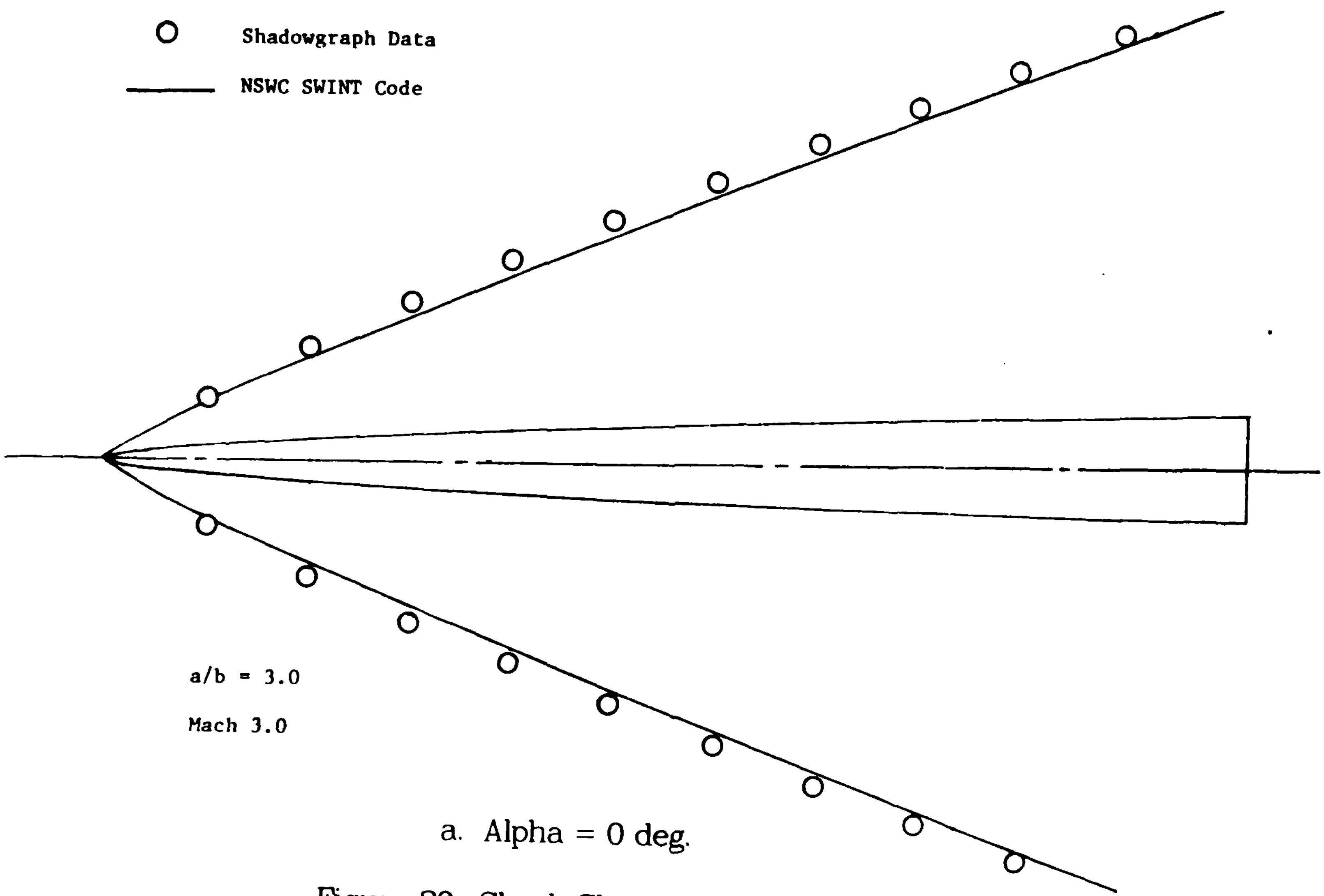

a. Alpha = 0 deg.

Figure 20. Shock Shape vs. NSWC Code

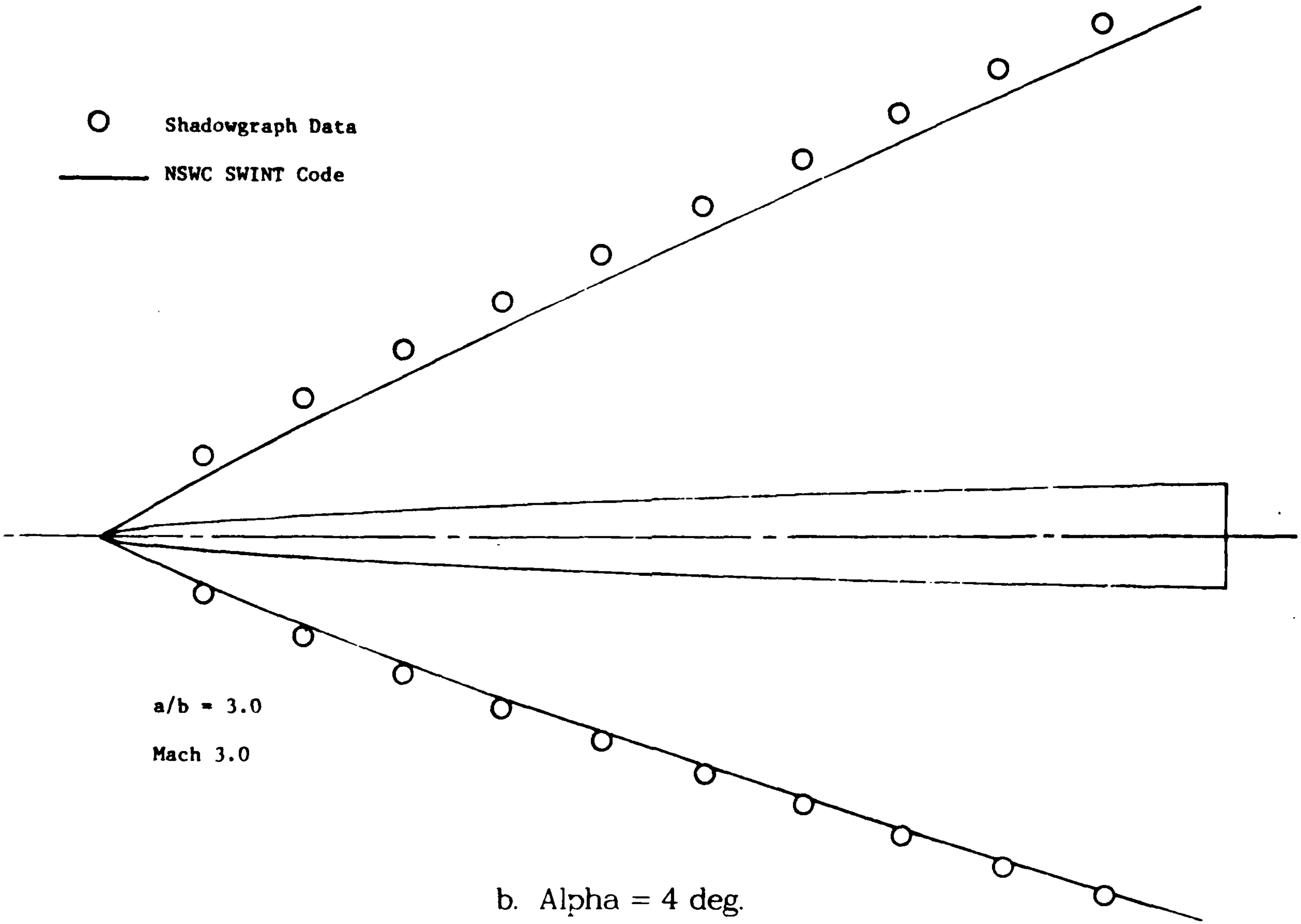

b. Alpha = 4 deg.

Figure 20. Shock Shape vs. NSWC Code (Continued)

AD-A193 525 WIND TUNNEL TESTS OF ELLIPTICAL MISSILE BODY CONFIGURATIONS AT MACH NUMBE..(U) AIR FORCE WRIGHT AERONAUTICAL LABS WRIGHT-PATTERSON AFB OH.. 2/2

UNCLASSIFIED D E SHEREDA ET AL. DEC 87 AFWAL-TR-87-3088 F/G 16/2.1 NL

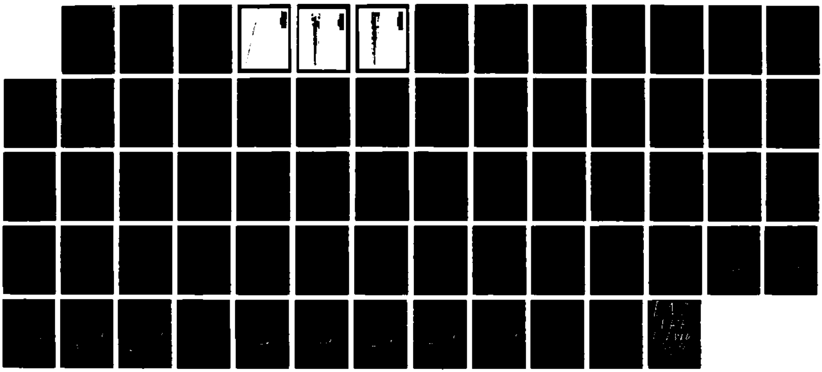

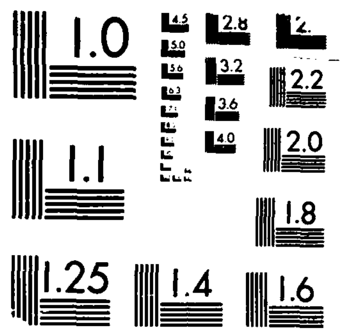

MICROCOPY RESOLUTION TEST CHART

URFAU STANDARDS-1963-A

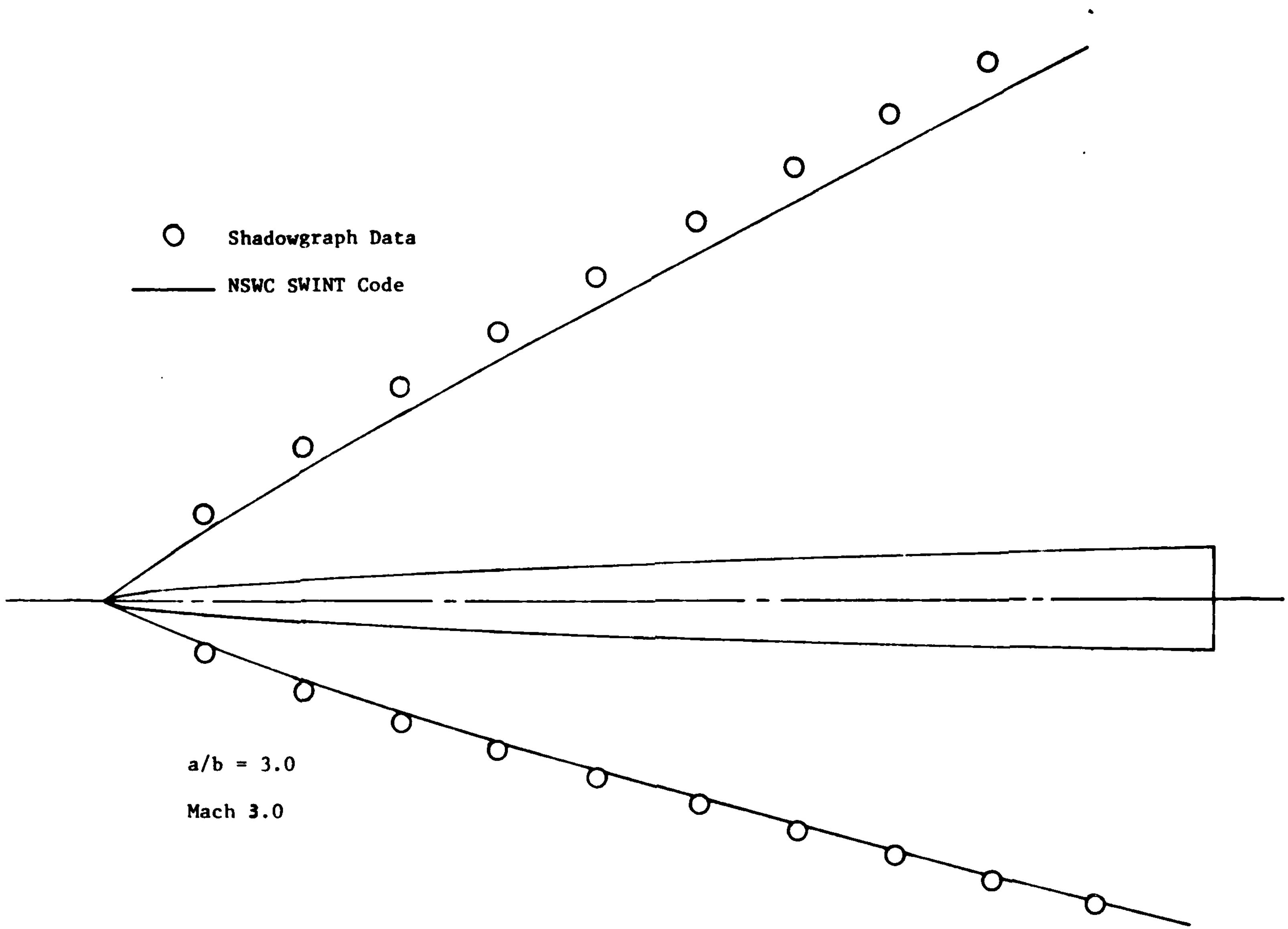

c. Alpha = 8 deg.

Figure 20. Shock Shape vs. NSWC Code (Continued)

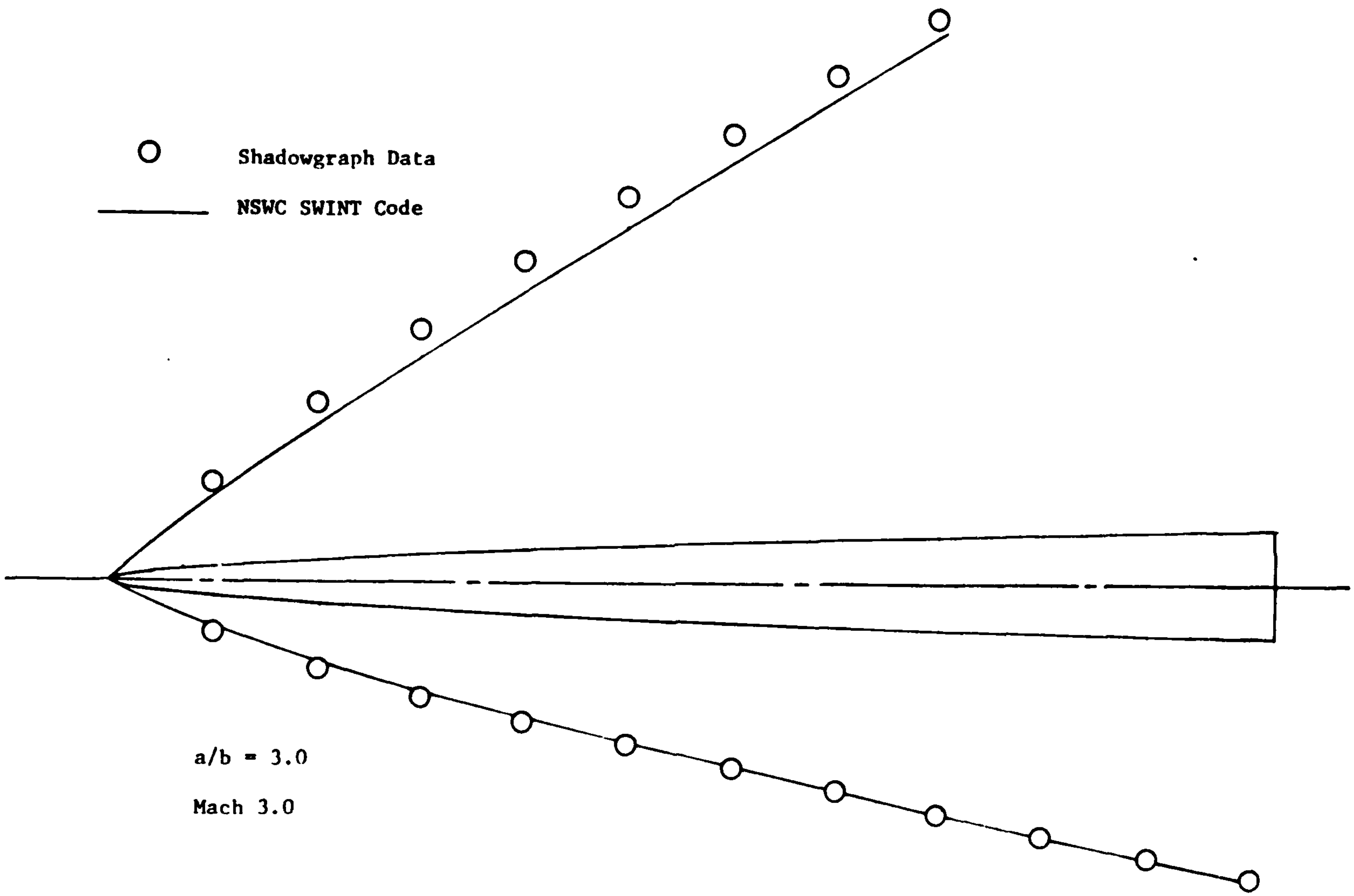

d. Alpha = 12 deg.

Figure 20. Shock Shape vs. NSWC Code (Concluded)

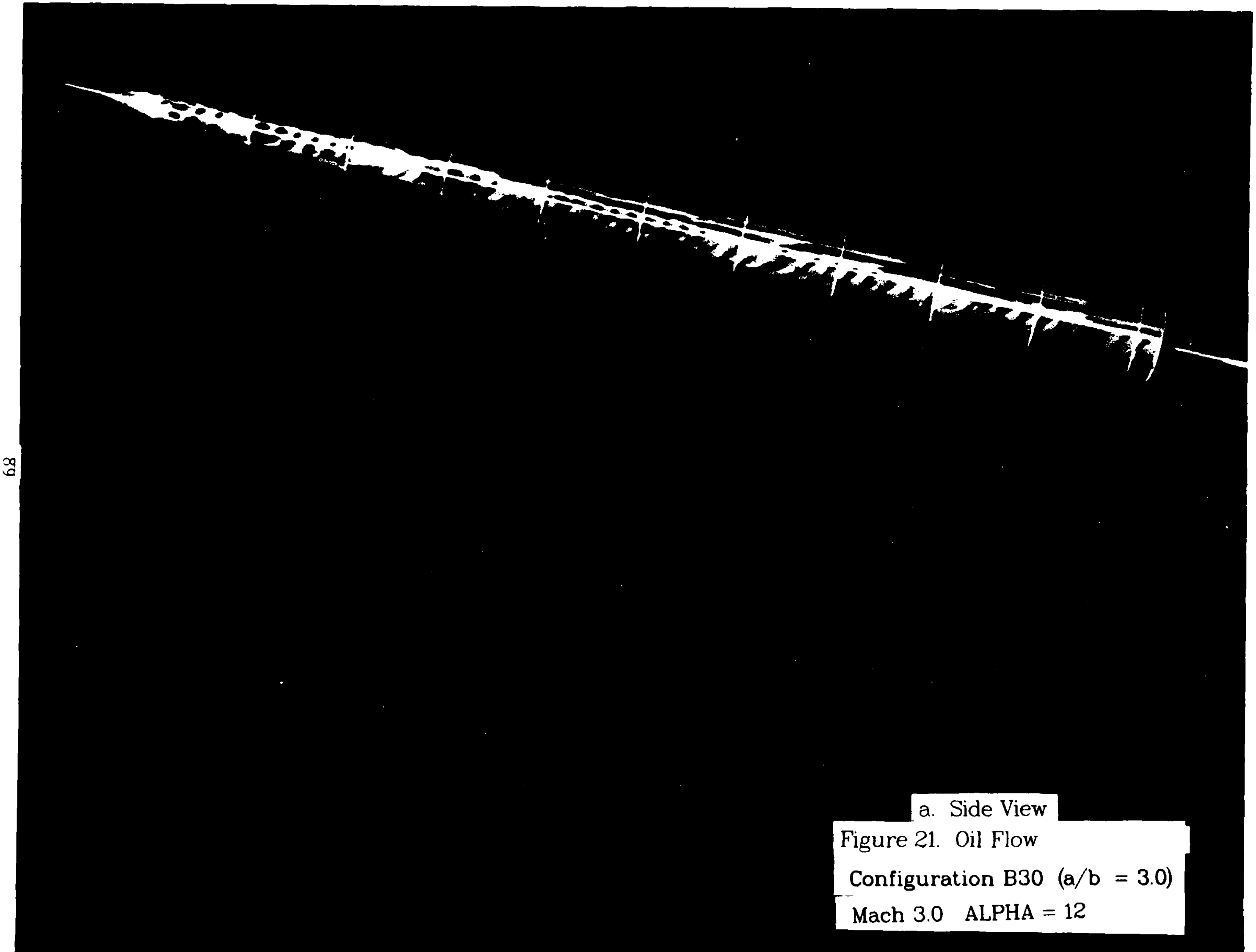

a. Side View

Figure 21. Oil Flow

Configuration B30 (a/b = 3.0)

Mach 3.0 ALPHA = 12

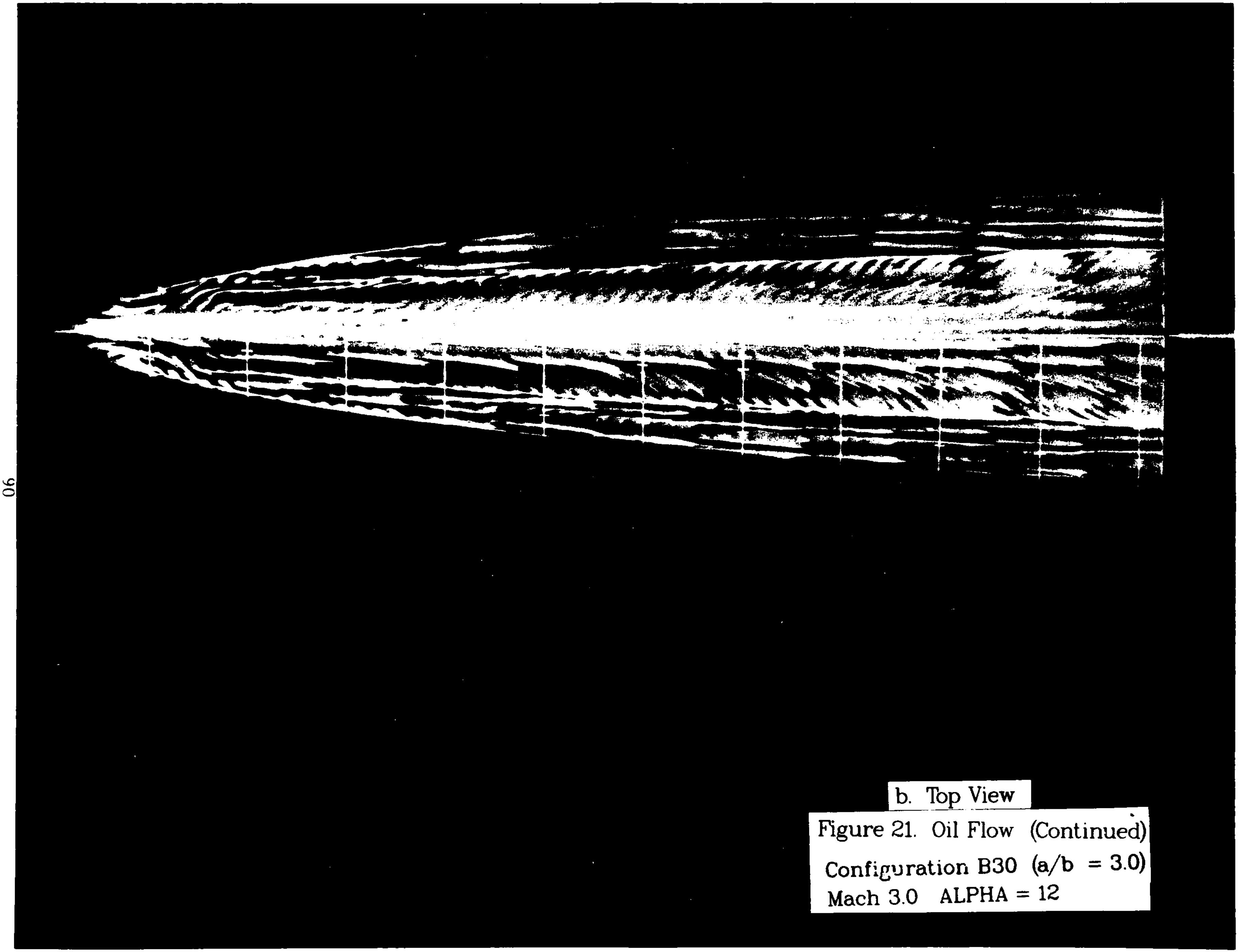

b. Top View

Figure 21. Oil Flow (Continued)
Configuration B30 (a/b = 3.0)
Mach 3.0 ALPHA = 12

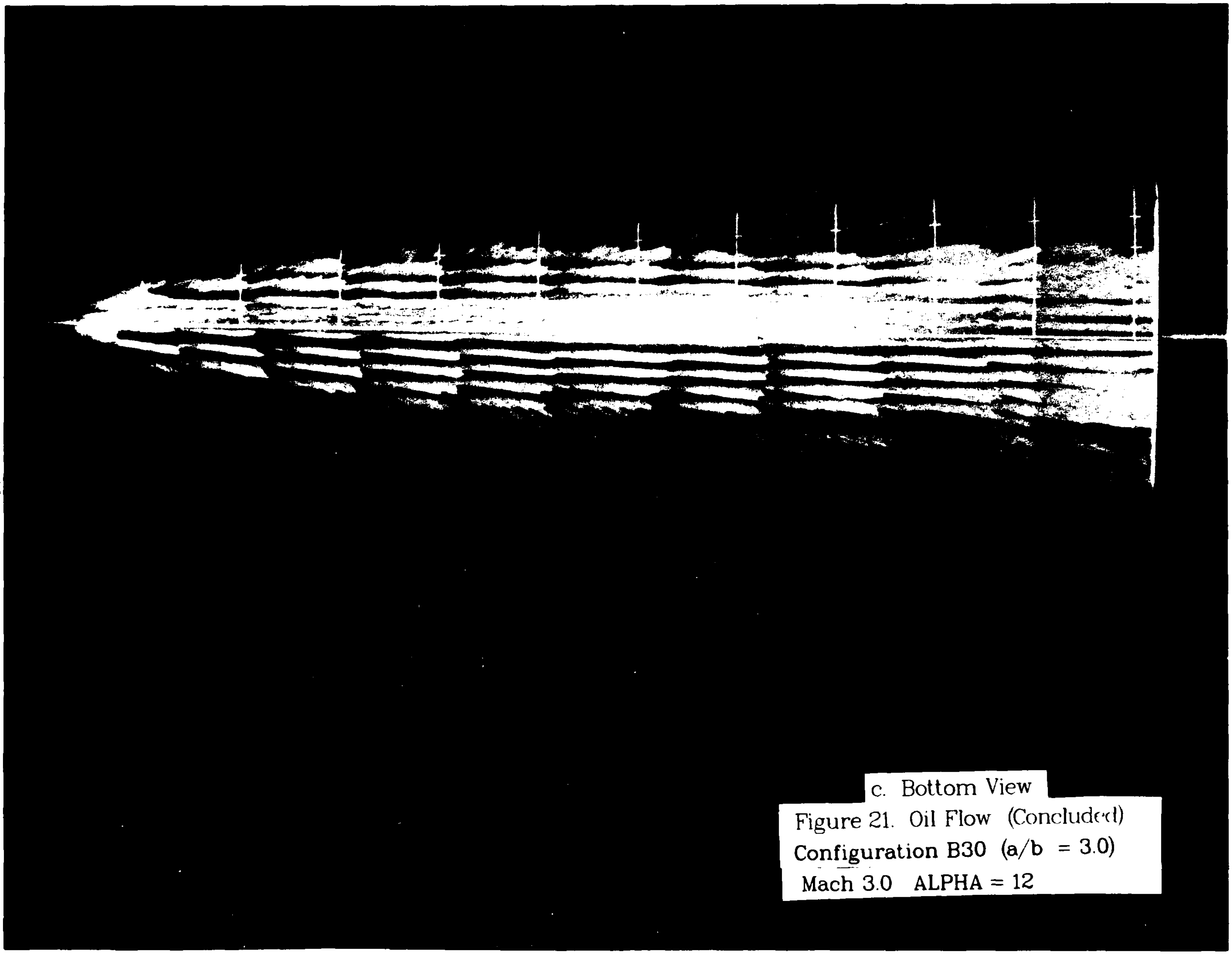

c. Bottom View

Figure 21. Oil Flow (Concluded)

Configuration B30 (a/b = 3.0)

Mach 3.0 ALPHA = 12

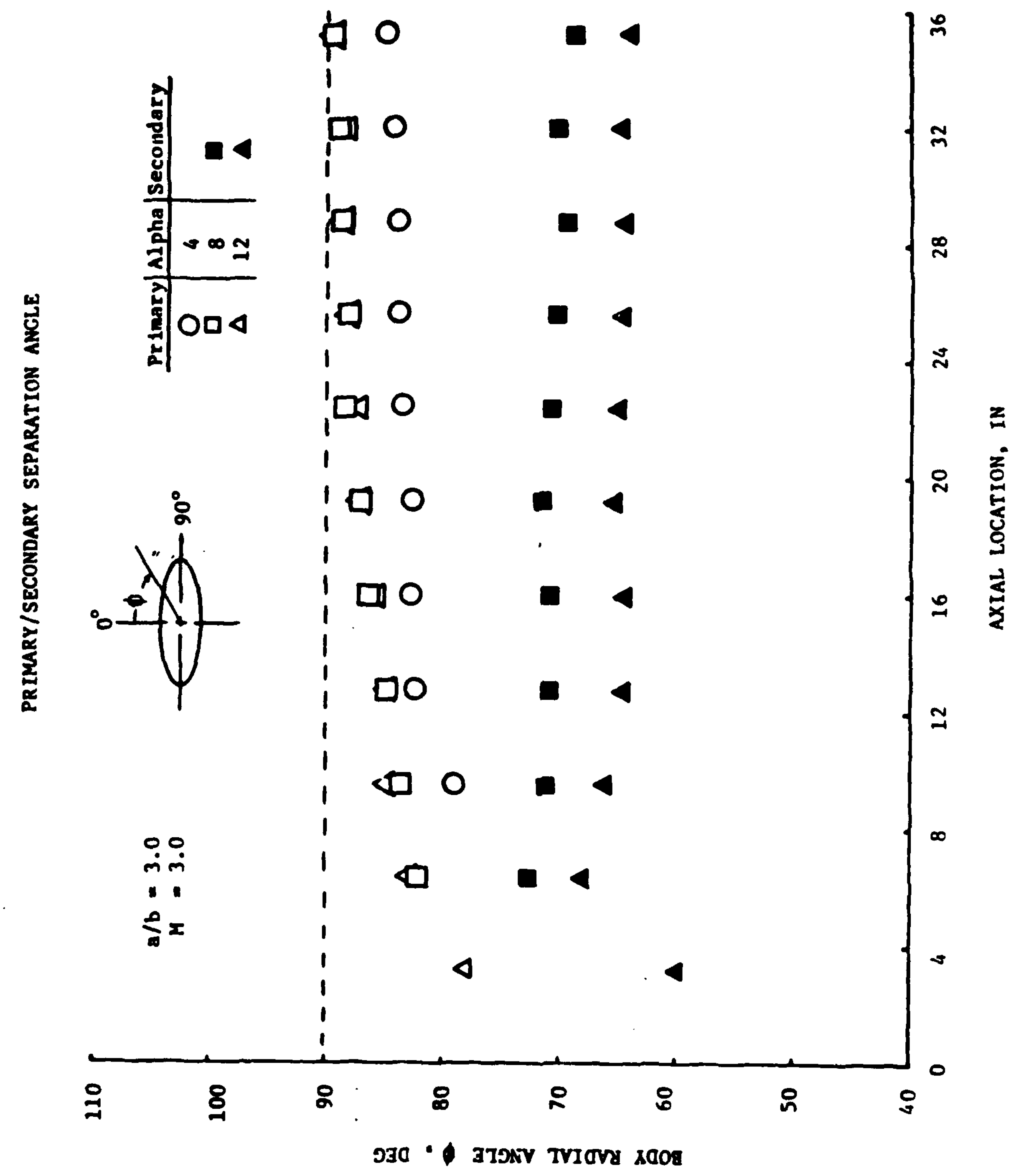

Figure 22. Separation Angle vs. Axial Location

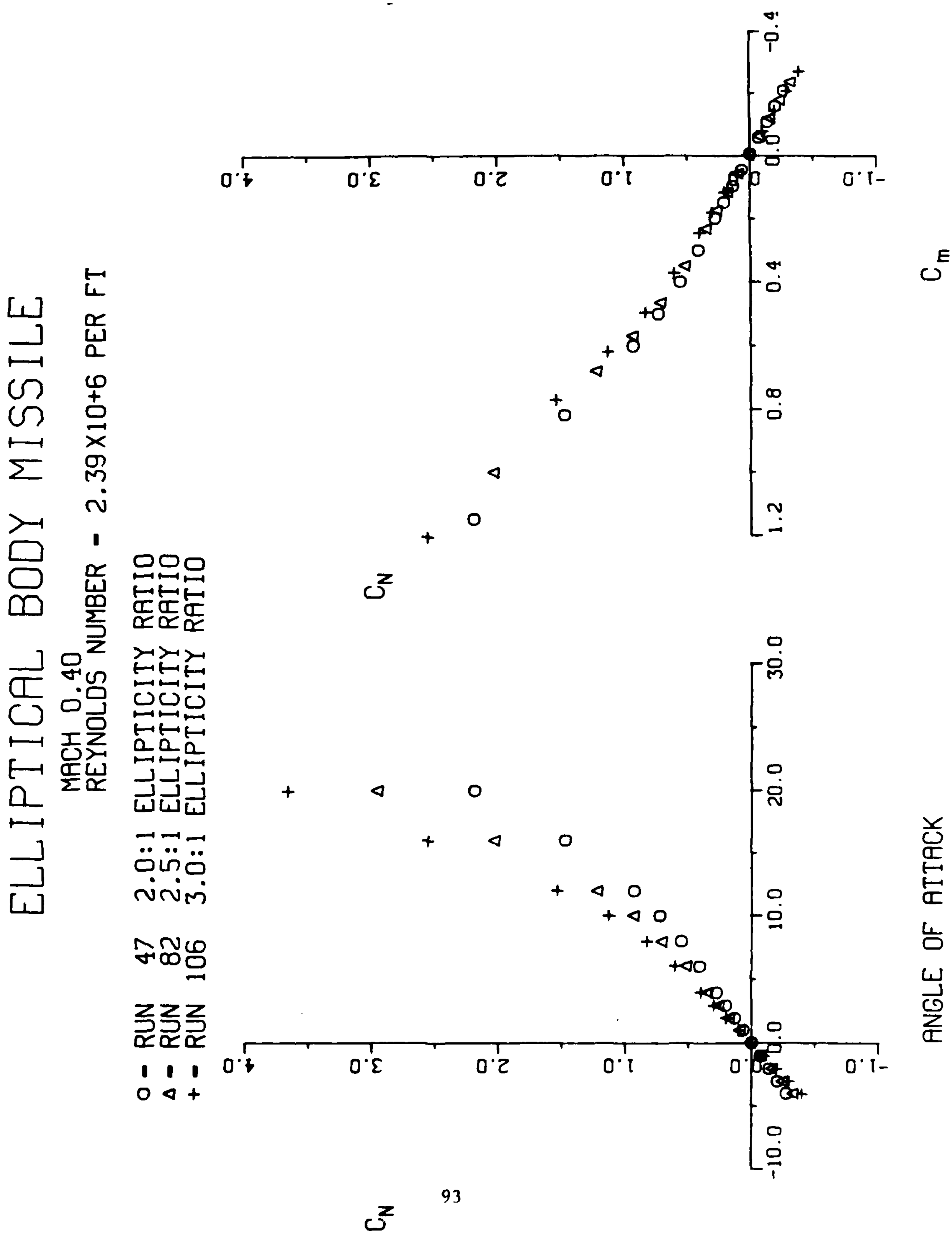

Figure 23. Ellipticity Ratio Effects, M = 0.4

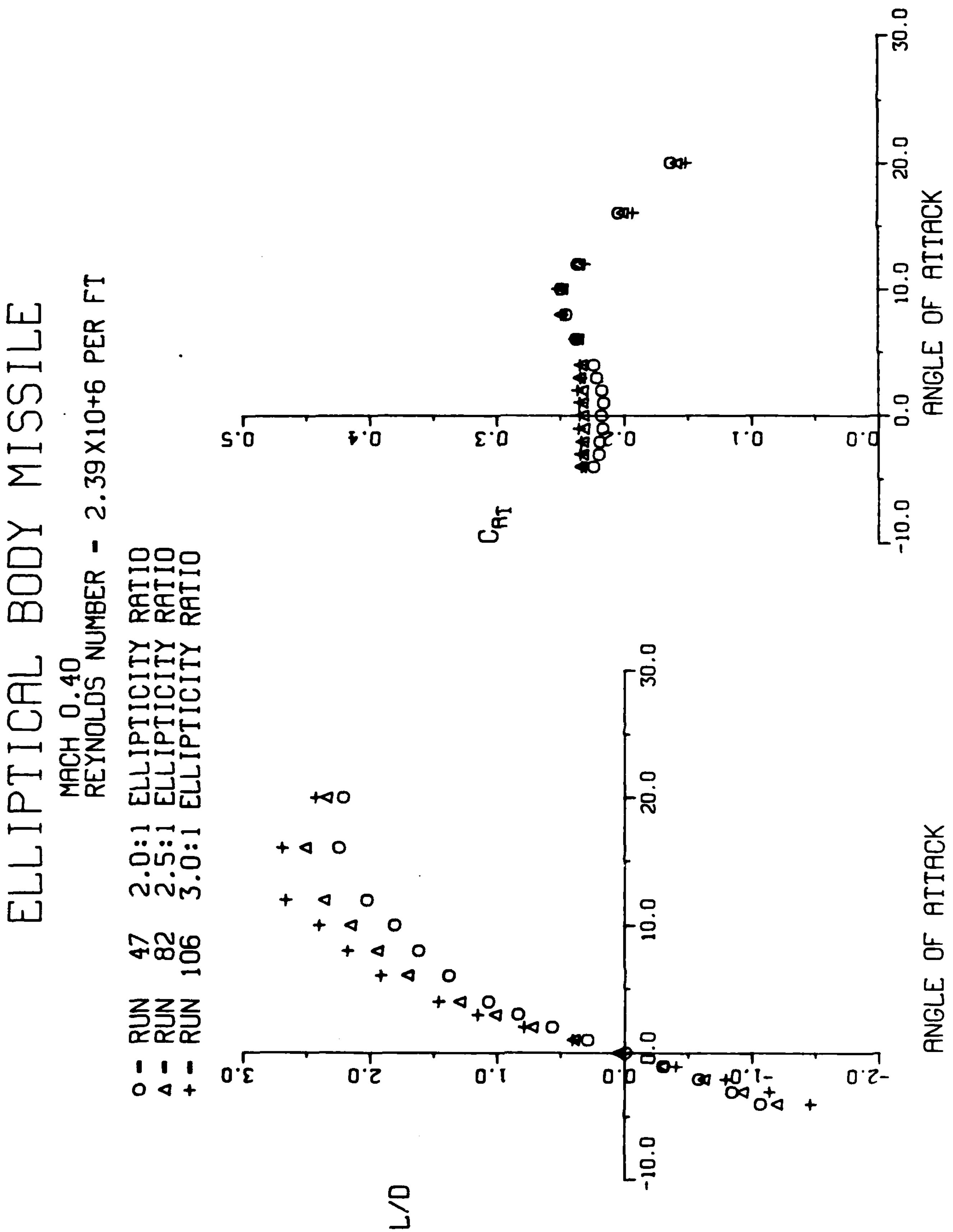

Figure 23. Ellipticity Ratio Effects, M = 0.4 (Concluded)

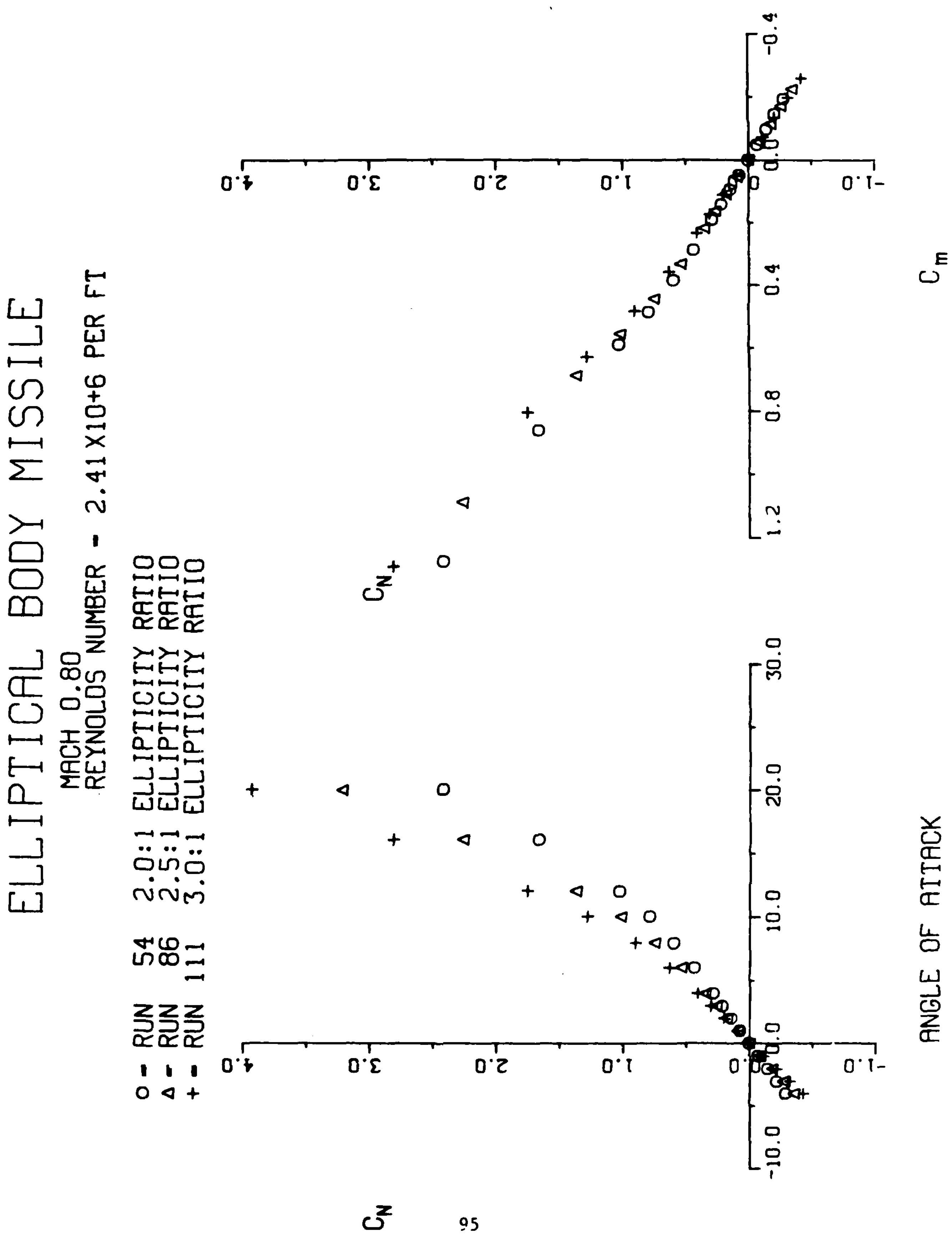

Figure 24. Ellipticity Ratio Effects, M = 0.8

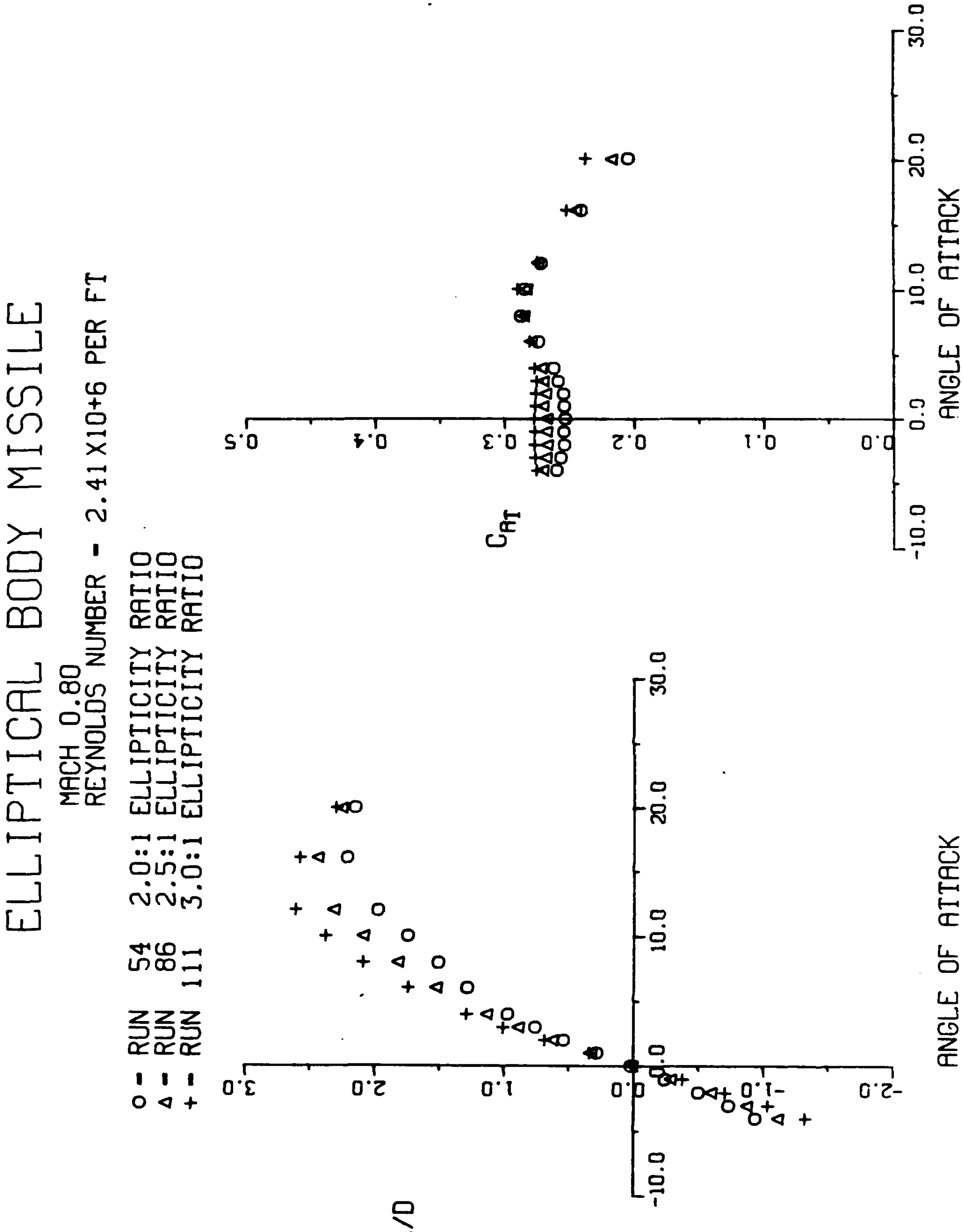

Figure 24. Ellipticity Ratio Effects, M = 0.8 (Concluded)

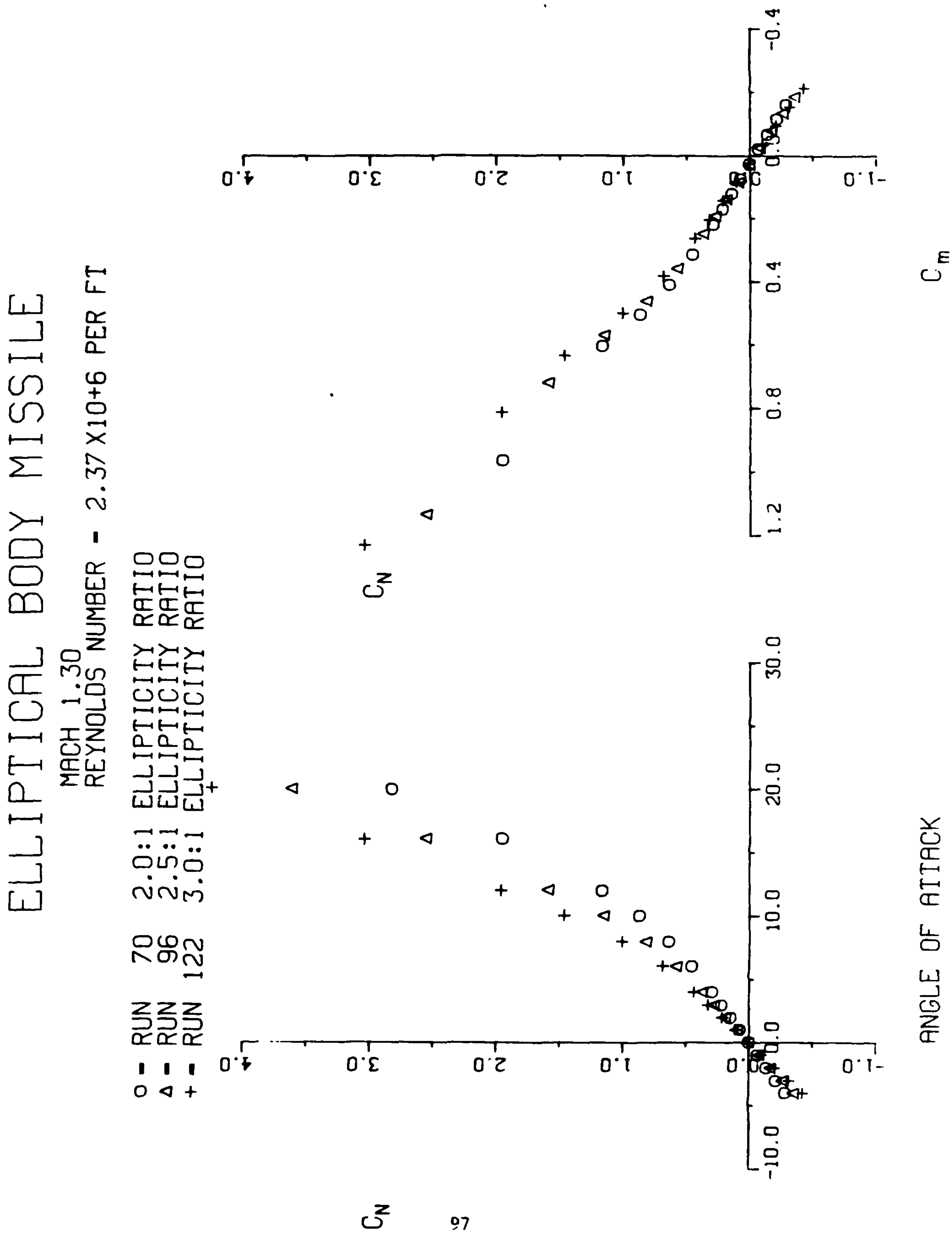

Figure 25. Ellipticity Ratio Effects, M = 1.3

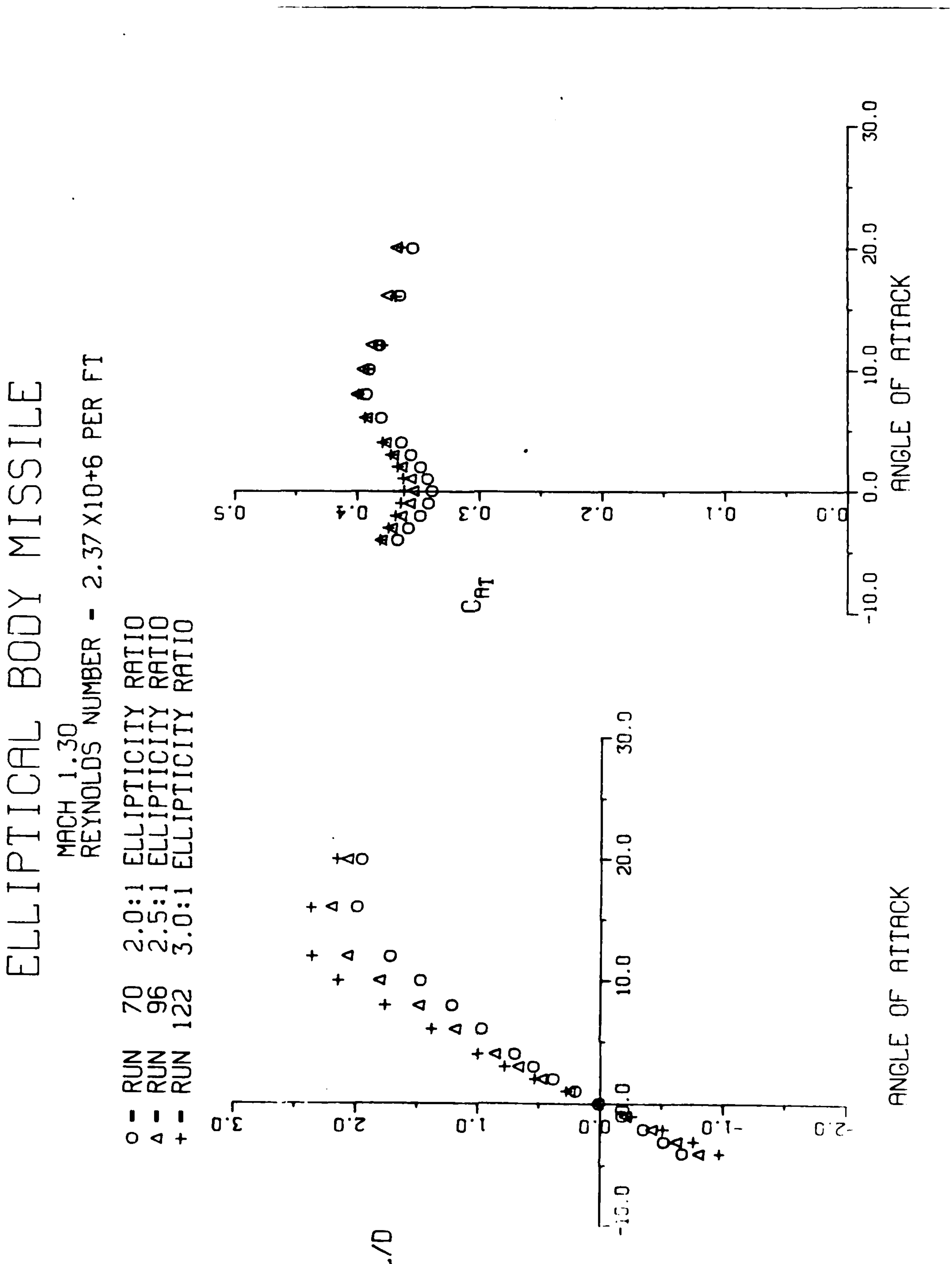

Figure 25. Ellipticity Ratio Effects, M = 1.3 (Concluded)

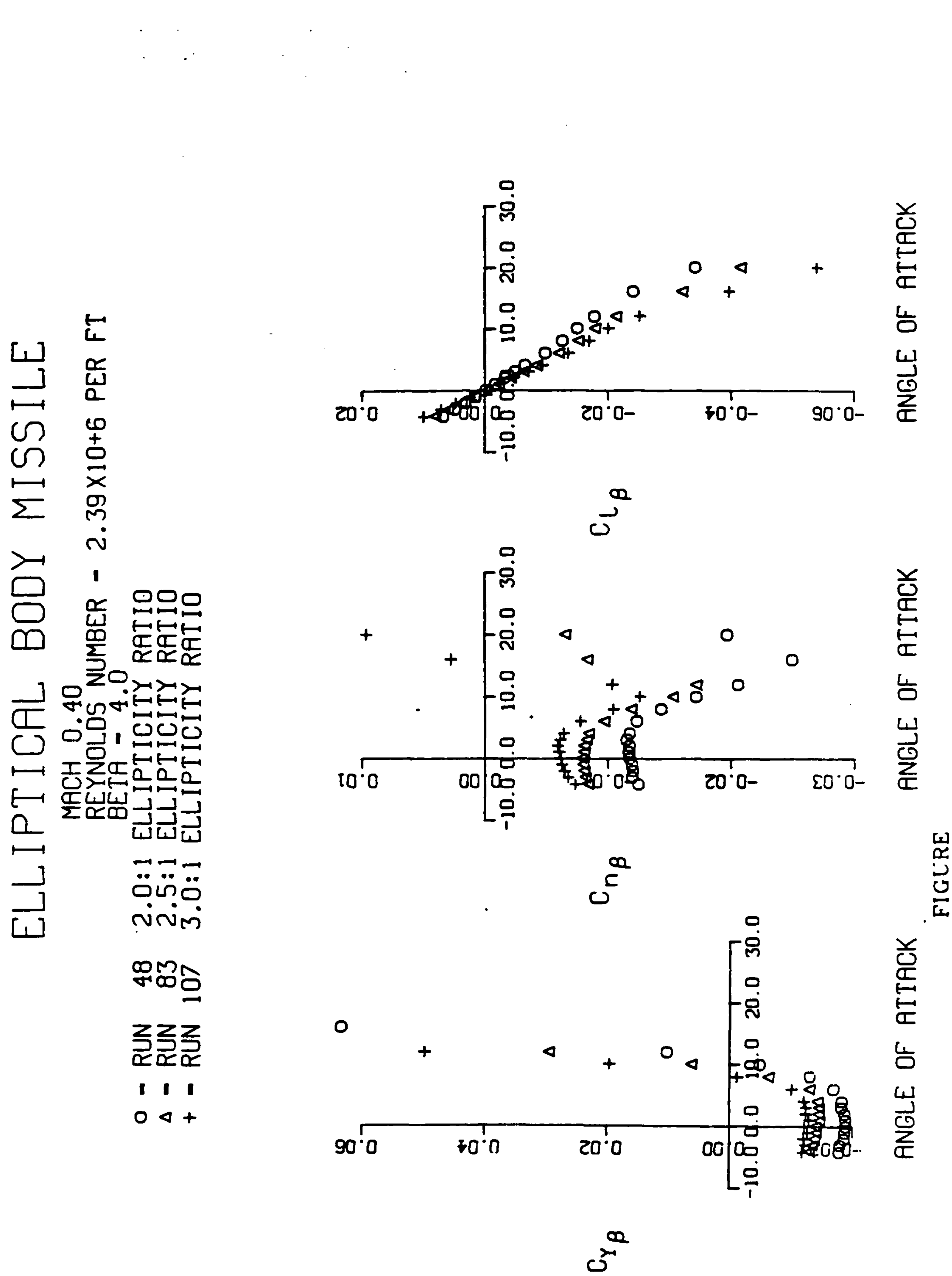

Figure 26. Stability Derivatives, M = 0.4

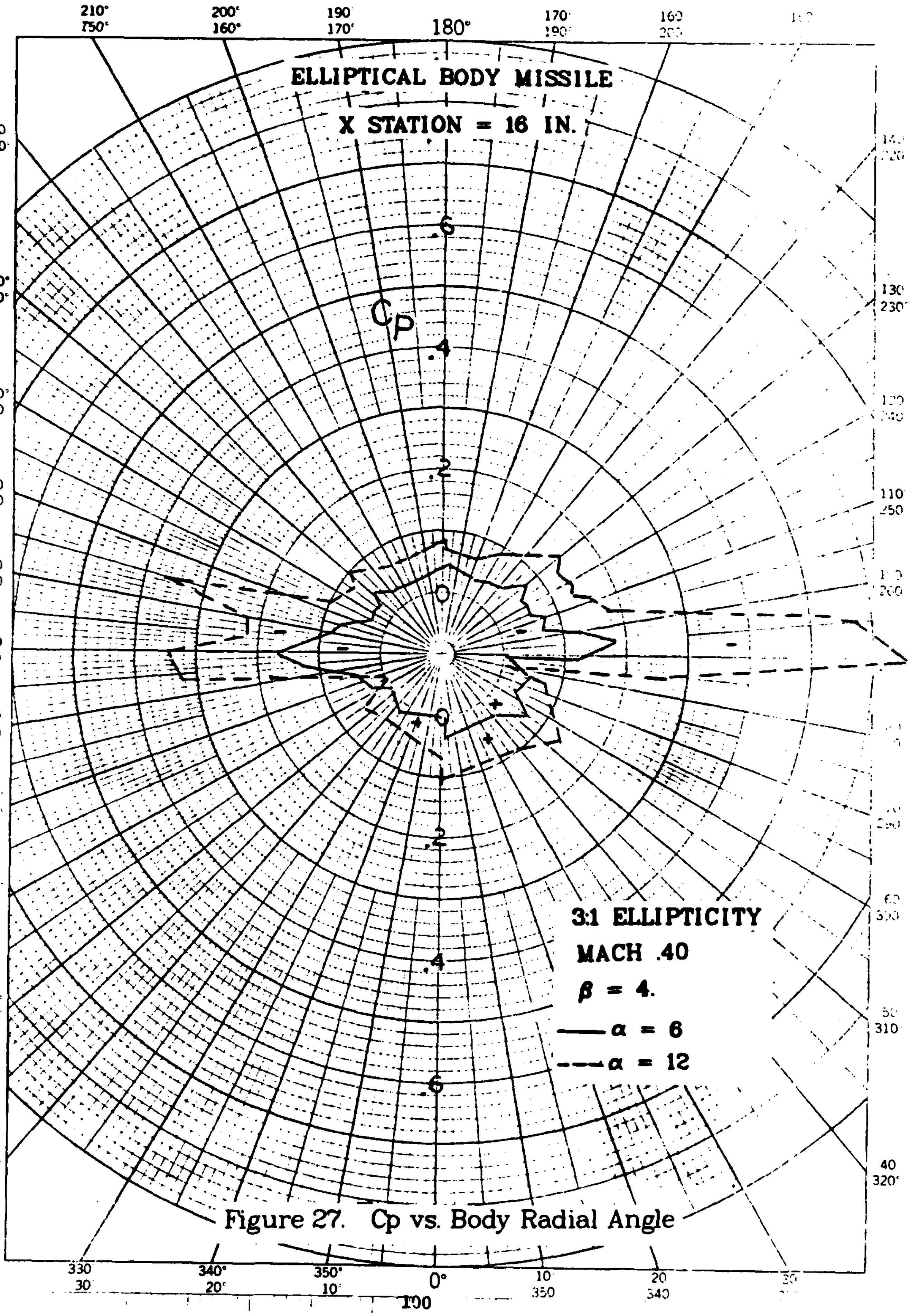

Figure 27. Cp vs. Body Radial Angle

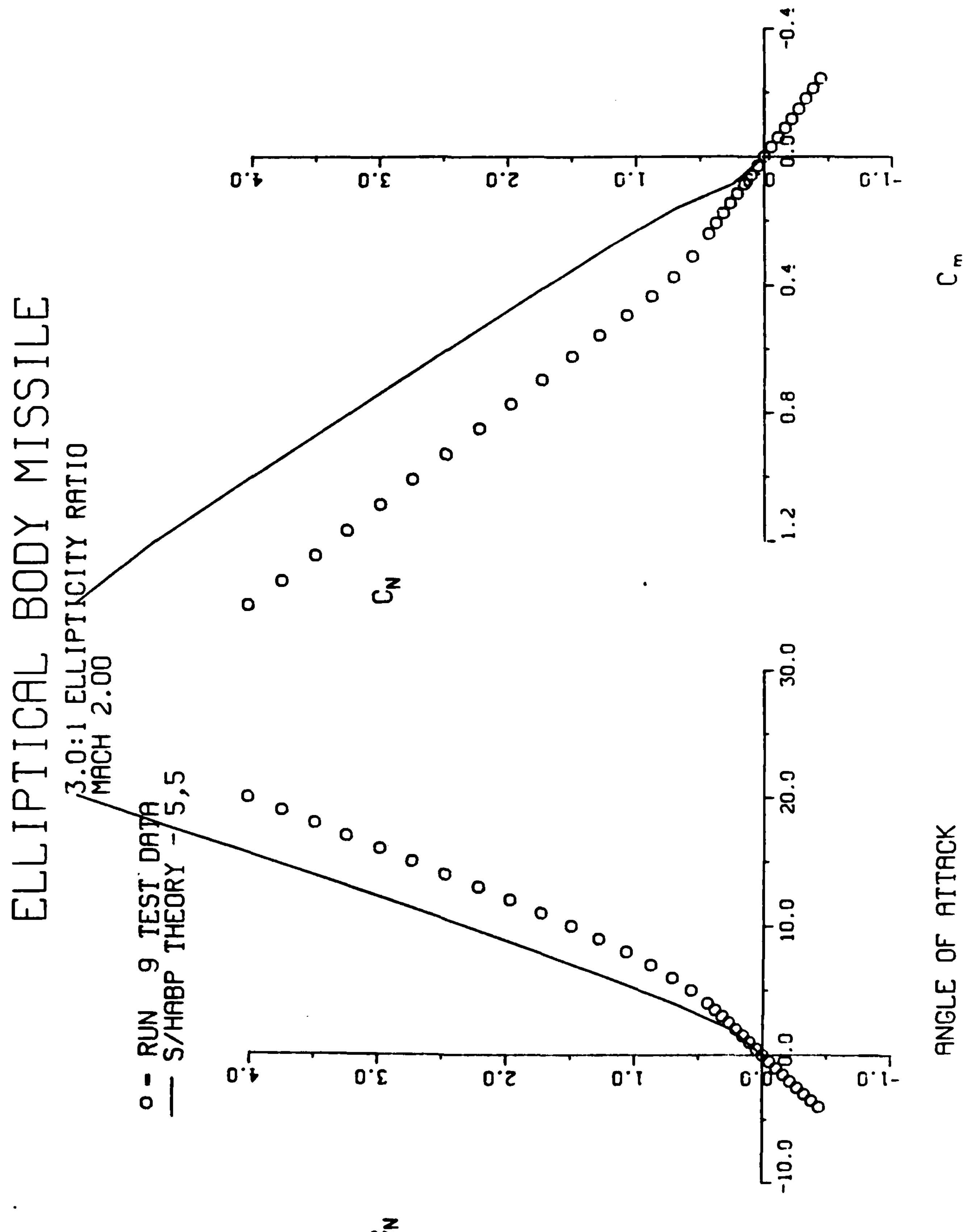

Figure 28. Force And Moment Comparisons, M = 2.0

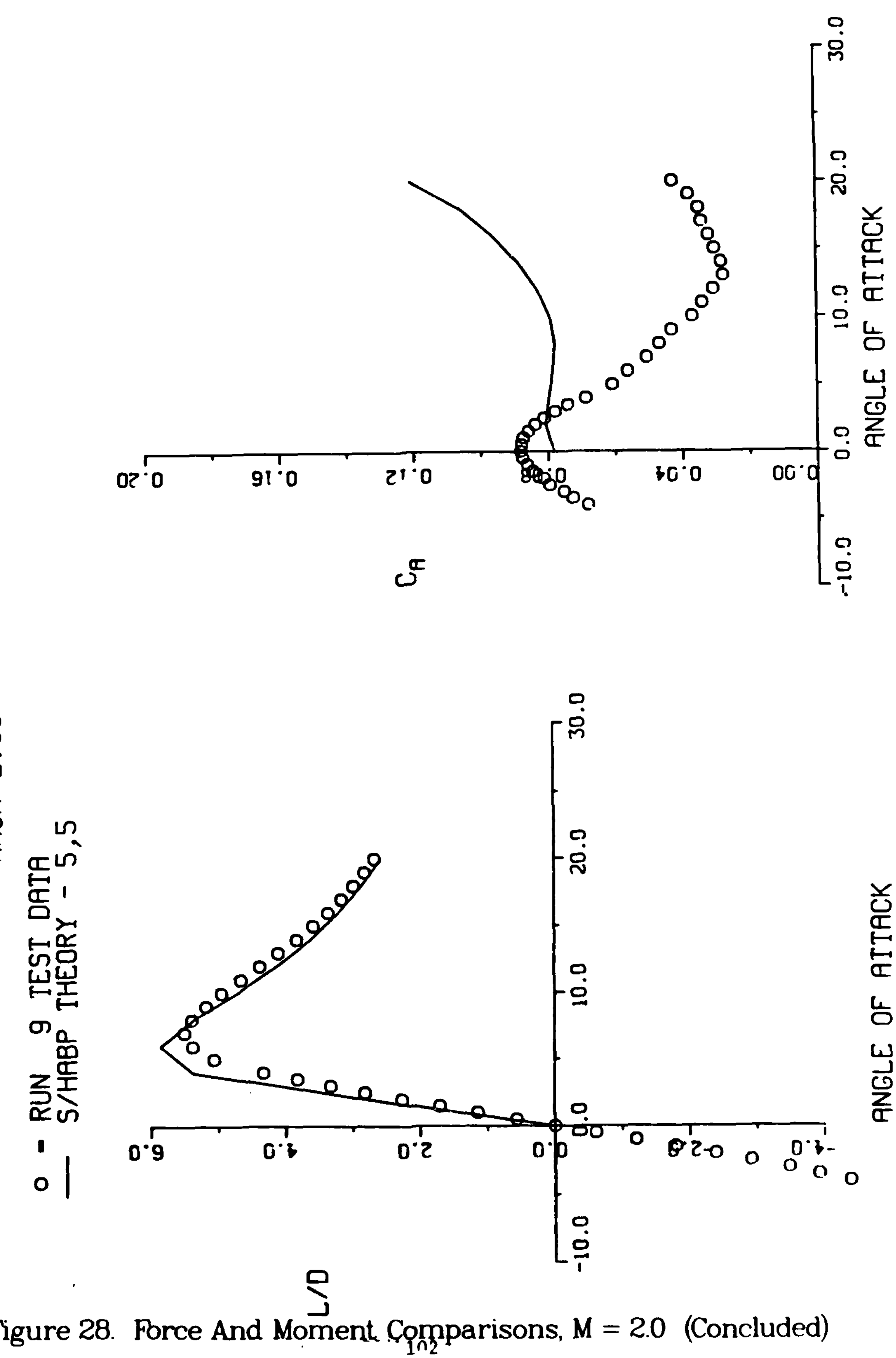

Figure 28. Force And Moment Comparisons, M = 2.0 (Concluded)

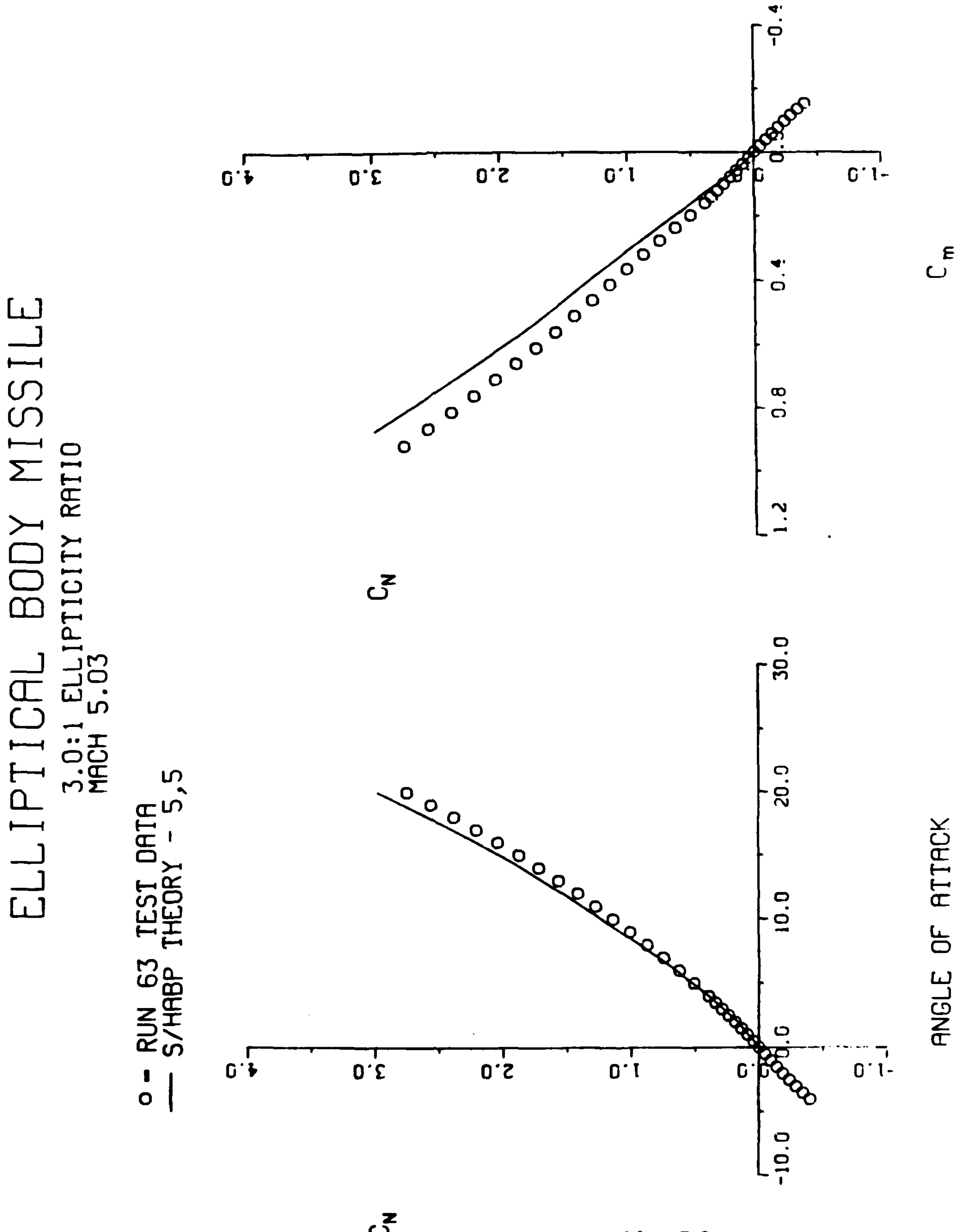

Figure 29. Force And Moment Comparisons, M = 5.0

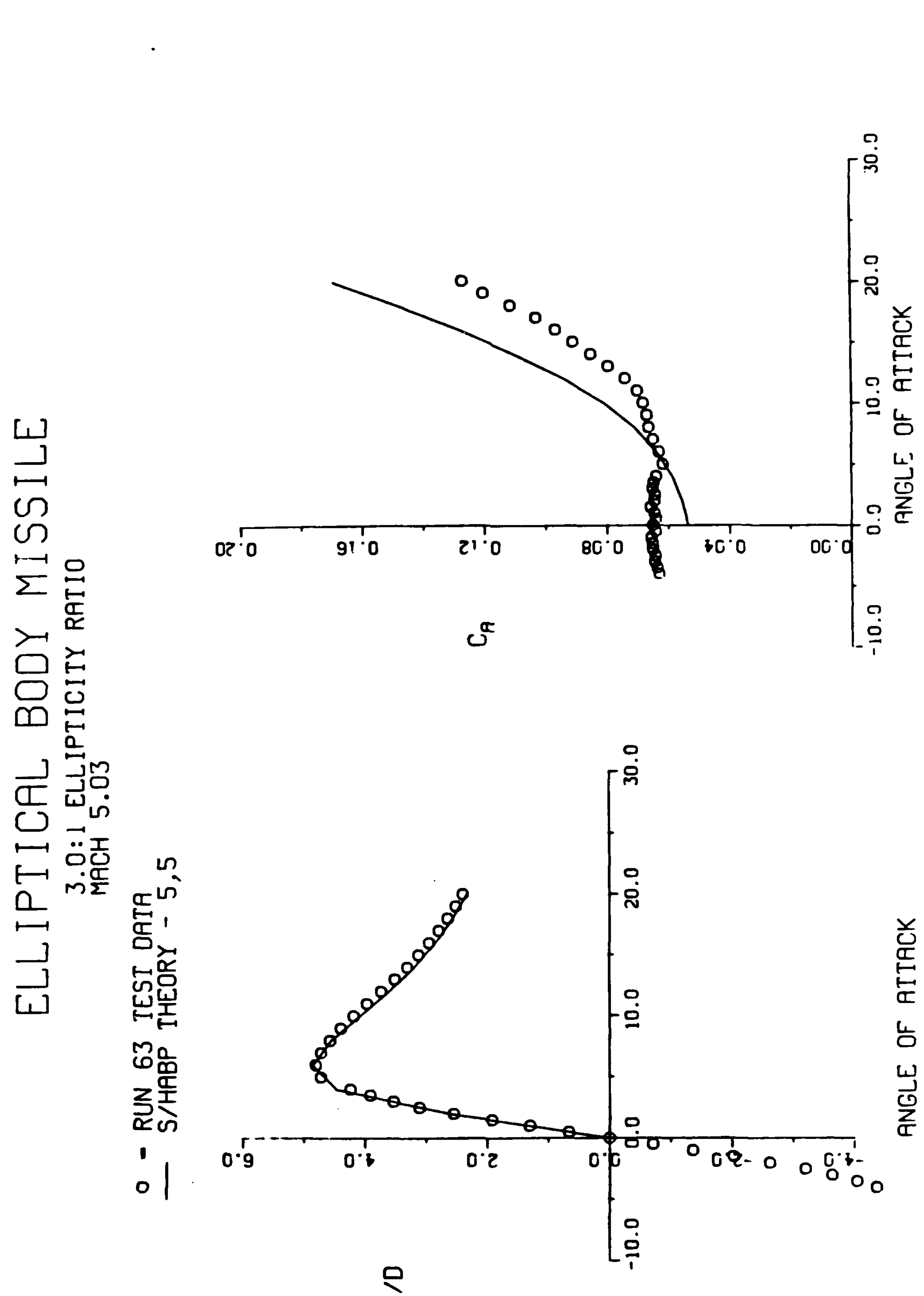

Figure 29. Force And Moment Comparisons, M = 5.0 (Concluded)

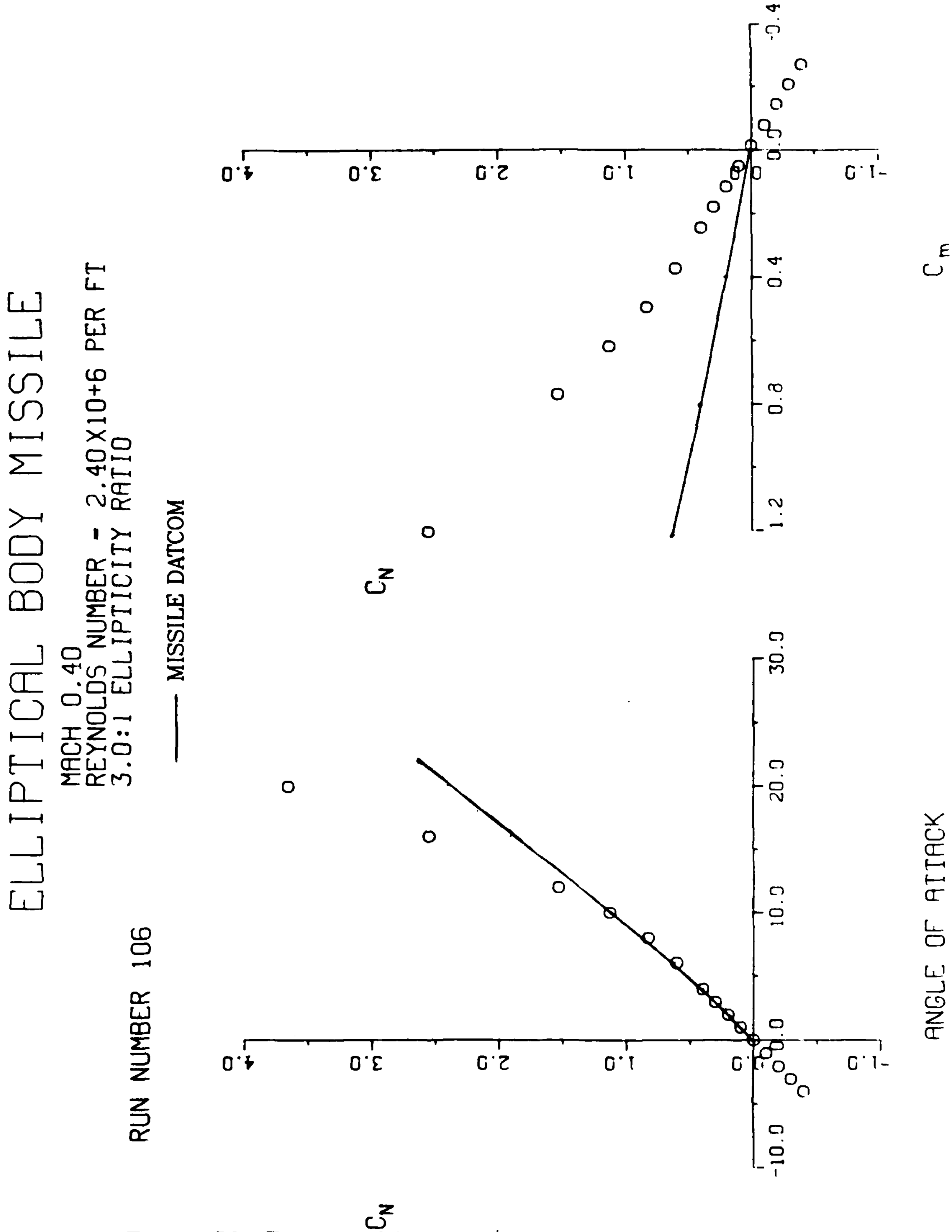

Figure 30. Force And Moment Comparisons, M = 0.4

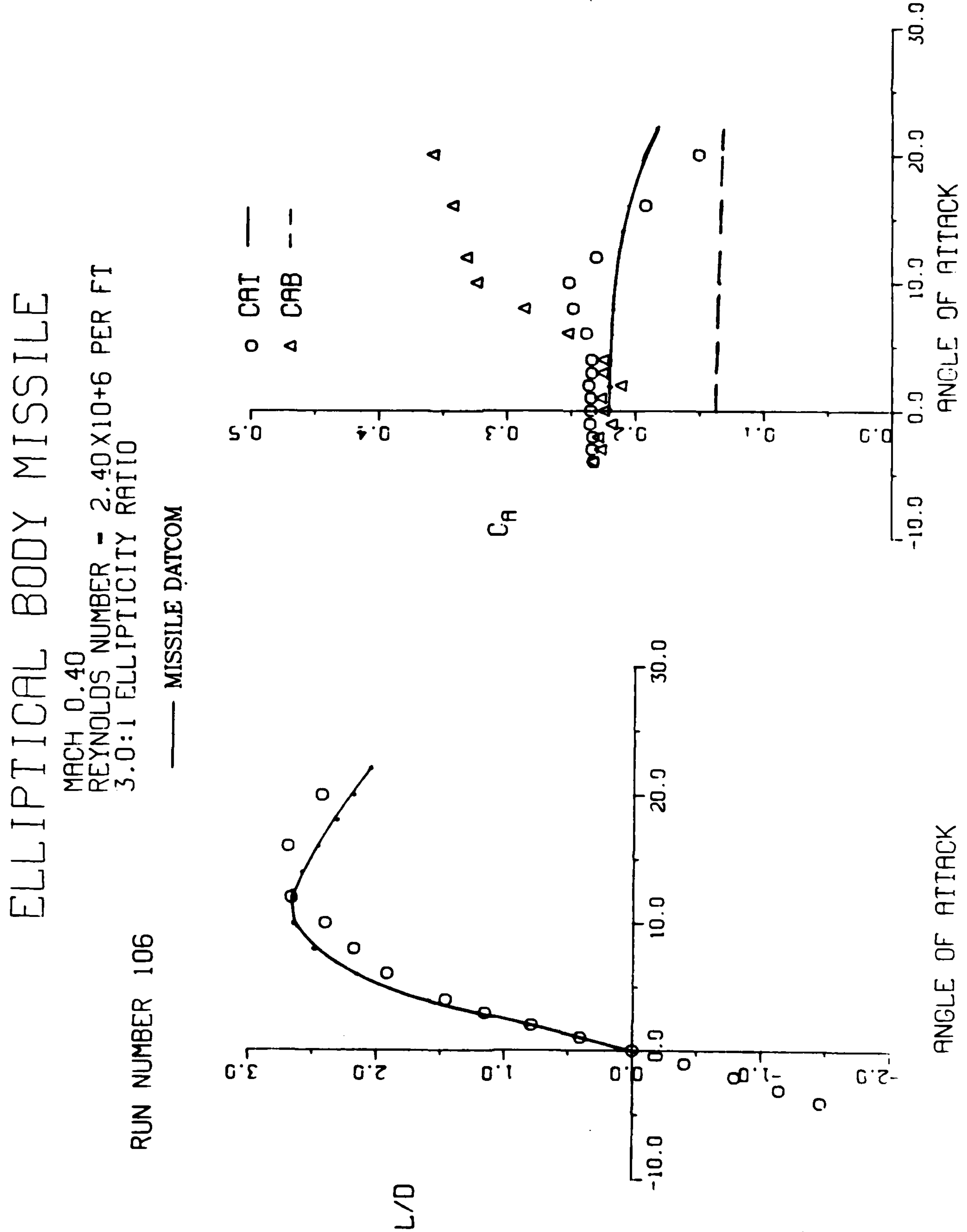

Figure 30. Force And Moment Comparisons, M = 0.4 (Concluded)

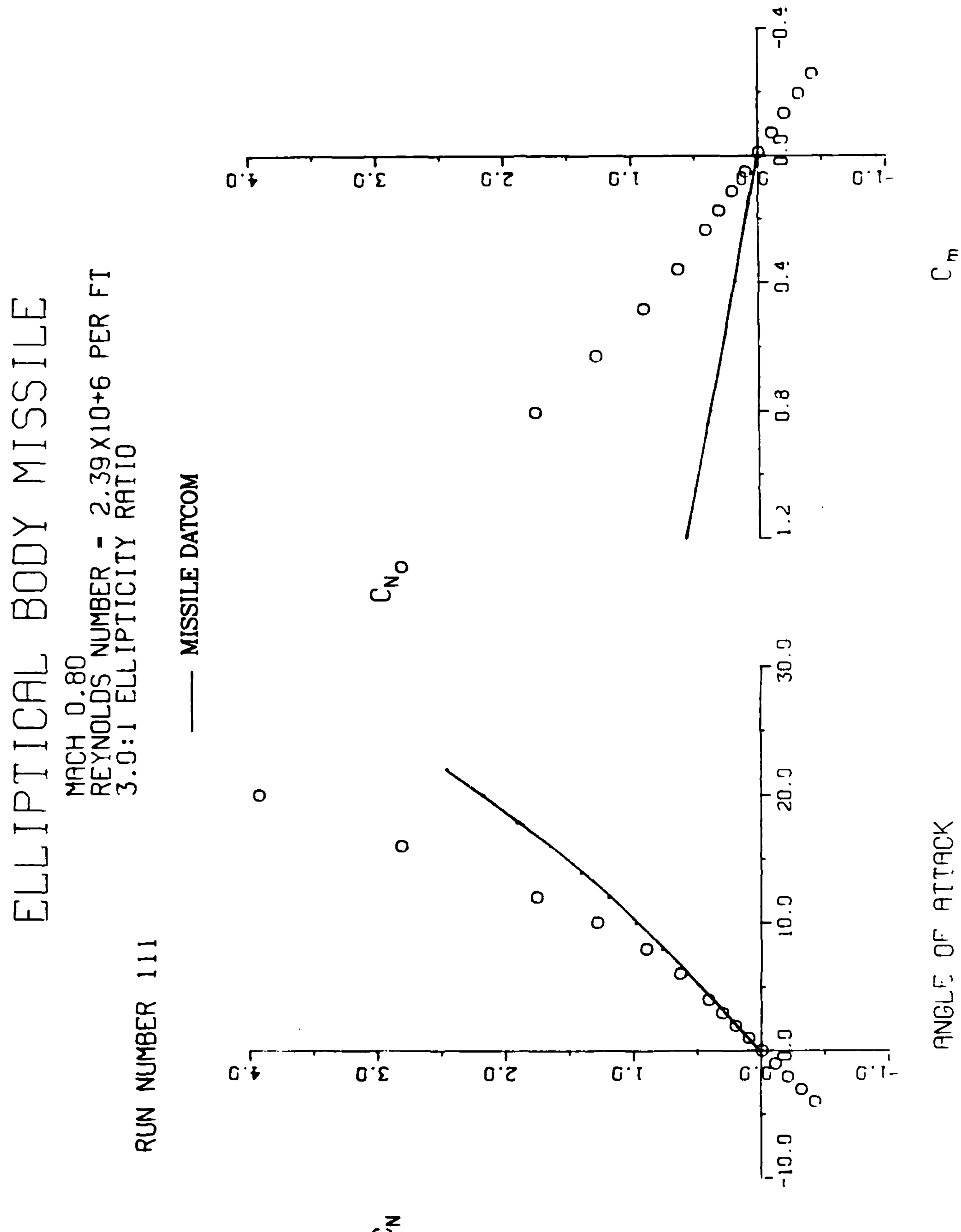

Figure 31. Force And Moment Comparisons, M = 0.8

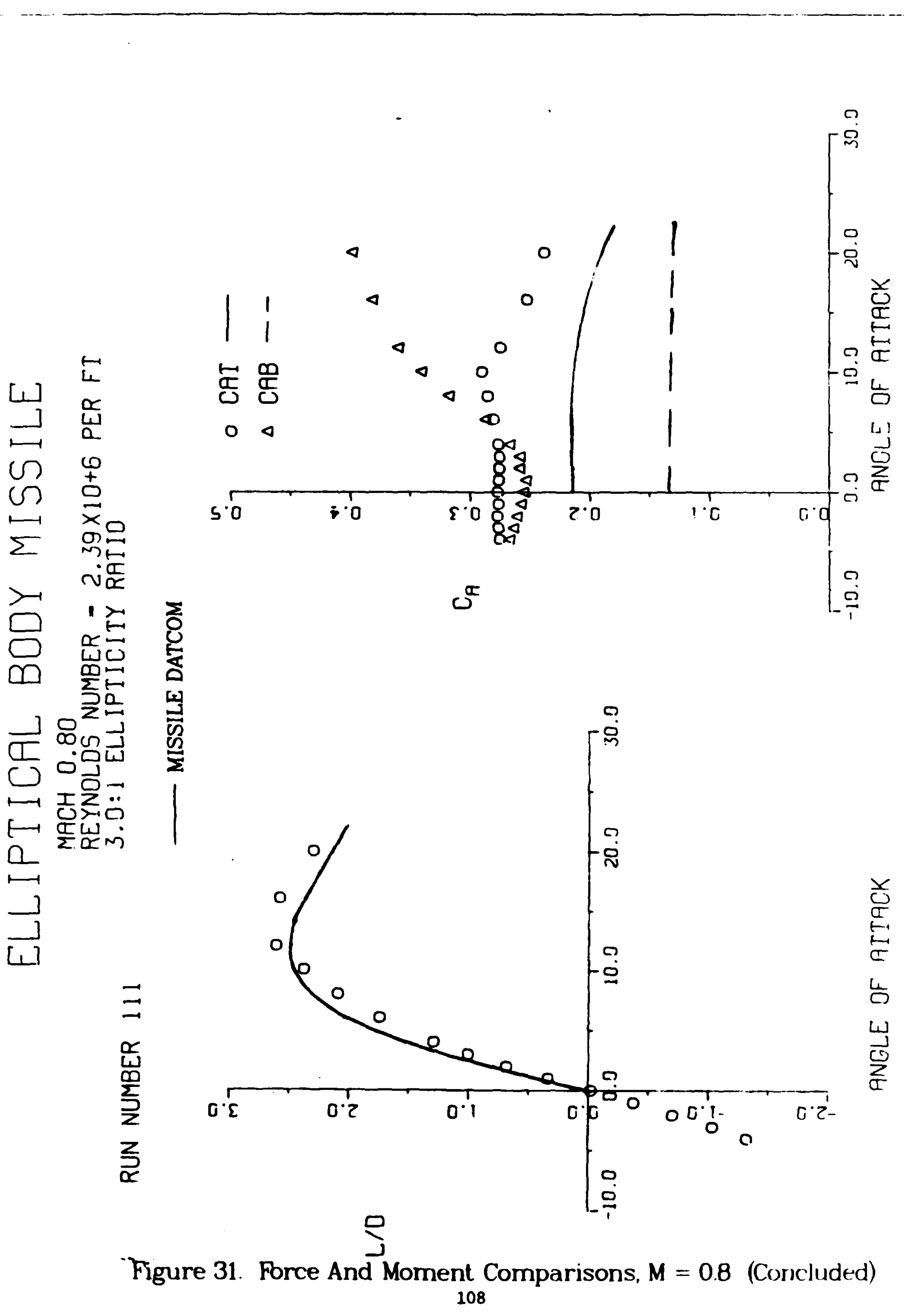

Figure 31. Force And Moment Comparisons, M = 0.8 (Concluded)

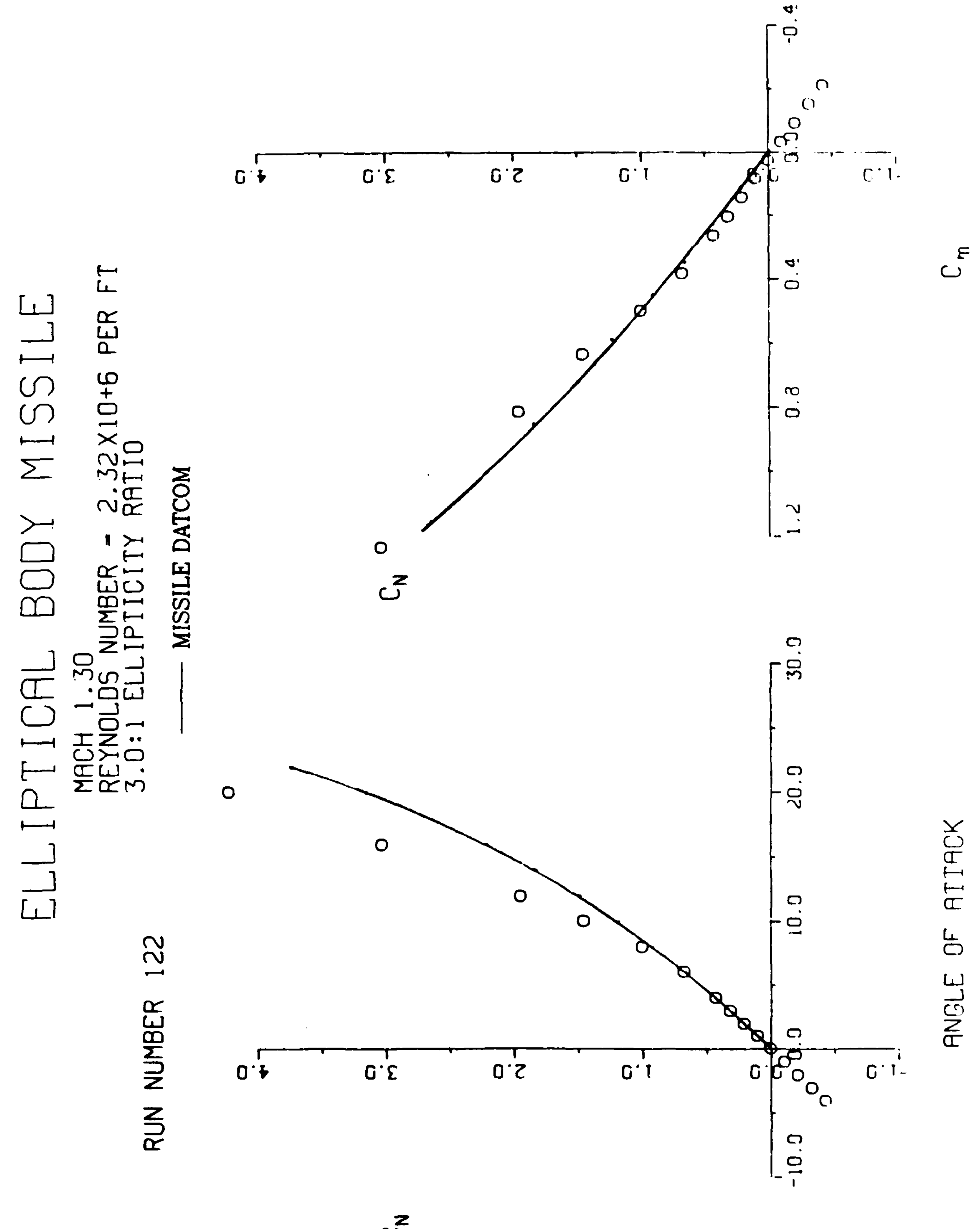

Figure 32. Force And Moment Comparisons, M = 1.3

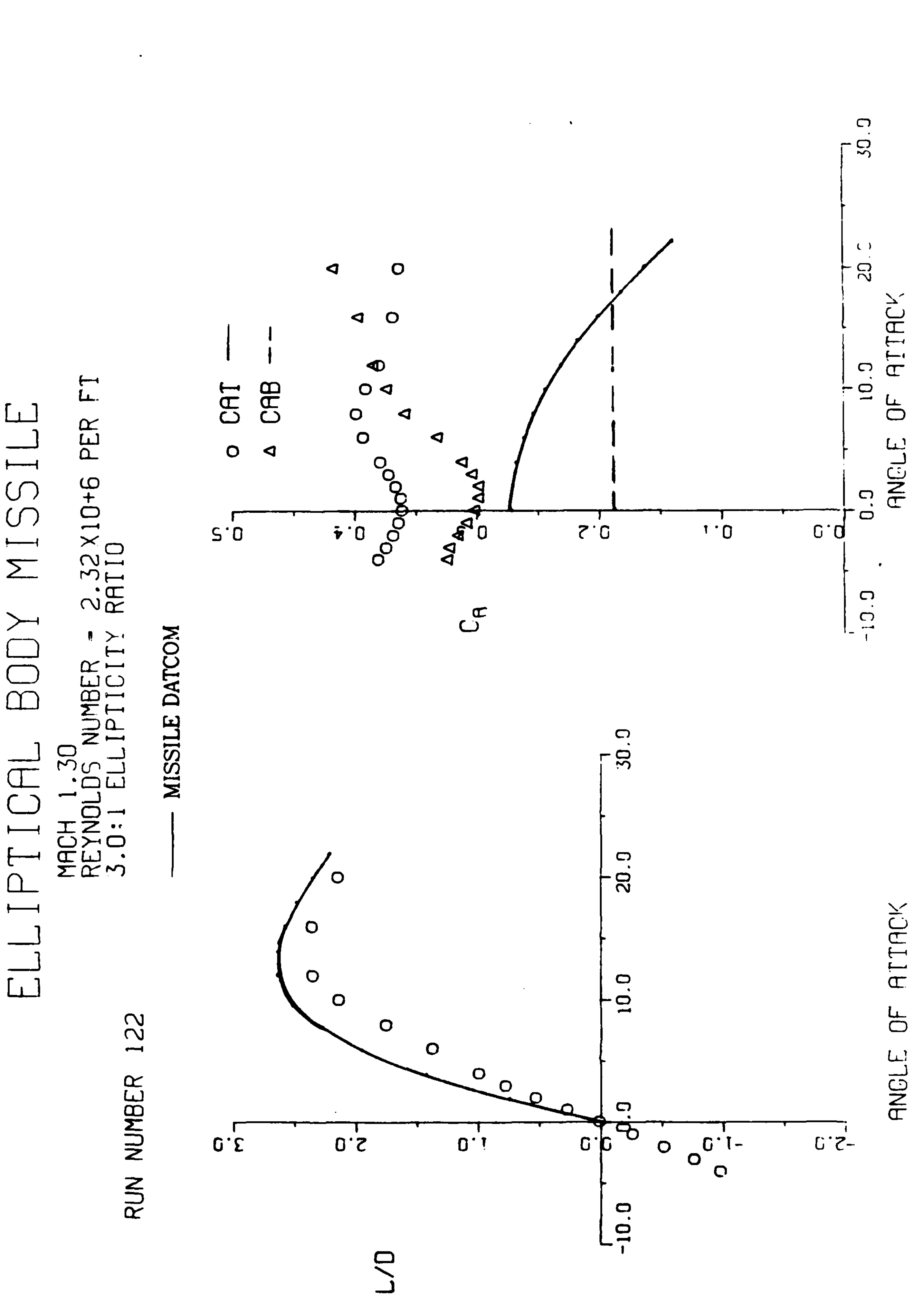

Figure 32. Force And Moment Comparisons, M = 1.3 (Concluded)

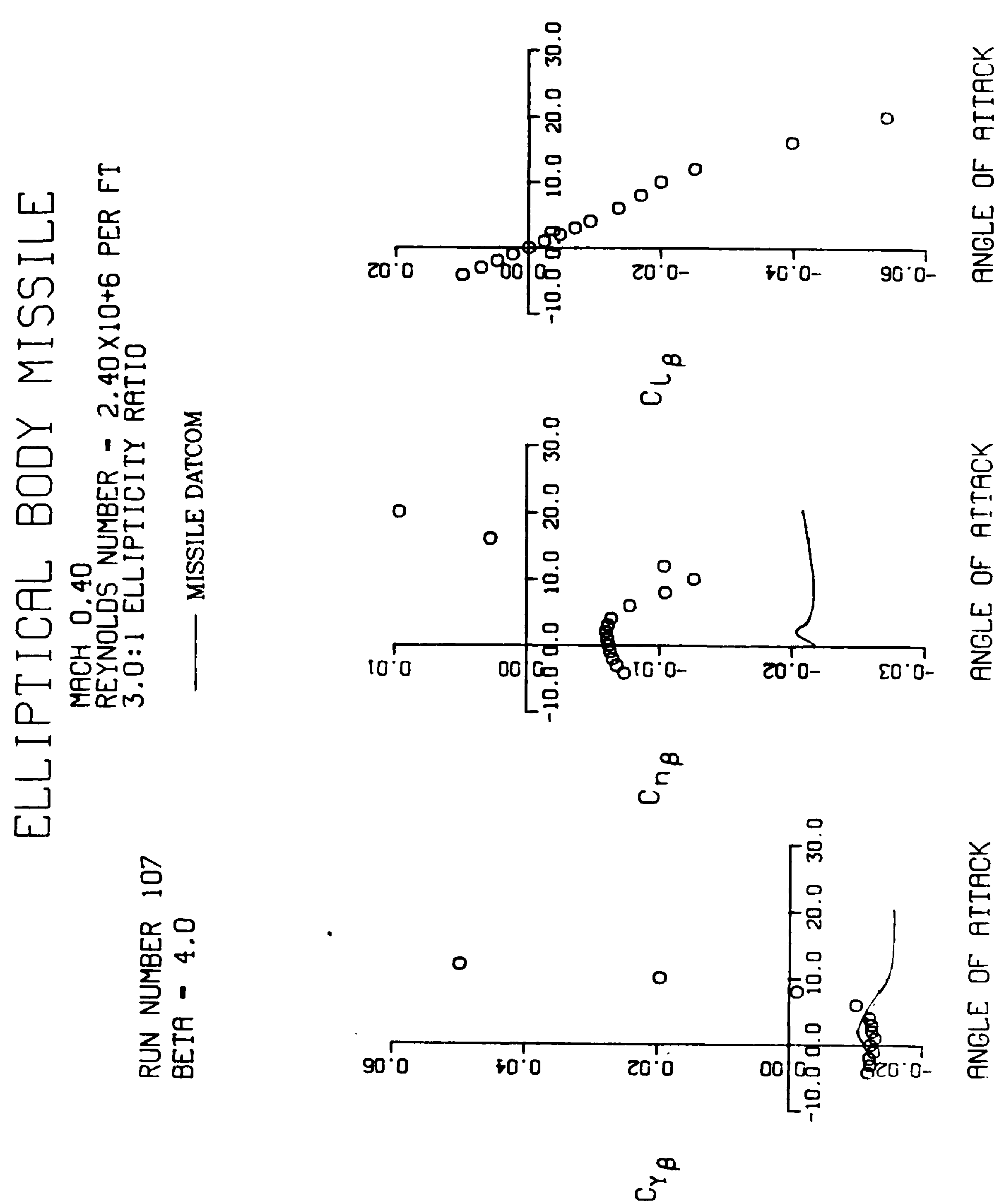

Figure 33. Lateral Directional Comparisons, M = 0.4

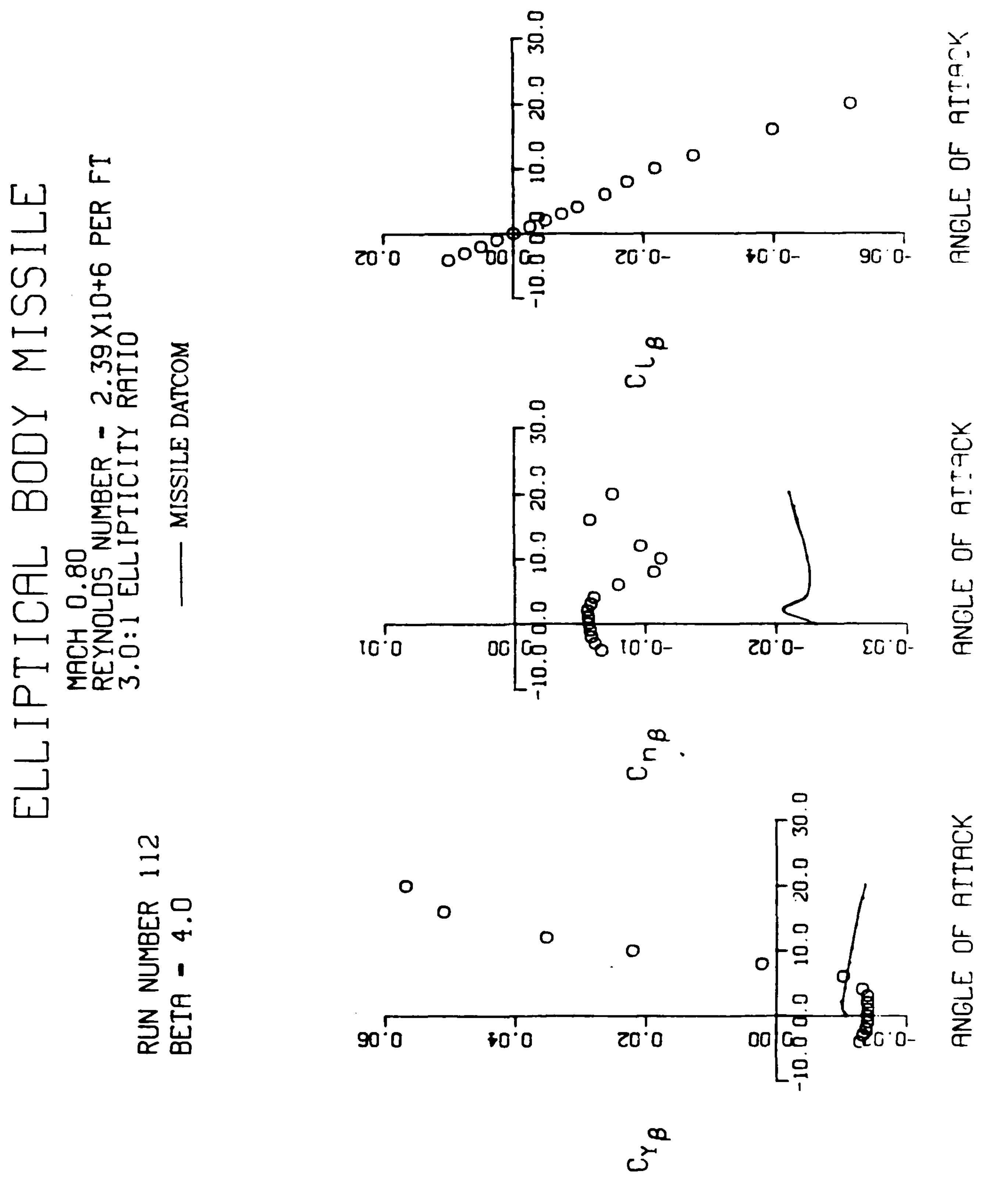

Figure 34. Lateral Directional Comparisons, M = 0.8

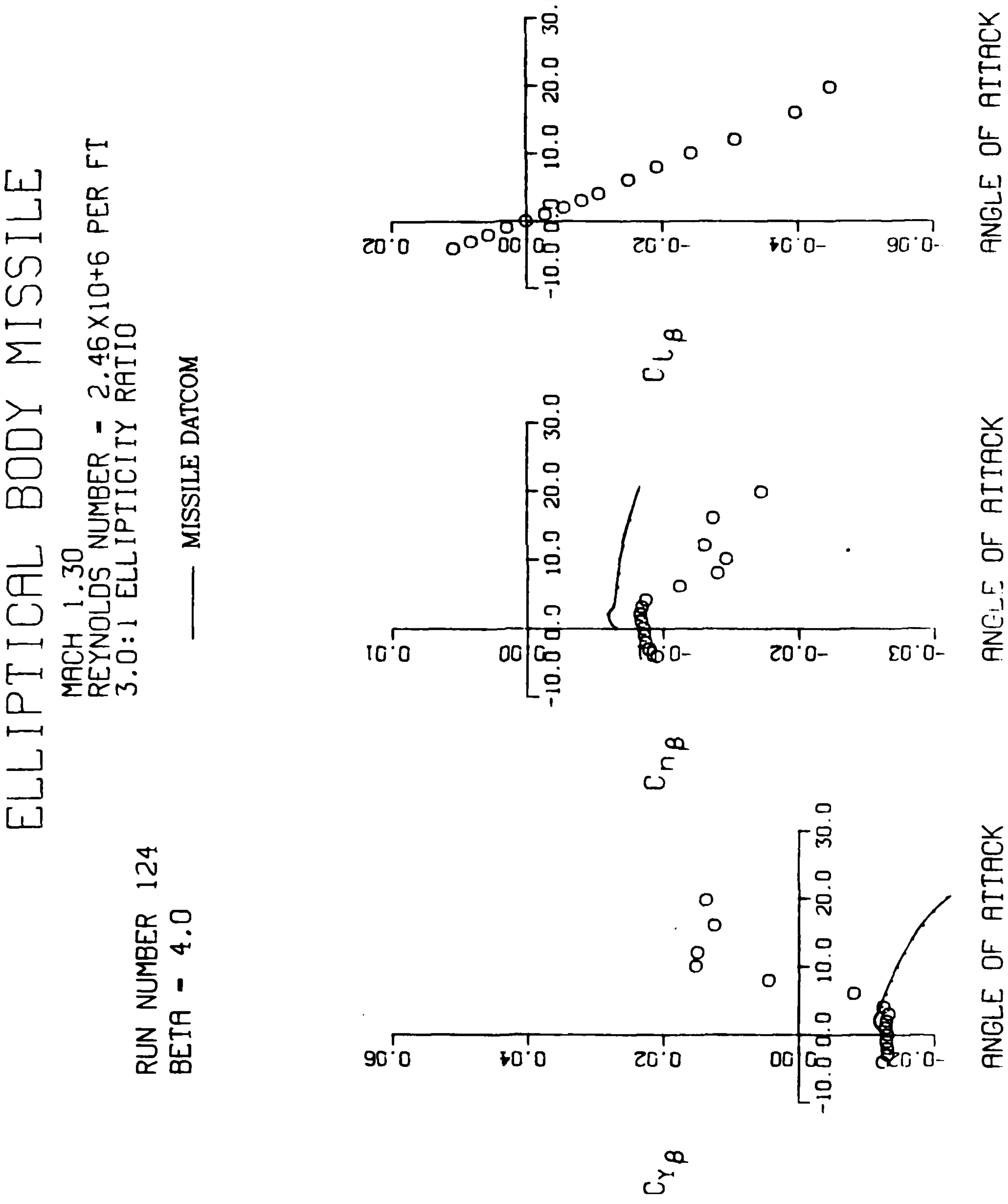

Figure 35. Lateral Directional Comparisons, M = 1.3

a/b = 2.5

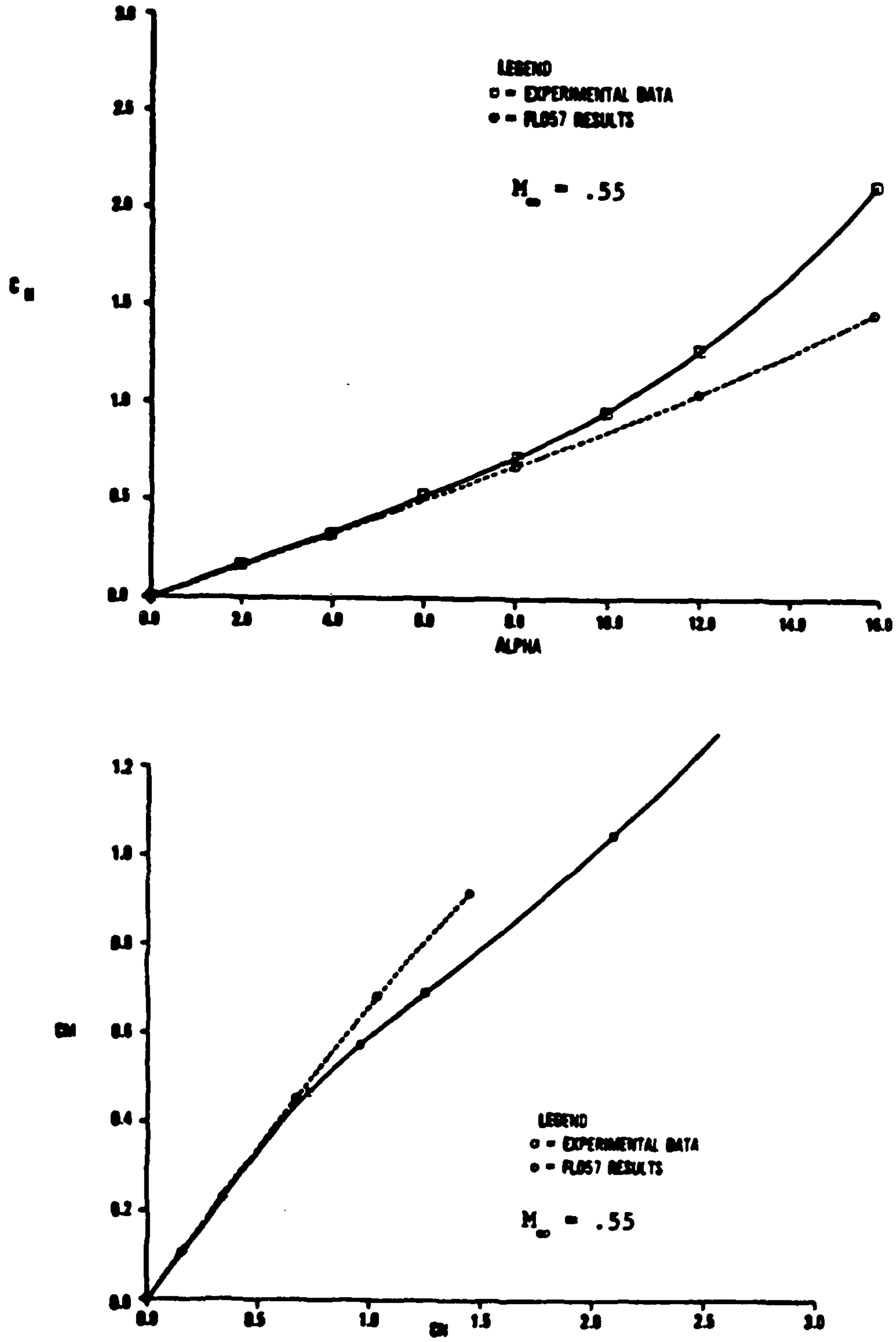

a. Mach 0.55

Figure 36. FLO57 Force And Moment Comparisons

a/b = 2.5

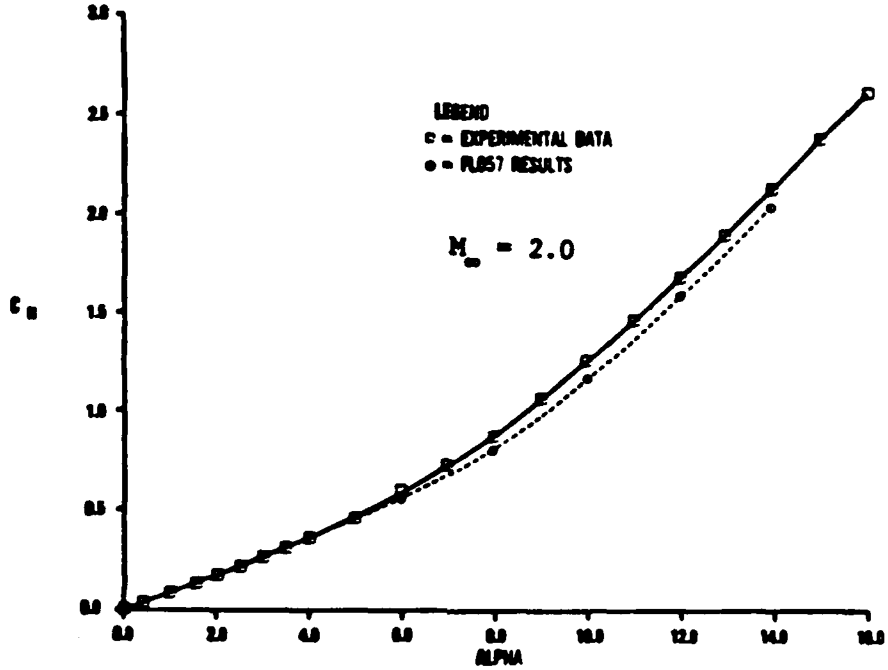

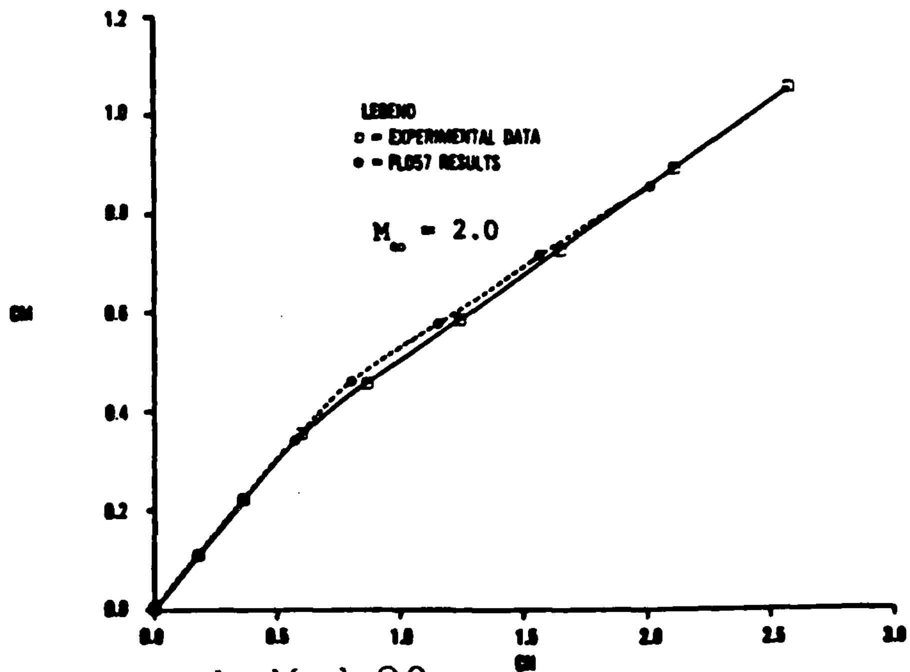

b. Mach 2.0

Figure 36. FL057 Force And Moment Comparisons (Concluded)

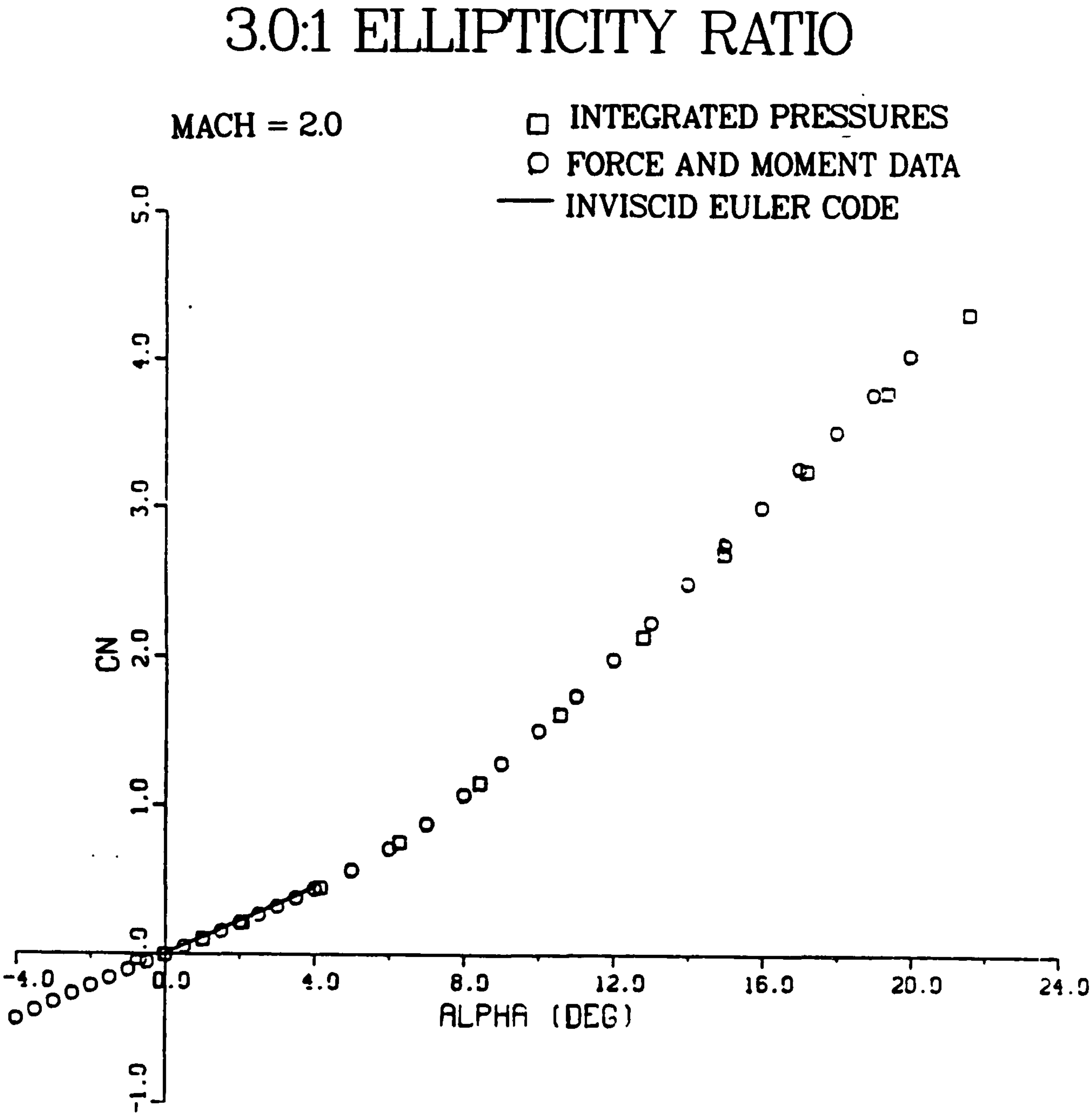

Figure 37. Integrated Pressure Comparisons, M = 2.0

3.0:1 ELLIPTICITY RATIO

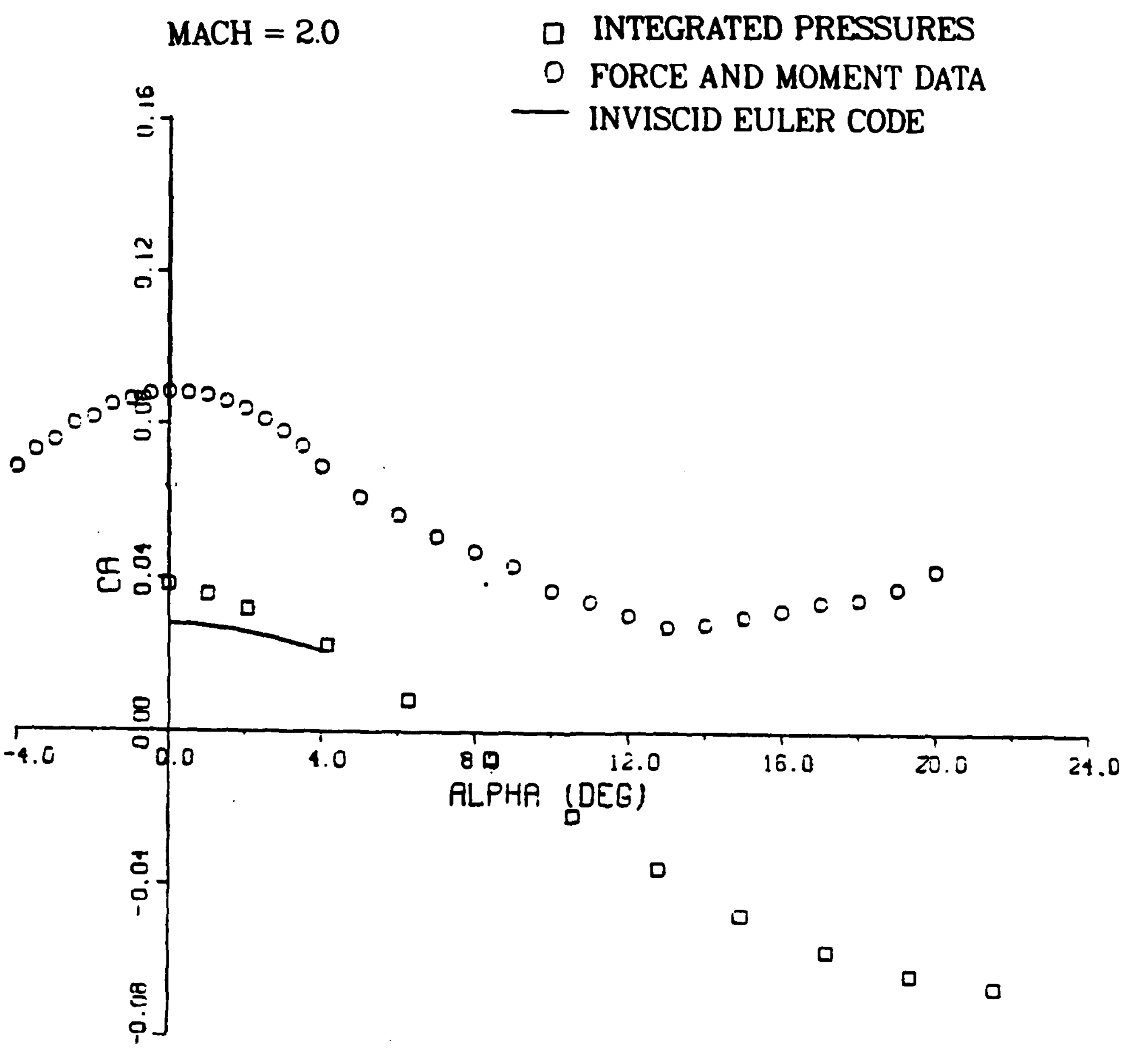

Figure 37. Integrated Pressure Comparisons, M = 2.0 (Continued)

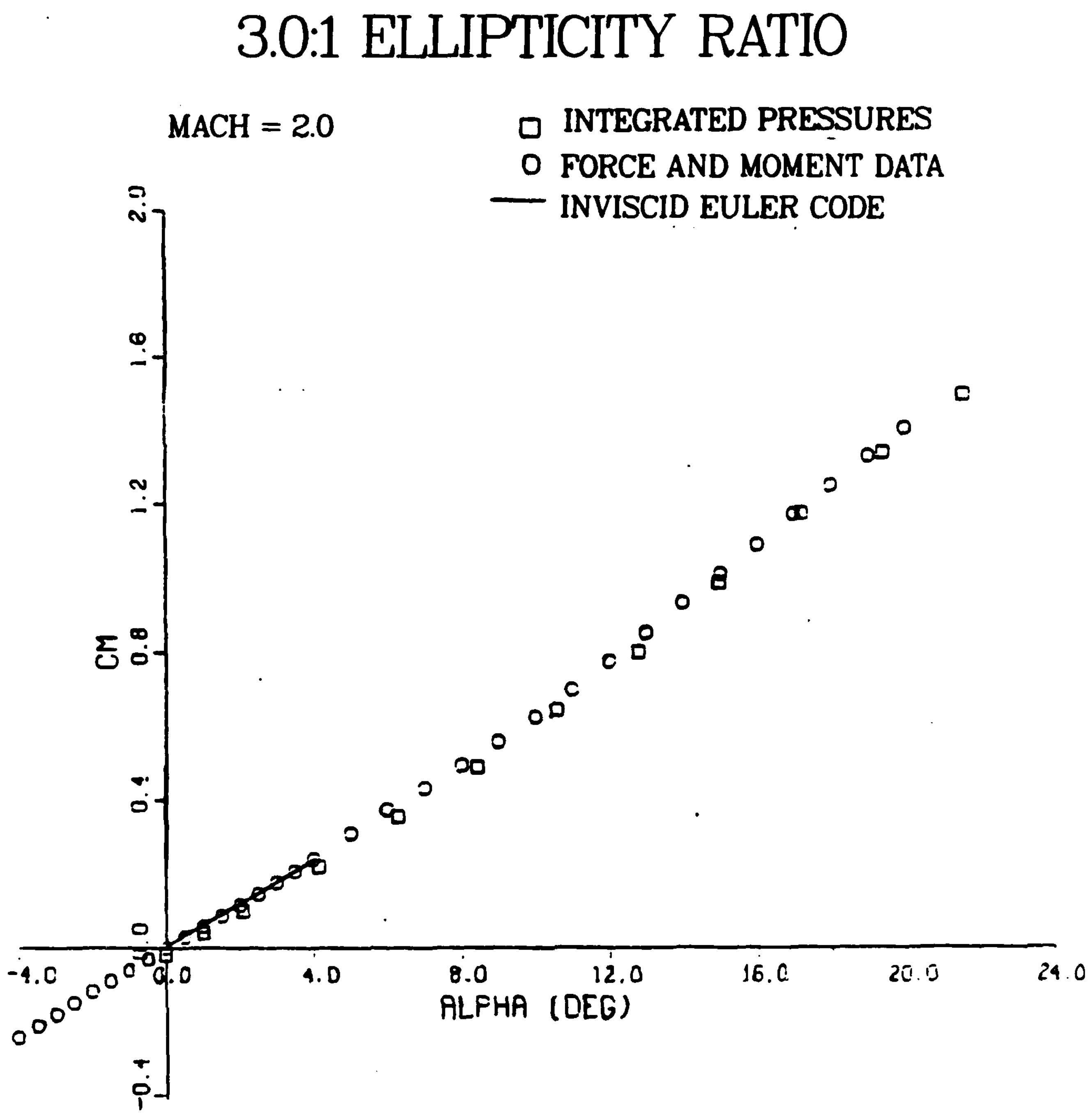

Figure 37. Integrated Pressure Comparisons, M = 2.0 (Concluded)

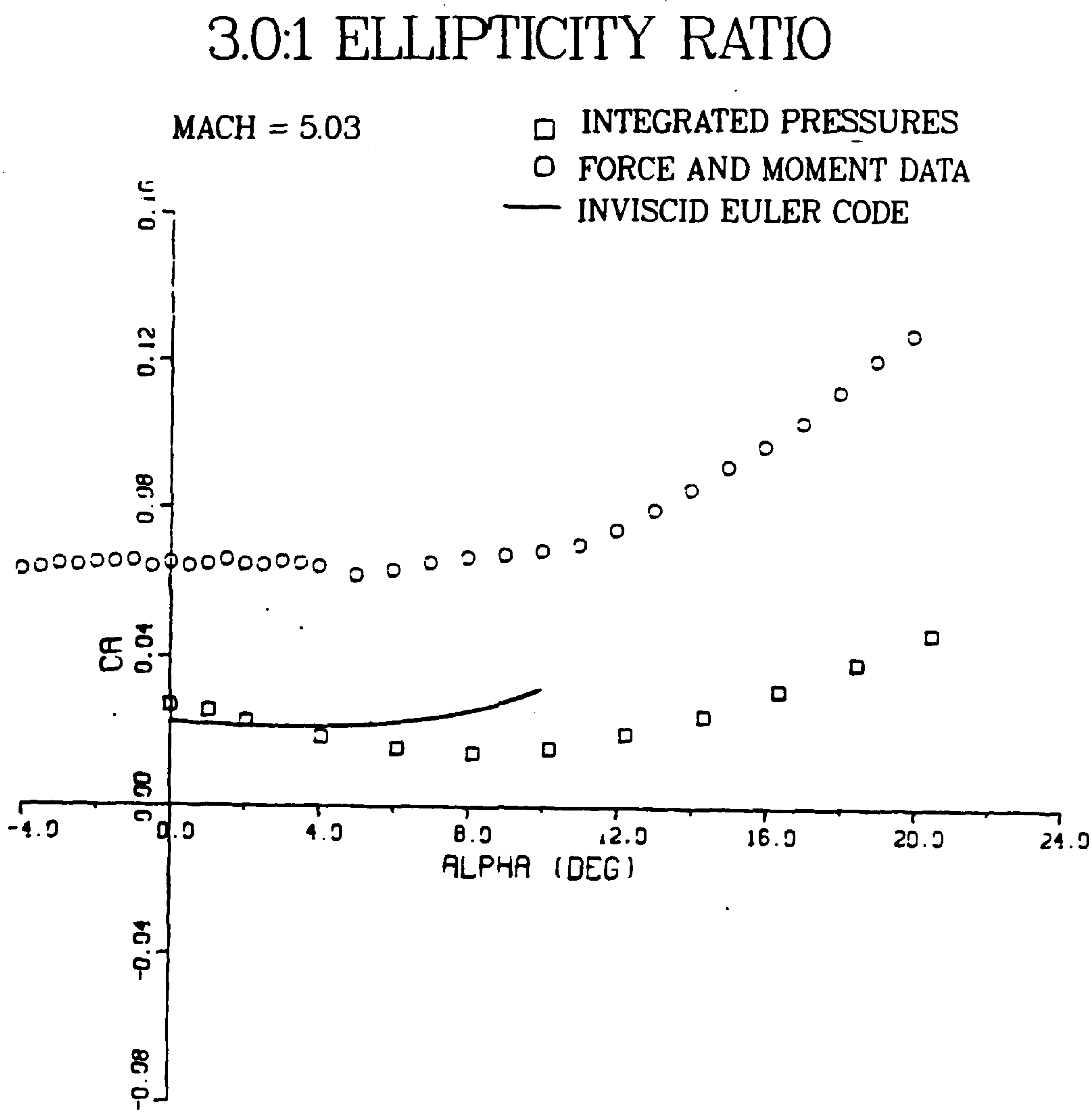

Figure 38. Integrated Pressure Comparisons, M = 5.0

3.0:1 ELLIPTICITY RATIO

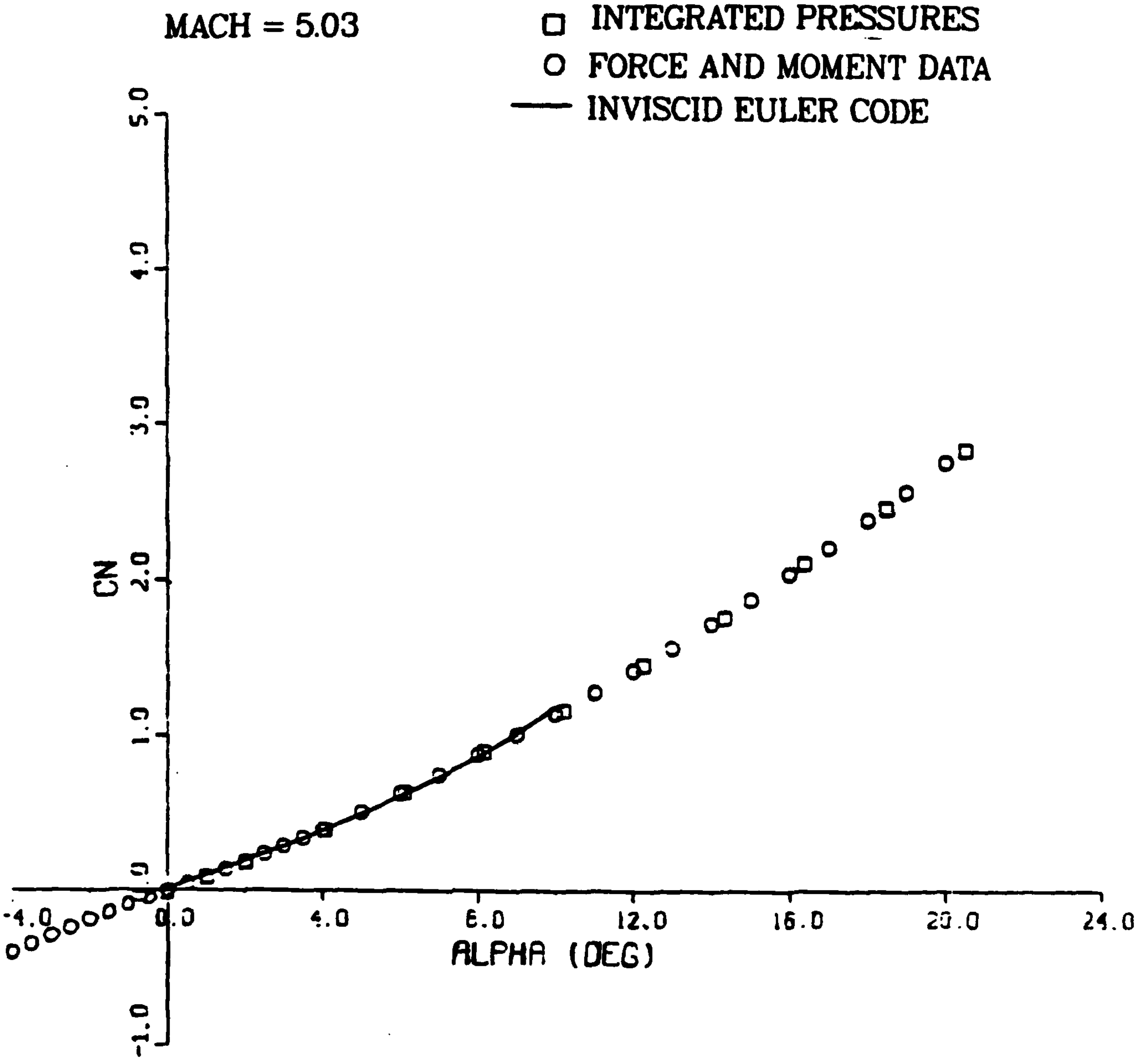

Figure 38. Integrated Pressure Comparisons, M = 5.0 (Continued)

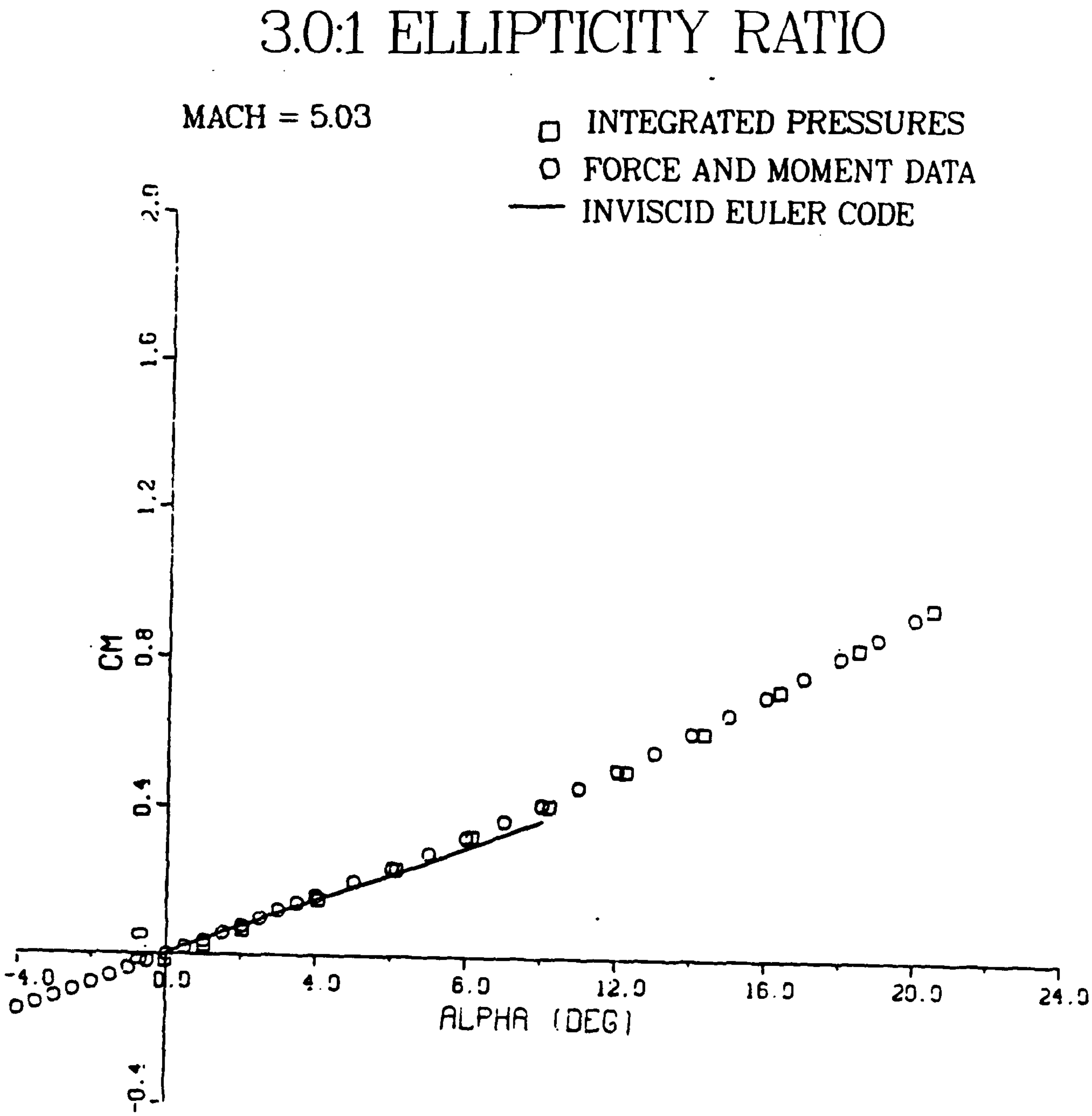

Figure 38. Integrated Pressure Comparisons, M = 5.0 (Concluded)

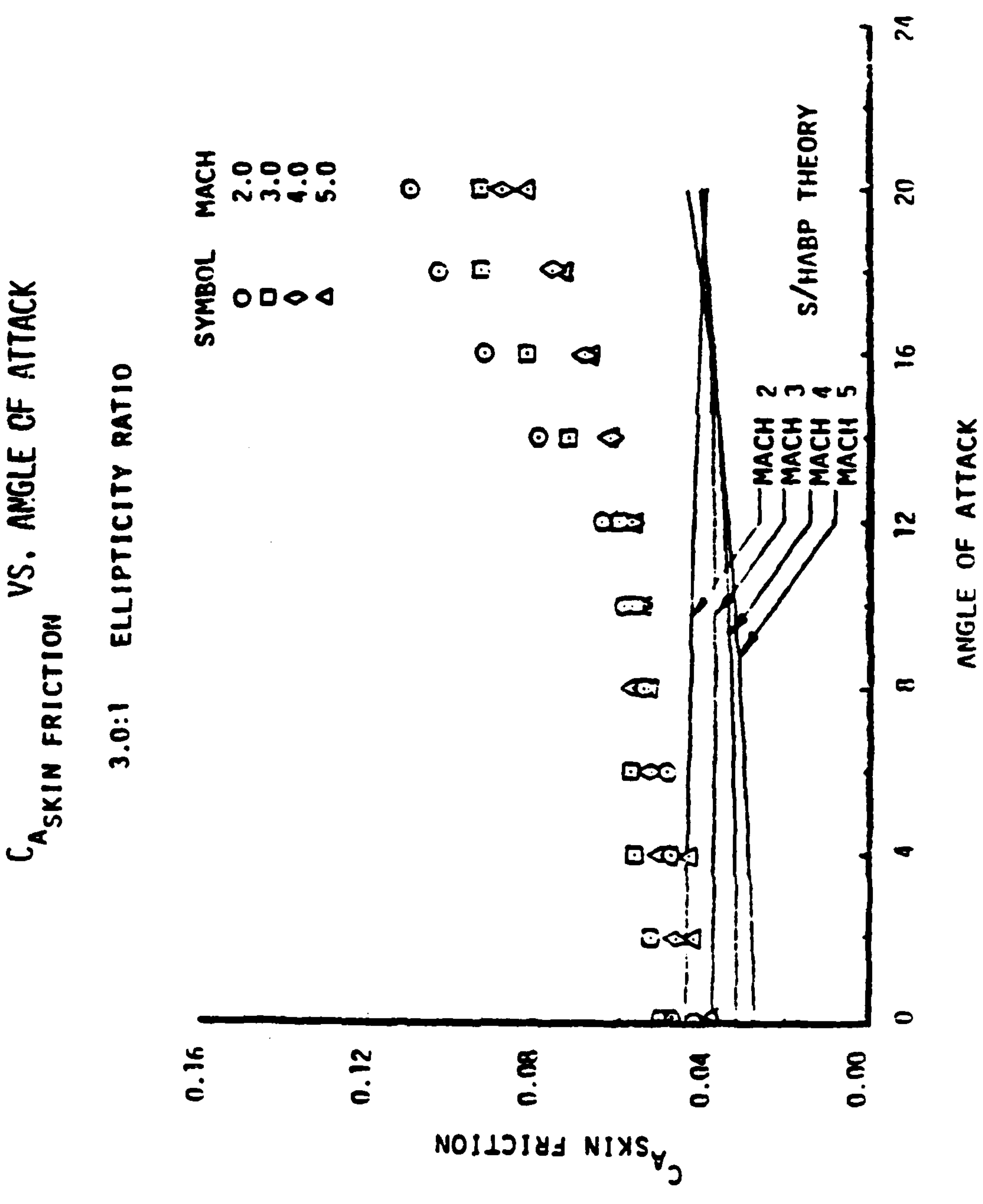

Figure 39. Skin Friction Coefficient vs. Angle Of Attack

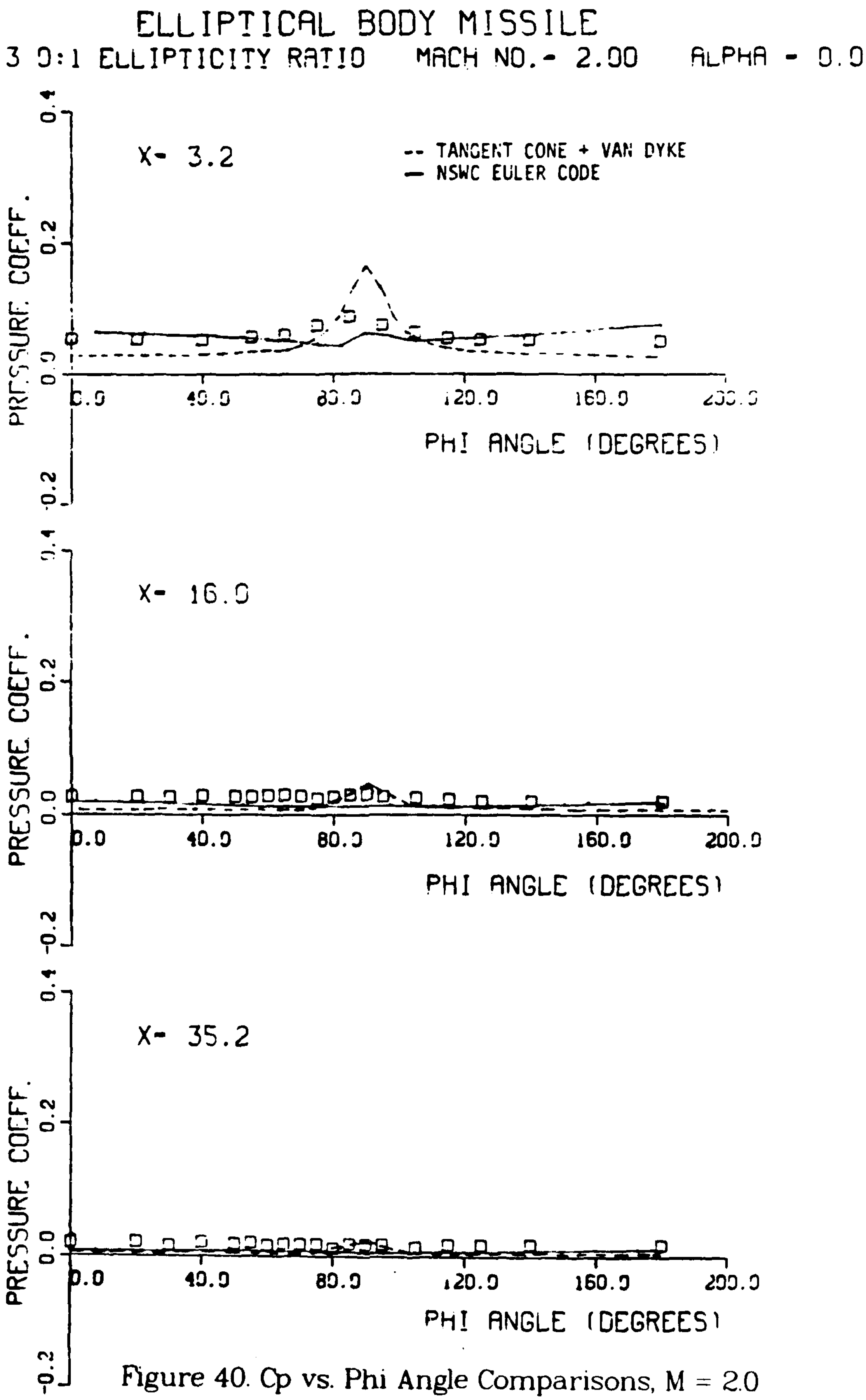

Figure 40. Cp vs. Phi Angle Comparisons, M = 2.0

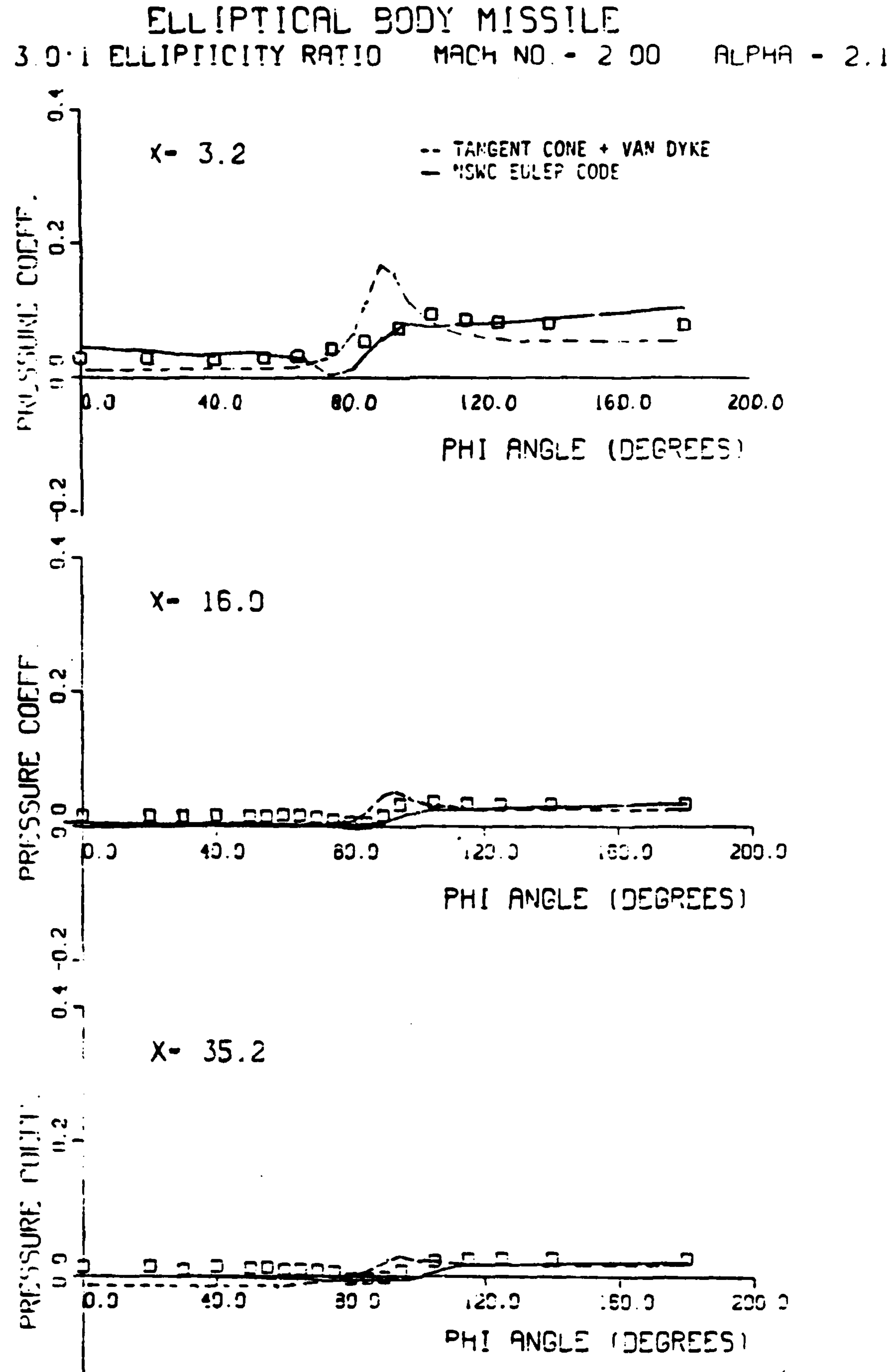

Figure 40. Cp vs. Phi Angle Comparisons, M = 2.0 (Continued)

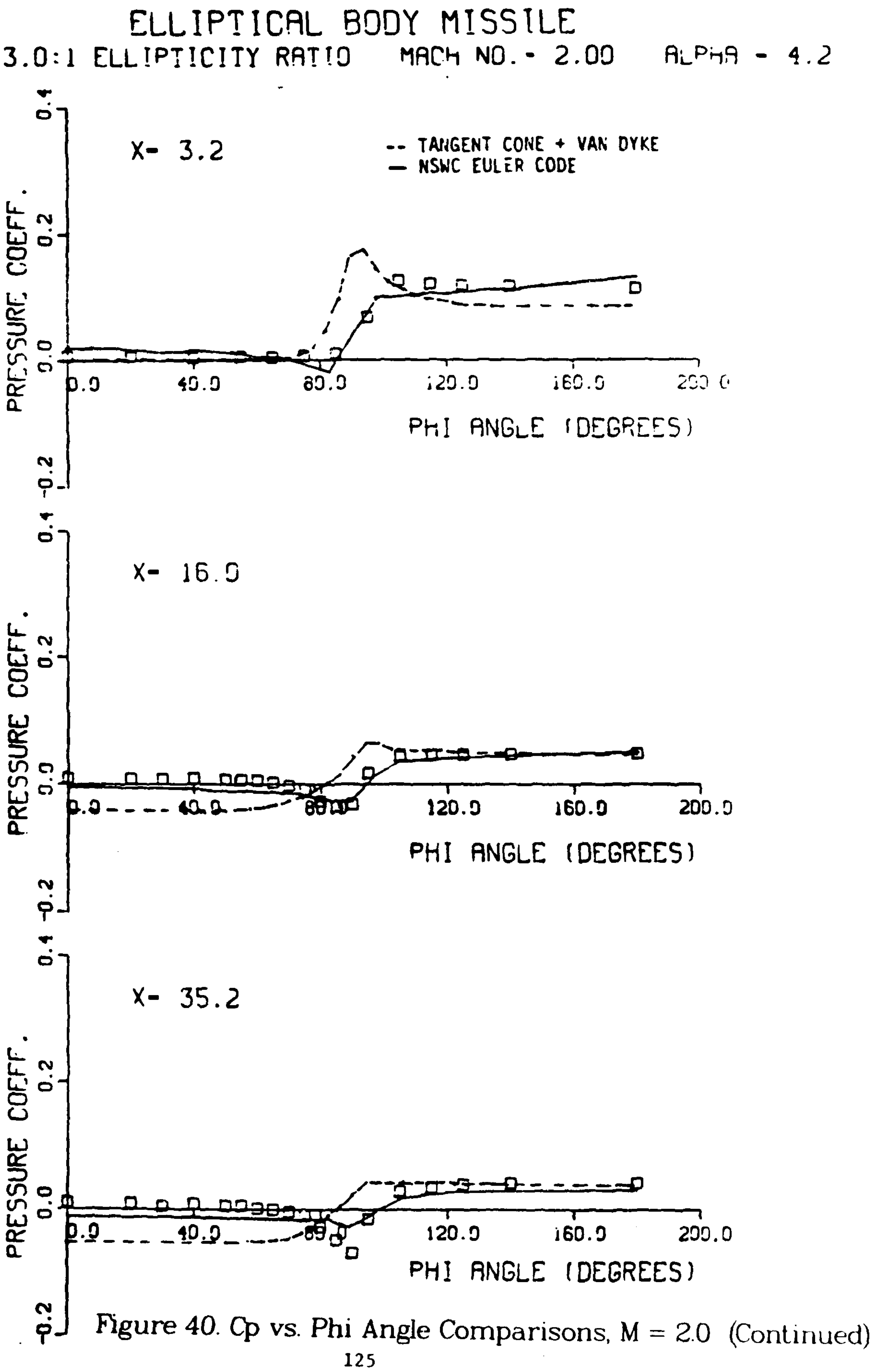

Figure 40. Cp vs. Phi Angle Comparisons, M = 2.0 (Continued)

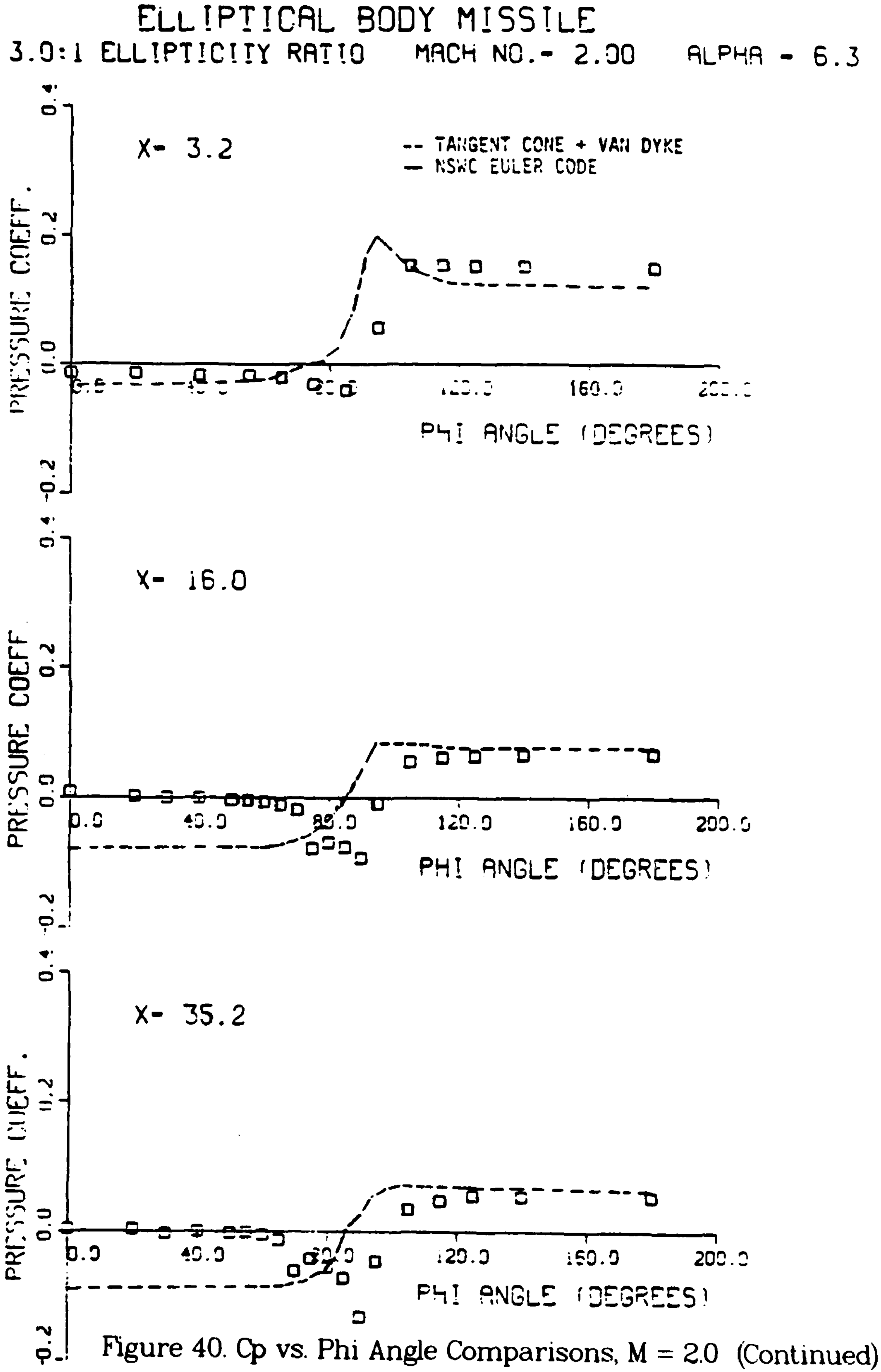

Figure 40. Cp vs. Phi Angle Comparisons, M = 2.0 (Continued)

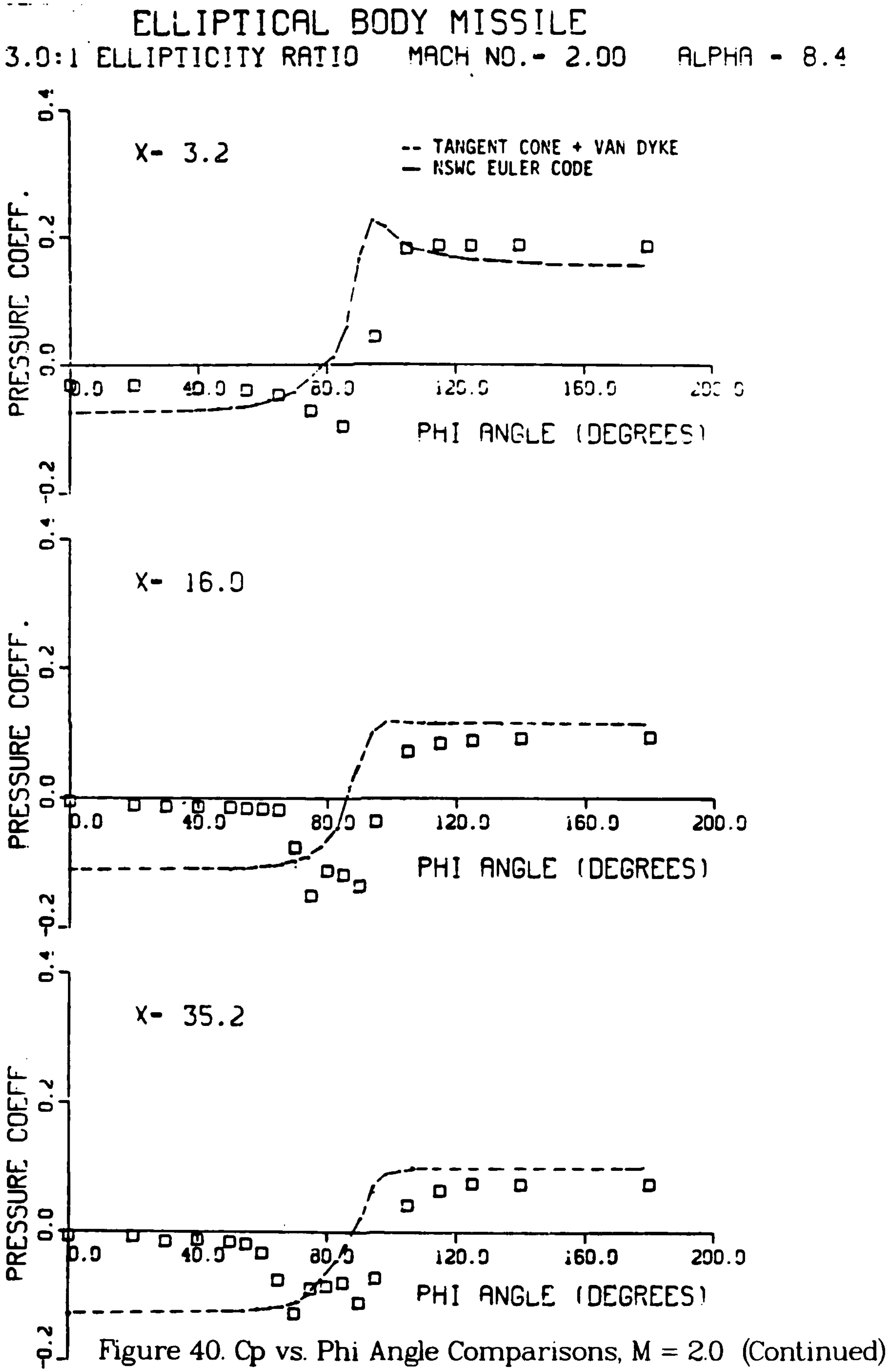

Figure 40. Cp vs. Phi Angle Comparisons, M = 2.0 (Continued)

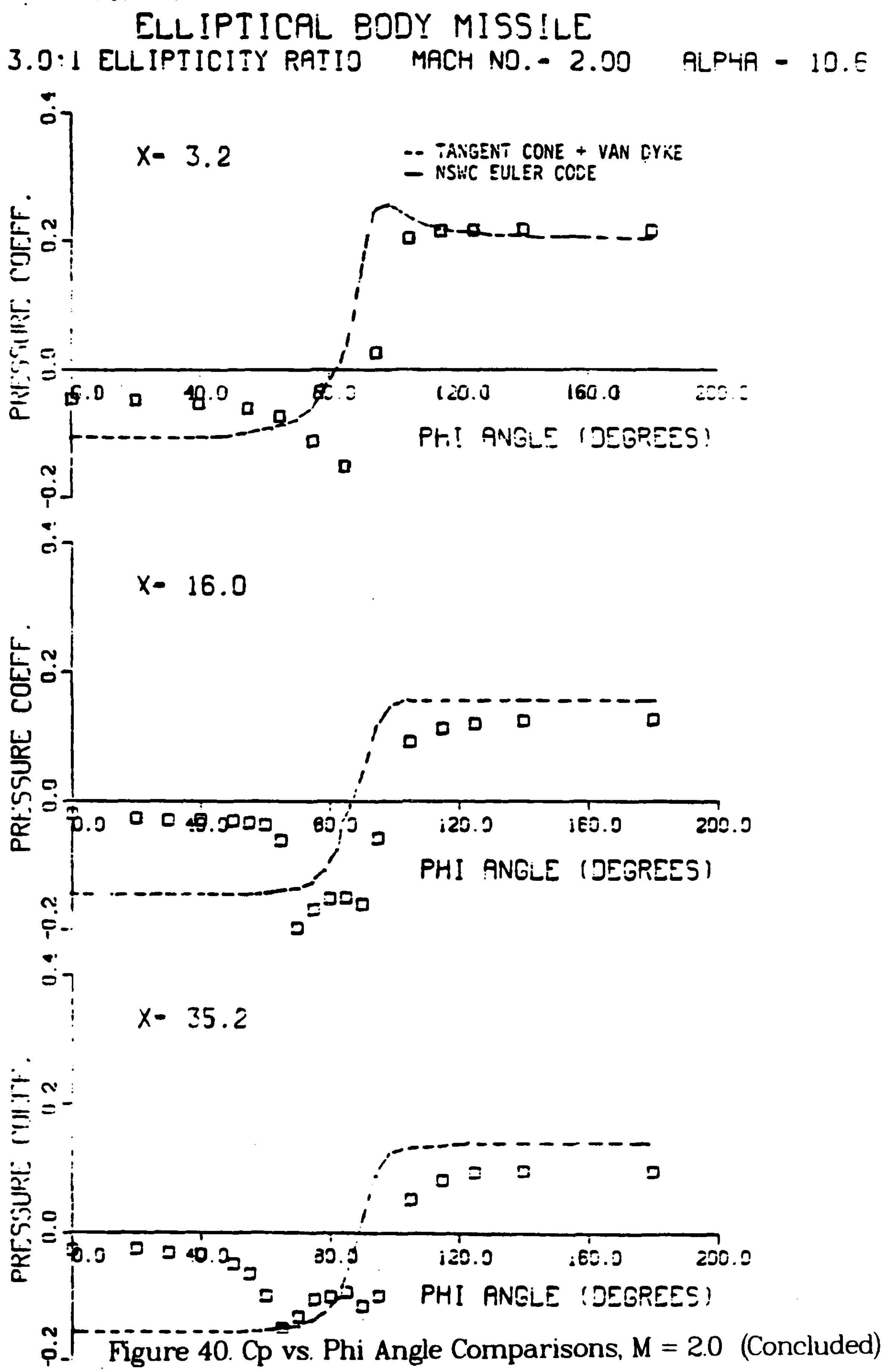

Figure 40. Cp vs. Phi Angle Comparisons, M = 2.0 (Concluded)

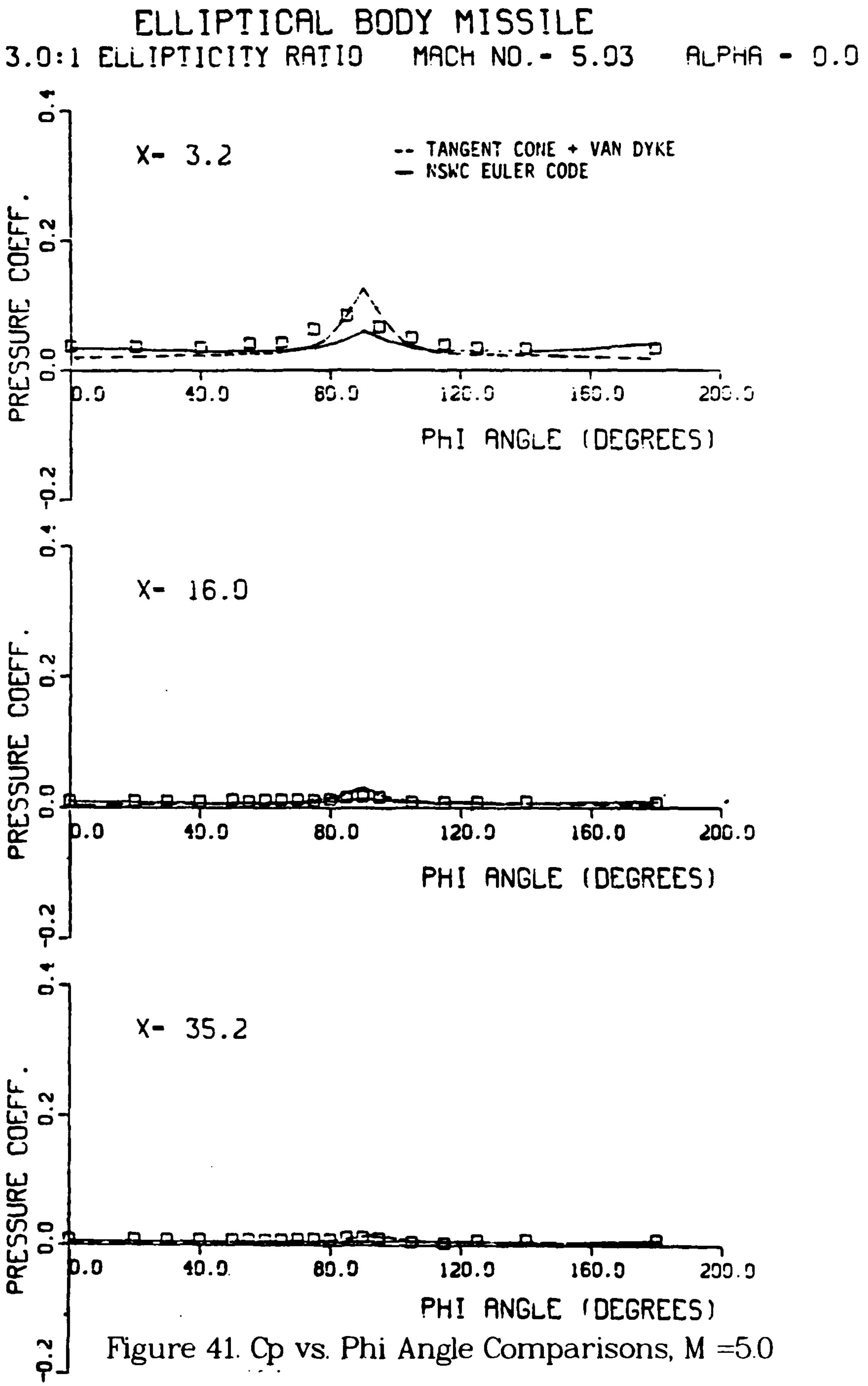

Figure 41. Cp vs. Phi Angle Comparisons, M =5.0

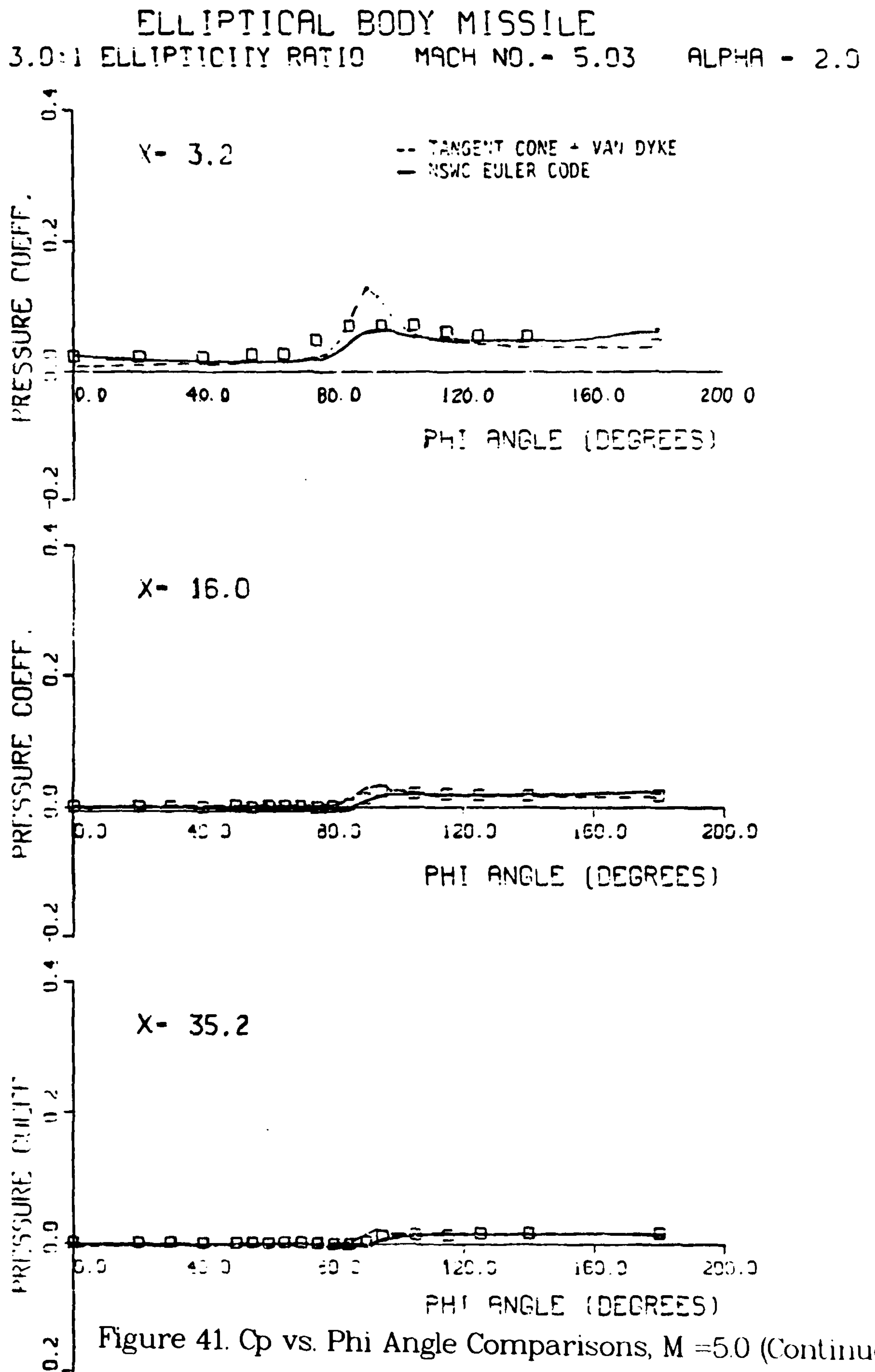

Figure 41. Cp vs. Phi Angle Comparisons, M =5.0 (Continued)

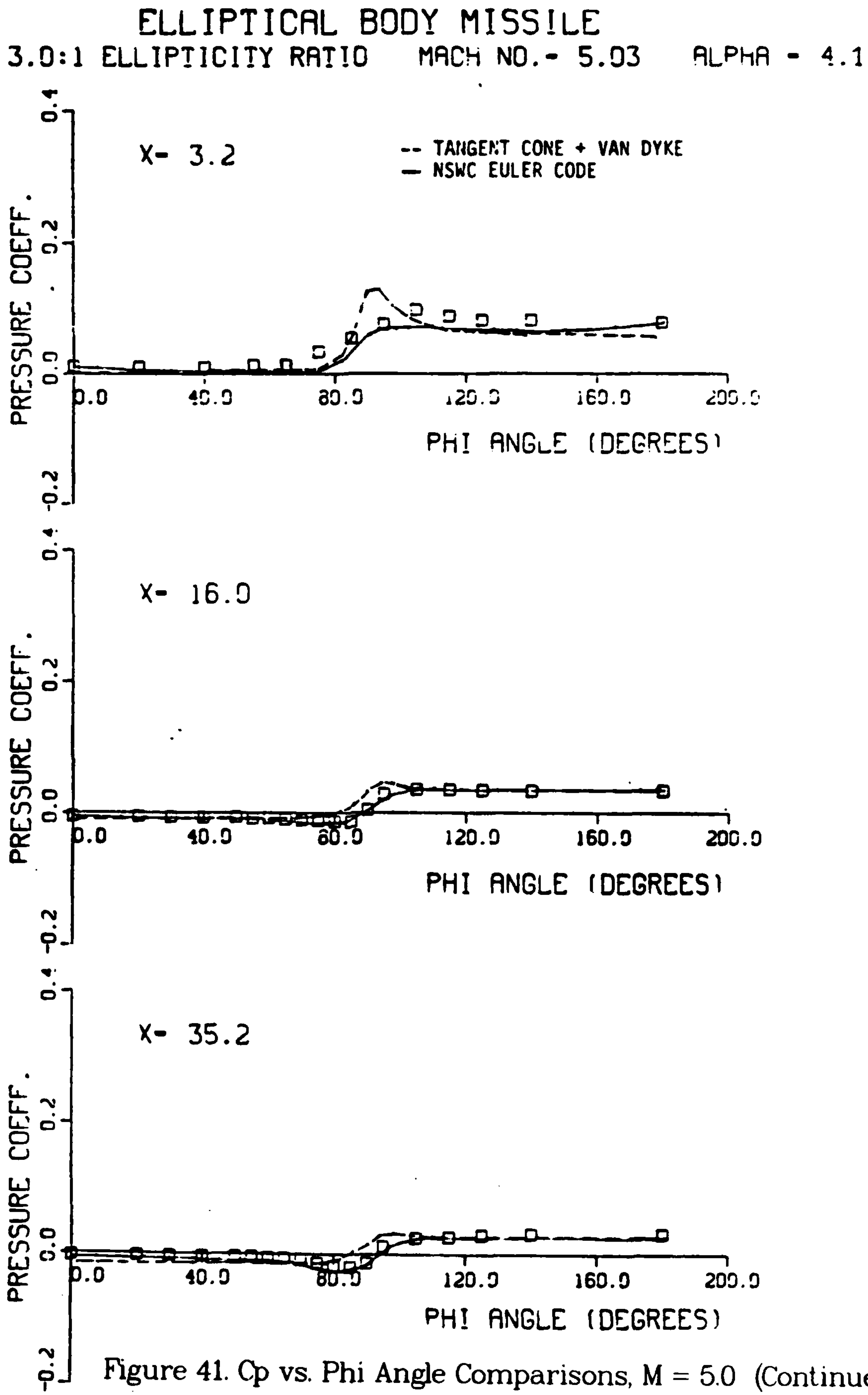

Figure 41. Cp vs. Phi Angle Comparisons, M = 5.0 (Continued)

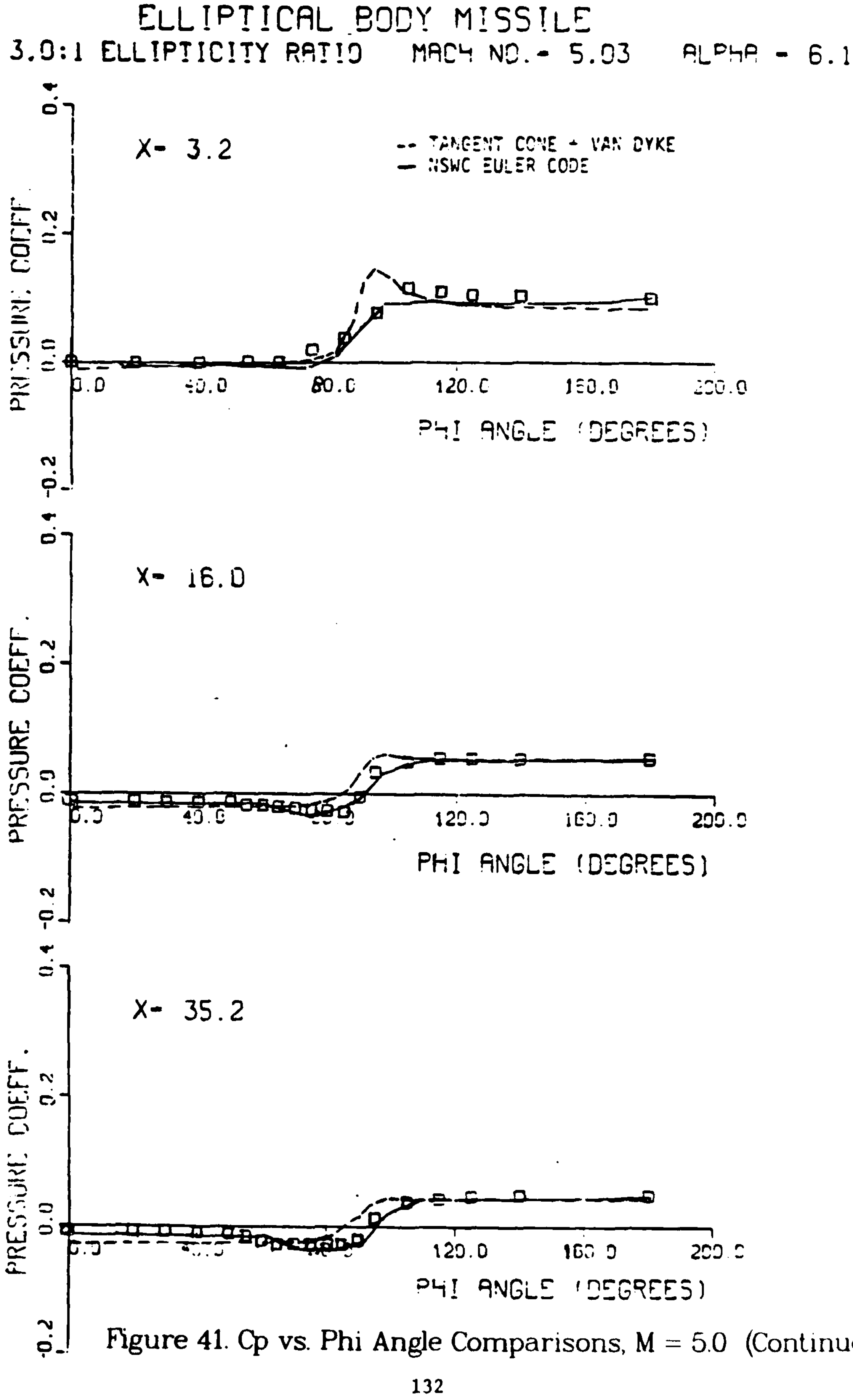

Figure 41. Cp vs. Phi Angle Comparisons, M = 5.0 (Continued)

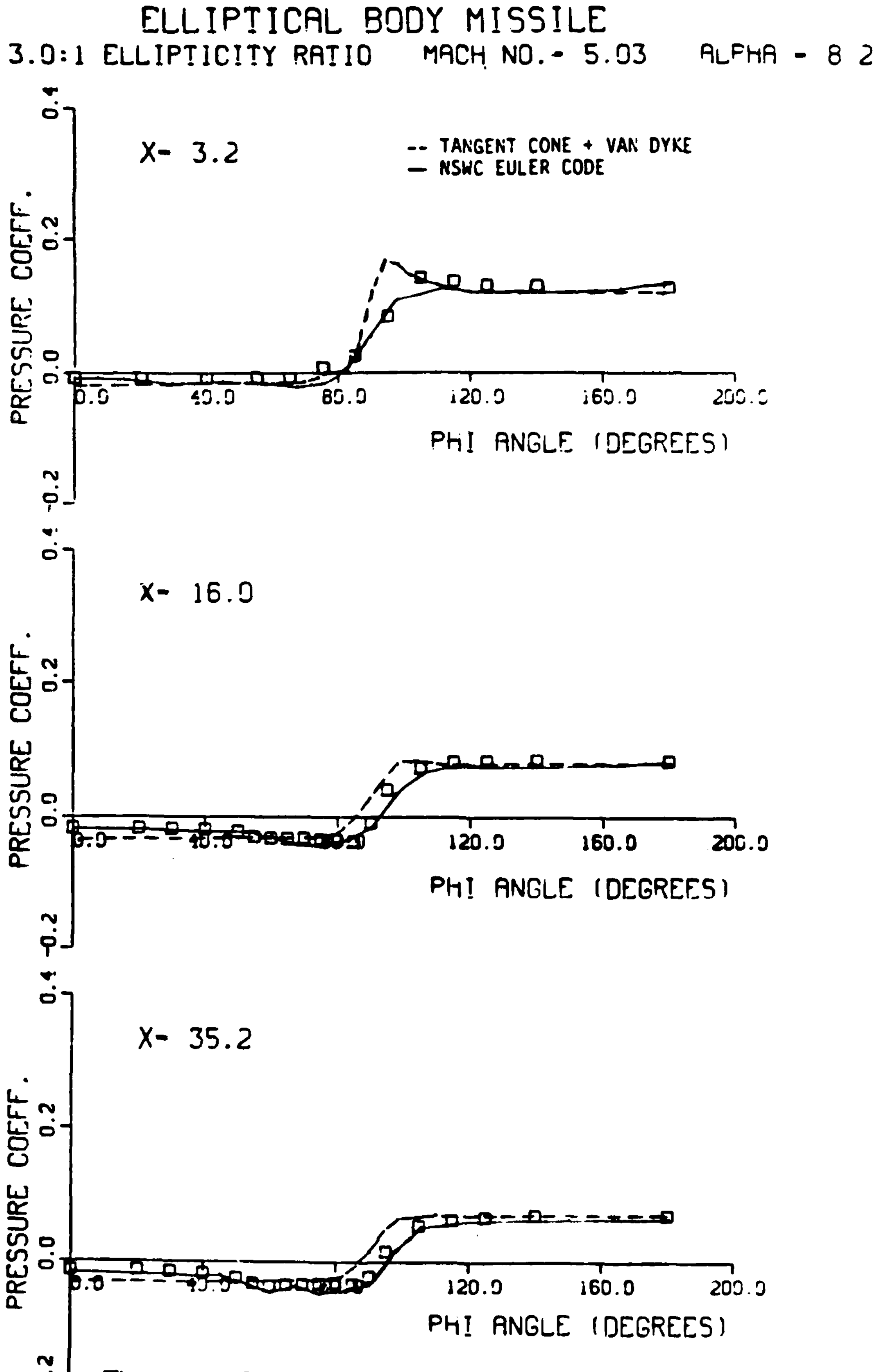

Figure 41. Cp vs. Phi Angle Comparisons, M = 5.0 (Continued)

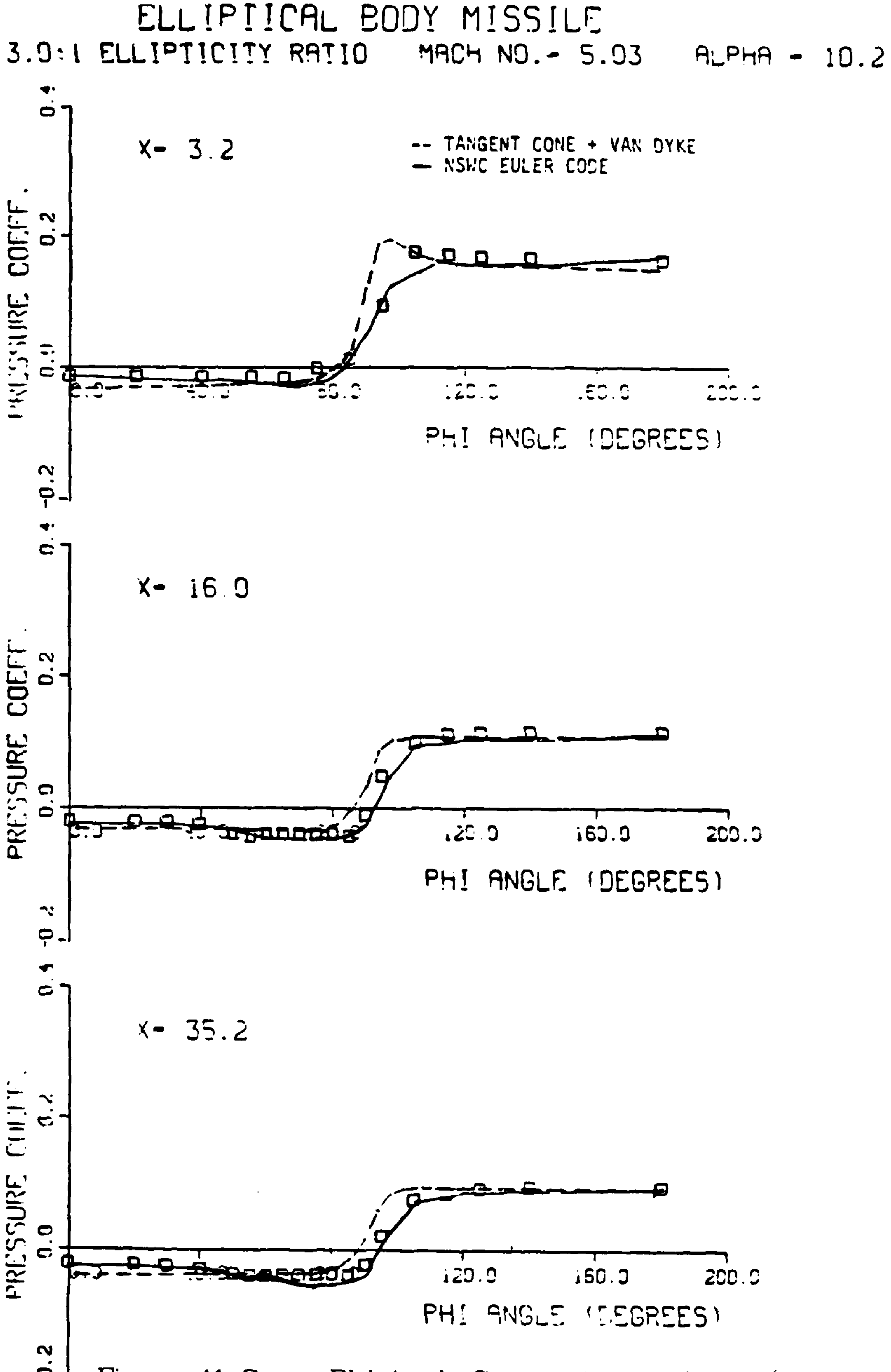

Figure 41. Cp vs. Phi Angle Comparisons, M =5.0 (Concluded)

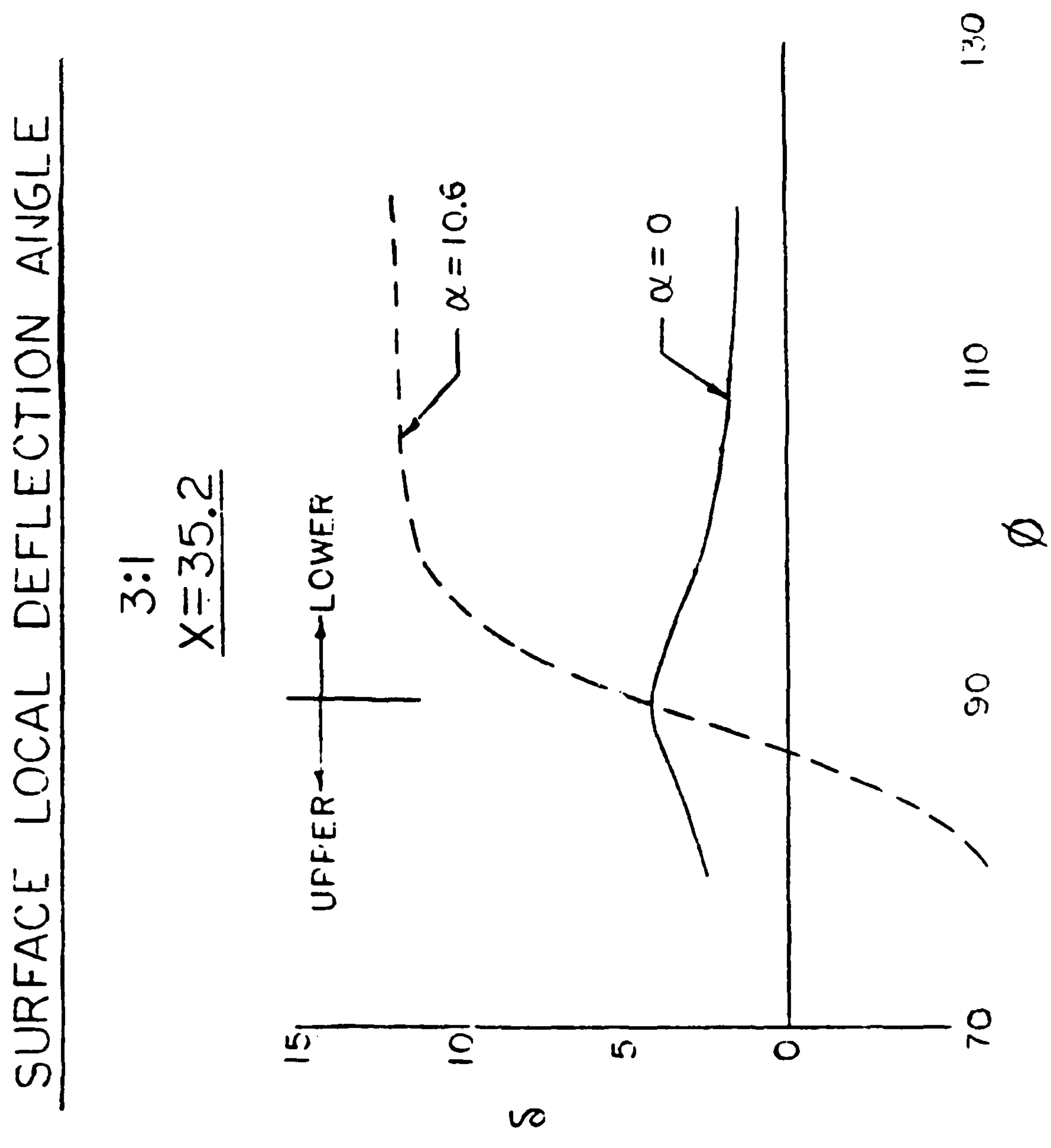

Figure 42. Local Deflection Angle vs. Phi Angle

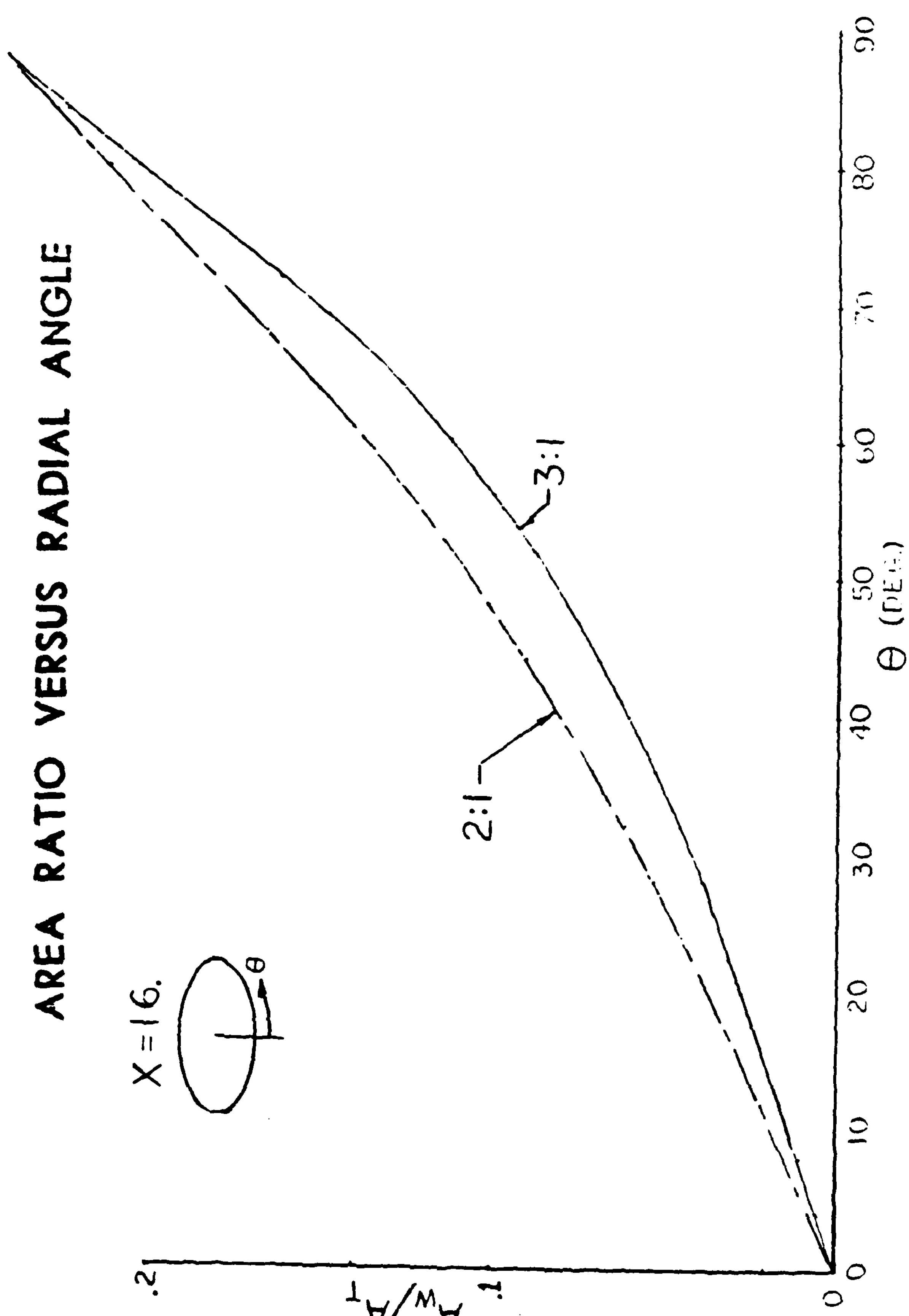

Figure 43. Area Ratio vs. Radial Angle

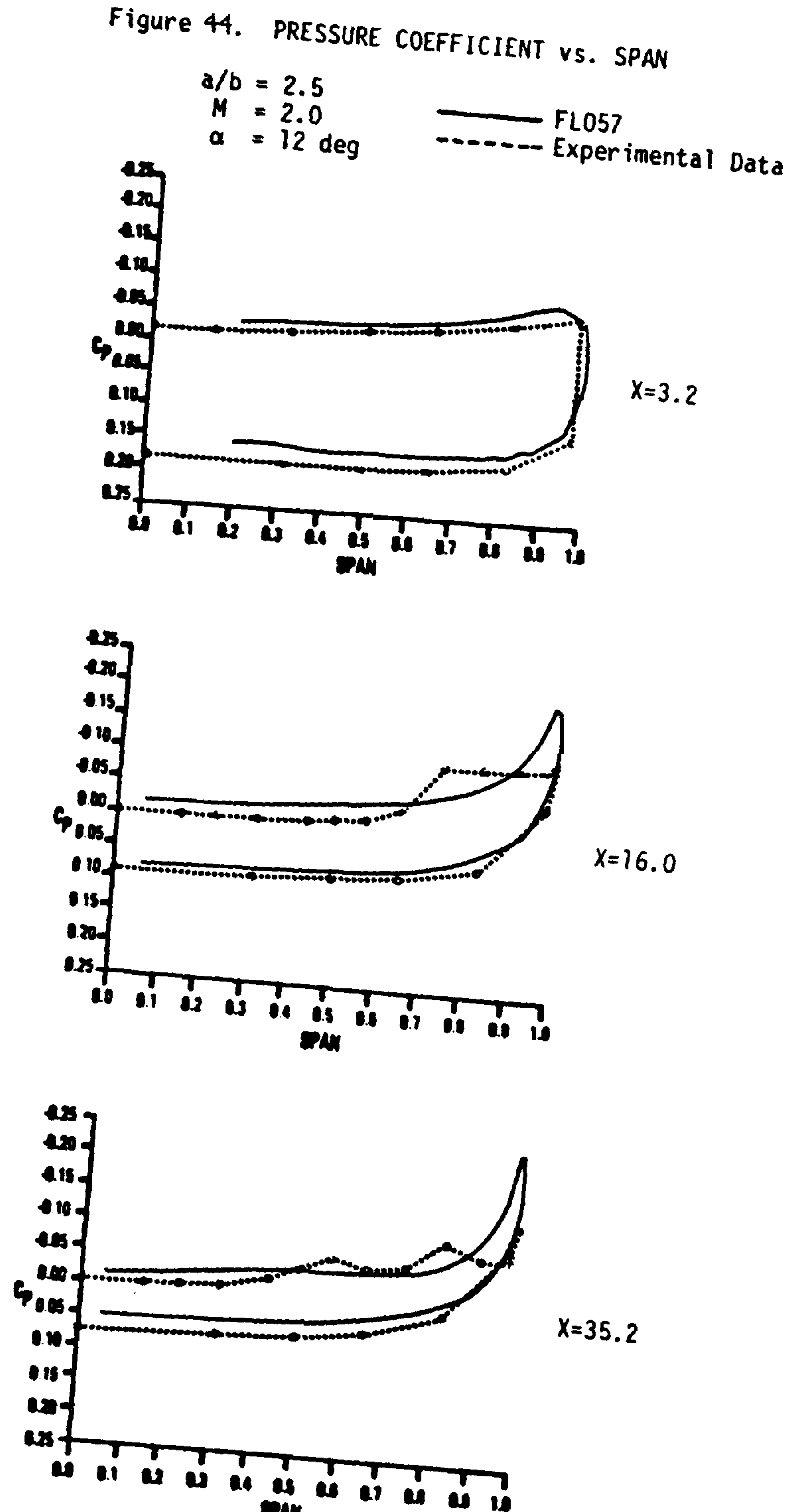

Figure 44. FLO57 Comparisons – Cp vs. Span

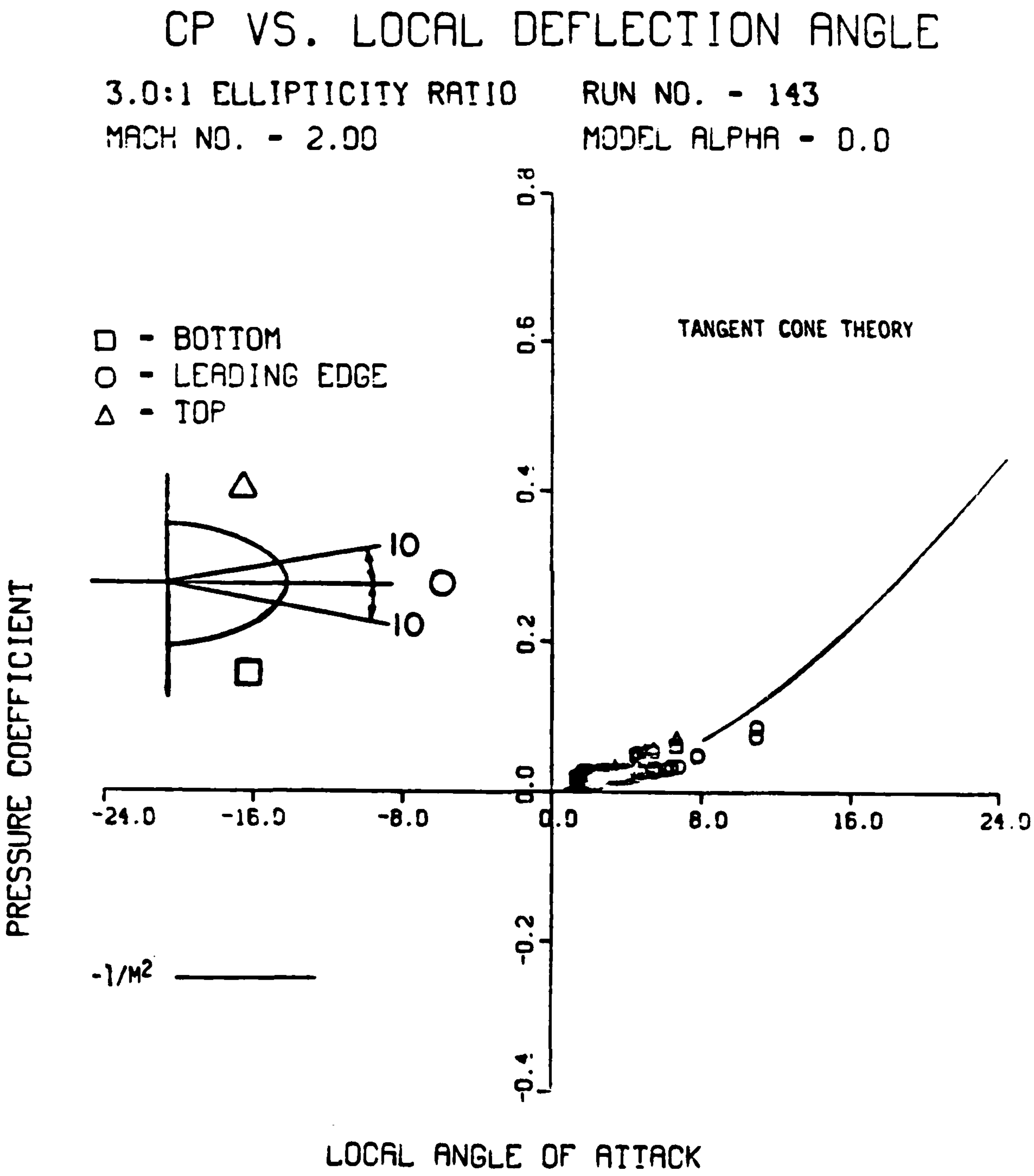

Figure 45. Cp vs. Local Deflection Angle, M = 2.0

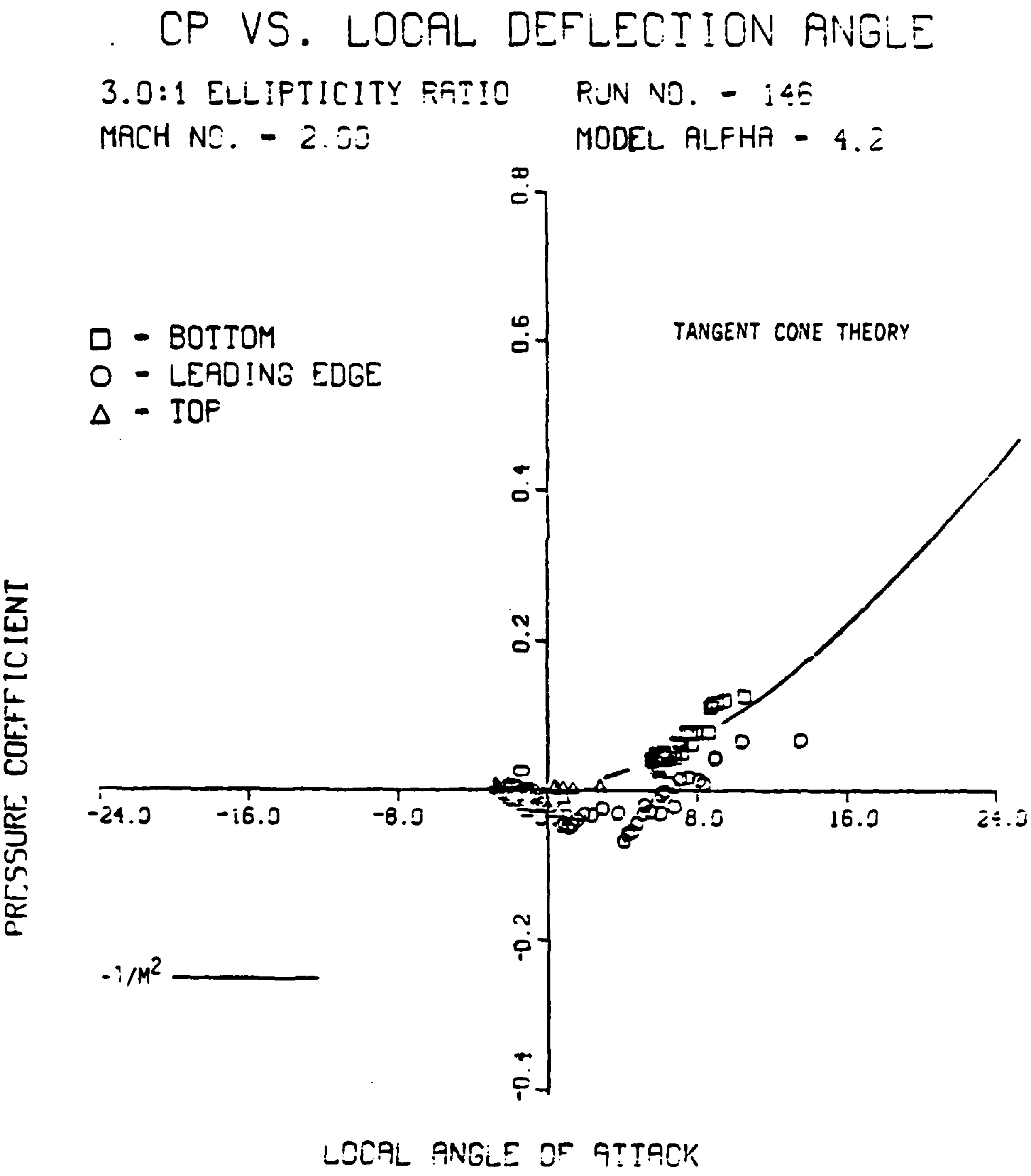

Figure 45. Cp vs. Local Deflection Angle, M = 2.0 (Continued)

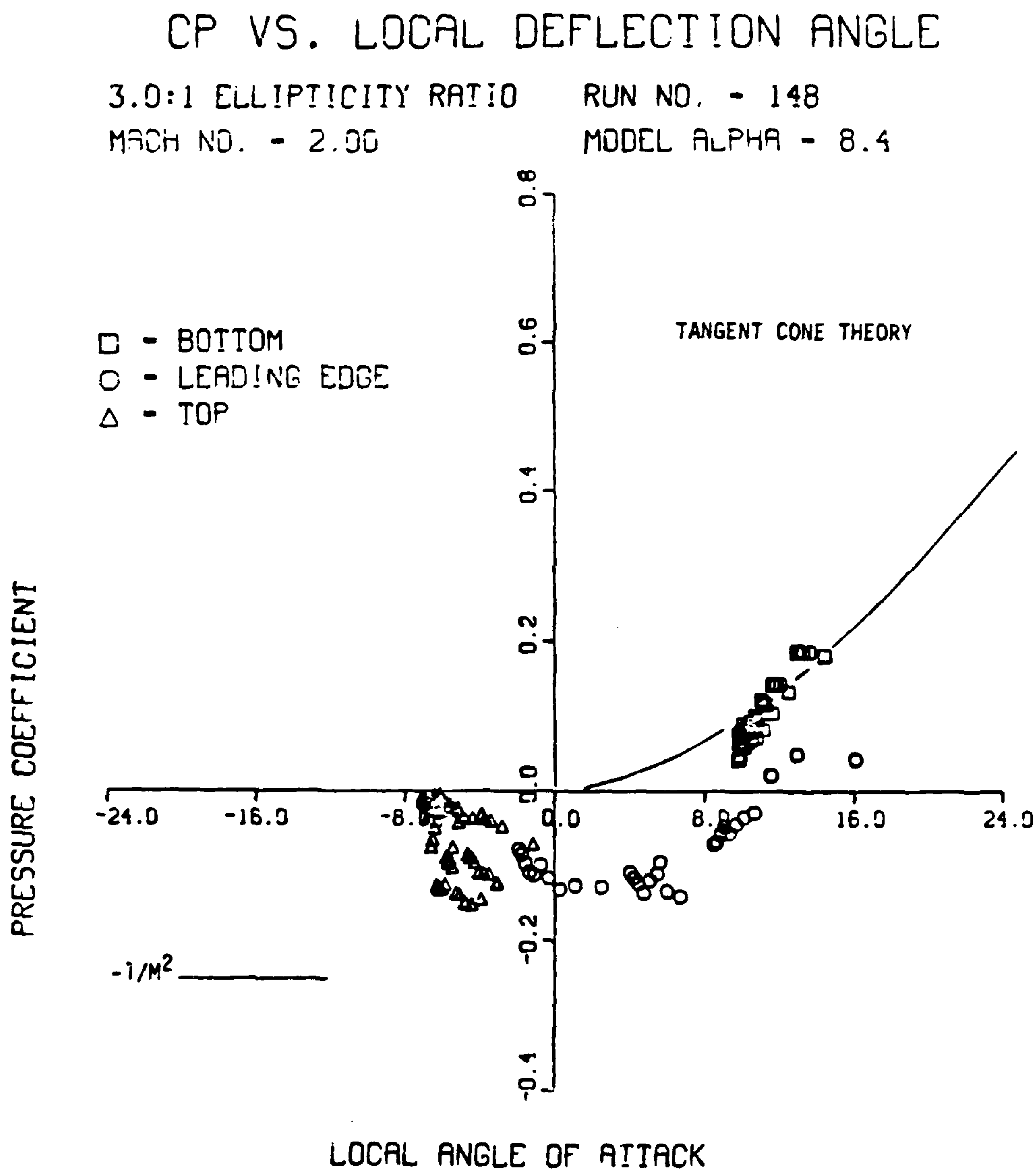

Figure 45. Cp vs. Local Deflection Angle, M = 2.0 (Continued)

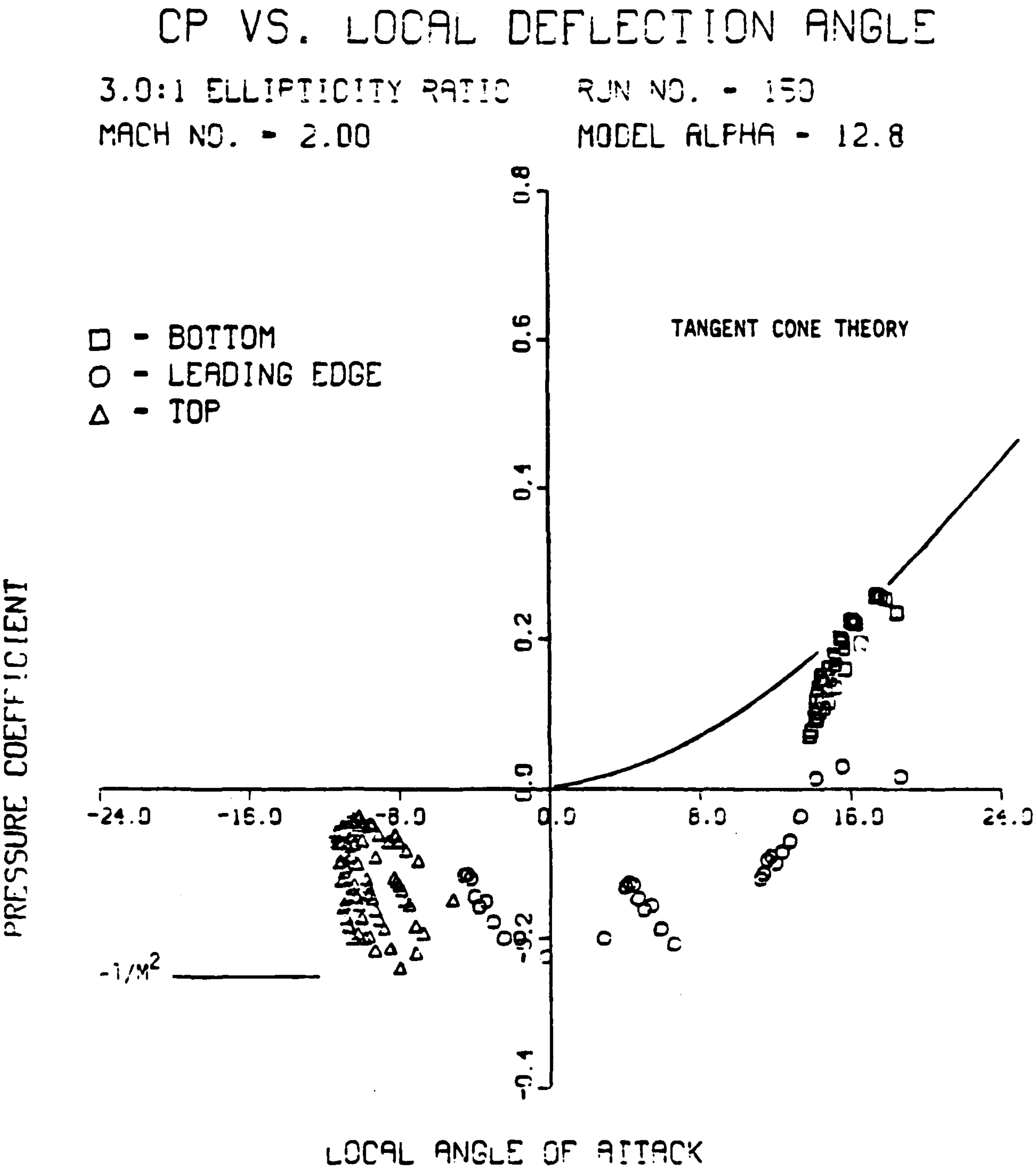

Figure 45. Cp vs. Local Deflection Angle, M = 2.0 (Continued)

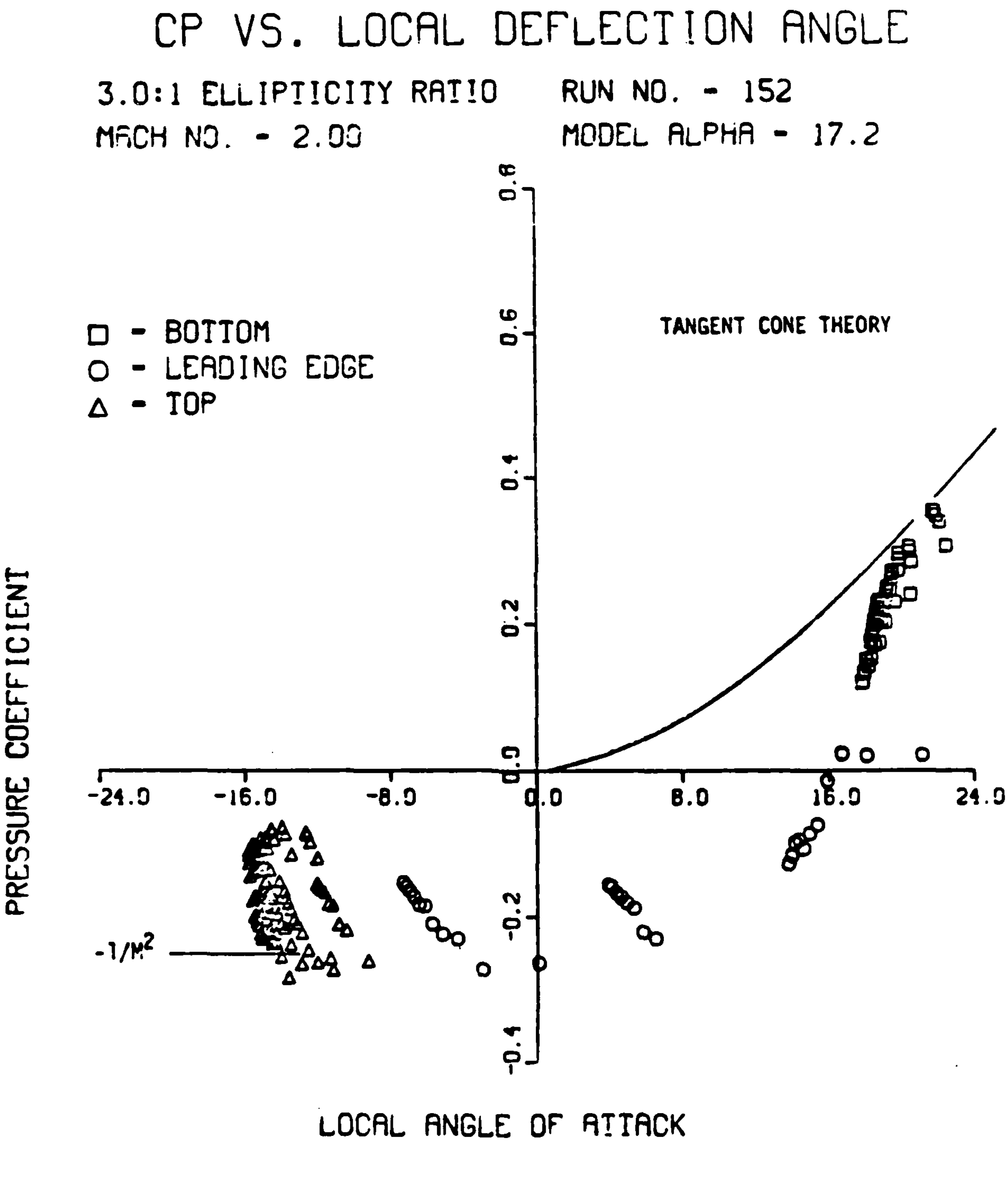

Figure 45. Cp vs. Local Deflection Angle, M = 2.0 (Continued)

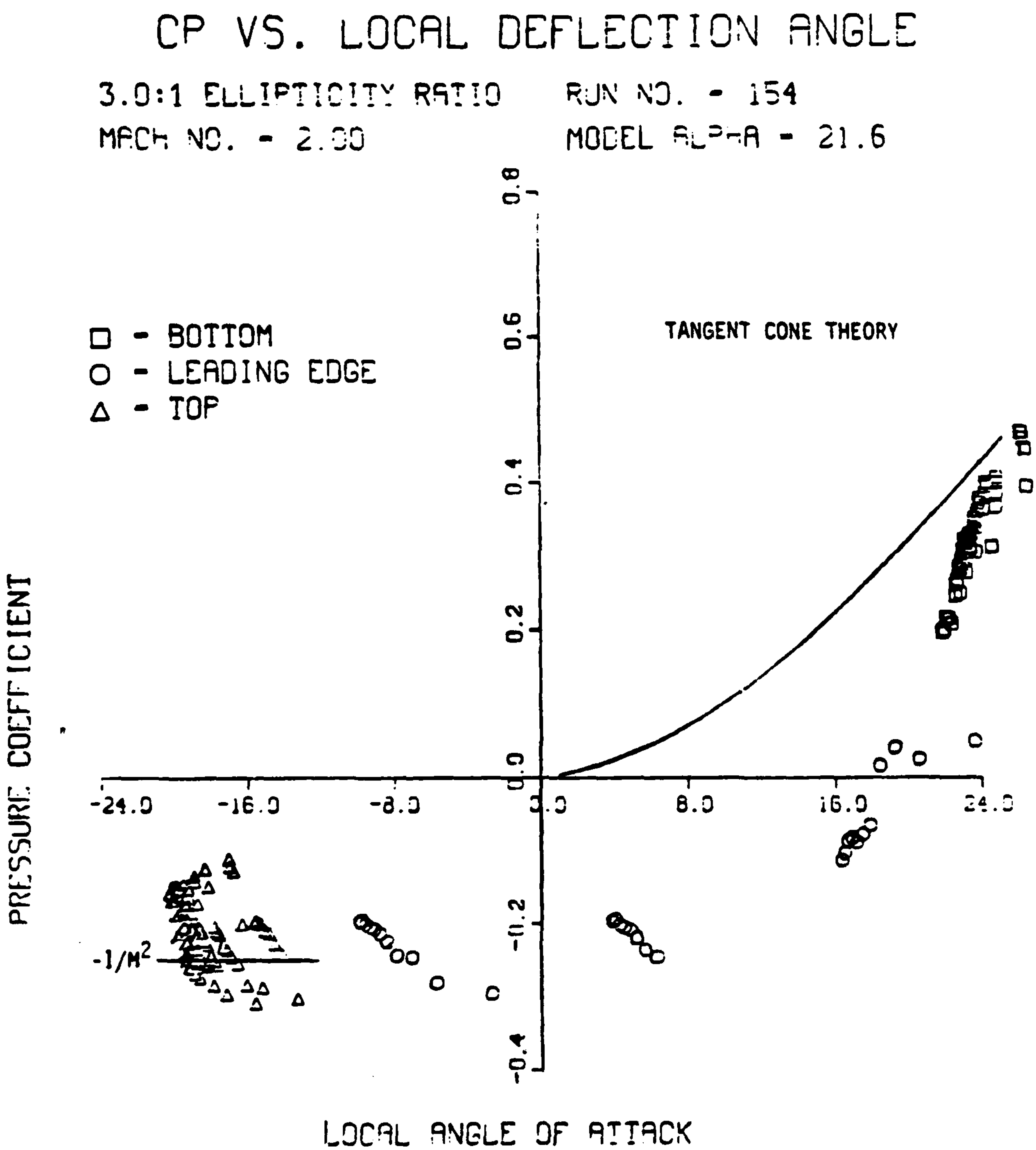

Figure 45. Cp vs. Local Deflection Angle, M = 2.0 (Concluded)

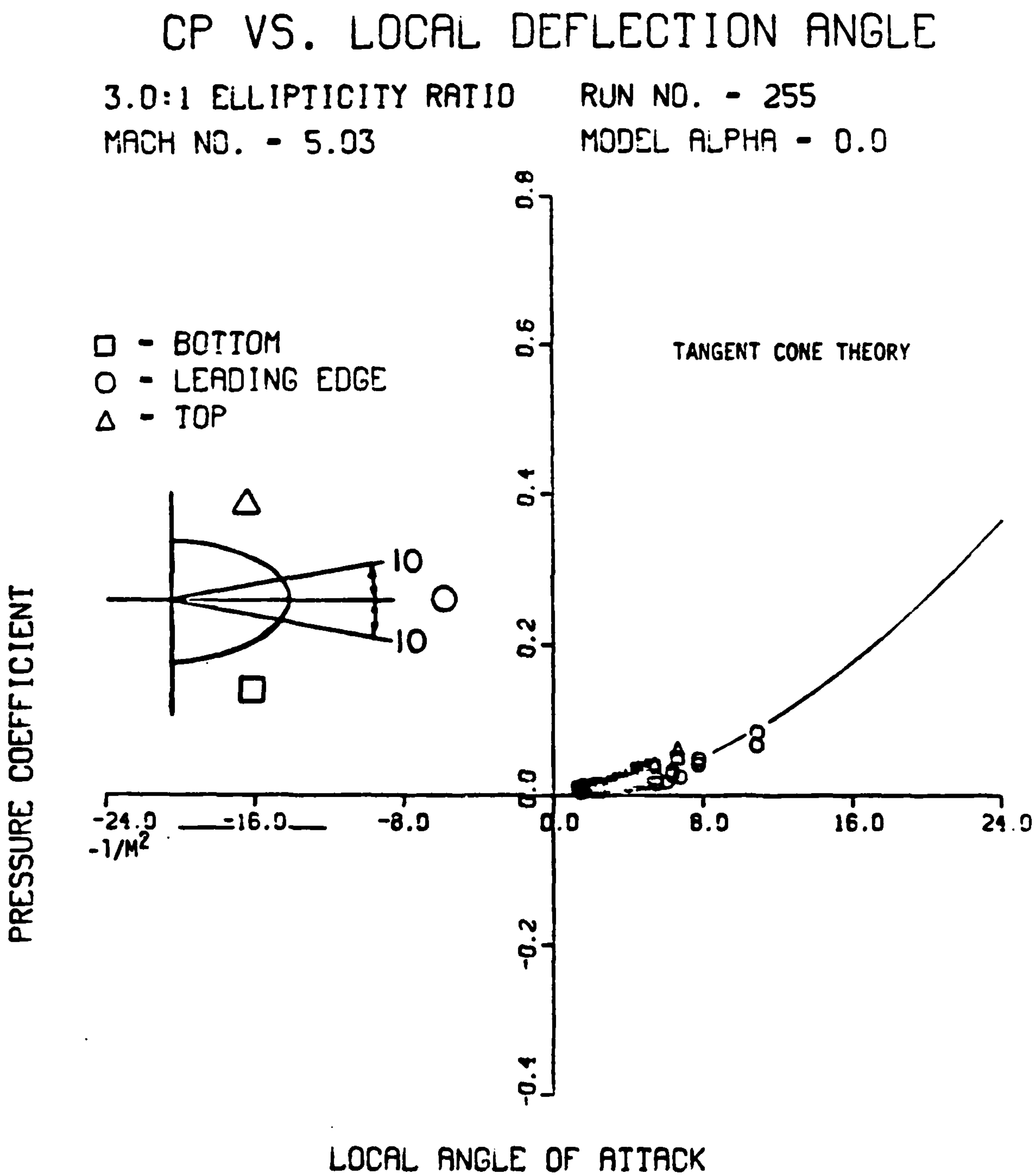

Figure 46. Cp vs. Local Deflection Angle, M = 5.0

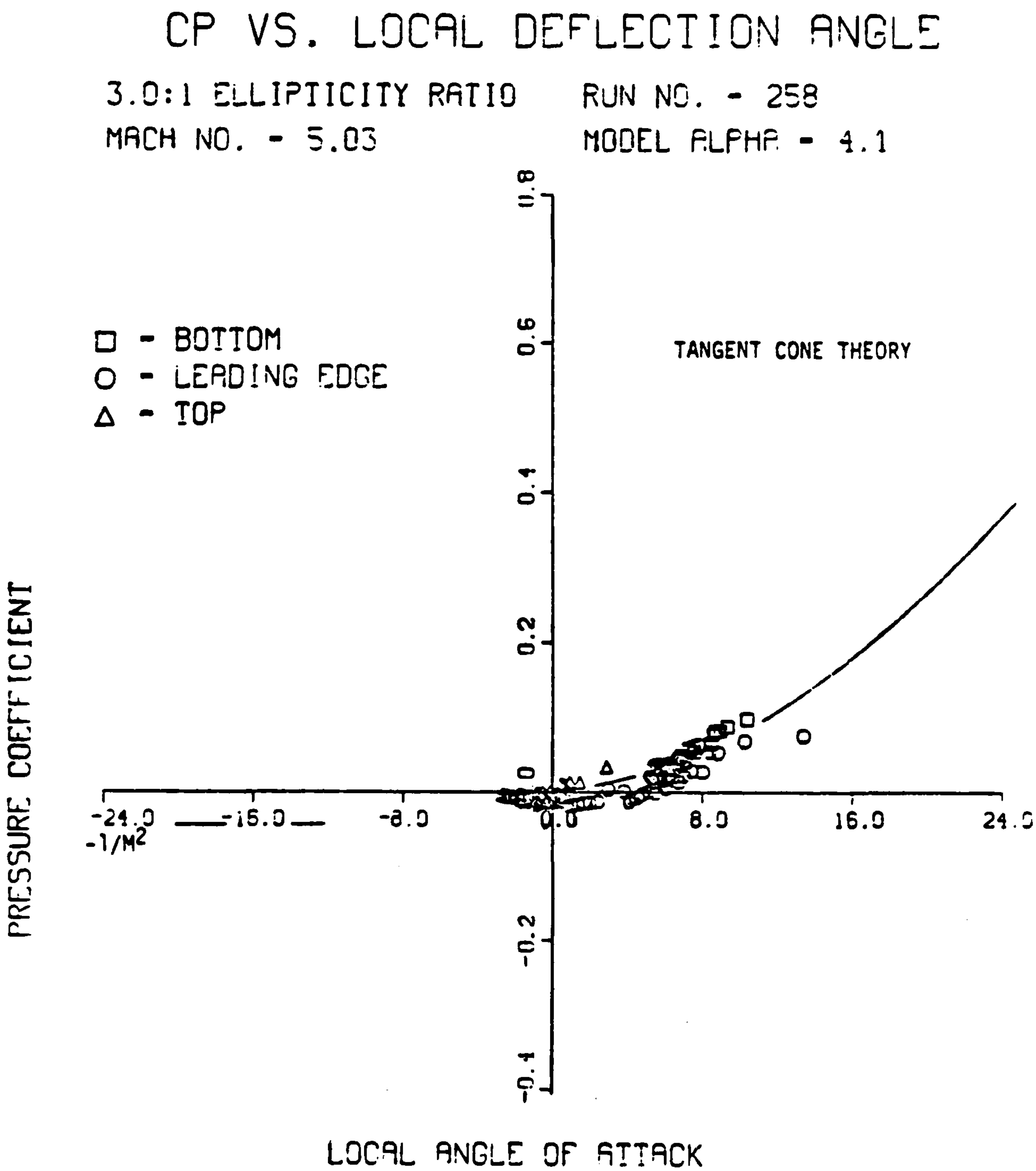

Figure 46. Cp vs. Local Deflection Angle, M = 5.0 (Continued)

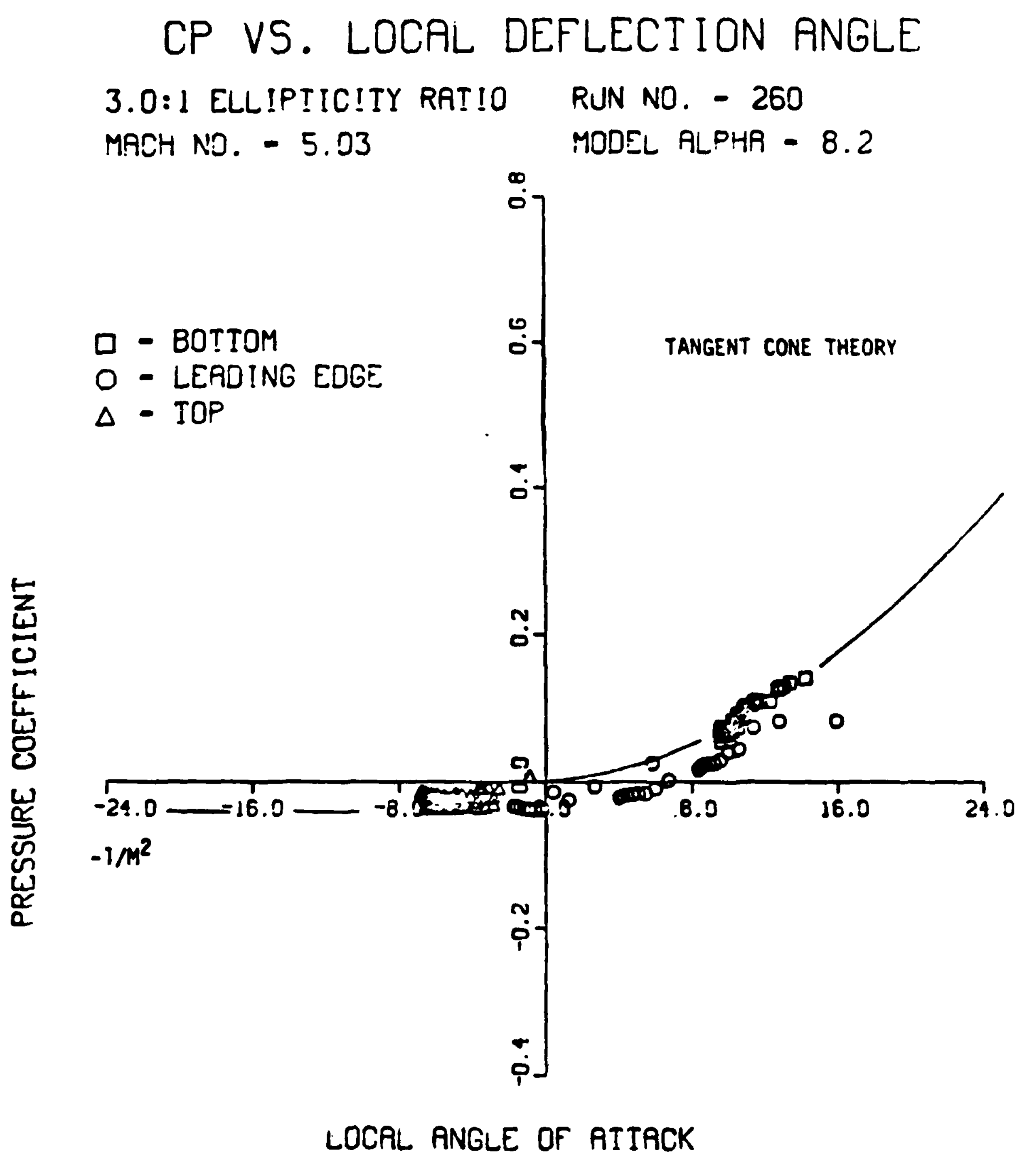

Figure 46. Cp vs. Local Deflection Angle, M = 5.0 (Continued)

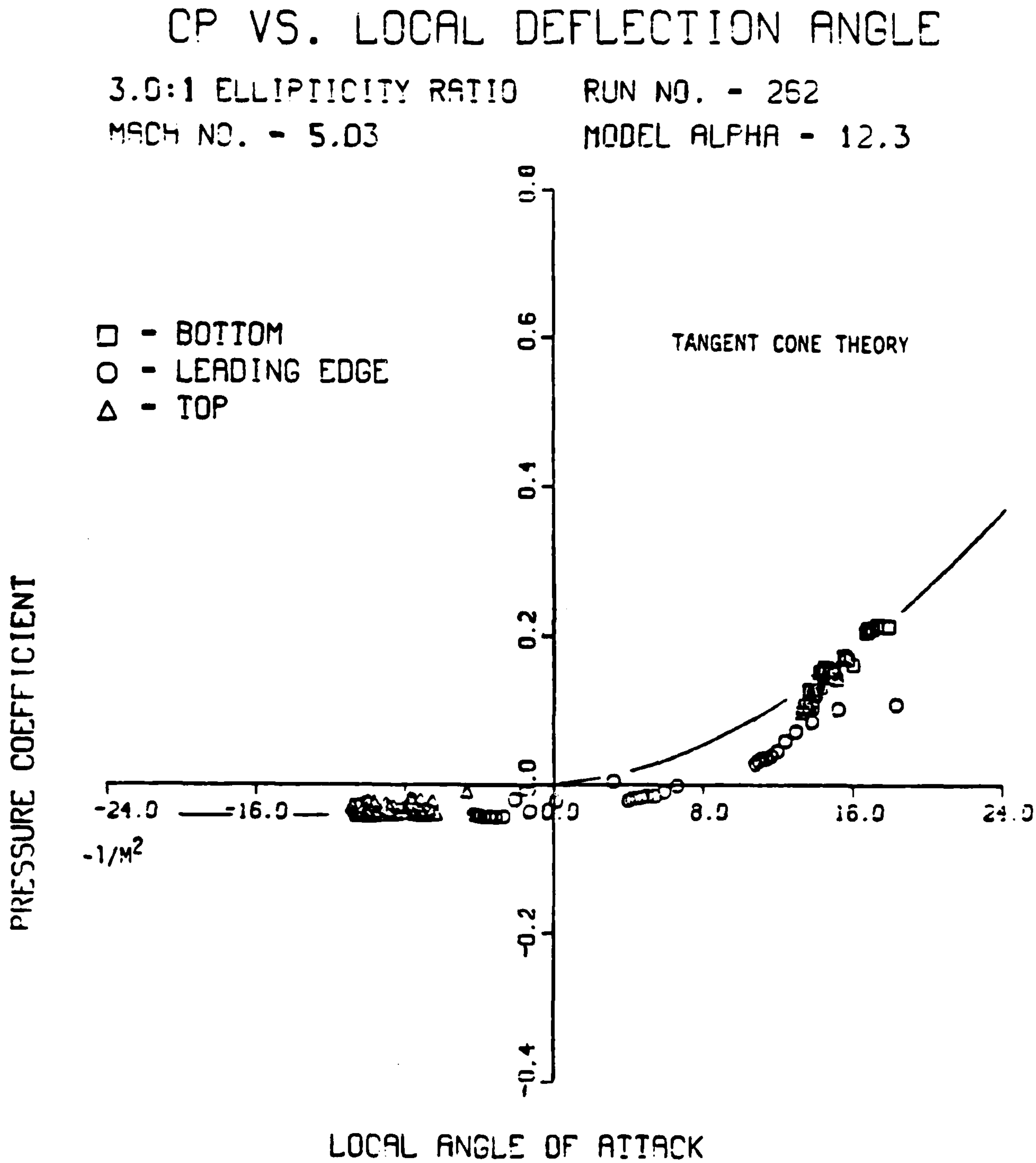

Figure 46. Cp vs. Local Deflection Angle, M = 5.0 (Continued)

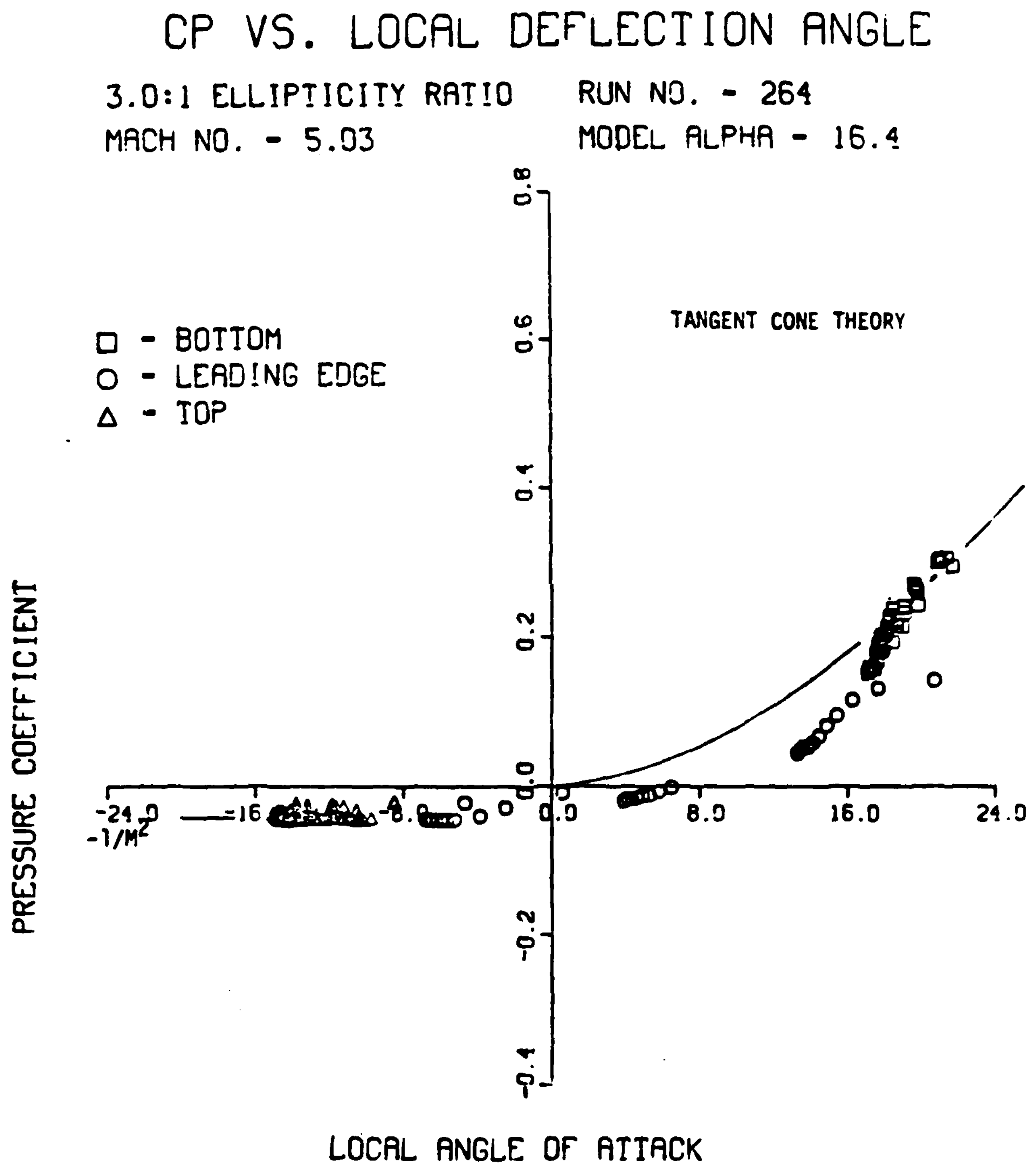

Figure 46. Cp vs. Local Deflection Angle, M = 5.0 (Continued)

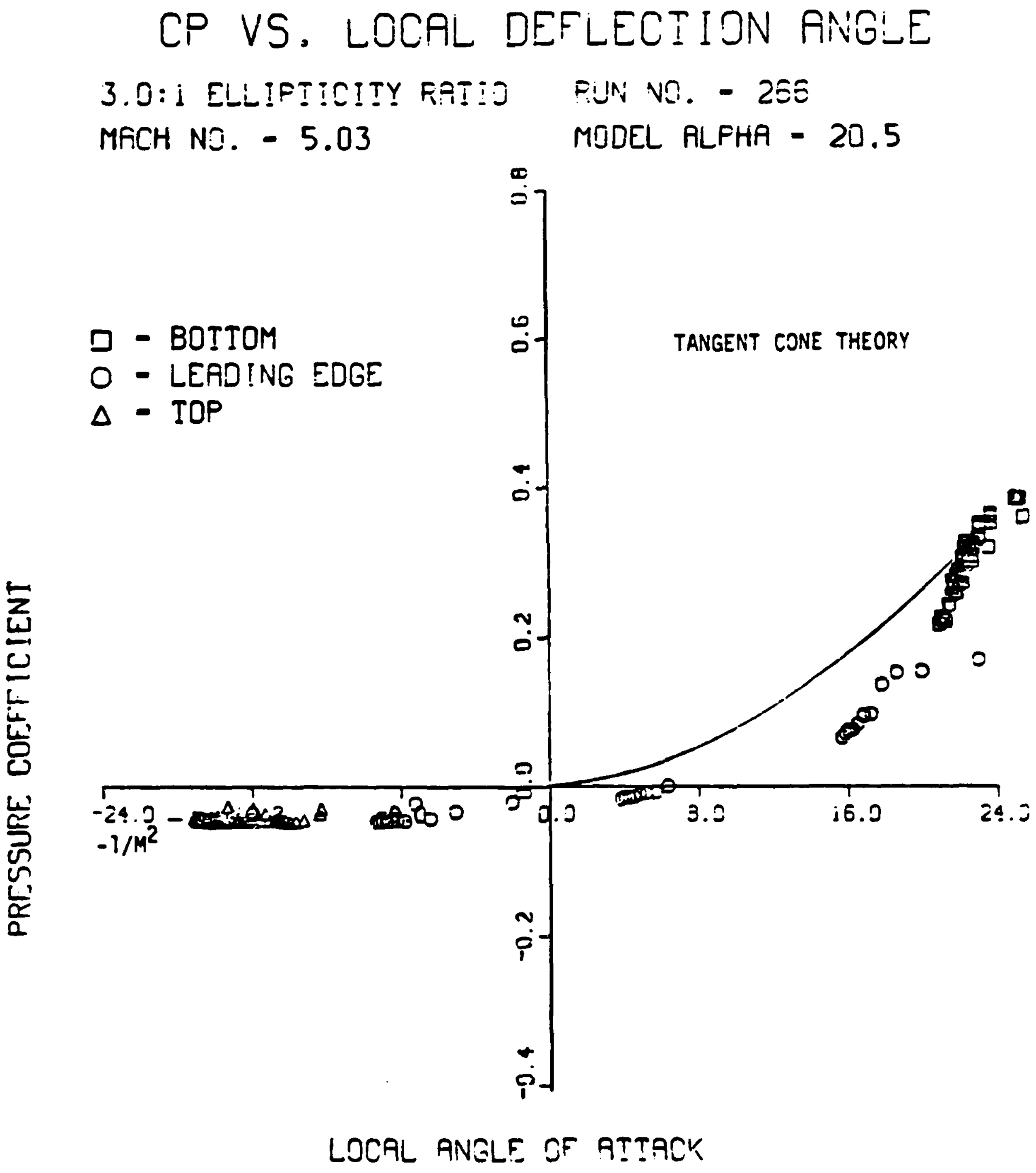

Figure 46. Cp vs. Local Deflection Angle, M = 5.0 (Concluded)

NOMENCLATURE

A, A_R	Reference area, 27.210 $inch^2$
AB	Base area, 27.210 $inch^2$
ALPHA	Angle of attack, degree
a	Semimajor (horizontal) span at X, inch
a_{max}	Semimajor span at model base, in. (see Table 1)
BETA	Sideslip angle, degree
b	Semiminor (vertical) height at X, inch
b_{max}	Semiminor height at model base, inch (see Table 1)
CA, C_A	Forebody axial force coefficient, body axes, CAT-CAB
CAB	Base axial force coefficient, body axes, -(PBA-P)AB/Q*A
CAT	Total axial force coefficient, body axes, total axial force/Q*A
CDS, C_D	Drag coefficient (based on CA), stability axes
CLL, C_l	Rolling moment coefficient, body axes, rolling moment/Q*A*L
CLM, C_m	Pitching moment coefficient, body axes, pitching moment, Q*A*L
CLN, C_n	Yawing moment coefficient, body axes, yawing moment/Q*A*L
CLS, C_L	Lift Coefficient (based on CA), stability axes
CN, C_N	Normal force coefficient, body axes, normal force/Q*A
CODE	Model configuration number
CONFIG	Model configuration designation
Cp	Pressure coefficient, $(P-P_\infty/Q)$
CY, Cy	Side force coefficient, body axes, side force/Q*A
L, l_R	Reference length, Diameter (inch)
L/D_S	Lift-to-drag ratio (based on CA), stability axes
LM	Model length, 36.000 inch
M	Free-stream Mach number
MU	Dynamic viscosity based on free-stream temperature, lbf-sec/ft^2

NOMENCLATURE (Continued)

NCP	Normal force center-of-pressure location, body axes, inches from nose; XMRP-(CLM-L/CN) or XMRP-(CLM-AO*L/CN-AO) for ALPHA = 0 and BETA = 0
P	Free-stream static pressure, psia
PBA	Average base pressure (PBT + PBB + PBL + PBR)/4, psia
PBi	Base pressure, i = T, B, L, and R, where T, B, L, and R are top, bottom, left, and right looking upstream, respectively, psia
psfa	Pound per square foot area
psia	Pound per square inch area
psid	Pound per square inch differential
PHI	Roll angle, degree
PREF	Reference pressure for ZOC pressure module, psia
PT	Tunnel stilling chamber pressure, psia
PT2	Total pressure downstream of a normal shock, psia
Q	Free-stream dynamic pressure, psia
RE	Free-stream unit Reynolds number, ft^{-1}
RHO	Free-stream density, lbm/ft^3
RUN	Data set identification number
T	Free-stream static temperature, °R
TT	Tunnel stilling chamber temperature, °R, or °F
V	Free-stream velocity, ft/sec
X	Axial location from nose of model, inch
XMRP	Axial distance from model nose to model moment-reference location, 24.000 inch
YCP	Side force center-of-pressure location, body axes, inches from nose, XMRP - (CLN*L/CY)

☆U.S.Government Printing Office: 1988 -- 548-054/80758

END
DATE
FILMED
7-88
DTIC